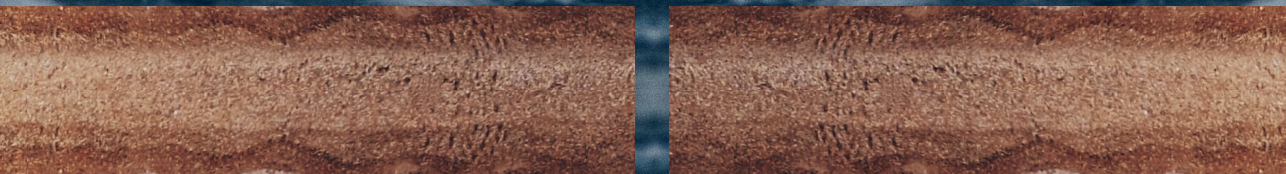


# Static and dynamic solid-water interfaces

Charge regulation, diffusio-osmosis and heterogenous electrokinetics



Ben Werkhoven

# **Static and Dynamic Solid-Water Interfaces**

**charge regulation, diffusio-osmosis and heterogeneous  
electrokinetics**

ISBN: 978-94-6380-682-4

A catalogue record is available from the Utrecht University Library.

Cover design by Ben Werkhoven and Guus Becking

# **Static and Dynamic Solid-Water Interfaces**

**charge regulation, diffusio-osmosis and heterogeneous  
electrokinetics**

**Statische en Dynamische Grensvlakken tussen Vaste Stoffen en Water  
ladingsregulatie, diffusio-osmose en heterogene elektrokinetica**

(met een samenvatting in het Nederlands)

## **Proefschrift**

ter verkrijging van de graad van doctor aan de Universiteit Utrecht op gezag van de rector magnificus, prof. dr. H.R.B.M. Kummeling, ingevolge het besluit van het college voor promoties in het openbaar te verdedigen op

maandag 13 januari 2020 des middags te 2.30 uur

DOOR

**Ben Lucas Werkhoven**

geboren op 14 juni 1991  
te Utrecht

**Promotor:** Prof. dr. R.H.H.G. van Roij

# Contents

<b>List of publications</b>	<b>v</b>
<b>1. Introduction</b>	<b>1</b>
1.1. Statistical physics . . . . .	1
1.2. Solid-water interfaces . . . . .	1
1.2.1. Adsorption and desorption . . . . .	2
1.2.2. The electric double layer . . . . .	4
1.3. Electrokinetics . . . . .	6
1.3.1. Fluid flow . . . . .	6
1.3.2. Electrokinetic transport properties . . . . .	8
1.4. Outline . . . . .	9
<b>2. Theory of ions in fluids</b>	<b>13</b>
2.1. Equilibrium . . . . .	13
2.1.1. Density functional theory . . . . .	13
2.1.2. Planar geometry . . . . .	15
2.1.3. Charge regulation . . . . .	17
2.2. Out-of-equilibrium . . . . .	20
2.2.1. Dynamical density functional theory . . . . .	20
2.2.2. Fluid flow . . . . .	22
2.2.3. The Onsager matrix in electrokinetic systems . . . . .	23
<b>I. Static Interface &amp; Static Fluid</b>	<b>24</b>
<b>3. CsCl ion adsorption on muscovite mica</b>	<b>26</b>
3.1. Introduction . . . . .	28
3.2. Interfacial structure . . . . .	29
3.3. Surface complexation model . . . . .	30
3.4. Development of the surface complexation model . . . . .	33
3.4.1. Low salinity limit: H <sup>+</sup> adsorption . . . . .	34
3.4.2. High coverage limit: anion coadsorption . . . . .	35

3.5. Summary & conclusion . . . . .	38
<b>4. Cs<sup>+</sup>/Ca<sup>2+</sup> competition on muscovite mica</b>	<b>39</b>
4.1. Introduction . . . . .	40
4.2. Interfacial structure . . . . .	40
4.3. Cs <sup>+</sup> /Ca <sup>2+</sup> competition . . . . .	44
4.4. Discussion & conclusion . . . . .	47
<b>II. Static Interface &amp; Dynamic Fluid</b>	<b>50</b>
<b>5. Transport in heterogeneous electrokinetic systems</b>	<b>53</b>
5.1. Introduction . . . . .	54
5.2. Transport In electrokinetics . . . . .	54
5.3. From local to global linear response . . . . .	57
5.3.1. Local linear Response . . . . .	57
5.3.2. Global linear response . . . . .	58
5.3.3. Entrance effects . . . . .	62
5.4. The Onsager matrix . . . . .	64
5.5. Validating the formalism . . . . .	67
5.6. Reverse electrodyalisis . . . . .	69
5.7. Summary & conclusion . . . . .	75
<b>6. Diffusio-osmotic entrance effects and interaction between channels</b>	<b>76</b>
6.1. Introduction . . . . .	78
6.2. Charge of the exterior . . . . .	79
6.3. Interacting channels . . . . .	82
6.3.1. Cell model . . . . .	82
6.3.2. The channel-channel interaction . . . . .	84
6.3.3. Optimisation . . . . .	86
6.4. Summary & conclusion . . . . .	90
<b>III. Dynamic Interface &amp; Dynamic Fluid</b>	<b>92</b>
<b>7. Flow-induced surface charge heterogeneity: Numerical approach</b>	<b>95</b>
7.1. Introduction . . . . .	96
7.2. Theory . . . . .	98
7.3. Steady state . . . . .	100

7.4. Dynamics . . . . .	103
7.5. Summary & conclusion . . . . .	105
<b>8. Flow-induced surface charge heterogeneity: Analytical approach</b>	<b>107</b>
8.1. The (linearised) Poisson-Nernst-Planck equations . . . . .	108
8.2. Solving the equations . . . . .	109
8.3. Three electrokinetic regimes . . . . .	113
8.3.1. Reaction-dominated regime . . . . .	114
8.3.2. Diffusion-dominated regime . . . . .	116
8.3.3. The conduction-dominated regime . . . . .	118
8.4. Summary & conclusion . . . . .	120
<b>APPENDICES</b>	<b>122</b>
<b>A. Part I</b>	<b>123</b>
A.1. Surface complexation model . . . . .	123
A.2. $\text{Cs}^+/\text{H}^+$ competition model . . . . .	125
A.3. Hydroxide coadsorption . . . . .	127
A.4. Lateral interaction between adsorbed ions . . . . .	129
<b>B. Part II</b>	<b>131</b>
B.1. Poisson-Boltzmann identities . . . . .	131
B.2. Symmetry Onsager matrix . . . . .	132
B.3. Derivation $\mathbf{G}^{\text{vol}}$ . . . . .	134
B.4. Entrance effects . . . . .	135
B.5. Simulation domain . . . . .	136
B.6. Validation theory: parameter variation . . . . .	137
<b>C. Part III</b>	<b>139</b>
C.1. Current of surface charges . . . . .	139
C.2. Simulation domain . . . . .	140
C.3. Electric body force . . . . .	142
C.4. The system size . . . . .	143
C.5. Derivation of zeta potential and net charge current . . . . .	144
<b>Bibliography</b>	<b>147</b>
<b>Discussion and Outlook</b>	<b>159</b>
<b>Samenvatting voor iedereen</b>	<b>161</b>

**Acknowledgements**

**171**

**About the author**

**173**

# List of publications

This thesis is based on the following articles:

- Chapters 3 & 4  
Sander J.T. Brugman\*, Ben L. Werkhoven\*, Eleanor R. Townsend, Paolo Accor-dini, René van Roij, and Elias Vlieg, *Monovalent - divalent cation competition at the muscovite mica surface: experiment and theory*, Journal of Colloid and Interface Science **559**, 291 (2020)
- Chapter 5  
Ben L. Werkhoven and René van Roij, *Coupled water, charge and salt transport in heterogeneous nano-fluidic systems*, submitted, arXiv preprint:1911.13156
- Chapter 6  
Ben L. Werkhoven and René van Roij, *Scaling up diffusio-osmotic currents: from single channel to membrane*, in preparation
- Chapter 7  
B. L. Werkhoven, J.C. Everts, S. Samin, and René van Roij, *Flow-induced surface charge heterogeneity in electrokinetics due to Stern-layer conductance coupled to reaction kinetics*, Physical Review Letters, **120**, 264502 (2018)
- Chapter 8  
B. L. Werkhoven, S. Samin, and René van Roij, *Dynamic Stern layers in charge-regulating electrokinetic systems: three regimes from an analytical approach*, the European Physical Journal Special Topics **227**, 2539 (2019).

\* These authors contributed equally

All works are part of the D-ITP consortium, a program of the Netherlands Organisation for Scientific Research (NWO) that is funded by the Dutch Ministry of Education, Culture and Science (OCW). This work is a part of an Industrial Partnership Program of the Netherlands Organization for Scientific Research (NWO) through FOM Concept agreement FOM-15-0521. Financial support was provided through the Exploratory Research (ExploRe) programme of BP plc.



# Chapter 1.

## Introduction

### 1.1. Statistical physics

Atomic theory is surely one of the most important theories of modern science. This theory states that matter consists of tiny, Ångstrom-sized ( $\sim 10^{-10}$  m) particles in perpetual motion, called atoms. The roots of atomic theory can be traced back the ancient Greek philosophers Democritus and Leucippus, who postulated nearly 2500 years ago that everything is composed of indivisible particles in perpetual motion, with an empty space or vacuum separating them. Here we find the origin of the name 'atom', which is derived from the Greek word ἄτομον (atomon) for indivisible. By now, we know now that atoms actually are divisible, and are composed of electrons, protons, quarks etc., but since atoms only break under extreme circumstances this is of no concern to us here. In this thesis we can safely regard atoms and molecules (groups of covalently bound atoms) as the primary constituents of matter.

Since atoms are so small, macroscopic matter consists of a vast number of atoms. The goal of statistical physics is to consider such large collections of atoms and/or molecules and derive properties of these collections, such as pressure, volume and temperature, without explicitly calculating the behaviour of each single constituent. We know that the statistics of such large collections give accurate characterisations of macroscopic systems, due to the enormous number of atoms. This feature makes statistical physics such a widely applicable and important theory in physics, and the best framework to describe the thermodynamic properties of macroscopic systems. In this thesis, we will apply statistical physics to a common and important system: a solid surface in contact with water.

### 1.2. Solid-water interfaces

What is so interesting about interfaces? Many macroscopic systems have a relatively large volume to surface area ratio, and for this reason the bulk properties are seldom

affected by the interface. It is, however, at the interface where different phases interact. In our everyday life, the vast majority of interactions between different objects or phases occur through contact forces (excluding gravity and an occasional encounter with electromagnetism). Contact forces are very short ranged and thus, naturally, mediated by the interface, so understanding static and dynamic interfacial properties is an important endeavour.

An important reason to focus on solid-water interface specifically is because they are ubiquitous, since water itself is ubiquitous, and solid-water interfaces are consequently encountered in a wide variety of fields, such as geology, catalysis and biology. In order to describe solid-water interfaces we must account for ions, atoms and/or molecules that carry a net charge, because there are always ions present in water. Even perfectly deionised water has a pH equal to 7, which means that trace amounts ( $0.1 \mu\text{M}$ ) of  $\text{H}_3\text{O}^+$  and  $\text{OH}^-$  ions remain due to self-ionisation of  $\text{H}_2\text{O}$ . Moreover, exposing deionised water to air under standard atmospheric conditions results in dissolution of  $\text{CO}_2$ , lowering the pH to approximately 6 ( $1 \mu\text{M}$  concentration  $\text{H}_3\text{O}^+$ ). Moreover, all naturally occurring water has a small amount of other ionic species, NaCl being the most ubiquitous. In short, water always contains ions, and as we will discuss below, ions can have a significant effect on the solid-water interface.

### 1.2.1. Adsorption and desorption

Why do ions affect the solid-water interface? To understand this, two points must be discussed. Firstly, ions interact differently with water than with a solid, so the solid-water interface presents a unique environment to the ions. The interface can be either a favourable region, such that ions are attracted to it, or an unfavourable region such that ions are repelled from it. In general, this results in two distinct scenarios: ions either desorb (an ion is released and expelled from the interface) or adsorb (an ion is attracted and confined to the interface).

Secondly, ions carry a net charge. If the ad- and desorption processes are different for the positively and the negatively charged ions, the interface acquires a net charge. This makes the solid-water interface very different from bulk water and solid, which are (in general) electrically neutral on scales beyond the molecular length. An interface with a non-zero net charge will interact strongly with ions dissolved in the water phase, giving the interface unique features not encountered in the bulk. We will discuss these features in Section 1.2.2, but first we should address why ions ad- or desorb in the first place.

A solid-water interface with a non-zero net charge may sound, at first, as a rare occurrence. Surprisingly, however, it has been well established that the vast majority of surfaces spontaneously obtain a non-zero charge when submersed in water, even

insulators like silica [1], clay [2] and PMMA [3]. The ad- and desorption mechanisms through which materials obtain a surface charge vary, but are commonly categorised as chemisorption and physisorption of ions. Chemisorption is the process where an ion binds to the surface by forming a covalent bond, or is released from the surface by breaking one. For example, the main mechanism via which silica obtains a net surface charge is by the deprotonation of silanol (SiOH) surface groups [4]. Physisorption is the process where an ion is constrained to the surface by other forces. There are many different mechanisms for physisorption, e.g. the van der Waals force, but one of the most common mechanisms, when water is the solvent, is due to the hydration shell of the ion [5, 6].

When salt dissolves in water, the cation (positively charged ion) and the anion (negatively charged ion) separate. Since water molecules have permanent dipoles, ions obtain a shell of water molecules with their dipole moment directed radially towards (anion) or away from (cation) the ion. This is the hydration shell. An ion adsorbs to the interface if the system, as a whole, gains a net free energy if it sheds or rearranges its hydration shell when positioned at the solid surface. The ion can either be in direct contact with the surface (inner-sphere adsorption), or the ion and the surface are bridged by a hydration water molecule (outer-sphere adsorption), see Fig. 1.1. The free energy of this shell, and thus the free energy gained or lost upon adsorption, depends on parameters such as the size and charge of the ion [7–9]. Every ion therefore has a different adsorption or desorption energy, which, in addition, depends on the hydration water layer of the surface [5].

Adsorption and desorption are, in principle, the result of complicated, many-body interactions. However, while the mechanisms and specifics of chemi- and physisorption vary greatly, the result is the same for all: an ion adsorbs (desorbs) to (from) the surface, i.e. it is confined (expelled) in the direction perpendicular to the surface, because there is a local minimum (maximum) in the free energy landscape close to the surface. This minimum/maximum can have different origins (covalent bonds, van der Waals forces etc.), but its presence has profound implications for the solid-water interface.

Adsorption and desorption are, in principle, the result of complicated, many-body interactions. However, while the mechanisms and specifics of chemi- and physisorption vary greatly, the result is the same for all: an ion adsorbs (desorbs) to (from) the surface, i.e. it is confined (expelled) in the direction perpendicular to the surface, because there is a local minimum (maximum) in the free energy landscape close to the surface. This minimum/maximum can have different origins (covalent bonds, van der Waals forces etc.), but its presence has profound implications for the solid-water interface.

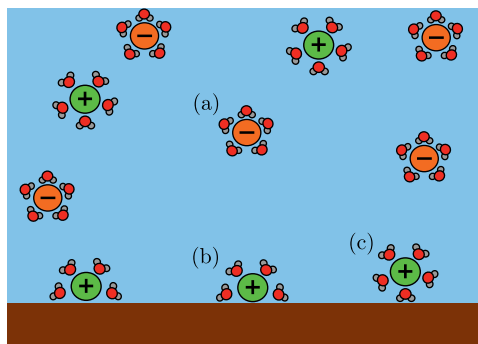


**Figure 1.1.:** Artistic representation of (a) a hydrated free ion, (b) an inner-sphere adsorbed ion and (c) an outer-sphere adsorbed ion. Only the hydration-shell water molecules are shown, the remaining ones are represented by the blue background.

### 1.2.2. The electric double layer

The result of all these ionic adsorption and desorption processes is a net charge at the solid-water interface. The macroscopic system as a whole is intrinsically charge neutral, so there must be an equal amount of charge with opposite sign in the fluid. This results in a capacitor, where the charge on the water/solid boundary is separated from an equal but opposite amount of charge in the fluid. This capacitor is known as the Electric Double Layer (EDL), and it will feature prominently throughout this thesis. In fact, the EDL truly is the main protagonist of this thesis.

Historically, the first model to describe the EDL was constructed by Helmholtz [10], who stated that free ions in the fluid will adsorb on top of the surface charges and form a second layer of charges on top of the first (hence *Electric Double Layer*). At first glance, this model makes sense, as it minimises the electrostatic energy  $U$  of the configuration. However, the Helmholtz model does not take thermal fluctuations into account, and even though it minimises the energy it is a configuration with a very low entropy  $S$ . In other words, the Helmholtz model minimises the energy  $U$ , rather than the Helmholtz free energy  $F = U - TS$  (with  $T$  the temperature), even though, ironically,  $F$  bears Helmholtz's name.

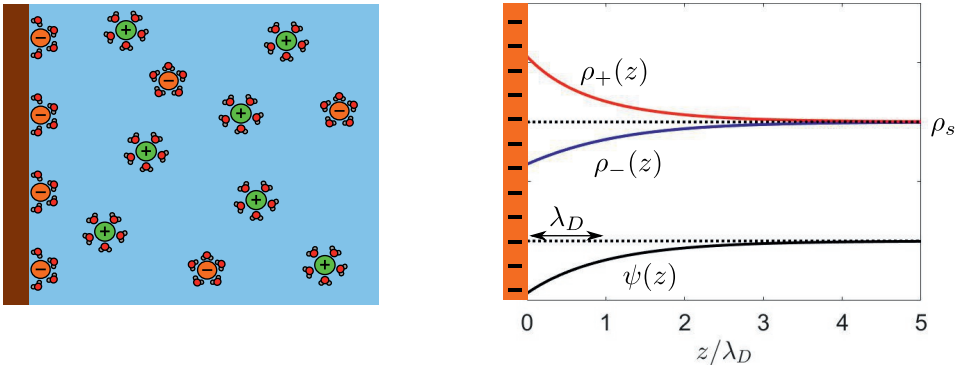


**Figure 1.2.:** The Electric Double Layer of a negatively charged surface in contact with a monovalent ionic solution of salinity  $\rho_s$ , with cation density  $\rho_+(z)$ , anion density  $\rho_-(z)$  and electrostatic potential  $\psi(z)$ , with  $z$  the distance to the surface.

A significant improvement upon Helmholtz's model was formulated by Gouy [11], who realised that thermal fluctuations play an important role in determining the structure of the EDL. For example, if the surface carries a net negative charge, cations will be attracted to the surface and anions are repelled from the surface. However, instead of forming a condensed layer of only cations and excluding all anions, a concentration *gradient* will form towards the surface. The cation concentration will

thus gradually increase, and the anion concentration will gradually decrease, with respect to the bulk value upon approaching the interface. The equilibrium profile will be such that the electrostatic stress and the osmotic pressure (resulting from concentration gradients) cancel each other. The result is a diffuse region next to the charged surface, with an excess of counter ions and a deficit of co-ions but both able to diffuse into the water phase. This region is commonly referred to as the ‘diffuse layer’. The size of the diffuse layer of the EDL depends on the salt concentration, and is characterised by the so-called Debye length  $\lambda_D$ , see Fig. 1.2, which for water is typically between a few Å and a few hundred nanometers.

The formalism that Gouy developed is still the most widely used formalism to describe the EDL, and is known as the Poisson-Boltzmann formalism. As the name implies, this formalism is based on a combination of the Poisson equation of electrostatics and the Boltzmann distribution from statistical physics. The Poisson equation relates the electrostatic potential  $\psi$  to the local charge density  $q_e$

$$\nabla^2\psi(\mathbf{r}) = -\frac{q_e(\mathbf{r})}{\epsilon} = -\frac{e}{\epsilon} \sum_i z_i \rho_i(\mathbf{r}). \quad (1.1)$$

Here  $\rho_i$  and  $z_i$  are the density and valency of ion species  $i$ ,  $e$  is the proton charge,  $k_B$  Boltzmann’s constant,  $T$  the temperature and  $\epsilon$  the permittivity of the solvent ( $T$  and  $\epsilon$  are presumed to be spatial constants). Within the Poisson-Boltzmann formalism, a mean-field Boltzmann distribution for the ion densities  $\rho_i$  provides a second relation between  $\psi$  and the ion densities. In this mean-field Boltzmann distribution, the ion densities are shifted with respect to the bulk value by the Boltzmann weight of the local mean-field electrostatic energy, i.e.

$$\rho_i(\mathbf{r}) = \rho_{b,i} e^{-z_i \frac{e}{k_B T} \psi(\mathbf{r})}, \quad (1.2)$$

with  $\rho_{b,i}$  the density in the bulk water phase. Additionally, since the bulk water phase is charge neutral, i.e.  $\sum_i z_i \rho_{b,i} = 0$ , we have that the electric field vanishes far from the interface, which allows us to fix  $\psi = 0$  in the bulk. Combining Eqs. (1.1) and (1.2) we find the Poisson-Boltzmann equation [12–15]

$$\nabla^2\psi(\mathbf{r}) = -\frac{e}{\epsilon} \sum_i z_i \rho_{b,i} e^{-z_i \frac{e}{k_B T} \psi(\mathbf{r})}, \quad (1.3)$$

which provides a self-consistency relation for the electrostatic potential. As a boundary condition to the Poisson-Boltzmann equation we use Gauss’s law of electrostatics,

which couples the electrostatic potential to the surface charge,

$$\hat{\mathbf{n}} \cdot \nabla \psi = -\frac{z_\sigma e \sigma}{\epsilon}, \quad (1.4)$$

where  $\sigma > 0$  is the areal density of surface charges (dimension  $e/\text{nm}^2$ ),  $z_\sigma$  the sign of the surface charge and  $\hat{\mathbf{n}}$  the unit vector normal to the charged surface (pointing into the fluid).

The above treatment serves as an intuitive method to understand the physics underlying the Poisson-Boltzmann equation. There is a more rigorous derivation to derive Eq. (1.3) from Density Functional Theory, which we will explain in Section 2.1.1. In Section 2.1.2 we discuss the relevant length scales and present the most important solution to the Poisson-Boltzmann equation, a charged flat plate.

## 1.3. Electrokinetics

The EDL is an important equilibrium property of the solid-water interface. However, since water is a fluid, it is often in motion. A straightforward question follows: what happens when water is not stationary, but flowing past the solid? The combination of an EDL combined with fluid flow is the basis of the field of electrokinetics. In this thesis, we consider typical electrokinetic systems composed of micro- and/or nanofluidic channels [12, 16–20]. The novel properties of nanofluidic channels arise due to their small size. The smaller the size, the higher the area to volume ratio is. The higher the area to volume ratio is, the more pronounced the interfacial properties are. The EDL is confined to the surface (up to a few hundred nanometres), which means that the EDL can greatly affect the properties of a nanofluidic device. By tuning the system size and the solution properties, electrokinetic channels exhibit interesting behaviour which is absent or negligible in larger channels. Nanofluidic devices thus provide a playground to investigate solid-water interfaces, but the unique properties of solid-water interfaces have also led to applications in a wide variety of well-established research fields [12, 21] such as geology [22], catalysis [23] and (blue-)energy harvesting [24, 25]. The great potential of nanofluidic devices is additionally attested by biological systems, which show an amazing control over permeability and selectivity of nanochannels [12, 26–28].

### 1.3.1. Fluid flow

Before discussing electrokinetic systems, let us first discuss fluid flow in general. Motion of a fluid at position  $\mathbf{r}$  and time  $t$  is quantified by the fluid-velocity vector  $\mathbf{u}(\mathbf{r}, t)$ . The most important and well-established equation to describe the flow of

viscous, incompressible fluids is the Navier-Stokes equation,

$$\rho_m \frac{\partial \mathbf{u}}{\partial t} + \rho_m (\mathbf{u} \cdot \nabla) \mathbf{u} = -\nabla p + \eta \nabla^2 \mathbf{u} + \mathbf{f}, \quad \nabla \cdot \mathbf{u} = 0. \quad (1.5)$$

The first equation is based on Newton's second law of motion (see [13, 29] for a derivation), and essentially concerns conservation of linear momentum. On the left hand side of Eq. (1.5) is the full (material) time derivative of the velocity vector, i.e. the acceleration, with  $\rho_m$  the mass density of the fluid, and on the right hand side of Eq. (1.5) the force density of the fluid element at position  $\mathbf{r}$  at time  $t$ . The second equation ensures that the fluid volume is conserved. It is derived from the conservation of mass, but since water is incompressible under all conditions considered in this thesis, this relation reduces to the conservation of volume. In Eq. (1.5), we have already explicitly taken two of the most important forces that act on the fluid into account: the gradient of the total pressure  $p$  and the internal viscous forces in the fluid, with  $\eta$  the viscosity. All other body forces, such as gravity, are represented by the body force  $\mathbf{f}$  (dimensions  $\text{N/m}^3$ ).

A common and very useful simplification of Eq. (1.5) is Stokes equation, which is used for fluids where the inertial terms, represented by the left hand side of Eq. (1.5), are small compared to the viscous force. The ratio between inertial and viscous forces are quantified by the Reynolds number  $\text{Re}$ ,

$$\text{Re} = \frac{\rho_m u_0 \ell}{\eta}, \quad (1.6)$$

where  $u_0$  and  $\ell$  are a typical velocity and length scale of the system of interest, respectively. If  $\text{Re} \ll 1$ , one can safely set the left hand side of Eq. (1.5) to zero. This approximation is commonly used for fluid flow on very small scale (in which case  $\ell$  is small). For example, for water in microfluidic systems, the type of systems we will consider in this thesis, we typically have that  $\ell \approx 1 \mu\text{m}$ ,  $u_0 < 1 \text{ mm/s}$ ,  $\rho_m \approx 10^3 \text{ kg/m}^3$  and  $\eta \approx 10^{-3} \text{ Pa s}$ , such that  $\text{Re} < 10^{-3}$ .

The most important body force we will consider in this thesis is the electric body force. If the fluid carries a certain non-zero net charge density  $q_e$  (for example in the Electric Double Layer, see Section 1.2.2), and if there is an electric field  $\mathbf{E}$ , the fluid will experience the electric body force  $\mathbf{f}_e = q_e \mathbf{E}$ . Stokes's equation then reduces to

$$0 = -\nabla p + \eta \nabla^2 \mathbf{u} + q_e \mathbf{E}, \quad \nabla \cdot \mathbf{u} = 0. \quad (1.7)$$

Note that a significant advantage of the Stokes equation compared to the Navier-Stokes equation is that Eq. (1.7) is linear, while Eq. (1.5) is nonlinear in the fluid velocity  $\mathbf{u}$ .

### 1.3.2. Electrokinetic transport properties

To illustrate how fluid flow past a charged surface leads to interesting phenomena, let us consider a classic electrokinetic system. Suppose we have a channel with charged surfaces, with an associated EDL, which connects two large water reservoirs. We enforce a fluid flow through the channel by applying a pressure drop  $\Delta p$  across the channel. If the EDL is absent, water will flow and is transported from one reservoir to the other, and this would be the end of the story. However, due to the presence of the EDL, there is now a volume charge present next to the solid-water interface. The moving fluid carries some of this charge with it, effectively generating an electric current known as the streaming current. The EDL thus makes it possible to generate an electric current by imposing a fluid flow through the channel.

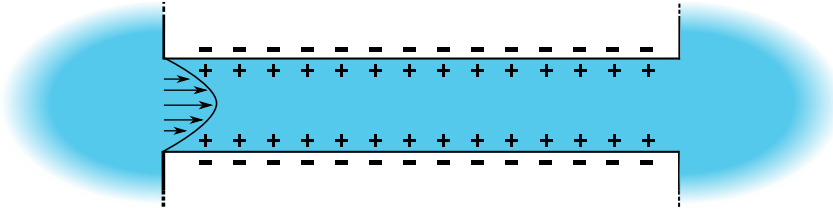


**Figure 1.3.:** A typical electrokinetic system: a channel with charged surfaces connecting two fluid reservoirs.

In steady state, the streaming current can, however, only exist if the two water reservoirs are electrically connected. Actually, it is more common and natural that the two reservoirs are not electrically connected. Even if the reservoirs are not electrically connected, however, there is still fluid flow through the EDL that generates a streaming current. The only way the total current can then vanish in steady state, is for the system to develop an electric field to counteract the charge transport of the streaming current. This electric field, known as the streaming electric field, implies a voltage drop  $\Delta V_S$  across the channel, the streaming potential. The magnitude of  $\Delta V_S$  depends on the fluid velocity, and has been shown by Helmholtz [30] and Smoluchowski [31] to be linearly related to the applied pressure drop  $\Delta p$ , expressed in the so-called the Helmholtz-Smoluchowski equation

$$\Delta V_S = -\frac{\zeta \epsilon}{\eta G_{\text{ch}}} \Delta p, \quad (1.8)$$

where  $\epsilon$ ,  $\eta$  and  $G_{\text{ch}}$  are the dielectric permittivity, shear viscosity and conductivity of the fluid, and  $\zeta$  or zeta potential is the electrostatic potential at the slipping plane, which is the plane that separates the mobile fluid from the immobile fluid at the solid-water

interface. The zeta potential is usually well approximated by the potential drop across the diffuse layer [32].

Just like a fluid flow induces a voltage drop across the channel, electrokinetic systems have the interesting property that the inverse is also true: an imposed voltage drop induces a fluid flow. This can be seen from Eq. (1.7). The EDL provides the space charge density  $q_e$ , such that an imposed electric field generates a non-zero electric body force  $\mathbf{f}_e$ , which induces a fluid flow. This shows a symmetry in linear-response (electrokinetic) transport, which is actually a general property of electrokinetics: due to the presence of the EDL, different modes of transport and driving forces are coupled. For example, if the salinity of the two reservoirs differ, the resulting salinity gradient will not only induce a fluid flow but also an electric current, while a fluid flow or voltage drop induce a salt flux.

The majority of electrokinetic systems are concerned with three different types of transport: a volume flux or volumetric flow rate  $Q$ , a charge flux or electric current  $I$  and a net salt flux  $J$ . These fluxes can be generated by a pressure drop  $\Delta p$ , voltage drop  $\Delta V$  and salt chemical potential drop  $\Delta\mu$  over the channel (for a dilute electrolyte,  $\mu = k_B T \log \rho_s$ , with  $\rho_s$  the salinity of the electrolyte). Within linear-response theory, the induced fluxes are linear in the driving forces, and can be conveniently expressed using a generalised  $3 \times 3$  conductivity matrix  $\mathbf{G}$ :

$$\begin{pmatrix} Q \\ I \\ J \end{pmatrix} = \frac{A}{\ell} \mathbf{G} \begin{pmatrix} \Delta p \\ \Delta V \\ \Delta\mu \end{pmatrix}, \quad (1.9)$$

where  $A$  and  $\ell$  are the cross-section area and length of the channel. The interesting properties of electrokinetic systems arise from the off-diagonal components of  $\mathbf{G}$ , such that, for example, a salinity drop not only induces a salt flux  $J$  between the two reservoirs, but also a fluid flow and electric current. The (majority of the) off-diagonal components are due to the Electric Double Layer. The EDL creates gradients in the cation concentration, anion concentration and electrostatic potential normal to the surface, which consequently affects fluxes parallel to the surface (as explained above). The conductivity matrix  $\mathbf{G}$  is crucial in order to quantify the transport behaviour of electrokinetic systems.

## 1.4. Outline

This thesis is divided into three main parts. In the first part both the fluid and the solid-water interface is in equilibrium, in the second part the fluid is flowing but the

interface remains static, and in the final part both the fluid and the interface are treated as fully dynamic systems. In turn, each part is subdivided in two chapters. Every first chapter introduces the most important concepts of that part, and can thus be read on its own, but the second chapter of each part builds upon the knowledge or model introduced in the preceding chapter. Each chapter is prefaced with a short summary of the results of that chapter, and in which section those results are discussed.

Chapter 2, however, is not part of any of the three parts. This chapter is reserved for a discussion of theories that are already well established in literature, and are, for the sake of brevity, not included in the three parts. These involve calculations that are strictly not necessary to understand the material discussed in the chapters themselves, and only serve as additional background information for the interested reader.

In part I, we consider a system where the fluid is undisturbed and the solid-water interface is in its equilibrium state. The solid of interest in this part is muscovite mica, a type of clay, and we investigate the adsorption behaviour of different types of ions: in Chapter 3 we focus on  $\text{Cs}^+$  while in Chapter 4 we focus on  $\text{Ca}^{2+}$  and the competition between  $\text{Ca}^{2+}$  and  $\text{Cs}^+$ . We present the results from two different experimental techniques, Surface X-Ray Diffraction and Atomic Force Microscopy. Demanding that a model reproduces the results from these two very different measurements techniques imposes several restrictions on that model. This forced us to refine models currently used in literature, as these are unable to reproduce both data sets simultaneously. The model we develop is able to do this, which makes it more likely that this model accurately represents the actual physical processes at the mica-water interface.

In part II we consider an electrokinetic system, where the fluid is now flowing while the solid-water interface itself remains static. In this part, we study the effects of the Electric Double Layer on the transport properties of such electrokinetic systems. In Chapter 5 we introduce a general formalism to describe heterogeneous channels. We derive a global linear response equation from a well-established local linear response equation. The former can incorporate lateral heterogeneities which the latter cannot. As an example, we analyse diffusio-osmosis, which involves a channel with intrinsic heterogeneities due to an imposed salinity gradient, and validate our model by comparing it with numerical solutions of the governing equations. We then use the derived formalism to analyse a common electrokinetic system used in Reverse Electrodialysis, a promising method that generates an electric current from mixing sea and river water. In Chapter 6, we shift the focus from the interior to the exterior of the channel, and find that, if a salinity gradient is imposed, the transport properties of the channel are influenced by the exterior of the channel. The effect increases drastically if we embed a single channel in an array of channels to mimic a membrane. We find that adjacent channels reduce the transport through the channels, and thus that the behaviour of a single channel is not straightforwardly extrapolated to an array of channels. We

investigate how to distribute the channels over the membrane, and the effect of the length and radius of the individual channels, in order to optimise the electric current per unit membrane area.

In part III both the fluid and the solid-water interface are treated in a fully dynamic fashion. Earlier studies have found that the surface charges of solid-water interfaces are not static entities, but are dynamic just like the ions dissolved in water. We investigate the consequences of dynamic surface charges for electrokinetic systems, first numerically in Chapter 7, and then analytically in Chapter 8. The numerical calculations allow us to fully investigate the steady state as well as the dynamic behaviour, which we then use to provide an alternative explanation of experimental observations. The analytical analysis allows us to dive deeper into the governing equations and identify three time scales and three associated qualitatively different regimes that govern the behaviour of the system. This provides an intuitive picture to understand this rather complicated system.



# Chapter 2.

## Theory of ions in fluids

### 2.1. Equilibrium

#### 2.1.1. Density functional theory

Density Functional Theory (DFT) is a theoretical statistical-physics formalism that is used to describe inhomogeneous classical fluids in equilibrium. DFT started as theory for inhomogeneous electron gases [33], but was later extended to apply to classical fluids [34]. This chapter only serves to explain how to obtain the Poisson-Boltzmann formalism from DFT, and set up a basis from which to extend it. For a more detailed overview and derivation of DFT we refer the reader to other, more extensive studies on DFT [13, 35–37].

Density Functional Theory is a very successful framework to describe the equilibrium properties of inhomogeneous fluids. The governing equation of Density Functional Theory is derived from the notion that the equilibrium density profiles  $\rho_i^{\text{eq}}(\mathbf{r})$  are given by the minimum of the grand potential functional  $\Omega[\rho_i(\mathbf{r})]$ , for an  $n$ -component fluid given by

$$\Omega[\{\rho_i(\mathbf{r})\}] = \mathcal{F}[\{\rho_i(\mathbf{r})\}] + \sum_{i=1}^n \int d\mathbf{r} \rho_i(\mathbf{r}) (V_{\text{ext},i}(\mathbf{r}) - \mu_i), \quad (2.1)$$

with  $\mu_i$  the chemical potential of species  $i$ ,  $V_{\text{ext},i}(\mathbf{r})$  the external potential acting on species  $i$ , and  $\mathcal{F}[\{\rho_i(\mathbf{r})\}]$  the intrinsic Helmholtz free energy functional. The governing equation of DFT states that  $\Omega$  is minimised by the equilibrium density profile, and is therefore given by

$$\left. \frac{\delta \Omega}{\delta \rho_i(\mathbf{r})} \right|_{\rho_i(\mathbf{r})=\rho_i^{\text{eq}}(\mathbf{r})} = \left. \frac{\delta \mathcal{F}}{\delta \rho_i(\mathbf{r})} \right|_{\rho_i(\mathbf{r})=\rho_i^{\text{eq}}(\mathbf{r})} + V_{\text{ext},i}(\mathbf{r}) - \mu_i = 0. \quad (2.2)$$

In order to use DFT, the Helmholtz free energy functional  $\mathcal{F}[\rho_i(\mathbf{r})]$  must be identified. There is, however, no general method to obtain the Helmholtz free energy functional, such that approximating  $\mathcal{F}$  is one of the most important steps when using DFT. There are few exceptions where  $\mathcal{F}$  can be determined exactly, the most important one being the Helmholtz free energy functional of an ideal gas,  $\mathcal{F}_{\text{id}}$ , given by

$$\mathcal{F}_{\text{id}}[\rho_i(\mathbf{r})] = k_{\text{B}}T \sum_{i=0}^n \int d\mathbf{r} \rho_i(\mathbf{r}) \left( \log \rho_i(\mathbf{r}) \Lambda_i^3 - 1 \right), \quad (2.3)$$

with  $\Lambda_i = \frac{h}{\sqrt{2\pi m_i k_{\text{B}}T}}$  the thermal wavelength (with  $m_i$  the mass of the particle and  $h$  Planck's constant). What then remains, is to determine the contribution to  $\mathcal{F}$  due to the particle interactions, commonly referred to as the excess Helmholtz free energy functional  $\mathcal{F}_{\text{exc}} = \mathcal{F} - \mathcal{F}_{\text{id}}$ . Even though there is no general method to obtain  $\mathcal{F}_{\text{exc}}$ , a set of approaches exist to approximate  $\mathcal{F}_{\text{exc}}$ , for example the Local Density Approximation and Weighted Density Approximation [13, 35–37].

In order to obtain the Poisson-Boltzmann formalism, we incorporate the electrostatic interactions between the charged particles. In order to do so, we approximate the Helmholtz excess free energy as the mean-field electrostatic energy,

$$\mathcal{F}_{PB}[\rho_i(\mathbf{r})] = \frac{1}{2}e \int d\mathbf{r} \left( \sum_i z_i \rho_i(\mathbf{r}) + q_{\text{ext}}(\mathbf{r}) \right) \psi(\mathbf{r}), \quad (2.4)$$

where  $\psi$  is the electrostatic potential,  $e$  the elementary charge,  $z_i$  the valency of particle  $i$  and  $e q_{\text{ext}}(\mathbf{r})$  an externally imposed charge density (dimensions  $e/\text{m}^3$ ). The (dimensionless) electrostatic potential  $\phi(\mathbf{r}) = e\psi(\mathbf{r})/(k_{\text{B}}T)$  for a homogeneous dielectric bulk liquid is given by Coulomb's law, the inverse of the Poisson equation (1.1),

$$\phi(\mathbf{r}) = \lambda_B \int d\mathbf{r}' \frac{\sum_i z_i \rho_i(\mathbf{r}') + q_{\text{ext}}(\mathbf{r}')}{|\mathbf{r} - \mathbf{r}'|} \quad (2.5)$$

with  $\lambda_B = e^2/(4\pi\epsilon k_{\text{B}}T)$  the Bjerrum length. Inserting  $\mathcal{F} = \mathcal{F}_{\text{id}} + \mathcal{F}_{PB}$  in the governing equation of DFT, Eq. (2.2), we find the Boltzmann equation for the ion densities,

$$\rho_i^{\text{eq}}(\mathbf{r}) = \rho_{b,i} e^{-z_i \frac{e}{k_{\text{B}}T} \psi(\mathbf{r})}, \quad (2.6)$$

where we have equated  $\mu_i = k_{\text{B}}T \log \rho_{b,i} \Lambda_i^3$ , with  $\rho_{b,i}$  the bulk concentration (i.e. the concentration far from the external charges, where the electric field and potential vanish). Combined with the Poisson equation (1.1), Eq. (2.6) gives the Poisson-Boltzmann

equation [12–14] as discussed in Section 1.2.2,

$$\nabla^2 \psi(\mathbf{r}) = -\frac{e}{\epsilon} \sum_i z_i \rho_{b,i} e^{-z_i \frac{e}{k_B T} \psi(\mathbf{r})}. \quad (2.7)$$

Lastly, we determine the total equilibrium grand potential  $\Omega_{\text{EDL}} = \Omega[\{\rho_i^{\text{eq}}(\mathbf{r})\}]$  of the EDL, using Eqs. (2.1), (2.3), (2.4) and (2.6), to obtain

$$\begin{aligned} \Omega_{\text{EDL}} &= \mathcal{F}[\{\rho_i^{\text{eq}}(\mathbf{r})\}] - \sum_i \int_{V_w} d\mathbf{r} \mu_i \rho_i^{\text{eq}}(\mathbf{r}) \\ &= k_B T \int_{V_w} d\mathbf{r} \left[ \sum_i \rho_{b,i} e^{-z_i \phi^{\text{eq}}(\mathbf{r})} \left( -1 - \frac{1}{2} z_i \phi^{\text{eq}}(\mathbf{r}) \right) + \frac{1}{2} q_{\text{ext}}(\mathbf{r}) \phi^{\text{eq}}(\mathbf{r}) \right], \end{aligned} \quad (2.8)$$

where  $\phi^{\text{eq}}(\mathbf{r})$  is the (dimensionless) electrostatic potential of the equilibrium configuration, as determined by Eq. (2.7). Here, the integral is over the volume of the water phase  $V_w$ , since the only external potential is the hard-wall potential of the solid. This result will be used for future calculations in Section 2.1.2 and Section 2.1.3.

### 2.1.2. Planar geometry

There is no general closed-form solution to the Poisson-Boltzmann Equation (2.7). However, an analytical solution exists in one case which we will often use in this thesis: the case of planar geometry in contact with a half space of an electrolyte containing a single monovalent salt of bulk salinity  $\rho_s$ . Translation symmetry in the direction parallel to the charged surface allows us to write as  $q_{\text{ext}}(\mathbf{r}) = z_\sigma \sigma \delta(x)$ , with  $z_\sigma$  the sign of the surface charge and  $\sigma$  the areal density of surface charges. Therefore we can write the Poisson-Boltzmann equation (2.7), with Gauss's law as a boundary condition, as

$$\frac{\partial^2 \phi}{\partial x^2} = \lambda_D^{-2} \sinh \phi(x), \quad \left. \frac{\partial \phi}{\partial x} \right|_{x=0} = -z_\sigma 4\pi \lambda_B \sigma, \quad \phi(\infty) = 0, \quad (2.9)$$

where  $\lambda_D = (8\pi \lambda_B \rho_s)^{-1/2}$  is the Debye length, which characterises the thickness of the EDL. Eq. (2.9) can be solved analytically. Defining  $\kappa_D = \lambda_D^{-1}$ ,  $\sigma^* = (2\pi \lambda_B \lambda_D)^{-1}$  the solution can be written as

$$\phi(x) = 2 \log \frac{1 + \gamma e^{-\kappa_D x}}{1 - \gamma e^{-\kappa_D x}} = 4 \operatorname{arctanh} \left( \gamma e^{-\kappa_D x} \right), \quad (2.10)$$

where  $\gamma$  is an integration constant that follows from the boundary conditions,

$$\gamma = \tanh \frac{1}{4} \phi_0 = z_\sigma \frac{\sigma^*}{\sigma} \left( \sqrt{1 + \left( \frac{\sigma}{\sigma^*} \right)^2} - 1 \right), \quad (2.11)$$

with  $\phi_0 = \phi(0)$  the electrostatic potential at the surface. Using Eq. (2.10) we can find a relation between the surface charge density  $\sigma$  and the surface potential  $\phi_0$ ,

$$z_\sigma \sigma = \sigma^* \sinh \frac{1}{2} \phi_0, \quad (2.12)$$

also known as the Gouy-Chapman equation [38].

Lastly, we write down  $\Omega_{\text{EDL}}$ , the equilibrium grand potential free energy of the EDL. First, we can derive from Eq. (2.8) the convenient relation

$$\frac{\delta \Omega_{\text{EDL}}}{\delta q_{\text{ext}}(\mathbf{r})} = k_B T \phi(\mathbf{r}). \quad (2.13)$$

By definition of the functional derivative, therefore,  $\Omega_{\text{EDL}}$  can thus in principle be determined by incrementally increasing the external surface charge by an infinitesimally amount, with the increase in  $\Omega_{\text{EDL}}$  given by Eq. (2.13). Since the external charge distribution in this case is planar, we can greatly simplify  $\Omega_{\text{EDL}}$  due to translational symmetry in the lateral direction,

$$\delta \Omega_{\text{EDL}} = z_\sigma k_B T A \delta \sigma \phi(x=0), \quad \Rightarrow \quad \frac{\beta \Omega_{\text{EDL}}}{k_B T A} = z_\sigma \int_0^\sigma d\sigma' \phi_0(\sigma'), \quad (2.14)$$

with  $A$  the area of the charged surface and  $\phi_0(\sigma)$  as given by Eq. (2.12). Eq. (2.14) shows that  $\Omega_{\text{EDL}}$  is simply the reversible work it takes to charge the surface, because it takes an energy  $\phi_0(\sigma)$  to add an infinitesimal surface charge  $d\sigma$ . Note that  $\phi_0(\sigma)$  includes all entropic contributions of the EDL.

There are three important length scales that emerge in the Poisson-Boltzmann formalism. The first is the Bjerrum length  $\lambda_B = e^2/(4\pi\epsilon k_B T)$ , the distance between two (monovalent) ions at which the electrostatic energy equals the thermal energy  $k_B T$ . Note that  $\lambda_B$  is a property of the solvent only, and for water at room temperature we have  $\lambda_B \approx 0.7$  nm. This (partly) explains why water is such a good solvent to dissolve ions: if two ions are separated by a distance as small as 0.7 nm the thermal fluctuations are sufficient to separate the ions. The second, and arguably most important length scale is the Debye length, the typical thickness of the EDL. The Debye length  $\lambda_D$  typically takes values between 1 nm ( $\rho_s = 100$  mM) and 100 nm ( $\rho_s = 10$   $\mu$ M) for

water at room temperature. Even though Eq. (2.10) technically only holds for infinitely large surfaces, the small size of  $\lambda_D$  and thus the EDL makes the solution of the planar case widely applicable. All the above equations are accurate if the surface does not curve significantly over the range of a few  $\lambda_D$ . A third and final length is the Gouy-Chapman length  $\lambda_C = (2\pi\lambda_B\sigma)^{-1}$ . This length is most important in relation to  $\lambda_D$ , since  $\lambda_D/\lambda_C = \sigma/\sigma^*$ . The Gouy-Chapman length sets the boundary between two regimes. If  $\lambda_C \gg \lambda_D$ , the surface is weakly charged, and we can linearise Eqs. (2.12) and (2.10).

### 2.1.3. Charge regulation

As discussed in Section 1.2.1, many surfaces obtain a surface charge due to ad- or desorption reactions of the ions dissolved in water. The ions typically adsorb on discrete sites because of their finite size or because of a fixed density of surface groups. The most common and well-known equation to describe ad- and desorption processes is the Langmuir equation, which we will derive here. There are several methods to derive this equations. First we will show the most straightforward method using the chemical rate equation, but afterwards we set up a Density Functional Theory for the surface charges that will be useful when we consider the non-equilibrium behaviour of the surface charges.

Here we consider a basic example, where a single neutral surface group SC acquires a charge due to the desorption of a cationic counter ion  $C^+$ ,  $SC \rightleftharpoons S^- + C^+$ . Such a charging process is described by the rate equation (for simplicity we will assume that the chemical reaction consists of a single elementary step),

$$\frac{d\{SC\}}{dt} = k^{\text{des}}\{SC\} - k^{\text{ads}}[C^+]\{S^-\}. \quad (2.15)$$

Here the curly brackets indicate areal densities, and the square brackets a volumetric density. The adsorption rate is denoted by  $k^{\text{ads}}$ , while  $k^{\text{des}}$  denotes the desorption rate. In equilibrium, the left hand side of Eq. (2.15) is vanishes, and since the total density of surface groups  $\Gamma = \{SC\} + \{S^-\}$  is a material constant it is possible to solve for the density of charged surface group  $\{S^-\}$

$$\{S^-\} = \sigma = \frac{\Gamma}{1 + \rho_{C,s}/K_C} = \frac{\Gamma}{1 + (\rho_{C,b}/K_C)e^{-\phi_0(\sigma)}}, \quad (2.16)$$

with  $K_C \equiv \{S^-\}[C^+]/\{SC\} = k^{\text{des}}/k^{\text{ads}}$  the equilibrium constant,  $\rho_{C,s}$  and  $\rho_{C,b}$  the  $C^+$  density at the surface and the bulk respectively, and  $\phi_0(\sigma)$  the electrostatic potential

at the surface, Eq. (2.12). Note that we have used the Boltzmann distribution (2.6) for the final step in (2.16), also known as the Langmuir adsorption equation [39–41].

Eq. (2.16) is in principle straightforwardly extended to an arbitrary number of reactions and surface sites using a similar analysis. Instead of calculating the new version of Eq. (2.16) for every reaction mechanism, we set up a convenient formalism to incorporate an arbitrary number of reactions, including multiple reaction steps, which gives the same result as the full extensive calculations. We pose the problem in terms of adsorption coefficients  $\alpha_i$ , defined as the ratio between the local ionic density and the equilibrium constant, and assign one to every separate reaction step. In the case of multiple reaction steps, the different coefficients of each reaction step must be multiplied to find the coefficient associated to a surface group. The resulting product can then be used in the same way as the coefficients of a single reaction.

To clarify, consider the case of an anion  $A^-$  coadsorbing along with the cation  $C^+$  on a neutral surface site  $S$ . We thus have



The adsorption coefficients then are defined as

$$\alpha_{SC} = \frac{\rho_{C,s}}{K_C}, \quad \alpha_{SCA} = \frac{\rho_{A,s}}{K_A} \quad (2.18)$$

with  $K_{SC}$  and  $K_{SCA}$  the equilibrium constants of the reactions in Eq. (2.17). The equilibrium areal densities can then be found by dividing the coefficient associated to that surface group by 1 plus the sum of the coefficients of all other surface groups,

$$\sigma_{SCA} = \Gamma \frac{\alpha_{SC}\alpha_{SCA}}{1 + \alpha_{SC} + \alpha_{SC}\alpha_{SCA}}; \quad \sigma_{SC} = \Gamma \frac{\alpha_{SC}}{1 + \alpha_{SC} + \alpha_{SC}\alpha_{SCA}}, \quad (2.19)$$

where  $\sigma_{SCA}$  and  $\sigma_{SC}$  are the areal densities of the surface groups  $SC^+$  and  $SCA$ . By identifying the ad- or desorption coefficients we can then expand Eq. (2.19) to include more different reactions or reaction steps. Note, however, by comparing Eq. (2.16) and (2.19) that a desorption coefficient must be defined inversely compared to the adsorption coefficient; for Eq. (2.16) we must define  $\alpha_S = K_C/\rho_{C,s}$ .

Here we will show how the same adsorption equations can be found using DFT. The first step in order to set up a Density Functional for the surface charges is to find the entropy of the adsorbed ions. This will be different from the ideal gas, Eq. (2.3), because the surface charges are confined to specific sites, i.e. the surface groups. To determine the entropy of the charged surface, we must thus determine the total number of configurations to distribute a fixed number of charges  $Z$  over a fixed number of sites  $N$ . For simplicity we will assume a single ion species ad- or desorption process, such

that we only have two distinct surface groups. The same method can be applied to more surface groups, although this is a more elaborate calculation. The entropy of the surface is proportional to the logarithm of the number of configurations to distribute  $Z$  entities over  $N$  sites,

$$\frac{S}{k_B} = \log \frac{N!}{Z!(N-Z)!}. \quad (2.20)$$

Assuming  $N \gg 1$  and  $Z \gg 1$ , which is the case for all macroscopic surfaces, we can use Stirling's formula to write

$$-\frac{S}{k_B A} = (\Gamma - \sigma) \log \left( \frac{\Gamma - \sigma}{\Gamma} \right) + \sigma \log \frac{\sigma}{\Gamma}, \quad (2.21)$$

with  $A$  the area of the surface,  $\sigma = \frac{Z}{A}$  the number of surface charges per unit area and  $\Gamma = \frac{N}{A}$  the number of adsorption sites per unit area. Under the approximation that  $\sigma \ll \Gamma$ , Eq. (2.21) reduces to the 2D analogue of the ideal gas free energy functional Eq. (2.3), with  $\Gamma$  the two-dimensional analogue of  $\Lambda^{-3}$ . However, since  $\sigma$  can, by definition, not exceed  $\Gamma$ , Eq. (2.21) shows that as  $\sigma$  approaches  $\Gamma$  and the entire lattice becomes filled, the entropy decreases to zero and is therefore thermodynamically unfavourable.

All that remains now is to determine the energy of the adsorbed ions. Ad- and desorption do not occur spontaneously, but only if an ion gains a certain amount of (free) energy upon ad- or desorption, commonly referred to as the Gibbs adsorption/desorption free energy, denoted here as  $k_B T g$ . The total free energy of adsorption is then straightforwardly incorporated in the free energy by adding  $Z$  times the Gibbs adsorption energy. A great advantage of the DFT formalism is that it gives a clear path to incorporate additional interactions. For example, we can incorporate a lateral interaction between adsorbed ions by adding an energy  $k_B T \chi$  if two neighbouring sites are occupied. This allows us to write down the surface free energy functional  $\mathcal{F}_S$  as

$$\mathcal{F}_s = k_B T \int d\mathbf{r}_s \left( (\Gamma - \sigma(\mathbf{r}_s)) \log \left( 1 - \frac{\sigma(\mathbf{r}_s)}{\Gamma} \right) + \sigma(\mathbf{r}_s) \log \frac{\sigma(\mathbf{r}_s)}{\Gamma} + g\sigma(\mathbf{r}_s) + \frac{1}{2} \chi \sigma(\mathbf{r}_s)^2 \right). \quad (2.22)$$

The last term, representing the lateral interaction between surface groups, is very similar to the way electrostatic interactions are included in  $\mathcal{F}_{\text{exc,PB}}$ , Eqs. (2.4) & (2.5). The main difference is the range of the interaction: the Coulomb interaction

is characterised by the factor  $|\mathbf{r} - \mathbf{r}'|^{-1}$ , but for nearest neighbour interactions we replace this with  $\delta(\mathbf{r} - \mathbf{r}')$  in order to arrive at (2.22). It has been suggested that a possible mechanism for such a nearest neighbour interaction occurs when two adjacent adsorbed ions share the water molecules of their hydration shell, giving rise to an energetically more favourable condition than two separate adsorbed ions [42].

As is the case in DFT, the equilibrium condition is given by the concentration profile that minimises the total free energy. To obtain the full equilibrium condition, however, we must take both the EDL ( $\Omega_{\text{EDL}}$ ) and the adsorbed ions ( $\mathcal{F}_s$ ) into account, both a function of  $\sigma$  (see Eq. (2.14)). The equilibrium condition with a charge regulation boundary condition is then determined by

$$\frac{\delta}{\delta\sigma} (\Omega_{\text{EDL}} + \mathcal{F}_s) = 0. \quad (2.23)$$

Above, Eq. (2.14), we have written  $\Omega_{\text{EDL}}$  such that this derivative is straightforward,

$$\frac{\partial\Omega_{\text{EDL}}}{\partial\sigma} = z_\sigma k_B T \phi_0(\sigma). \quad (2.24)$$

The equilibrium condition for  $\sigma$  is then found as the self-consistency relation

$$\sigma = \frac{\Gamma}{1 + e^{g + \phi_0(\sigma) + \chi\sigma}}. \quad (2.25)$$

By comparing Eq. (2.16) and Eq. (2.25) we identify  $g = \log \frac{\rho_{C,b}}{K_C}$ . Here,  $\log \rho_{C,b}$  represents the entropy change when an ion is exchanged between the bulk and the surface, while, on the other hand,  $\log K_C$  incorporates other free energy changes as an ion adsorbs such as a van der Waals interaction energy or a change in the hydration state of the ion. Eq. (2.25) is known as the Frumkin isotherm [43], from which we obtain the Langmuir isotherm Eq. (2.16) if  $\chi = 0$ .

## 2.2. Out-of-equilibrium

### 2.2.1. Dynamical density functional theory

The DFT formalism introduced above only holds for equilibrium systems. It is, however, possible to extend DFT to a dynamic formalism, called Dynamic Density Functional Theory (DDFT) [44–46]. DDFT is a theoretical framework to obtain the diffusive particle current  $\mathbf{j}_i^{\text{dif}}$  from an (equilibrium) Density Functional. The main assumption of DDFT is that the particle current in overdamped systems is proportional to the

gradient of the local chemical potential  $\mu(\mathbf{r}, t)$ , which is obtained by assuming that the main DFT equation, Eq. (2.2), holds for the out-of-equilibrium density profiles  $\rho_i(\mathbf{r}, t)$ ,

$$\mu_i(\mathbf{r}, t) = \left. \frac{\delta \mathcal{F}}{\delta \rho_i(\mathbf{r})} \right|_{\rho_i(\mathbf{r})=\rho_i(\mathbf{r}, t)} + V_{\text{ext},i}(\mathbf{r}, t). \quad (2.26)$$

The (diffusive) flux of species  $i$  is then given by

$$\begin{aligned} \mathbf{j}_i^{\text{dif}}(\mathbf{r}, t) &= -\frac{D_i}{k_B T} \rho_i(\mathbf{r}, t) \nabla \mu_i(\mathbf{r}, t) \\ &= -\frac{D_i}{k_B T} \rho_i(\mathbf{r}, t) \nabla \left( \left. \frac{\delta \mathcal{F}[\rho_i]}{\delta \rho_i(\mathbf{r})} \right|_{\rho_i(\mathbf{r})=\rho_i(\mathbf{r}, t)} + V_{\text{ext}}(\mathbf{r}, t) \right), \end{aligned} \quad (2.27)$$

where we introduced diffusion coefficients  $D_i$  for the ions. For example, in the case of the Poisson-Boltzmann functional  $\mathcal{F} = \mathcal{F}_{\text{id}} + \mathcal{F}_{\text{PB}}$  (Eqs. (2.3) and (2.4)) we find

$$\mathbf{j}_i^{\text{dif}}(\mathbf{r}, t) = -D_i (\nabla \rho_i(\mathbf{r}, t) + z_i \rho_i(\mathbf{r}, t) \nabla \phi(\mathbf{r}, t)). \quad (2.28)$$

It is straightforward to show that in equilibrium,  $\mathbf{j}_i^{\text{dif}} = 0$ , Eq. (2.28) reduces to the Boltzmann distribution Eq. (2.6). In order to solve for the density profile  $\rho_i(\mathbf{r}, t)$ , Eq. (2.27) must be combined with the conservation of particles, mathematically expressed by the continuity equation

$$\frac{d\rho_i(\mathbf{r}, t)}{dt} = \frac{\partial \rho_i}{\partial t} + (\mathbf{u} \cdot \nabla) \rho_i(\mathbf{r}, t) = -\nabla \cdot \mathbf{j}_i^{\text{dif}}(\mathbf{r}, t), \quad (2.29)$$

where  $\mathbf{u}$  is the fluid velocity vector. Note that we used the full (material) derivative of  $\rho_i(\mathbf{r}, t)$  in defining the continuity equation in order to account for advection. In the case of incompressible fluids,  $\nabla \cdot \mathbf{u} = 0$ , we incorporate the second term on the left hand side of Eq. (2.29), representing advection, in a generalised, total particle current  $\mathbf{j}_i = \mathbf{j}_i^{\text{dif}} + \mathbf{u} \rho_i$ , such that

$$\mathbf{j}_i(\mathbf{r}, t) = -D_i (\nabla \rho_i(\mathbf{r}, t) + z_i \rho_i(\mathbf{r}, t) \nabla \phi(\mathbf{r}, t)) + \mathbf{u}(\mathbf{r}, t) \rho_i(\mathbf{r}, t), \quad (2.30)$$

more commonly known as the Nernst-Planck equation [12, 13, 41], which allows us to write Eq. (2.29) conveniently as

$$\frac{\partial \rho_i}{\partial t} = -\nabla \cdot \mathbf{j}_i(\mathbf{r}, t). \quad (2.31)$$

### 2.2.2. Fluid flow

As discussed in Section 1.3.1, the flow of a Newtonian fluid is governed by the Navier-Stokes equation (1.5), which reduces to Stokes equation when viscous forces are much larger than inertial forces,

$$0 = -\nabla p + \eta \nabla^2 \mathbf{u} + q_e \mathbf{E}, \quad \nabla \cdot \mathbf{u} = 0, \quad (2.32)$$

where the second equation enforces the incompressibility of the fluid. A textbook example where it is possible to solve Eq. (2.32) is a pressure driven flow through a confined geometry, for example in a cylindrical pipe or between two parallel plates. Here, fluid will flow in the direction parallel to the surfaces, denoted by the (Cartesian) coordinate  $z$ . In this section we consider the flow profile without an EDL, so  $q_e = 0$ . For a pressure driven flow profile through parallel plate geometry Eq. (2.32) reduces to

$$-\frac{\partial p}{\partial z} + \eta \frac{\partial^2 u_z}{\partial x^2} = 0, \quad b \partial_x u_z(0) = u_z(0), \quad -b \partial_x u_z(H) = u_z(H), \quad (2.33)$$

with  $x$  the (Cartesian) coordinate normal to the surface and  $H$  the distance between the plates, located at  $x = 0$  and  $x = H$ . Here we have included a slip boundary condition at the plates, quantified by the so-called slip length  $b$ . For surfaces where the friction between the fluid and the surface is large, the fluid is essentially motionless at the fluid-solid boundary and  $b = 0$ , although there are many surfaces with  $b \neq 0$ , where the friction is small enough to allow for a non-zero fluid velocity at the surface [47–49].

Due to the incompressibility condition, we find that the pressure gradient  $\partial_z p$  must be constant. Eq. (2.33) is then straightforwardly solved to find

$$u_z(x) = -\frac{\partial_z p}{2\eta} (x(H-x) + Hb), \quad (2.34)$$

also known as the Hagen-Poiseuille flow profile which is parabolic in  $x$  and maximal in the center of the channel. The analysis is very similar for a cylindrical geometry [29], although we must keep in mind that the Laplacian in Eq. (2.32) takes a different form in cylindrical coordinates, and that all derivatives must vanish on the channel axis by virtue of rotational symmetry. The resulting flow profile is likewise parabolic and maximal on the channel axis,

$$u_z(r) = -\frac{\partial_z p}{4\eta} (R^2 - r^2 + 2Rb), \quad (2.35)$$

with  $r$  the radial coordinate and  $R$  the channel radius.

### 2.2.3. The Onsager matrix in electrokinetic systems

Lastly, we will consider transport in electrokinetic systems. As explained in Section 1.3.2, transport in electrokinetic systems can be quantified with a generalised conductivity matrix  $\mathbf{G}$ , which relates the globally applied driving forces to the generated fluxes. The conductivity matrix  $\mathbf{G}$ , a global linear response matrix, can be derived from the so-called Onsager matrix  $\mathbf{L}$  [50–54], which relates the local fluxes to the local driving forces. The majority of electrokinetic systems are concerned with three different types of transport: a volume flux or volumetric flow rate  $Q$ , a charge flux or electric current  $I$  and a net salt flux  $J$ ,

$$\begin{aligned} Q &= \int dA \hat{\mathbf{n}} \cdot \mathbf{u}, \\ I &= e \int dA \hat{\mathbf{n}} \cdot \left( \sum_i z_i \mathbf{j}_i \right), \\ J &= \int dA \hat{\mathbf{n}} \cdot \left( \sum_i \mathbf{j}_i \right), \end{aligned} \quad (2.36)$$

with  $A$  the cross section area of the channel,  $\hat{\mathbf{n}}$  the normal vector (of unit length) to this cross section,  $i$  runs over all transported species and  $z_i$  the valency of these species. For simplicity, we consider here only one salt species, with salinity  $\rho_1$  and  $\rho_2$ , and thus only one salt flux. All three fluxes can be generated by a pressure gradient  $\partial_z p$ , a voltage gradient  $\partial_z V$  and/or a salt chemical potential gradient  $\partial_z \mu$  over the channel ( $\mu = k_B T \log \rho_s$ , with  $\rho_s$  the salinity of the electrolyte), where  $\partial_z = \partial/\partial z$ . Charge neutrality demands that  $z_1 \rho_1 = z_2 \rho_2$ , and thus that  $\partial_z \mu_1 = \partial_z \mu_2 = \partial_z \mu$ . Within linear response theory, the Onsager matrix  $\mathbf{L}$ , a symmetric  $3 \times 3$  matrix, connects the driving forces and the generated fluxes,

$$\begin{pmatrix} Q \\ I \\ J - (\rho_1 + \rho_2)Q \end{pmatrix} = \mathbf{A} \mathbf{L} \begin{pmatrix} -\partial_z p \\ -\partial_z V \\ -\partial_z \mu \end{pmatrix}. \quad (2.37)$$

The flux opposite to  $\partial_z \mu$  is the (local) excess salt flux  $J_{\text{exc}} = J - (\rho_1 + \rho_2)Q$ , which ensures that  $\mathbf{L}$  is symmetric (see Section B.2 for a derivation). Eq. (2.37) is a local linear response equation, since the gradients,  $\mathbf{L}$  and  $\rho_{1,2}$  can (in principle) vary along the channel, as opposed to the global linear response quantified by the conductivity matrix  $\mathbf{G}$  introduced in Section 1.3.2. The Onsager matrix can, in principle, be determined from microscopic theories, and can subsequently be extended to the global linear response matrix  $\mathbf{G}$ , to be discussed in detail in Chapter 6.

## **Part I.**

# **Static Interface & Static Fluid**





## Chapter 3.

# CsCl ion adsorption on muscovite mica

*In this chapter we consider a model system, consisting of a flat surface (muscovite mica) in contact with water containing a monovalent salt (CsCl). The mica-water interface will obtain a net charge because of ad- and desorption reactions of ions in the interface. In this chapter, we study the equilibrium properties of this interface. In order to shed light on this complicated system, we combine data of two different experimental techniques, Surface X-Ray Diffraction and Atomic Force Microscopy. Both give very different information about the interface, imposing more restrictions on the surface complexation model, a minimal set of adsorption reactions (surface complexation model), we construct in this chapter that can interpret both data sets simultaneously. In developing this model, we find that the interface is much more complex than is typically assumed.*

*In this chapter we will extensively discuss the results and the underlying theory. For details of the experimental work, performed by our collaborators S. Brugman and E. Vlieg of Radboud University Nijmegen, we refer the interested reader to the original article [55].*

- *Section 3.2*  
*Presentation of a comprehensive picture of the mica-Cs<sup>+</sup>-Cl<sup>-</sup>-water interface*
- *Section 3.3 and 3.4*  
*Construction of a minimal surface complexation model that simultaneously reproduces both Surface X-Ray Diffraction and Atomic Force Microscopy data sets*
- *Sections 3.4.1 and 3.4.2*  
*Identification of anion coadsorption reaction as well as a lower intrinsic surface charge of muscovite mica than expected (based on the crystallographic properties)*

### 3.1. Introduction

The adsorption of cations at mineral surfaces is usually studied under ideal conditions, e.g. by using a single salt, in order to avoid overcomplicating the system. However, in real-world natural environments such as seawater, many different ionic species are present, all competing for the same adsorption sites. A typical example is encountered during low salinity water flooding in enhanced oil recovery. In certain reservoirs, injecting water with low salinity was found to release more initially bound oil molecules than water with high salinity; however, the precise mechanism of this phenomenon is still unknown [56]. One possible mechanism is the exchange of divalent cations, which bridge polar oil components to the mineral surface, with monovalent cations under low salinity conditions [56, 57]. To understand these complex competition processes, experiments that contain multiple ionic species at the same time need to be conducted. However, many frequently-used experimental techniques, such as surface force apparatus (SFA) [58, 59] and atomic force microscopy (AFM) [42, 60], are not capable of differentiating between cations in a mixture containing multiple salts, due to the ‘chemical blindness’ of these techniques.

On the other hand, surface X-ray diffraction (SXR) can be used to investigate a single ion species in an ionic mixture in two ways. If the experimental X-ray energy is close to an absorption edge of one of these ions, anomalous SXR experiments can be used [61–63]. In these experiments, the element-specific distribution of an ion of interest at the interface can be determined, provided that the X-ray absorption edge energy, at which the element absorbs a photon, is experimentally accessible. A second way to investigate a single ion species in a mixture is by looking at the difference in diffracted intensity, which scales with electron density. A heavy cation will thus have a larger effect on the diffraction pattern than a lighter cation. In a mixture of heavy and light ion species, the electron density will be in between that of only the light cation and only the heavy cation. By using this, it is possible to determine the adsorbed occupancies of both cationic species by using the difference in electron density. In this chapter, we use the latter method to follow the adsorption of cations at the mineral surface. In this case it is not possible to use anomalous diffraction because the X-ray adsorption edge of the light atom is not experimentally accessible.

Our aim is to identify the relevant mechanisms governing the mineral-electrolyte interface. SXR, however, is only sensitive to the interfacial structure and does not yield information about the charge of the surface. The surface charge can be obtained by for example zeta potential or AFM measurements [64]. To fully understand the interface, we should ideally combine both the interfacial composition and electrostatic data in a single model. Here we construct a surface complexation model that simultaneously describes both cation coverages measured using SXR data and electric double layer

data previously reported by Bera et al. [65]. The SXRDR data was obtained in direct collaboration with S. Brugman and E. Vlieg from the Radboud University in Nijmegen. For more information on the experimental details, we refer the interested reader to article this chapter is based on [55].

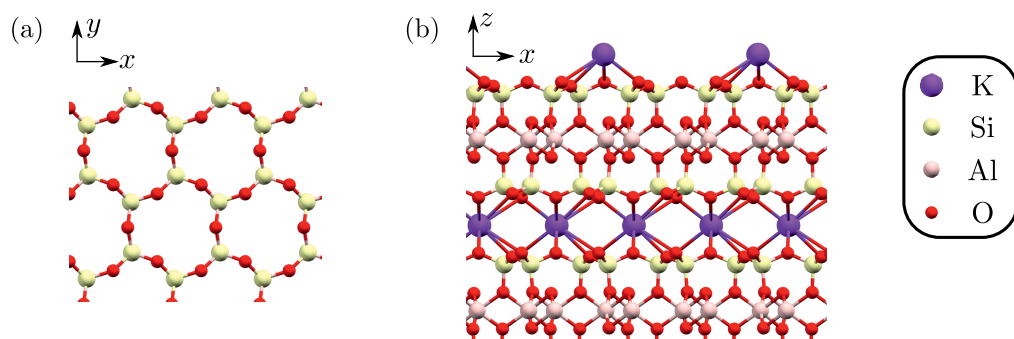


**Figure 3.1.:** Schematic representation of a (a) top (without  $K^+$  ions) and (b) side view of a mica surface.

Muscovite's ideal chemical formula  $KAl_2(Si_3Al)O_{10}(OH)_2$  is an excellent mineral model system for this experiment. After cleavage of muscovite, a clean and atomically flat (001) surface is exposed [66], shown in Fig. 3.1. It is known that this surface is negatively charged due to isomorphous substitution of 25% of Si by Al [67]. The negative charge is compensated by the presence of 0.5 monolayer of  $K^+$  ions. These  $K^+$  ions are located above the center of the six-membered  $SiO_4$  ring, called the cavity site. By submerging muscovite in an electrolyte solution, loosely bound surface  $K^+$  ions can be exchanged by other cations, e.g.  $Cs^+$  or  $Ca^{2+}$  [68, 69]. Previous research showed that  $Cs^+$  strongly adsorbs to muscovite and significantly changes the diffracted intensity due to its strong X-ray scattering [70–73]. This strong change in diffracted intensity can be used to determine the amount of adsorbed  $Cs^+$  ions on the mica surface.

## 3.2. Interfacial structure

Fig. 3.2 shows the electron density according to the CsCl interfacial structure model as a function of height as obtained from SXRDR, for different concentrations and temperatures. The electron density profiles show that  $Cs^+$  adsorbs above the center of the muscovite cavity at a height of  $2.16 \pm 0.05 \text{ \AA}$  (Fig. 3.2) for both salt concentrations, which is in agreement with literature [6, 70, 72–76]. This peak corresponds to  $Cs^+$  occupancies of  $39 \pm 5\%$  and  $66 \pm 5\%$   $Cs^+$  for 25 mM and 475 mM CsCl, respectively, which is in excellent agreement with previous work on CsI [73]. The peak in electron

density observed at a height of 4.8 Å above the surface is attributed to the first water layer [73]. All other structural parameters were similar to previous work [73] and are not discussed here, since we focus on the exchange of the cation.

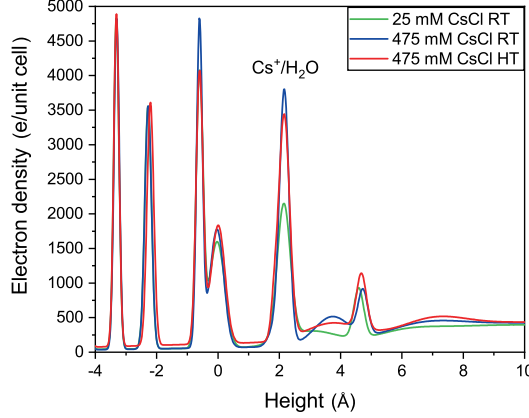
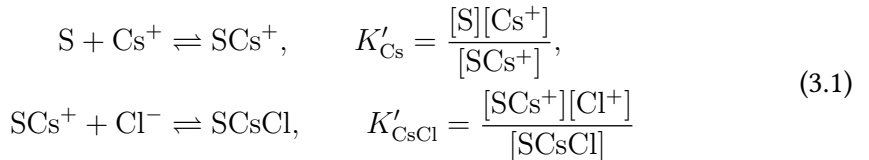


**Figure 3.2.:** Laterally averaged electron density perpendicular to the muscovite surface for (a) pure CsCl and solutions for salinities 25 mM (green) and 475 mM (blue) at room temperature (RT) and for salinity 475 mM (red) at  $63 \pm 2^\circ \text{C}$  (HT).

The measurements at high temperature (HT) were performed at  $63 \pm 2^\circ \text{C}$  and showed that the  $\text{Cs}^+$  occupancy at a CsCl concentration of 475 mM remains constant within the error bars ( $67 \pm 5\%$ ) compared to room temperature ( $66 \pm 5\%$ ). Moreover, the cation remains located at the same height ( $2.16 \pm 0.05 \text{ \AA}$ ).

### 3.3. Surface complexation model

For the pure CsCl electrolyte, we use a surface complexation model similar to the one explained in Section 2.1.3. In this model, a  $\text{Cs}^+$  ion can adsorb above the muscovite cavity, and  $\text{Cl}^-$  ions can coadsorb along with the adsorbed  $\text{Cs}^+$ . The exact location of the  $\text{Cl}^-$  ion is not important for this model, as long as it occurs in the Stern layer, see Fig. 3.3. In the coadsorption model we incorporate the following two adsorption processes



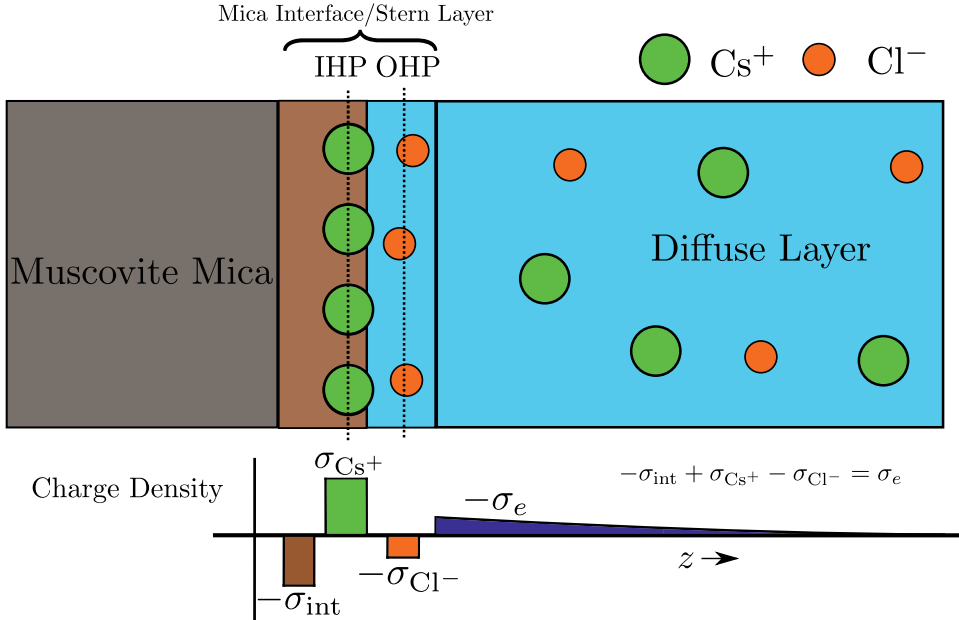


**Figure 3.3.:** A schematic representation of the muscovite mica - CsCl electrolyte interface, as based on the analysis presented in this chapter. The interface consists of an interfacial region (brown) where the intrinsic charge of mica  $-\sigma_{\text{int}}$  is located, an Inner Helmholtz Plane (IHP) where the adsorbed  $\text{Cs}^+$  ions are located (areal density  $\sigma_{\text{Cs}^+}$ ), an Outer Helmholtz Plane (OHP) with the coadsorbed  $\text{Cl}^-$  anions (areal density  $\sigma_{\text{Cl}^-}$ ) and the diffuse layer. The net surface charge density  $\sigma_e = -\sigma_{\text{int}} + \sigma_{\text{Cs}^+} - \sigma_{\text{Cl}^-}$  is the sum of the intrinsic,  $\text{Cs}^+$  and  $\text{Cl}^-$  contributions to the surface charge. The diffuse layer charge is equal in magnitude but opposite in sign to the net surface charge  $\sigma_e$ , since the system as a whole is charge neutral. The  $\text{Cs}^+$  ions in the IHP are confined in all three dimensions, and are therefore measurable with SXRD. The  $\text{Cl}^-$  ions are confined to the OHP in the direction perpendicular to the surface and are laterally fully disorder and thus, while not visible in non-specular SXRD data, contribute to the surface charge. The ions in the diffuse layer are not confined in any direction.

where S denotes an empty (ion-free) adsorption site (i.e. an empty cavity). We denote the equilibrium adsorption reaction constant of the  $\text{Cs}^+$  adsorption reaction by  $K'_{\text{Cs}}$  and the adsorption reaction constant of the  $\text{Cl}^-$  coadsorption by  $K'_{\text{CsCl}}$ . Note that  $K'_{\text{Cs}}$  and  $K'_{\text{CsCl}}$  are defined such that these have the dimensions of concentration (in units of mol/L). The pK value of an adsorption reaction is then defined as  $\text{pK} \equiv -^{10}\log K'$ . We then incorporate these adsorption reactions in the Poisson-Boltzmann formalism, as explained in Sections 1.2.2 & 2.1.2, and combine it with a charge regulation mechanism as explained in Section 2.1.3. We express the areal coverage of the surface groups SCs and SCsCl,  $\theta_{\text{SCs}}$  and  $\theta_{\text{SCsCl}}$  respectively, in terms of the areal densities  $\sigma_{\text{SCs}}$  and  $\sigma_{\text{SCsCl}}$

as obtained from this charge regulation mechanism,

$$\begin{aligned}\theta_{\text{SCs}} &= \frac{\sigma_{\text{SCs}}}{\Gamma} = \frac{\frac{\rho_{\text{Cs}}}{K'_{\text{Cs}}} e^{-\phi_0}}{1 + \frac{\rho_{\text{Cs}}}{K'_{\text{Cs}}} e^{-\phi_0} + \frac{\rho_{\text{Cs}}^2}{K'_{\text{Cs}} K'_{\text{CsCl}}}}, \\ \theta_{\text{SCsCl}} &= \frac{\sigma_{\text{SCsCl}}}{\Gamma} = \frac{\frac{\rho_{\text{Cs}}^2}{K'_{\text{Cs}} K'_{\text{CsCl}}}}{1 + \frac{\rho_{\text{Cs}}}{K'_{\text{Cs}}} e^{-\phi_0} + \frac{\rho_{\text{Cs}}^2}{K'_{\text{Cs}} K'_{\text{CsCl}}}},\end{aligned}\tag{3.2}$$

with  $\rho_{\text{Cs}} = [\text{Cs}^+]$  the bulk  $\text{Cs}^+$  concentration,  $\Gamma$  the total areal density of adsorption sites. Furthermore,  $\phi_0 = e\psi_0/k_{\text{B}}T$ , with  $\psi_0$  the electrostatic potential at the surface,  $e$  the elementary charge,  $k_{\text{B}}$  Boltzmann's constant and  $T$  the temperature. In order to keep the number of fit parameters to a minimum, we do not include any Stern-layer capacitances in this model [40, 41]. The dimensionless surface potential  $\phi_0$  is a function of the net charge density  $e\sigma_e$  of the surface, or net surface charge density, via the Gouy-Chapman equation (2.12). The net surface charge can be obtained by adding the (negative) intrinsic surface charge of muscovite,  $-e\sigma_{\text{int}}$ , to the positive contribution due to the  $\text{Cs}^+$  ions,  $e\sigma_{\text{Cs}^+} = e\sigma_{\text{SCs}} + e\sigma_{\text{SCsCl}}$  and the negative contribution of the  $\text{Cl}^-$  ions,  $-e\sigma_{\text{Cl}^-} = -e\sigma_{\text{SCsCl}}$ , to obtain  $e\sigma_e = e\sigma_{\text{SCs}} - e\sigma_{\text{int}} = e\sigma_{\text{Cs}^+} - e\sigma_{\text{Cl}^-} - e\sigma_{\text{int}}$ . The net surface charge density  $e\sigma_e$  can be probed by AFM [65], since by charge neutrality the total charge in the diffuse layer must be equal to  $-e\sigma_e$ . Fig. 3.3 gives a schematic representation of the muscovite mica-CsCl electrolyte interface, based on the experimental SXR and AFM data, and the minimal surface complexation model.

For a given  $\Gamma$ ,  $K'_{\text{Cs}}$ ,  $K'_{\text{CsCl}}$  and salinity  $\rho_{\text{Cs}}$ , we can solve Eq. (3.2) and the Gouy-Chapman equation (2.12) for the areal densities  $\sigma_{\text{Cs}}$  and  $\sigma_{\text{CsCl}}$  and surface potential  $\phi_0$ . These algebraic equations were solved using the Mathematica software package. The two reaction constants are found by fitting the above described surface complexation model to the SXR and AFM data. The SXR data gives the total  $\text{Cs}^+$  occupancy, which in our model is equal to the sum of all surface groups that include a  $\text{Cs}^+$  ion, i.e.  $\theta_{\text{Cs}^+} = (\theta_{\text{SCs}} + \theta_{\text{SCsCl}})$ , while the AFM data provides the net surface charge  $e\sigma_e$ . One surface complexation model must predict both parameters in accordance with the AFM and SXR data.

### 3.4. Development of the surface complexation model

In order to understand the competition between  $\text{Cs}^+$  and  $\text{Ca}^{2+}$ , the subject of Chapter 4, we develop here a surface complexation model using both SXRD and surface charge data based on the  $\text{Cs}^+$ -mica data only. The  $\text{Cs}^+$  adsorption isotherm, shown in Fig. 3.4a, shows the  $\text{Cs}^+$  occupancy as a function of salinity for previously reported data for CsCl (in green) [72] and CsI (in black) [73] as well as occupancies of CsCl of the current work (in red), which are in excellent agreement with each other. Together with the net surface charge as measured by Bera et al. (Fig. 3.4b) [65], we use the  $\text{Cs}^+$  occupancies to develop a surface complexation model.

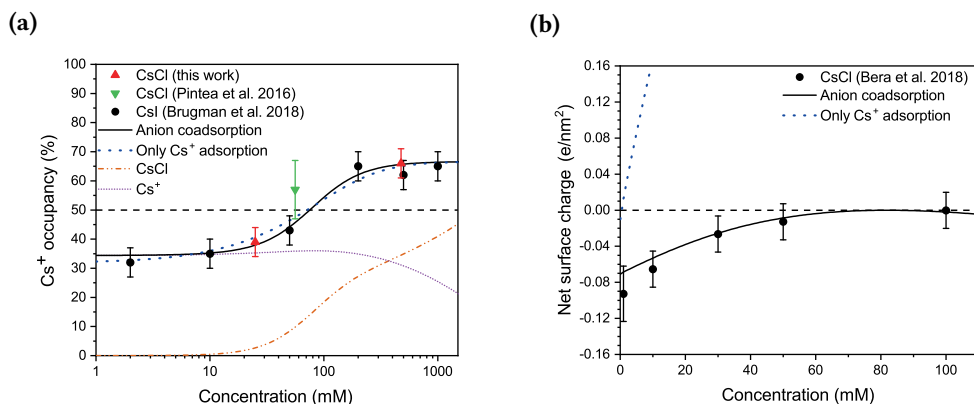


**Figure 3.4.:** (a) Occupancy of adsorbed  $\text{Cs}^+$  at the basal muscovite surface at room temperature as a function of the CsCl or CsI concentration [72, 73]. The dashed line at 50% indicates the occupancy of  $\text{Cs}^+$  required to compensate the muscovite negative surface charge. The other lines indicate the occupancy of both  $\text{Cs}^+$  (purple dotted) and CsCl (orange dot-dashed) species following from the best adsorption model fit and  $\text{Cs}^+$  occupancy (blue dotted) if no  $\text{Cl}^-$  coadsorption is taken into account. (b) Net surface charge as measured using AFM by Bera et al. [65]. The dashed line indicates a neutral net surface charge. The solid black lines in both (a) and (b) shows the best fit of the chloride coadsorption model with a negative intrinsic surface charge equivalent to a coverage of  $36 \pm 1\%$ ,  $\text{pK}_{\text{Cs}} = 1.2 \pm 0.3$  and  $\text{pK}_{\text{CsCl}} = 0.7 \pm 0.2$ .

The adsorption isotherm does have the ‘S-curve’ shape typical for an adsorption isotherm, with a transition from a low coverage plateau (approximately 35%) at low salinity to a high coverage plateau (approximately 65%) at high salinity. A muscovite surface without any adsorbed ions has an intrinsic negative surface charge of  $1 e$  per unit cell, which can be exactly compensated by a monovalent cation occupancy of 50% (dashed line in Fig. 3.4a). Fig. 3.4b, however, shows that the net surface charge of the muscovite-electrolyte interface does not exceed  $-0.1 e/\text{nm}^2$ , corresponding to approximately 3% of the total number of adsorption sites. The  $\text{Cs}^+$  coverage data

thus shows that  $\text{Cs}^+$  alone does not compensate the intrinsic surface charge; below approximately 10 mM the  $\text{Cs}^+$  occupancy becomes as low as 30%, whereas above 200 mM the  $\text{Cs}^+$  occupancy levels off at approximately 65%, both deviating significantly from the expected value of 50% for charge neutrality. Both limits thus show unexpected behaviour, and in order to explain both of these limits, the standard surface complexation model must be adjusted.

### 3.4.1. Low salinity limit: $\text{H}^+$ adsorption

For the lowest salinity values measured, the coverage converges to approximately 35%, which is 15% smaller than the expected 50%. This seems to suggest that the muscovite-electrolyte interface carries a net surface charge equivalent to approximately 15% of the total number of adsorption sites. A unit cell of muscovite has an area of  $0.47 \text{ nm}^2$ , which, since the system as a whole must be charge neutral, would imply that a net surface charge of  $-0.64 e/\text{nm}^2$  has to be compensated by a charge in the electric double layer. However, this is an order of magnitude higher than the net surface charge measured by AFM [65], shown in Fig. 3.4b as a function of salinity. Additionally, such high surface charges do not agree with previous SFA [58, 59], AFM [64] and zeta potential [77–79] measurements for muscovite mica at a pH value close to 6.

Additional positive charge in the Stern layer is thus required for a net surface charge that is compatible with literature.  $\text{Cs}^+$  adsorption mainly takes place in an inner-sphere (as explained in Section 1.2.1) configuration in the muscovite cavity site, as was also observed in the current work [6, 70]. Outer-sphere  $\text{Cs}^+$  is thus not expected to give a large contribution in positive charge. There are no other cations present in solution, except for hydronium. We therefore investigated the possible adsorption of  $\text{H}_3\text{O}^+$  [73]. The concentration of  $\text{H}_3\text{O}^+$  is, at  $\text{pH} \approx 6$ , in the order of  $\mu\text{M}$ , which means that the affinity of  $\text{H}_3\text{O}^+$  to muscovite should be high, which was indeed observed before [58, 59, 80, 81]. To investigate possible  $\text{H}_3\text{O}^+$  adsorption we adopt a  $\text{Cs}^+/\text{H}^+$  competition model, as has been used before [58, 77, 81, 82]. Typically, it is assumed that adsorption only takes place at half of the total adsorption sites (one per unit cell). We have adjusted this model in order to be able to account for coverages exceeding 50%. In the  $\text{Cs}^+/\text{H}^+$  competition model,  $\text{H}^+$  would outcompete and fully replace  $\text{Cs}^+$  at low salinity, with the inverse happening at high salinity. This, however, is not corroborated by the data shown in Fig. 3.4a, which shows that  $\text{Cs}^+$  occupancy saturates to a non-zero value for decreasing salinity. The data suggests, therefore, that  $\text{Cs}^+$  does not compete with a different cation at low salinities; if it did, the coverage would decrease more strongly as the salinity decreases. Note that at very low salinities ( $\ll 2 \text{ mM}$ ) the  $\text{Cs}^+$  occupancy must eventually, of course, converge to zero. The best fit of the  $\text{Cs}^+/\text{H}^+$ -competition model is found to be unsatisfactory, even if a Stern layer

capacitance is included (see Appendix A.2). Based on the data presented in this thesis we conclude that the  $\text{Cs}^+/\text{H}^+$ -competition model is not appropriate to describe the muscovite-electrolyte interface under our experimental conditions.

The shortcomings of the  $\text{Cs}^+/\text{H}^+$  competition model have been noted before in the case of muscovite mica [83, 84] and silica [85]. Nevertheless, this conclusion is unexpected, as previous studies clearly show that the zeta potential and net surface charge of muscovite mica do depend on the pH of the solution [64, 77, 78, 84, 86]. Here we should note, however, that the same experiments show that in the presence of 1 mM of salt, the zeta potential of muscovite is relatively independent of pH for  $\text{pH} > 6$ , suggesting that at these pH values the protons are (almost) entirely outcompeted by the cations (which is thus corroborated by our data). Furthermore, this assertion agrees with a surprisingly small value of  $\text{pK}_\text{H}$  found by some studies [84, 86].

If there is no  $\text{Cs}^+/\text{H}^+$  competition, the low  $\text{Cs}^+$  coverage at low salinity must have a different origin. Previous studies have already emphasized that protons behave differently from other cations concerning competitive adsorption on a wide variety of surfaces [87]. For example, a hysteresis of the coverage with pH was observed in the case of muscovite [81], and it was suggested that muscovite mica undergoes an irreversible reaction with protons which penetrate into the lattice and decrease the intrinsic surface charge of muscovite mica. A different study found similar effects for calcinated mica [86], whereas others showed that the cation/proton adsorption models cannot capture the pH dependence of muscovite mica and suggested that oxonium ions behave fundamentally different than the other cations [83]. If protons indeed penetrate the muscovite lattice irreversibly and alter the intrinsic surface charge when muscovite is brought in contact with an aqueous solution, this could explain why in our case the  $\text{Cs}^+$  occupancy levels off to approximately 35% instead of a value closer to 50% as expected beforehand. Our measurements therefore confirm the observation that the preparation of the muscovite samples is of great importance to the cation adsorption. In order to incorporate this in our surface complexation model, which can only describe reversible adsorption processes, we consider the intrinsic surface charge of muscovite,  $-e\sigma_{\text{int}}$ , as a fit parameter.

### 3.4.2. High coverage limit: anion coadsorption

The high-salinity saturation value of approximately 65% shows that  $\text{Cs}^+$  adsorbs in a structure in which approximately every 2 out of 3 adsorption sites are covered. However, from basic adsorption mechanics one would expect the coverage to saturate at 100% for high salinities. The  $\text{Cs}^+$  coverage can only level off at a value lower than 100% if there is a process that prohibits  $\text{Cs}^+$  from adsorbing on every adsorption site. A honeycomb lattice where an unoccupied site is surrounded by 6 occupied sites, as

shown in Fig. 3.5, would be a plausible configuration: to fill this unoccupied site, a  $\text{Cs}^+$  ion would need to break the hydration shell and overcome the high electrostatic repulsion of the surrounding six adsorbed ions at the expense of a significant (free-) energy penalty (see Fig. 3.5). In order to incorporate the observed maximum coverage into the model, we assign a larger area of occupation to the cations than the area of an adsorption site, as was first proposed by Pashley [58]. This effectively reduces the maximum coverage below unity. See the Appendix A.1 for more details.

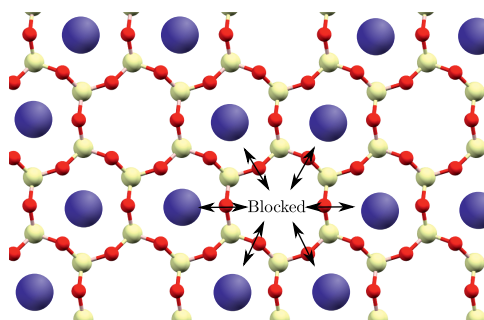


**Figure 3.5.:** Top-view schematic representation of the hypothesised blocking mechanism that limits the maximum coverage where 2 out of 3 sites are occupied.

Actually, there is another issue with the high salinity occupancy. The  $\text{Cs}^+$  occupancies of 65% at high salinity suggest an unusually large positive surface charge. The overcompensation of 15% over the intrinsic surface charge of 50% (which is an even larger overcompensation if we adjust the intrinsic surface charge to a lower value as argued above) would result in an unusually high, positive surface charge. Most importantly, however, the variation in the  $\text{Cs}^+$  occupancy as measured by SXRD (see Fig. 3.4a) is not at all comparable to the variations in the net surface charge (see Fig. 3.4b). This implies that the variations observed in the  $\text{Cs}^+$  coverage are largely charge neutral variations. An additional, negative contribution to the total surface charge is therefore required, especially at large salinities. The most obvious candidate is the coadsorption of  $\text{Cl}^-$ , as was already suggested by previous studies for  $\text{Cs}^+$  [74],  $\text{Rb}^+$  [88] and  $\text{K}^+$  [89], although for the latter two this was only observed for higher salinities than considered in our study. The site density of muscovite is approximately 4 sites per  $\text{nm}^2$ , so a coverage of 33% corresponds to a local concentration at the surface exceeding 4 M within the Stern layer (assuming for simplicity a thickness of 0.5 nm). Considering the  $\text{Cs}^+$  coverage values, even at low salinities, the formation of cation-anion complexes is thus quite plausible. Previous SXRD measurements have, on the other hand, found no evidence of (structured) anion adsorption [73, 90]. However, SXRD can only exclude ordered anion coadsorption, whereas a more disordered struc-

ture would still be possible. Such a disordered structure is actually plausible since the cavities are already filled by the  $\text{Cs}^+$  ions, and as a result the  $\text{Cl}^-$  adsorbed on top is expected to be distributed more homogeneously as it is laterally less confined [91], see Fig. 3.3 for a schematic representation. At the expense of a third fit parameter ( $\text{pK}_{\text{CsCl}}$ ) we can include this coadsorption process in the model. This parameter is related to a (free) energy gain for the  $\text{Cl}^-$  ion to be close to the adsorbed  $\text{Cs}^+$ , which, similar to cation adsorption, can likely be related to the reorganisation of the hydration shell of  $\text{Cl}^-$ . A surface complexation model cannot, however, explain where this (free) energy gain originates from, only that it must exist.

Here we will only consider  $\text{Cl}^-$  as the coadsorbing anion, as it is the most abundant anion. The only other anions present are  $\text{OH}^-$  and  $\text{HCO}_3^-$  (the  $\text{CO}_3^{2-}$  concentration is negligible close to  $\text{pH} = 6$ ), which, contrary to  $\text{Cl}^-$ , do not vary with the salinity and therefore give different predictions. However, as mentioned above, the surface charge of muscovite mica has been shown to be relatively independent of  $\text{pH}$  for  $\text{pH} > 6$ , making it unlikely that either  $\text{OH}^-$  and  $\text{HCO}_3^-$  (or even  $\text{CO}_3^{2-}$ ) have a significant effect on the muscovite mica-water interface. See Appendix A.3 for an analysis of such a model.

The  $\text{Cl}^-$ -coadsorption model (black solid lines in Fig. 3.4) is able to simultaneously, and satisfactorily, fit the  $\text{Cs}^+$  occupancies and the net surface charge, as can be seen from the solid lines in Fig. 3.4. The best fit was obtained with an intrinsic surface charge  $\sigma_{\text{int}}/\Gamma = 0.36 \pm 0.01$ ,  $\text{pK}_{\text{Cs}} = 1.2 \pm 0.3$  and  $\text{pK}_{\text{CsCl}} = 0.7 \pm 0.2$ . Although the  $\text{pK}_{\text{CsCl}}$  value and the intrinsic surface charge cannot be compared to previous studies, the  $\text{pK}_{\text{Cs}}$  value deviates significantly from previously determined values. However, the values in previous studies were found either by using a  $\text{Cs}^+/\text{H}^+$  competition model [58, 71, 81], and/or by ignoring the electrostatic interactions to the adsorption model [71, 81]. The  $\text{pK}_{\text{Cs}}$  found here is a direct result of the adapted model which, we should note, is a minimal model needed to explain both the SXRD and the AFM data. If we consider  $\text{Cs}^+$  adsorption without coadsorption, and only consider the SXRD data, we find  $\text{pK}_{\text{Cs}} = 3.5$  as a best fit (blue dotted line in Fig. 3.4a), which is much closer to previously reported values [71]. This value is, however, completely incompatible with the net surface charge data [65] (blue dotted line Fig. 3.4b). In fact, a surface complexation model without an anion coadsorption reaction predicts a (large) positive net surface charge for all considered salinities, and is therefore unable to reproduce both data sets. The best-fit  $\text{pK}_{\text{Cs}}$  value also deviates significantly from Molecular Dynamic simulations [76]. This discrepancy can possibly be attributed to the different conditions between the Molecular Dynamics simulations and the Langmuir adsorption models, as the former operates in the  $NpT$  ensemble and a salt-free environment, while the latter operates in the  $\mu VT$  ensemble and does incorporate the anions.

### 3.5. Summary & conclusion

Even though we have found adequate fits for both data sets, this of course does not mean that the proposed model is a complete description of the muscovite-electrolyte interface. For example, the  $\text{Cl}^-$ -coadsorption model predicts a strongly decreasing net surface charge for salinities exceeding 100 mM due to the increasing  $\text{Cl}^-$  (co)adsorption. However, we must keep in mind that for salinities exceeding 100 mM the Poisson-Boltzmann theory begins to break down as the Debye length becomes comparable to the ion size, and a more advanced theory would be required for these high salinities. Furthermore, we have implicitly assumed that the  $\text{Cl}^-$  and  $\text{I}^-$  coadsorption constants are equal (i.e.  $\text{p}K_{\text{CsCl}} = \text{p}K_{\text{CsI}}$ ). This is reasonable, since the CsI and CsCl data are in good agreement. A more complete model would not only take the different coadsorption constants into account, but also the different ionic radii of the two anions via a triple layer model. This would introduce additional fit parameters, more than we can reliably fit with the current data. It is clear, however, that the simplest model can reproduce both the SXRD and surface charge data requires anion coadsorption. This model will be used in the next chapter to describe the  $\text{Cs}^+/\text{Ca}^{2+}$  competition data.

Our results show that a minimal model even for a single salt muscovite-electrolyte interface includes two rarely included processes: (i) a reduced intrinsic surface charge (e.g. due to irreversible proton adsorption) and (ii) anion coadsorption. This emphasizes the point that the muscovite-electrolyte interface is a complex system, and cannot be fully described with a single cation/proton adsorption model. Although such models have been employed before with limited success, the present analysis with data from two different experimental techniques shows that these are merely effective models, and do not reflect physical properties. This minimal model shows the rich behaviour of solid-water interfaces and we encourage future research to further explore this complexity. We expect that similar processes occur at other solid-water interfaces, such as silica, for which it is also known that such cation/proton competition models are inadequate [85].

### Acknowledgements

We thank Sander Brugman and Elias Vlieg from the Radboud University in Nijmegen for gathering, sharing and discussing the SXRD data, and an overall fruitful cooperation on this project. We thank F. Mugele for kindly providing the AFM data.

# Chapter 4.

## $\text{Cs}^+/\text{Ca}^{2+}$ competition on muscovite mica

*We showed in the previous chapter that we can unite measurements of Surface X-Ray Diffraction with Atomic Force Microscopy measurements on mica in contact with an CsCl water solution using a minimal surface complexation model. For a detailed discussion of the surface complexation model, see Chapter 3. In this chapter, we expand upon the results of the previous chapter and include competition with  $\text{Ca}^{2+}$ . We will therefore not repeat an extensive introduction here, for this we refer the reader to Section 3.1. For details of the experimental work, performed by our collaborators S. Brugman and E. Vlieg of Radboud University Nijmegen, we refer the interested reader to the associated article [55].*

- *Section 4.2  
Presentation of a comprehensive picture of the mica- $\text{Ca}^{2+}$ -water interface*
- *Section 4.3  
Successful reproduction of both Surface X-Ray Diffraction and Atomic Force Microscopy data sets with a  $\text{Cs}^+/\text{Ca}^{2+}$  competition model*
- *Section 4.3  
Identification of the affinities of  $\text{Cs}^+$  and  $\text{Ca}^{2+}$ , and finding that the former has a higher affinity than the latter*
- *Section 4.4  
Relating the different affinities to the hydration shell of the ions*

## 4.1. Introduction

We consider the same system as in Chapter 3, an atomically flat muscovite mica surface in contact with water. While in the previous chapter we only considered a pure CsCl solution, in this chapter we consider both a pure CaCl<sub>2</sub> solution and a CaCl<sub>2</sub>/CsCl mixture. In all cases, of course, the muscovite mica surface obtains a net charge due to the de- and adsorption reactions of ions, and consequently leads to the development of an EDL (see Section 1.2.2 for a discussion of the EDL). First we discuss the SXRD data and the interpreted interfacial structure of the pure CaCl<sub>2</sub> case. Afterwards we will fit the measured occupancies and surface charge to the surface complexation model developed in Chapter 3.

As explained in Section 3.2, Cs<sup>+</sup> strongly adsorbs to muscovite and significantly changes the diffracted intensity due to its strong X-ray scattering [70–73]. This strong change in diffracted intensity can be used to determine the amount of adsorbed Cs<sup>+</sup> in a solution containing a mixture of Cs<sup>+</sup> and a lighter cation. We choose Ca<sup>2+</sup> as the light cation because of its biological and geophysical relevance (e.g. in seawater and (bio)mineralization). In this way, we can investigate the influence of concentration, valency and hydration energy on the adsorption at the muscovite-electrolyte interface. We will show that we can unite occupancies of adsorbed cations measured with SXRD and electric double layer data measured by AFM in a single surface complexation model. From the analysis of the Cs<sup>+</sup>/Ca<sup>2+</sup> competition, we find that Cs<sup>+</sup> has a higher affinity for the negatively charged muscovite mica surface than Ca<sup>2+</sup>, despite the lower valency of Cs<sup>+</sup>.

## 4.2. Interfacial structure

Analysis of the measured crystal truncation rods for muscovite mica in contact with pure CaCl<sub>2</sub> solutions shows that Ca<sup>2+</sup> adsorbs above the center of the cavity in an inner-sphere configuration [92]. Contrary to Cs<sup>+</sup>, our data for Ca<sup>2+</sup> indicate different heights at different concentrations:  $2.30 \pm 0.20$  Å at 25 mM and  $1.79 \pm 0.10$  Å at 475 mM (Fig. 4.1). These heights correspond to outward displacements with respect to the bulk K<sup>+</sup> position of  $0.59 \pm 0.20$  Å and  $0.09 \pm 0.10$  Å, respectively. Because of the low occupancy of the relatively light Ca<sup>2+</sup> cation, it is more difficult to pinpoint the exact Ca<sup>2+</sup> position. At a concentration of 25 mM, there is another peak in electron density visible around 1.6 Å, which in principle could also correspond to Ca<sup>2+</sup> adsorption. During the fitting procedure we found that a model with a Ca<sup>2+</sup> cation at this position gave an inadequate fit. We therefore concluded that this is water located above the cavity. The peaks found for both Ca<sup>2+</sup> (and Cs<sup>+</sup>) conditions around 4.6–4.9 Å were

attributed to a hydration layer [73]. Besides this layer, two additional water layers complete the interfacial model.

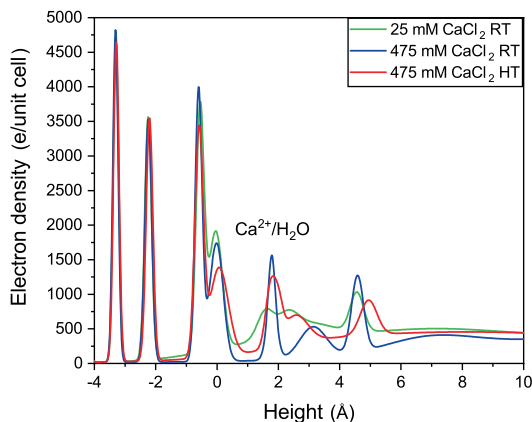


**Figure 4.1.:** Laterally averaged electron density perpendicular to the muscovite surface for pure CaCl<sub>2</sub> solutions for salinities 25 mM (green) and 475 mM (blue) at room temperature (RT) and for salinity 475 mM (red) at  $63 \pm 2$  ° C (HT).

A wide range of values for the height and location of Ca<sup>2+</sup> have been reported in literature. Molecular Dynamics and Monte Carlo studies showed that Ca<sup>2+</sup> adsorption is favourable at the negatively charged substitution site, i.e. where Si is substituted by Al. [76, 93]. To investigate the possibility of this alternative adsorption site, a model in which Ca<sup>2+</sup> was located above the Si/Al atoms instead of above the cavity was used to fit the measured crystal truncation rods. This significantly lowered the quality of the fit and therefore we reject this alternative adsorption site. The difference between the adsorption height we find here and that reported in literature might also be a consequence of the X-ray diffraction measurements, which are sensitive to spatially ordered parts of the interface. If indeed Ca<sup>2+</sup> has multiple adsorption states, SXRD might be more sensitive to the most ordered adsorption state, i.e. the adsorption site above the muscovite cavity which is closer to the surface than the adsorption site above the Si/Al atoms [76].

For divalent cations we expect half the occupancy of monovalent cations in order to compensate for the negative muscovite surface charge. Sr<sup>2+</sup> and Ba<sup>2+</sup> occupancies close to the expected 25% were previously reported for muscovite in contact with 10 mM SrCl<sub>2</sub> and BaCl<sub>2</sub> solutions [94]. The best fit of our measured crystal truncation rods for muscovite in contact with 25 mM CaCl<sub>2</sub> is obtained for a Ca<sup>2+</sup> occupancy of  $28 \pm 8\%$ , which is within the accuracy the same as the reported Sr<sup>2+</sup> and Ba<sup>2+</sup> occupancies. However, for high CaCl<sub>2</sub> concentrations, the Ca<sup>2+</sup> occupancy increases

to  $45 \pm 8\%$ . This suggests an excess surface charge of approximately  $+1.7e/nm^2$ , which is too high to compensate for in the diffuse layer [65, 78] and strongly suggests anion coadsorption. This can possibly explain the lower Ca<sup>2+</sup> height found at high salinity. Although there is no direct evidence of well-ordered anion coadsorption on monovalent cations [73, 90], except for the evidence presented in Chapter 3, there is some earlier evidence for the formation of CaCl<sup>+</sup> ion pairs. In an X-ray photoelectron spectroscopy study Xu and Salmeron found that Cl<sup>-</sup> could not be washed away fully from the Ca<sup>2+</sup>-mica surface [95]. Furthermore, the coadsorption of Cl<sup>-</sup> to Ca<sup>2+</sup> has been suggested before on montmorillonite [96] and gibbsite [97]. Our current data, however, does not provide enough information on the position and occupancy of the anion: just like in the Cs<sup>+</sup>-mica case, the anion is probably too disordered to be visible to SXR. D.

Previously, using SXR. D. the adsorption height on muscovite mica was found to increase with the ionic radius for monovalent Rb<sup>+</sup> and Cs<sup>+</sup> [72]. A similar trend was observed for divalent Sr<sup>2+</sup> and Ba<sup>2+</sup> [94]. This is summarized in Fig. 4.2a, which shows the adsorbed height as function of the unhydrated ionic radius. Interestingly,

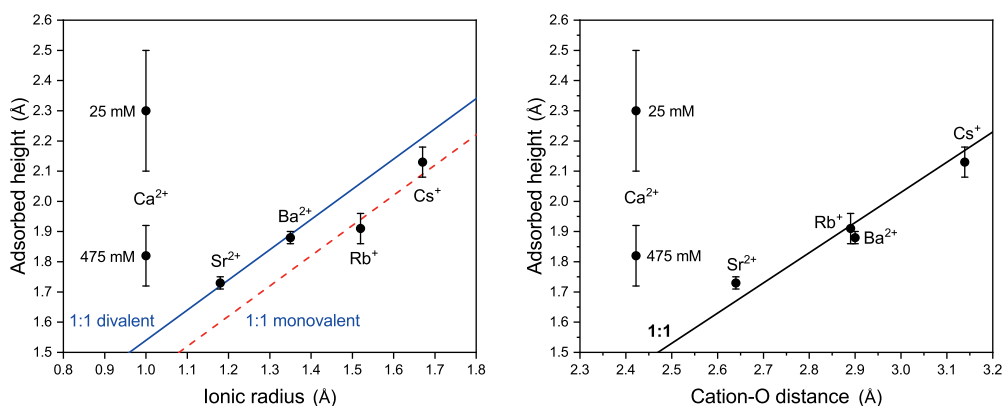


**Figure 4.2.:** Adsorbed height of cations determined using SXR as function of (a) the unhydrated ionic radius [98] and (b) the distance between the cation and the O atom of the first hydration shell. [99] The adsorption height was measured at a cation concentration of 11 mM for Rb<sup>+</sup> and 10 mM for both Sr<sup>2+</sup> and Ba<sup>2+</sup> [72, 94]. The Cs<sup>+</sup> adsorption height was found to be independent of concentration between 2 and 1000 mM [73]. The 1:1 monovalent (red, dashed) and 1:1 divalent lines (blue, solid) in (a) and the 1:1 line (black, solid) in (b) indicate the trend for heavier elements.

Ca<sup>2+</sup> clearly does not follow the divalent trend, neither for high nor for low salt concentrations. The Ca<sup>2+</sup> ion is significantly smaller than the other divalent cations and could be expected to adsorb at a height of approximately 1.54 Å above the surface,

according to the trend. The deviation from the trend might be caused by the strong hydration shell of Ca<sup>2+</sup>. The SXRDR interfacial structure shows that there is no water underneath the Ca<sup>2+</sup> ion and thus that Ca<sup>2+</sup> is only partially hydrated. Since the hydration energy of Ca<sup>2+</sup> is relatively high, and the ionic radius relatively small, it is more favourable for Ca<sup>2+</sup> to adsorb at a height larger than based purely on its ionic radius, since then Ca<sup>2+</sup> is able to retain more water molecules in its hydration shell. In Fig. 4.2b, the adsorbed height as function of the distance between the cation and O atom of the first hydration shell is shown. Here, an approximate 1:1 relationship is found for all cations, except for Ca<sup>2+</sup>. This once more shows the effect of the strong hydration of Ca<sup>2+</sup>.

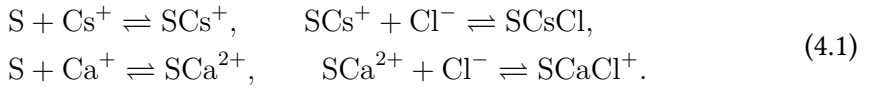
The measurements at high temperature (HT) were performed at  $63 \pm 2$  °C, and similar to Cs<sup>+</sup>, no significant changes in surface structure are observed for Ca<sup>2+</sup> at high temperature when compared to the room temperature structure. At high temperature, Ca<sup>2+</sup> is found to adsorb with an occupancy of  $47 \pm 8\%$  at a height of  $1.74 \pm 0.10$  Å (Fig. 4.1), compared to an occupancy of  $45 \pm 8\%$  at a height of  $1.79 \pm 0.10$  Å at room temperature.

The adsorption of cations takes place at the same adsorption site as was found for the single salt conditions, i.e. the cavity site. For Cs<sup>+</sup>, this is in agreement with literature, as only a small fraction of Cs<sup>+</sup> is reported to adsorb at other adsorption sites [6, 70]. As mentioned before, for divalent cations, including Ca<sup>2+</sup>, multiple adsorption sites were proposed in literature. Besides the partially hydrated cavity site, a partially hydrated adsorption site above the Si/Al atoms and a fully hydrated outer-sphere adsorption site were proposed [6, 76, 92, 93]. In our measurements, however, we observe neither of these alternative Ca<sup>2+</sup> adsorption sites. This means that these adsorption states are either not present, or, similar to the coadsorbed anions, too disordered to give a measurable signal. If indeed outer-sphere Ca<sup>2+</sup> is too disordered to observe, this would mean that the total Ca<sup>2+</sup> occupancy would be higher than reported in Figs. 4.3 & 4.4, and consequently the Cl<sup>-</sup> coverage would be higher too. For other divalent cations, such as Sr<sup>2+</sup> and Zn<sup>2+</sup>, total cation occupancies of  $0.64 \pm 0.16$  and  $0.38 \pm 0.02$  atom/surface unit cell were found at comparable pH values [92, 100]. Our inner-sphere Ca<sup>2+</sup> occupancies of  $0.56 \pm 0.16$  and  $0.90 \pm 0.16$  atom/surface unit cell are already close to or even higher than the total occupancy of the other cations, implying that the outer-sphere Ca<sup>2+</sup> occupancy should be low for a comparable total occupancy. This is in agreement with molecular dynamics simulations, which showed that for Ca<sup>2+</sup> and other divalent cations inner-sphere adsorption is more favourable than outer-sphere adsorption [76]. The interfacial structure we propose here does not require the extra Ca<sup>2+</sup> sites and gives a consistent description of SXRDR and AFM data. For completeness, the effect of additional outer-sphere Ca<sup>2+</sup> on the competition results will be discussed in more detail below.

### 4.3. Cs<sup>+</sup>/Ca<sup>2+</sup> competition

Fig. 4.3a shows the resulting cation occupancy as a function of solution composition derived from this structural model, for a total salt concentration of 25 mM. At a composition of around 75% Ca<sup>2+</sup> and 25% Cs<sup>+</sup>, both cations have similar occupancies, and therefore we can tentatively conclude that Cs<sup>+</sup> has a higher affinity to the muscovite basal plane than Ca<sup>2+</sup>. The electron density perpendicular to the surface (Fig. 4.3b) shows that the muscovite interfacial structure does not significantly change when the cation composition is varied, aside from the electron density at the position of the cations. Also at a total salt concentration of 475 mM, Cs<sup>+</sup> has a higher affinity to the muscovite basal plane than Ca<sup>2+</sup>, as both cations have equal occupancies around a solution composition of 80% Ca<sup>2+</sup> and 20% Cs<sup>+</sup> (Fig. 4.4a). Again, the interfacial structure does not change for varying cation compositions except for the cation electron density (Fig. 4.4b).

As in the case of the Cs<sup>+</sup>-adsorption isotherm, we can set up a surface complexation model to reproduce the cation coverage data measured by SXR, as well as the net surface charge of pure Cs<sup>+</sup>-mica and Ca<sup>2+</sup>-mica measured by Bera et al. using AFM [65]. In the Cs<sup>+</sup>/Ca<sup>2+</sup> competition model we also need to include coadsorption of an anion (Cl<sup>-</sup>) to Ca<sup>2+</sup>. A minimal model thus includes the following four adsorption reactions,



Again, only Cl<sup>-</sup> was chosen as the coadsorbing anion. We can then use the surface complexation model developed in the previous chapter, extended to include Ca<sup>2+</sup>/Cs<sup>+</sup> competition, to fit both the AFM net surface charge and the SXR cation coverage data (see Appendix A.1 for more details). From this fit, we obtain the four fit parameters pK<sub>Cs</sub>, pK<sub>CsCl</sub>, pK<sub>Ca</sub> and pK<sub>CaCl</sub>. The result is shown in Figs. 4.3 and 4.4. The parameters used for the best fit, which was obtained by fitting all room temperature data, were pK<sub>Cs</sub> = 1.3 ± 0.1, pK<sub>Ca</sub> = 0.9 ± 0.2, pK<sub>CsCl</sub> = 0.7 ± 0.1 and pK<sub>CaCl</sub> = 0.4 ± 0.1, and with the intrinsic surface charge of mica the same as used in Chapter 3 ( $\sigma_{\text{int}}/\Gamma = 36 \pm 1\%$ ). The pK<sub>Ca</sub> value is close to previously reported values, as it is directly related to the point of zero charge exhibited by Ca<sup>2+</sup>-mica around 15 mM [59, 82].

The surface complexation model can easily be extended to include a possible Ca<sup>2+</sup> outer-sphere contribution. In this case, the total Ca<sup>2+</sup> occupancy ( $\theta_{\text{Ca}^{2+}}$ ) will consist of  $\theta_{\text{Ca}^{2+}_{\text{IS}}}$  and  $\theta_{\text{Ca}^{2+}_{\text{OS}}}$ , where  $\theta_{\text{Ca}^{2+}_{\text{IS}}}$  is reported in Figs. 4.3 and 4.4. Within surface complexation models, the ratio between occupancies of different adsorption states of an ion, for example inner and outer-sphere, is independent of the (bulk) concentrations of

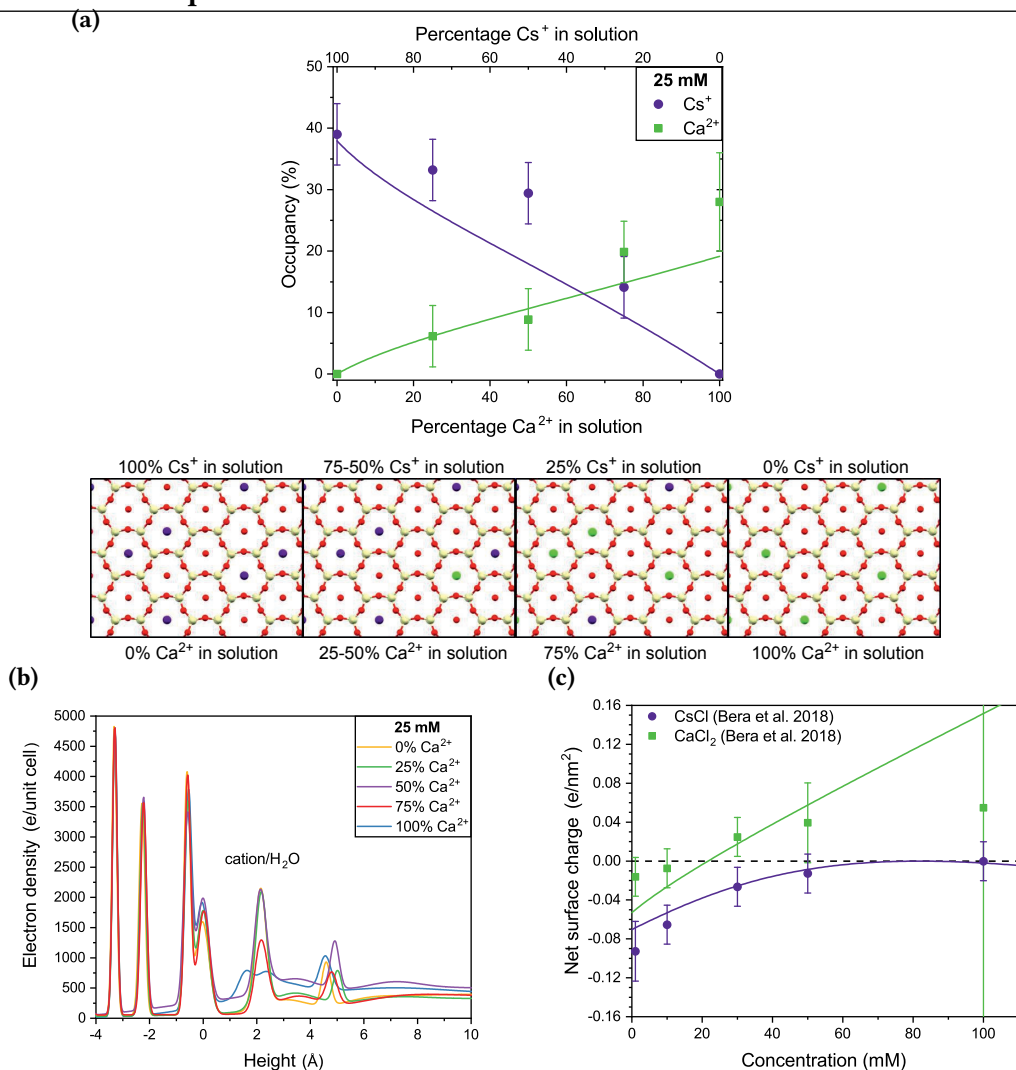


**Figure 4.3.:** (a) Upper panel: Inner-sphere Ca<sup>2+</sup> and Cs<sup>+</sup> occupancies for a total salt concentration of 25 mM at different relative concentrations. Lower panel: Illustration of adsorption of both cations above the center of the hexagonal cavity (Ca<sup>2+</sup> in green, Cs<sup>+</sup> in purple and water in red). Note that SXR is not sensitive to the local adsorption arrangements. (b) Electron density perpendicular to the surface for muscovite in contact with solutions of 25 mM with different Ca<sup>2+</sup>/Cs<sup>+</sup> ratios. (c) The associated net surface charge as measured using AFM by Bera et al. [65]. The solid lines in (a) and (c) show the best fit of the Cs<sup>+</sup>/Ca<sup>2+</sup> competition model, giving an intrinsic surface charge  $\sigma_{\text{int}}/\Gamma = 36 \pm 1\%$  and reaction constants given by  $\text{p}K_{\text{Cs}} = 1.3 \pm 0.1$ ,  $\text{p}K_{\text{CsCl}} = 0.7 \pm 0.1$ ,  $\text{p}K_{\text{Ca}} = 1.0 \pm 0.2$  and  $\text{p}K_{\text{CaCl}} = 0.4 \pm 0.1$ .

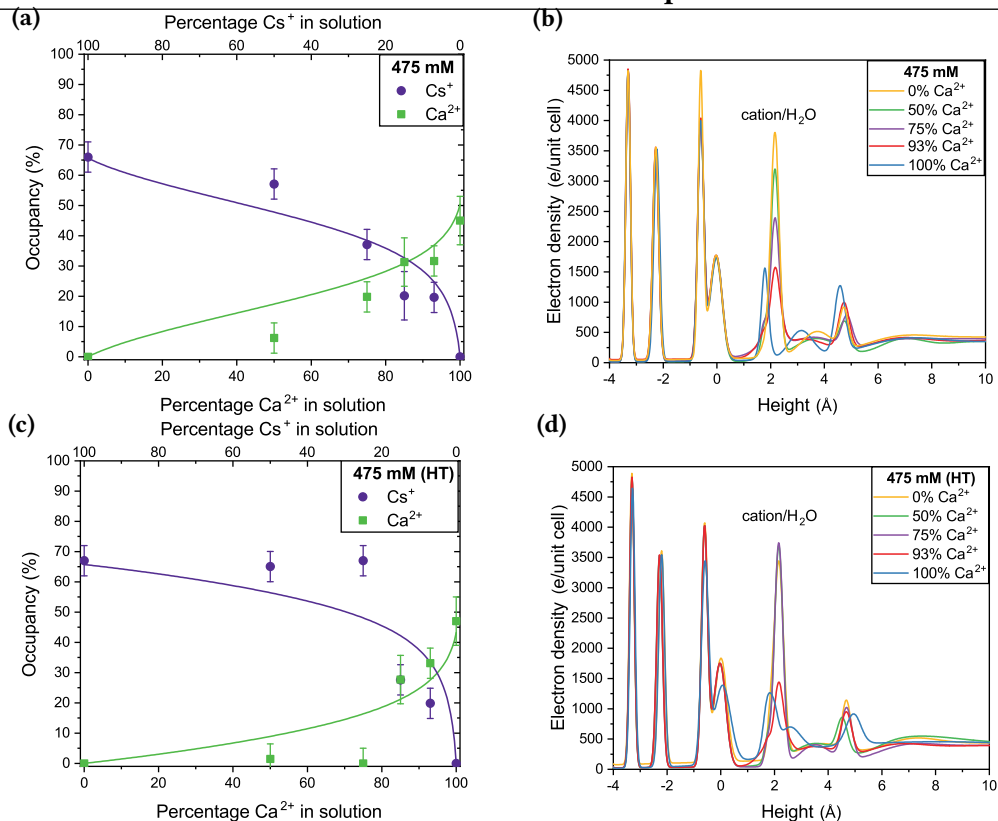


**Figure 4.4.:** (a) Measured and fitted inner-sphere Ca<sup>2+</sup> and Cs<sup>+</sup> occupancies and (b) electron density perpendicular to the surface for muscovite in contact with different Ca<sup>2+</sup>/Cs<sup>+</sup> ratios at a total salt concentration of 475 mM. The solid line in (a) is obtained with the same fit parameters as in Fig. 4.3. (c) Ca<sup>2+</sup> and Cs<sup>+</sup> occupancies and (d) electron density perpendicular to the surface for muscovite in contact with different Ca<sup>2+</sup>/Cs<sup>+</sup> ratios at a total salt concentration of 475 mM at a temperature of  $63 \pm 2$  °C. The typical fit shown as the solid lines in (c) is computed with the same fit parameters as in Fig. 4.3, except here for  $pK_{Ca} = 0.4$ .

the ion. If we assume, as an example, that  $\theta_{Ca_{OS}^{2+}} = 0.3 \times \theta_{Ca_{IS}^{2+}}$ , the model is still capable of reproducing the data. We find that the  $pK_{Cs}$  and  $pK_{CsCl}$  values are not affected by additional outer-sphere adsorption of Ca<sup>2+</sup>. As expected, the  $pK_{Ca}$  value decreases (becomes  $0.6 \pm 0.2$  in this case), whereas the  $pK_{CaCl}$  value increases (becomes  $1.0 \pm 0.1$ ). This means that the reported  $pK_{Ca}$  is possibly overestimated, whereas  $pK_{CaCl}$  is underestimated if outer-sphere adsorption of Ca<sup>2+</sup> occurs. More importantly, our surface complexation model is robust under these conditions and can qualitatively describe general trends observed in the data, such as the higher affinity of Cs<sup>+</sup> than

Ca<sup>2+</sup> for the muscovite basal plane. A similar analysis holds for, for example, an additional adsorption site above the Si/Al atom. This too is a second adsorption state, since there is not enough room to adsorb both in the cavity and above the Si/Al atom, although we should note that this additional site is not reflected in the SXRD data.

For the high temperature data set, the model has too many parameters to provide a unique fit. Since the temperature has changed significantly, we expect all reaction constants to change, but we cannot confidently predict all parameters with the current HT data. That is not to say, however, that we cannot obtain any information from the HT data. For example, we can fix three reaction constants and fit the fourth one to see if the fit improves compared to the RT values. This will of course not give a unique fit, but does give an indication how a reaction constant is likely to change under the increased temperature. Such an analysis suggests that decreasing  $pK_{Ca}$  (fit shown as the solid lines in Fig. 4.4c) or  $pK_{CaCl}$  compared to the other reaction constants improves the fit more than adjusting  $pK_{Cs}$  or  $pK_{CsCl}$  does. This simple analysis therefore suggests that, although the affinity of both Cs<sup>+</sup> and Ca<sup>2+</sup> will most likely decrease, the affinity of Ca<sup>2+</sup> probably decreases more compared to the affinity of Cs<sup>+</sup>. This qualitative trend is corroborated by the data in Fig. 4.4, which shows that Ca<sup>2+</sup> only manages to outcompete Cs<sup>+</sup> at an even higher Ca<sup>2+</sup> percentage compared to room temperature.

The uncertainties in the parameters were determined via the covariance matrix associated with the data and the model and by testing the effect of excluding part of the data. We find that the values of the cation adsorption constants,  $pK_{Cs}$  and  $pK_{Ca}$ , are very robust under such changes (variations less than 0.1 from the best fit values stated above), while the Cl<sup>-</sup> coadsorption constants,  $pK_{CsCl}$  and  $pK_{CaCl}$ , are slightly less robust (variations less than 0.5 from the best fit values stated above) depending on the data sets included in the fitting procedure. Furthermore, we know that the Poisson-Boltzmann theory used to fit the data generally becomes less reliable for salinities exceeding 100 mM, and is therefore less accurate for the measurements at 475 mM.

## 4.4. Discussion & conclusion

Instead of focussing on the specific value of the reaction constant, we focus on the results that are independent on the details of the model. One of the most important of these results is that we consistently find that  $pK_{Ca} < pK_{Cs}$ , i.e. that Ca<sup>2+</sup> has a lower affinity to the muscovite surface than Cs<sup>+</sup>. This point is also clearly derived from the SXRD data shown in Figs. 4.3 and 4.4. It thus seems that a higher valency does not necessarily lead to a higher affinity of an ion to a surface. However, surface complexation models cannot elaborate on the molecular origin of the value of the reaction constant, so based on the current analysis we can only speculate about this. It was

already suggested before that hydration of the ions is a major factor in determining the affinity of the ion to a surface [5, 100]. It has been shown above that the cations adsorb above the cavity, and must therefore lose a significant part of their hydration shell. Consequently, it is less favourable for a strongly hydrated ion, such as Ca<sup>2+</sup>, to adsorb, than for a more weakly hydrated ion such as Cs<sup>+</sup>. Furthermore, it has been shown that ions with a larger ionic radius (i.e. unhydrated radius), which are more polarisable than smaller ions, adsorb more readily to surfaces with a low dielectric constant [101]. This interpretation is consistent with the observations at high temperature.

We expect that an increasing temperature will weaken the hydration of ions since the solubility of both salts increases with increasing temperature [102]. This is further corroborated by studies on the residence time of water molecules in the hydration shell of ions, which is thought to be directly related to the hydration strength [103, 104]. It was found that for both Cs<sup>+</sup> and Ca<sup>2+</sup> the hydration strength decreases with temperature [104–107], suggesting that both hydration energies, and by extension adsorption free energies, decrease with increasing temperature. Similar behaviour under temperature variations was found for Cs<sup>+</sup> on kaolinite [108]. Given that Cs<sup>+</sup> is weakly hydrated at RT, it is plausible that its hydration shell is more easily disrupted than the hydration shell of Ca<sup>2+</sup>, as the temperature increases. This would decrease the affinity of Ca<sup>2+</sup> more than that of Cs<sup>+</sup>, as observed in the data. Within this light, we can also understand why we find that the anion coadsorbs weaker on Ca<sup>2+</sup> than on Cs<sup>+</sup>, as for this process the hydration structure must be disrupted too. However, the hydration of the cations is not the only factor. The hydration of the surface itself, which depends on the cation coverage, should also have a significant impact on the affinity [5, 100]. Other possibly relevant effects include the interfacial dielectric constant [109, 110] and the localization of the surface charge. A full analysis of this complex, many-body problem is outside the scope of this study presented in this chapter.

A second important conclusion, which has already been discussed in the previous chapter, is that an anion coadsorption process is required to fit the data. However, it is also clear that the current model can be further refined. For example, we could include a lateral interaction between the adsorbed ions, introduce a second Cl<sup>-</sup> coadsorption reaction on Ca<sup>2+</sup>, have both OH<sup>-</sup> and Cl<sup>-</sup> coadsorb, or even introduce a different (reversible) proton (co)adsorption reaction. Interestingly, we can improve the quality of the fit by including a lateral repulsion between the adsorbed Cs<sup>+</sup> ions and the adsorbed Ca<sup>2+</sup> ions (see Appendix A.4 for more details). Adding a second coadsorption reaction, however, did not increase the quality of the fit significantly. This model showed signs of overfitting, and based on the current data we refrain from concluding whether such an additional reaction contributes significantly. Such extensions, however, only further complicate the model and introduce more fit parameters. Given the number of parameters already in the model, we do not apply such extensions in the current

analysis. Even though the fit improves by including a lateral interaction between the ions, the model still exhibits the same qualitative behaviour as the proposed minimal model.

It is clear, thus, that the muscovite-electrolyte interface shows a greater complexity than is usually assumed. The question remains whether these conclusions are unique to muscovite mica or whether they also apply to other surfaces.

## **Acknowledgements**

We thank Sander Brugman and Elias Vlieg from the Radboud University in Nijmegen for gathering, sharing and discussing the SXRD data, and an overall fruitful cooperation on this project. We thank F. Mugele for kindly providing the AFM data.

## **Part II.**

# **Static Interface & Dynamic Fluid**





# Chapter 5.

## Transport in heterogeneous electrokinetic systems

*In this chapter we study the transport properties of a typical electrokinetic system: a channel connecting two water reservoirs. While the interface is, as in part I, static, in this part the fluid is free to move resulting in transport from one reservoir to the other. In this chapter, we analyse how this transport is influenced by the Electric Double Layer. We discuss three different types of transport, a water, charge and salt flux due to a pressure, voltage or salinity drop across the channel. A salinity gradient results, due to the Electric Double Layer, in a heterogeneous channel. In this chapter, we expand on previous theoretical formalisms in order to incorporate lateral heterogeneities. To validate the formalism, we compare its prediction with numerical solutions of the governing equations and find good agreement. We then use the formalism to analyse a common electrokinetic system used in Reverse Electrodialysis.*

*The main highlights of this chapter are:*

- *Section 5.3*  
*Derivation of a global linear response theory from a local linear response theory that can incorporate heterogeneities*
- *Section 5.5*  
*Validating the proposed formalism with exact numerical solutions of the governing equations*
- *Section 5.6*  
*Using the proposed formalism to analyse a common electrokinetic system, used in Reverse Electrodialysis, to harvest blue energy*

## 5.1. Introduction

Over the past decades, the interest in nano- and microfluidics devices has significantly increased as these systems are able to control the transport of fluid, and thus dissolved solutes, with microscopic precision. The small scale of nanofluidic devices leads to novel properties compared to macrofluidic devices, allowing applications to a wide variety of different research fields [12, 21]. The great potential of such devices is additionally attested by biological systems, which show an amazing control over permeability and selectivity of nanochannels [12, 26–28].

The unique properties of nano-fluidic devices derive ultimately from the relatively large surface to volume ratio. These properties make the field of nanofluidics of great importance for transport in porous materials such as porous rocks [22] and membranes [111]. Additionally, nano-fluidic devices offer new promising roads to desalination [112], DNA translocation [113–115] and renewable energy harvesting [116, 117]. For instance, they have been used to convert hydrostatic energy into electric power [118, 119] and to harvest energy from mixing salt and fresh water by Reverse Electrodialysis (RED) [120, 121], Pressure Retarded Osmosis (PRO) [122–124] or Capacitive Double Layer Expansion (CDLE) [125]. All of these nanofluidic devices are based on essentially the same system, composed of a channel with charged walls connecting two reservoirs with different reservoir conditions. Recent advances highlight the great potential for nanofluidics of Carbon Nanotubes (CNT) [126], Boron Nitride Nanotubes (BNNT) [127] and MoS<sub>2</sub> nanopores [128], which exhibit unique properties due to their small size and favourable electric properties.

## 5.2. Transport In electrokinetics

Fig. 5.1 shows a representation of a typical electrokinetic system we will consider in this chapter: a cylindrical channel with a charged surface of length  $\ell$  and radius  $R$  connecting two bulk reservoirs containing a 1:1 electrolyte at room temperature. In this chapter we consider three different driving forces for transport, a pressure drop  $\Delta p$ , a voltage drop  $\Delta V$  (electro-osmosis) and a salt chemical potential drop  $\Delta\mu$  (i.e. a salt concentration drop  $\Delta\rho$ , diffusio-osmosis) over the channel. These driving forces can induce three different fluxes, i.e. currents integrated over a cross section: a volume or water flux  $Q$  (m<sup>3</sup>/s), more commonly known as the volumetric flow rate, a charge flux or electric current  $I$  (A) and a net salt flux  $J$  (s<sup>-1</sup>).

Boundary Conditions	System
$\Delta\mu = 0, \Delta p = 0, \Delta V \neq 0$	Electro-osmosis
$\Delta\mu = 0, \Delta p \neq 0, I = 0$	Streaming potential
$\Delta\mu \neq 0, \Delta p = 0, I = 0$	Membranes/diffusio-osmosis
$\Delta\mu \neq 0, \Delta p \neq 0, I = 0,$	Pressure Retarded Osmosis & desalination
$\Delta\mu = 0, \Delta p \neq 0, I \neq 0$	Mechanical energy conversion
$\Delta\mu \neq 0, \Delta p = 0, I \neq 0$	Reverse Electrodialysis
$\Delta\mu = 0, Q = 0, \Delta V \neq 0$	Capacitive Double Layer Expansion

**Table 5.1.:** Collection of electro-kinetic systems and the associated boundary conditions, with  $\Delta p$ ,  $\Delta V$ , and  $\Delta\mu$  the pressure, voltage and chemical potential drop across the channel, and  $I$  and  $Q$  the electric current and volumetric flow rate through the channel.

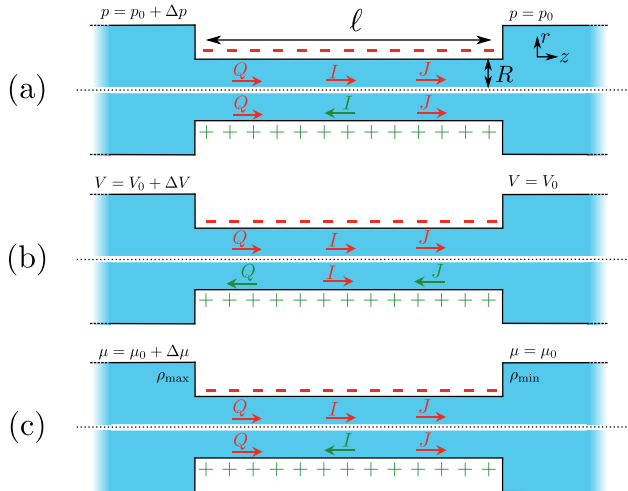


**Figure 5.1.:** A representation of a typical electrokinetic system with an imposed (a) pressure drop  $\Delta p > 0$ , (b) electrostatic potential drop  $\Delta V > 0$  or (c) a chemical potential drop  $\Delta\mu > 0$  across a cylindrical channel with length  $\ell$  and radius  $R$ . Here we consider both a positive (green) and negative (red) surface charge. The direction of the volumetric flow rate  $Q$ , electric current  $I$  and solute flux  $J$  depends on the sign of the surface charge and is indicated by the arrow and the colour. A red colour indicates that the flux is in the opposite direction to gradient of the applied driving force.

Within linear response, we quantify the relation between the driving forces,  $\Delta p$ ,  $\Delta V$  and  $\Delta\mu$ , and generated fluxes,  $Q$ ,  $I$  and  $J$ , by a conductivity matrix  $\mathbf{G}$ ,

$$\begin{pmatrix} Q \\ I \\ J \end{pmatrix} = \frac{A}{\ell} \mathbf{G} \begin{pmatrix} \Delta p \\ \Delta V \\ \Delta\mu \end{pmatrix}, \quad (5.1)$$

with  $A = \pi R^2$  the cross section area. The unique properties of nano-fluidic devices ultimately derive from the non-zero off-diagonal terms of  $\mathbf{G}$ , which highlight the highly interactive nature of nano-fluidic devices. If  $\mathbf{G}$  is known, we can use Eq. (5.1) to calculate the fluxes generated by any set of imposed driving forces. For instance, an electric short-circuit or closed-circuit channel is obtained by electrically connecting the ends of the channel, such that  $\Delta V = 0$ . If the salinities of the two reservoirs are different, i.e. diffusio-osmosis, Eq. (5.1) then gives the generated diffusio-osmotic electric current  $I_{\text{DO}}$  as

$$I_{\text{DO}} = \frac{A}{\ell} (G_{21}\Delta p + G_{22}\Delta V + G_{23}\Delta\mu) = \frac{A}{\ell} G_{23}\Delta\mu, \quad (5.2)$$

where we furthermore assumed a ‘mechanical closed-circuit’ condition, where water is free to flow (i.e.  $\Delta p = 0$ ).

Alternatively, it is also possible to impose the flux instead of the applied potentials. For example, in an electric open-circuit channel the two reservoirs are not electrically connected and therefore no electric current can flow in steady state. In this case the flux  $I = 0$  is imposed instead of the potential drop, but then too Eq. (5.1) can be used. Since  $\Delta\mu$  directly generates the current  $I_{\text{DO}}$  given by Eq. (5.2), the only way to obtain a vanishing  $I$  is for the system to develop a potential drop over the channel, commonly referred to as the diffusion potential  $\Delta V_{\text{dif}}$  [12], such that the induced electro-osmotic current  $I_{\text{EO}} = \frac{A}{\ell} G_{22}\Delta V$  exactly cancels the diffusio-osmotic current  $I_{\text{DO}}$ . The total current is simply the sum of the separate contributions,  $I_{\text{total}} = I_{\text{DO}}(\Delta\mu) + I_{\text{EO}}(\Delta V_{\text{dif}}) = 0$ , and we find

$$\Delta V_{\text{dif}} = -\frac{G_{23}}{G_{22}}\Delta\mu, \quad (5.3)$$

The above two examples show that whether a flux or a driving force is imposed, in either case Eq. (5.1) can be used to calculate the remaining fluxes/driving forces. There is a great variety of imposed fluxes or driving forces that result in many different electrokinetic systems. Many of such electrokinetic systems are known by specific

names, see Table 5.1, and Eq. (5.1) can be used for all possible combinations of driving forces.

In this chapter, we will show how we can obtain the conductivity matrix  $\mathbf{G}$  from a well-known microscopic linear response theory based by the Onsager matrix  $\mathbf{L}$  (as was shortly discussed in Section 2.2.3), which we will calculate analytically within the Poisson-Boltzmann formalism. We then show how to extend  $\mathbf{L}$ , which is in essence a local linear-response equation, to  $\mathbf{G}$ , which is a global linear-response equation. In order to validate our method, we compare predictions of Eq. (5.1) with solutions of the Poisson-Nernst-Planck-Stokes equations obtained using Finite Element Method (FEM). While FEM results are typically more precise, the great advantage of the proposed method is that these are much easier to implement and do not require complicated numerical techniques, and can thus be more easily used to analyse more complex nanofluidic systems. As an example, we will use the generalised conductivity matrix  $\mathbf{G}$  to show how to incorporate a charge regulation mechanism with a salinity gradient, and compare predictions of the generated current with experiments on Boron Nitride Nanotubes [127]. The proposed framework provides a general formalism to investigate all electrokinetic systems as listed in Table 5.1, but as an example we will use  $\mathbf{G}$  to analyse an electrokinetic system using Reverse Electrodialysis under a wide variety of parameters without the need for extensive numerical calculations with FEM. This analysis highlights the convenience and utility of the conductivity matrix  $\mathbf{G}$  for nanofluidics and electrokinetic systems in general.

## 5.3. From local to global linear response

### 5.3.1. Local linear Response

A well-known method to describe the transport properties of nano-fluidic channels is by the so-called Onsager matrix  $\mathbf{L}$  [50–54], which relates the local driving forces to the generated fluxes. Within linear response theory, the induced fluxes are linear in the driving forces

$$\begin{pmatrix} Q \\ I \\ J - 2\rho_s Q \end{pmatrix} = \mathbf{A}\mathbf{L} \begin{pmatrix} -\partial_z p \\ -\partial_z V \\ -\partial_z \mu \end{pmatrix}, \quad (5.4)$$

where  $\partial_z$  is the derivative with respect to the lateral Cartesian coordinate  $z$  and  $\mathbf{L}$  is a symmetric  $3 \times 3$  matrix. For electrokinetic systems, composed of channels with charged walls in contact with an electrolyte,  $\mathbf{L}$  can be determined fully analytically with the

Poisson-Boltzmann formalism (see Appendix B.1). The flux associated to  $\partial_z \mu$  is the excess salt flux  $J_{\text{exc}} = J - 2\rho_s Q$ , the total salt flux  $J$  minus the bulk advective salt flux, with  $\rho_s$  the salt concentration (salinity) at the channel axis. Defining the Onsager matrix in terms of  $J_{\text{exc}}$  rather than  $J$  ensures that  $\mathbf{L}$  is symmetric (see Appendix B.2 for more information) [50–52].

The disadvantage of Eq. (5.4), however, is that it relates the *local* driving forces to the fluxes, while Eq. (5.1) relates the *global* driving forces to the fluxes. Since the global rather than the local driving forces are experimentally imposed or measured, in order for Eq. (5.4) to be useful it must be extended to the same form as Eq. (5.1). This is straightforward if  $\mathbf{L}$  is constant throughout the channel, since then we can simply integrate Eq. (5.4) along the length of the channel and find that  $\mathbf{L} = \mathbf{G}$ . This is the case when a non-zero  $\Delta p$  and  $\Delta V$  is imposed, since only under extreme circumstances do these influence the properties of the channel. However, since the properties of the electric double layer are strongly affected by the salinity  $\rho_s$ , a non-zero  $\Delta \mu$  necessarily leads to a laterally varying salinity  $\rho_s$  and thus a laterally varying  $\mathbf{L}$ . In that case, therefore, it is no longer clear how to convert Eq. (5.4) to a global equation, except in the case of a small relative change in salinity across the channel. If, however, the salinity changes for example from 20 mM to 500 mM, as is the case for fresh to sea water, a clear method is required to obtain the fluxes from  $\mathbf{L}$ .

### 5.3.2. Global linear response

One method to obtain the fluxes as a function of the global driving forces as in Eq. (5.1), is to resolve Eq. (5.4) for every location  $z$  for a given value of the flux. Such adjustments have been successfully incorporated before [52, 53], but since the local driving forces are in principle unknown, this method gives the driving force as a function of the flux instead of the global driving forces as Eq. (5.1). Since the latter is clearly preferable, this method becomes rather cumbersome. Here we show how to extend  $\mathbf{L}$  to  $\mathbf{G}$ , while retaining the convenience of Eq. (5.1). In order to obtain  $\mathbf{G}$  from a heterogeneous  $\mathbf{L}(z)$  we start from the condition that all fluxes  $Q$ ,  $I$  and  $J$  are, in steady state and for non-leaky channels, constant throughout the channel (independent of  $z$ ). In order to calculate the fluxes as a function of the global driving forces, we divide the system into infinitesimally small segments of width  $dz$ , schematically represented in Fig. 5.2, and apply the Onsager equation, Eq. (5.4), for each segment

$$\vec{J} = A \left( \mathbf{L}(z_i) + \mathbf{L}^{\text{adv}}(z_i) \right) \cdot \left( -\frac{d\vec{F}_i}{dz} \right), \quad (5.5)$$

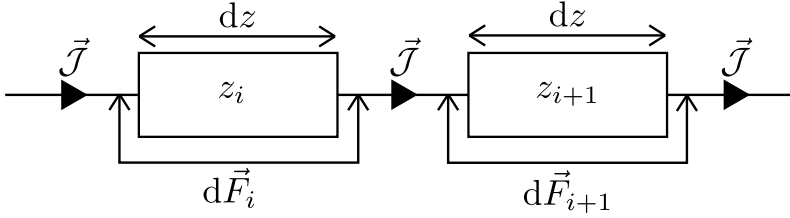


**Figure 5.2.:** Schematic representation of an electrokinetic system divided in infinitesimally small segments of width  $dz$ , with an applied driving force  $d\vec{F}_i$  over each segment and a flux  $\vec{J}$  through each segment. Each segment  $\mathbf{L}(z_i)$  and  $d\vec{F}_i$  can locally take different values, but  $\vec{J}$  is a spatial constant in steady state.

where  $\vec{J} = (Q, I, J)$  and  $d\vec{F}_i/dz = (\partial_z p, \partial_z V, \partial_z \mu)|_{z=z_i}$  is a vector that contains all fluxes and driving forces over the  $i$ th segment, respectively. Since  $Q$ ,  $I$  and  $J$  are defined by integrals over a cross section (see below, Eq. (5.20)), there are no contributions to  $\vec{J}$  from (possibly induced) radial forces  $\partial_r p$ ,  $\partial_r V$  and  $\partial_r \mu$ . Furthermore,  $\mathbf{L}^{\text{adv}}$  is the bulk advective salt flux, which accounts for the difference between  $J$  and  $J_{\text{exc}}$ ,

$$\mathbf{L}^{\text{adv}}(z) = 2\rho_s(z) \begin{pmatrix} 0 & 0 & 0 \\ 0 & 0 & 0 \\ L_{11} & L_{12} & L_{13} \end{pmatrix}, \quad (5.6)$$

with  $\rho_s(z)$  the salinity at the channel axis ( $r = 0$ ) at lateral position  $z$ . Note that  $\mathbf{L}^{\text{adv}}$  simply adds the local advective salt flux  $2\rho_s Q$  to the excess salt flux, since  $J = J_{\text{exc}} + 2\rho_s Q$ . This contribution must be included because in steady state, by virtue of the incompressibility of water and due to charge and ion number conservation,  $Q$ ,  $I$  and  $J$  and thus  $\vec{J}$  can not depend on  $z$  ( $J_{\text{exc}}$  can in principle depend on  $z$ ). We can obtain the global driving forces by summing (integrating in the continuum limit) all  $d\vec{F}_i$ ,

$$\Delta\vec{F} = - \int_0^\ell dz \frac{d\vec{F}}{dz} = \frac{1}{A} \int_0^\ell dz (\mathbf{L} + \mathbf{L}^{\text{adv}})^{-1} \cdot \vec{J}, \quad (5.7)$$

where  $\Delta\vec{F} = (\Delta p, \Delta V, \Delta \mu)$  is the vector containing all global driving forces. Inverting this equation we obtain the (constant) fluxes  $\vec{J}$  as a function of the global driving

forces  $\Delta\vec{F}$ ,

$$\vec{J} = A \left( \int_0^\ell dz (\mathbf{L} + \mathbf{L}^{\text{adv}})^{-1} \right)^{-1} \cdot \Delta\vec{F} \equiv \frac{A}{\ell} \mathbf{G} \cdot \Delta\vec{F}. \quad (5.8)$$

Here, the conductivity matrix  $\mathbf{G}$ , as defined in Eq. (5.1), can thus be obtained from  $\mathbf{L}$  as

$$\mathbf{G}^{-1} = \frac{1}{\ell} \int_0^\ell dz [(\mathbf{L}(\rho_s(z)) + \mathbf{L}^{\text{adv}}(\rho_s(z)))]^{-1}. \quad (5.9)$$

As stated before, the Onsager matrix  $\mathbf{L}$  can be determined analytically within Poisson-Boltzmann theory, and we can subsequently use Eq. (5.9) to find the conductivity matrix  $\mathbf{G}$ .

However, we can significantly simplify Eq. (5.9) by splitting the contributions to  $\mathbf{L}$  in a volume ( $\mathbf{L}^{\text{vol}}$ ) and a surface ( $\mathbf{L}^{\text{surf}}$ ) contribution,

$$\mathbf{L} = \mathbf{L}^{\text{vol}} + \mathbf{L}^{\text{surf}}, \quad (5.10)$$

where  $\mathbf{L}^{\text{vol}}$  consists of all contributions of the order  $R^0$  (or higher) and  $\mathbf{L}^{\text{surf}}$  consists of all terms proportional  $R^{-1}$ , with  $R$  the channel radius. We then treat the volume and surface contributions as separate conductors incorporated in a parallel circuit. To illustrate this, we consider an analogous electrical circuit where two resistors (conductors) are connected in parallel, as in Fig. 5.3. In principle, the induced fluxes  $Q$ ,

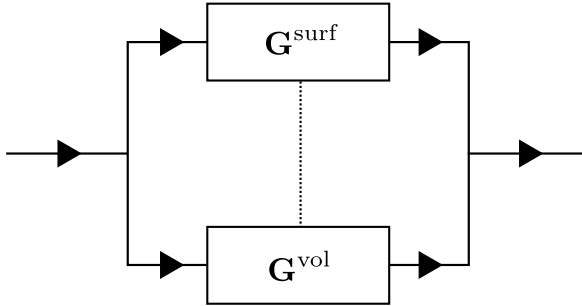


**Figure 5.3.:** Analogue electrical circuit representation of an electrokinetic system.

$I$  and  $J$  can flow via the EDL, represented by  $\mathbf{G}^{\text{surf}}$  or via the region outside the EDL, represented by  $\mathbf{G}^{\text{vol}}$  (each a sequence of many infinitesimally small conductors as in Fig. 5.2). These two are, in general, connected, represented by the dashed line (to be precise, every infinitesimal conductor is connected to its volume/surface counterpart).

We can, however, significantly simplify the system by disconnecting the surface and volume fluxes (i.e. removing the dashed line in Fig. 5.3), which can intuitively be understood by realising that all radial components of the fluxes are small or negligible (such that the interchange between volume and surface is also small). We expect this simplification to break down for small aspect ratios  $\ell/R$  and/or large heterogeneities across the channel.

The advantage of separating the volume and surface contributions is that the total conductance is now determined by the sum of the two separate conductances (note that  $\mathbf{G}^{\text{vol}}$  and  $\mathbf{G}^{\text{surf}}$  themselves can still originate from a laterally heterogeneous  $\mathbf{L}^{\text{vol}}$  and  $\mathbf{L}^{\text{surf}}$  respectively). We can analytically calculate  $\mathbf{G}^{\text{vol}}$ , by evaluating Eq. (5.9) with  $\mathbf{L}^{\text{surf}} = \mathbf{0}$  (see Appendix B.3 for a derivation). On the other hand, it is not possible to determine  $\mathbf{G}^{\text{surf}}$  analytically in the same way as  $\mathbf{G}^{\text{vol}}$ . In order to obtain an analytic expression we approximate  $\mathbf{G}^{\text{surf}}$  by  $\mathbf{L}^{\text{surf}}$  evaluated at the average salinity  $\bar{\rho} = \frac{1}{2}(\rho_{\min} + \rho_{\max})$ ,

$$\mathbf{G}^{\text{surf}} = \left( \frac{1}{\ell} \int_0^\ell dz \mathbf{L}^{\text{surf}}(z)^{-1} \right)^{-1} \approx \mathbf{L}^{\text{surf}}(\bar{\rho}), \quad (5.11)$$

where  $\rho_{\min}$  and  $\rho_{\max}$  are the salt concentration of the low and high salinity reservoir respectively. Note that we could also have chosen the geometric mean  $\bar{\rho}_{\text{geom}} = \sqrt{\rho_{\min}\rho_{\max}}$ , but we found the arithmetic mean to provide (slightly) more accurate predictions compared to the FEM results. The total conductivity matrix  $\mathbf{G}$  can then be approximated as

$$\mathbf{G} \approx \mathbf{G}^{\text{vol}} + \mathbf{G}^{\text{surf}} \approx \mathbf{G}^{\text{vol}} + \mathbf{L}^{\text{surf}}(\rho_s = \bar{\rho}), \quad (5.12)$$

with  $\mathbf{G}^{\text{vol}}$  given in Eq. (B.15) in Appendix B.3. As we will see below, Eq. (5.9) can accurately predict the FEM results over a large range of parameter values, and Eq. (5.12) is surprisingly accurate given the simplifications involved.

One significant advantage of the above formalism is that it is straightforward to also incorporate lateral heterogeneities other than a salinity gradient. For example, we will consider BNNTs and CNTs in this chapter, which obtain their surface charge from the adsorption of an  $\text{OH}^-$  ion. Because  $\text{OH}^-$  carries a net charge, the amount of  $\text{OH}^-$  adsorption depends on the surface charge itself via a mechanism known as charge regulation [41, 129, 130], and can be expressed as a Langmuir-type relation

$$\sigma(z) = z_\sigma e \Gamma \left( 1 + 10^{-\text{pH} + \text{pK}} e^{-e\psi_0(z)/k_B T} \right)^{-1}, \quad (5.13)$$

where  $z_\sigma$  is the valency of the surface charge ( $z_\sigma = -1$  for  $\text{OH}^-$  adsorption),  $\text{pK}$  the reaction constant of the charging mechanism,  $\Gamma$  is the areal density of chargeable surface sites, and  $\psi_0$  the surface potential. The relation between  $\sigma$  and  $\psi_0$  depends on the (local) salinity, given by the Poisson-Boltzmann formalism (see Appendix B.1), such that Eq. (5.13) is a self-consistency relation for the local surface charge  $\sigma(z)$ . Note that, for simplicity, we leave out a Stern layer capacitance from Eq. (5.13). Since  $\psi_0$  is a function of  $\rho_s$ , Eq. (5.13) implies a heterogeneous surface charge in the case of  $\Delta\mu \neq 0$  (diffusio-osmosis), which is straightforwardly included in the above formalism. The charge-regulation boundary condition, however, can significantly affect the resulting fluxes, as we will shown below, and has been shown to be important for the interpretation of measurements on CNTs [131, 132].

### 5.3.3. Entrance effects

One final point to address concerning  $\mathbf{G}$  is that a density profile  $\rho_s(z)$  is required in order to use Eq. (5.9). A straightforward example is of course a purely diffusive (i.e. linear) profile, although one should keep in mind that this is not necessarily accurate because the profile can be influenced by an advective fluid flow or an electric field [133]. The density profile in a finite channel is, however, also affected by entrance effects.

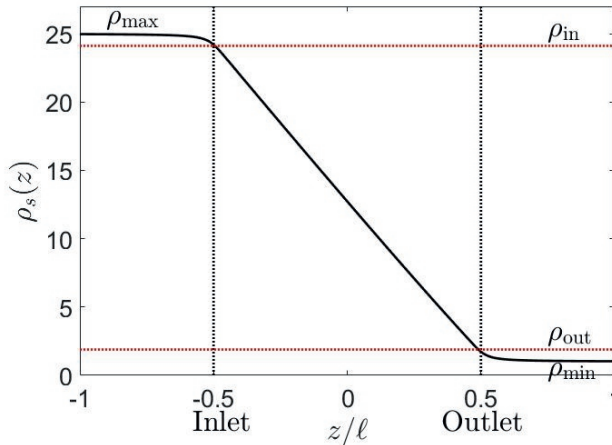


**Figure 5.4.:** Density profile at the axis of the channel calculated with FEM (black full line) for  $R = 60$  nm and  $\ell = 1500$  nm. The dashed red lines indicate the inlet and outlet salinity  $\rho_{\text{in}} \approx 2$  mM and  $\rho_{\text{out}} \approx 24$  mM, and the black dashed lines indicate the location of the inlet ( $z = -\frac{1}{2}\ell$ ) and outlet ( $z = \frac{1}{2}\ell$ ).

Due to the finite size of the channel, the salinity at the in- and outlet of the channel is

not exactly equal to reservoir salinities  $\rho_{\max}$  and  $\rho_{\min}$ . However, the salinity gradients in the far field of the reservoirs vanish, resulting in a region at the in- and outlet, outside the channel, with a salinity different from  $\rho_{\max}$  and  $\rho_{\min}$ . This is confirmed by FEM calculations, which show that the salinity at the inlet is lower than  $\rho_{\max}$ , and the salinity at the outlet is higher than  $\rho_{\min}$  (see Fig. 5.4). The corrections are not large, but one must keep in mind that the conductivity of the channel is, according to Eq. (5.9), most strongly affected by the smallest conductivity, i.e. the low salinity side. A small correction at the outlet can thus have significant effects on the total conductivity.

Fig. 5.4 shows the salinity at the channel axis as determined from FEM solutions of the PNPS equations. Even for a very needle-shaped channel ( $\ell/R = 25$ ), the in- and outlet salinities clearly differ from the reservoir salinities. The effect becomes more pronounced for shorter and/or wider channels with a small aspect ratio. For example, for  $\ell/R = 5$  the outlet salinity is a factor 4 larger than  $\rho_{\min}$  (see Appendix B.4). We denote the inlet salinity as  $\rho_{\text{in}}$  and the outlet salinity as  $\rho_{\text{out}}$ , which now explicitly depend on  $R$  and  $\ell$  due to the entrance effects (see Appendix B.4 for derivation). This correction is similar (although not equal) to the so-called access resistance [114], as it also slightly adjusts the salinity gradient. The chemical potential drop over the channel  $\Delta\mu_{\text{ch}}$  is consequently not equal to the chemical potential difference  $\Delta\mu = k_{\text{B}}T \log \frac{\rho_{\max}}{\rho_{\min}}$  between the two reservoirs, but actually

$$\Delta\mu_{\text{ch}} = k_{\text{B}}T \log \frac{\rho_{\text{in}}}{\rho_{\text{out}}}. \quad (5.14)$$

The distinction between  $\Delta\mu$  and  $\Delta\mu_{\text{ch}}$ ,  $\rho_{\max}$  and  $\rho_{\text{in}}$  and  $\rho_{\min}$  and  $\rho_{\text{out}}$  is a small but significant one, the more so for shorter and wider channels.

In this chapter we assume a linear profile

$$\rho_s(z) = \rho_{\text{in}} - \left( \frac{1}{2} + \frac{z}{\ell} \right) (\rho_{\text{in}} - \rho_{\text{out}}), \quad (5.15)$$

from  $\rho_{\text{in}}$  to  $\rho_{\text{out}}$ , for  $-\frac{1}{2}\ell < z < \frac{1}{2}\ell$ , where the in- and outlet salinities are given by (see Appendix B.4 for derivation)

$$\rho_{\text{out}} \approx \rho_{\min} + \frac{R}{\ell + 2R} \Delta\rho, \quad \rho_{\text{in}} \approx \rho_{\max} - \frac{R}{\ell + 2R} \Delta\rho, \quad (5.16)$$

with  $\Delta\rho = \rho_{\max} - \rho_{\min}$  the salinity difference between the reservoirs. Note that Eq. (5.15) introduces an explicit dependence on the channel length  $\ell$  in the formalism via  $\rho_{\text{in}}$  and  $\rho_{\text{out}}$ , as has indeed been shown to be a non-trivial parameter for diffusio-osmosis [134]. Only for infinitely long channels do we find that  $\rho_{\text{in}} = \rho_{\max}$  and

$\rho_{\text{out}} = \rho_{\text{min}}$ . In general, a salinity profile will be affected by the fluid flow and can be found by solving the convection-diffusion equation. However, the resulting exponential profile reduces to a linear profile if the fluid flow is not too large, more precisely if the Péclet number  $\text{Pe} = \frac{Q\ell}{\pi R^2 D} = (G_{11}\Delta p + G_{12}\Delta V + G_{13}\Delta\mu_{\text{ch}})/D$  is significantly smaller than unity. This is typically the case for diffusio-osmosis, except for very large slip lengths (exceeding tens of nanometers). In that case, the salinity profile must be adjusted to a profile predicted by a diffusion-convection system.

## 5.4. The Onsager matrix

So far we have explained how to extend the local linear response Onsager matrix  $\mathbf{L}$  to a global linear response conductivity matrix  $\mathbf{G}$ . As mentioned,  $\mathbf{L}$  originates partially from the surface charge of the channels walls, which can be either imposed or spontaneously originate from chemi- or physisorption of ions. This surface charge attracts oppositely charged ions to, and repels equally charged ions from, the surface, giving rise to a non-zero space charge close to the surface called the Electric Double Layer (EDL) (see Section 1.2.2 for a discussion of the EDL). The EDL consists of charge and concentration gradients perpendicular to the surface which extend into the fluid over a typical distance of the Debye length  $\lambda_D$ , and therefore affects the fluxes parallel to the surface. We assume here that the EDL is in its equilibrium configuration before the driving forces are applied, since the EDL equilibrates typically on a timescale of the order of nano- to microseconds [135]. This allows us to use the solutions of Poisson-Boltzmann formalism (see Appendix B.1 for expressions) to derive  $\mathbf{L}$ .

In this chapter we will consider an electrokinetic system as depicted in Fig. 5.1, with length  $\ell$ , radius  $R$ , salinity  $\rho_s(z)$  given by Eq. (5.15) and surface charge  $\sigma$ . The fluid flow is determined by the Stokes equation with an electric body force and the incompressibility condition [41],

$$-\nabla p + \eta \nabla^2 \mathbf{u} + e(\rho_+ - \rho_-)\mathbf{E} = 0, \quad \nabla \cdot \mathbf{u} = 0, \quad (5.17)$$

with the slip boundary condition

$$b\partial_r u_z(r = R) = u_z(r = R), \quad (5.18)$$

with the channel axis oriented in the  $z$  direction. Here  $p$  is the hydrostatic pressure (i.e. sum of the partial solvent pressure and osmotic pressure due to the ions),  $\mathbf{u}$  the fluid velocity vector,  $\eta$  the viscosity,  $\mathbf{E}$  the electric field,  $e$  the proton charge,  $\rho_{\pm}$  the local cation/anion number density,  $b$  the slip length and  $r \in [0, R]$  the coordinate normal to

the surface. The ion fluxes are given by the Nernst-Planck equation [41],

$$\mathbf{j}_i = -D_i \nabla \rho_i + z_i \frac{D_i e}{k_B T} \rho_i \mathbf{E} + \rho_i \mathbf{u}, \quad (5.19)$$

with  $k_B$  the Boltzmann constant,  $T$  the temperature and  $\rho_i$ ,  $D_i$ ,  $z_i$  the density, the diffusion constant and the valency of ion species  $i = \pm$ , respectively. We consider in this chapter a 1:1 salt, as this makes it possible to solve all equations analytically (although these are straightforwardly extended to a  $z:z$  salt). We obtain the fluxes as

$$\begin{aligned} Q &= 2\pi \int_0^R dr r u_z, \\ I &= 2\pi e \int_0^R dr r (j_{+,z} - j_{-,z}), \\ J &= 2\pi \int_0^R dr r (j_{+,z} + j_{-,z}), \end{aligned} \quad (5.20)$$

for a cylindrical geometry. Note that  $J$  is the total and not the excess salt flux  $J_{\text{exc}}$ .

By combining the above equations with the solutions of Poisson-Boltzmann formalism for a 1:1 salt [12, 40], the full  $3 \times 3$  Onsager matrix can be determined analytically. The majority of the matrix elements of  $\mathbf{L}$  are already known, although we do find a contribution to  $L_{23}^{\text{surf}}$ , the non-advective contributions of Eq. (5.21), that appears to have been overlooked in previous studies [127, 136]. It is an important contribution that cannot be ignored, and is in fact required by the symmetry of  $\mathbf{L}$ . This term is intimately linked to the heterogeneity of the EDL: since the Debye length  $\lambda_D$  is a function of  $z$ , diffusio-osmosis generates a lateral component to the electric field which contributes to the generated fluxes (see the associated article [137] for detailed discussion of this subtle contribution). For the sake of completeness, however, we present not just  $L_{32}$  but the full  $3 \times 3$  matrix.

Eq. (5.21) shows the Onsager matrix elements, with  $\lambda_B = \frac{e^2}{4\pi\epsilon k_B T}$  the Bjerrum length and  $\lambda_D = (8\pi\lambda_B\rho_s)^{-1}$  the Debye length,  $\epsilon$  the permittivity of water,  $\psi_0$  the surface potential,  $z_s$  the sign of the surface charge,  $D = \frac{1}{2}(D_+ + D_-)$  the average ion diffusion constant and  $\beta = \frac{D_+ - D_-}{D_+ + D_-}$  the mobility mismatch. The constants  $P_i$  are positive numbers and function of  $\rho_s$ ,  $\sigma$  and  $\psi_0$  only. For small surface charge,  $2\pi\lambda_B\lambda_D\sigma \ll 1$ , all these constants scale as  $P_i \sim \sigma^2 \sim \phi_0^2$ , while for large surface charge,  $2\pi\lambda_B\lambda_D\sigma \gg 1$ ,  $P_1 \approx \pi^2/2$ ,  $P_2 \sim \sigma$ ,  $P_3 \sim |\phi_0|$ ,  $P_4 \approx \pi^2/4$  and  $P_5 \sim \sigma$ . These constants are solutions to rather involved integrals, and the full expressions can be

found in Appendix B.1, and their derivation can be found in the article associated to this chapter [137].

$$\begin{aligned}
L_{11}^{\text{vol}} &= -\frac{R^2}{8\eta} \left(1 + \frac{4b}{R}\right) & L_{22}^{\text{vol}} &= \frac{2De^2}{k_B T} \rho_s & L_{11}^{\text{surf}} &= 0 \\
L_{12}^{\text{vol}} &= -\frac{\epsilon\psi_0 + z_\sigma b e \sigma}{\eta} & L_{23}^{\text{vol}} &= \beta \frac{2De}{k_B T} \rho_s & L_{12}^{\text{surf}} &= z_\sigma \frac{e\lambda_D}{2\pi\lambda_B\eta R} P_1, \\
L_{13}^{\text{vol}} &= \frac{1}{4\pi\lambda_B\eta} \left(\frac{b}{\lambda_D} P_2 + P_3\right) & L_{33}^{\text{vol}} &= \frac{2D}{k_B T} \rho_s & L_{13}^{\text{surf}} &= -\frac{\lambda_D}{8\pi\lambda_B\eta R} P_4, \\
L_{22}^{\text{surf}} &= \frac{2De^2}{k_B T} \left(\frac{2\rho_s\lambda_D}{R} P_2 \left(1 + \frac{k_B T}{2\pi\lambda_B\eta D}\right) - z_\sigma \beta \frac{\sigma}{R}\right) + 2e^2 \frac{b}{R} \frac{\sigma^2}{\eta}, \\
L_{23}^{\text{surf}} &= -\frac{2De}{k_B T} z_\sigma \left(\frac{\sigma}{R} - z_\sigma \beta \frac{2\rho_s\lambda_D}{R} P_2\right) - \frac{z_\sigma e}{2\pi\lambda_B\lambda_D\eta R} \left(\frac{1}{4\pi\lambda_B} P_5 + b\sigma P_2\right), \\
L_{33}^{\text{surf}} &= \frac{2D}{k_B T} \left(\frac{2\rho_s\lambda_D}{R} P_2 - z_\sigma \beta \frac{\sigma}{R}\right) + \frac{\rho_s\lambda_D}{\pi\lambda_B\eta R} \left(2P_2 - 4P_3 + \frac{b}{\lambda_D} P_2^2\right).
\end{aligned} \tag{5.21}$$

Note that  $L_{12}$  and  $L_{23}^{\text{surf}}$  change sign if  $z_\sigma$  changes sign, while the other components do not. This is directly reflected in Fig. 5.1, which shows that  $Q$  and  $J$  are always in the same direction while the direction of  $I$  with respect to  $Q$  and  $J$  depends on the sign of  $z_\sigma$ .

Most elements are known by specific names, for example in the context of electro-osmosis [41] and diffusio-phoresis [138];  $L_{11}$  is inversely proportional to the fluidic impedance  $Z_{\text{ch}} = \frac{\ell}{\pi R^2 L_{11}}$ ,  $L_{12}$  is proportional the streaming conductance  $S_{\text{str}} = \frac{\pi R^2}{\ell} L_{12}$ ,  $L_{13}$  is proportional to the diffusio-osmotic mobility  $D_{\text{DO}} = k_B T L_{13}$ ,  $L_{22}$  is the electric conductivity of the channel and  $L_{23}$  the diffusio-osmotic conductivity. Since we use the full nonlinear Poisson-Boltzmann equation for non- or weakly-overlapping EDLs to determine  $\mathbf{L}$ , we expect Eq. (5.21) to break down for salinities exceeding approximately 100 mM, when finite-size effect become significant, or for multivalent ions. Moreover, for strongly overlapping EDLs, both the solution to the Poisson-Boltzmann equation, and consequently the Onsager matrix Eq. (5.21), as well as the entrance effects, Eq. (5.16), must be adjusted, for example using the thin-pore limit [139].

Even though the formalism presented in this article still applies for strongly overlapping EDLs, the expressions for the Onsager matrix are modified in this regime and as a consequence a full analysis strongly overlapping EDLs is outside the scope of this article. We note, however, that Eq. (5.21) shows excellent agreement for  $R \approx 3\lambda_D$  (see Appendix B.6), but breaks down for  $R \approx 2\lambda_D$  with  $\lambda_D$  the Debye length associated to  $\rho_{\text{min}}$ .

## 5.5. Validating the formalism

Now that we have set up a formalism to extend the microscopic theory, represented by  $\mathbf{L}$ , to the global electrokinetic properties, represented by  $\mathbf{G}$ , we can compare the predictions of Eq. (5.9) and Eq. (5.12) with the FEM solutions of the Nernst-Planck equations (5.17)-(5.19) calculated using COMSOL Multiphysics, in order to validate the applicability of  $\mathbf{G}$  via Eq. (5.9) and Eq. (5.12). Here we will only focus on the diffusio-osmosis, as this inevitably includes significant lateral heterogeneities, for both a short-circuit and an open-circuit system as discussed above (Eq. (5.2) and Eq. (5.3)).

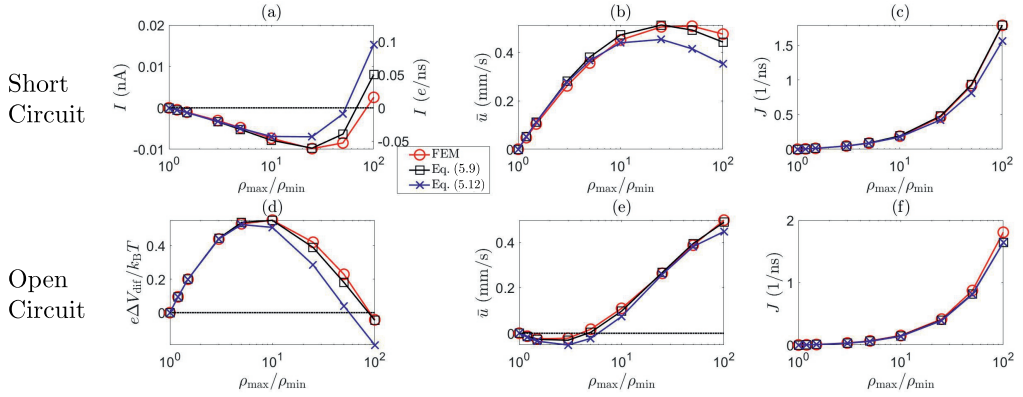


**Figure 5.5.:** The short-circuit electric current  $I$ , open-circuit potential  $\Delta V_{\text{dif}}$ , average fluid velocity  $\bar{u} = \frac{Q}{\pi R^2}$  and salt flux  $J$  as a function of  $\rho_{\text{max}}/\rho_{\text{min}}$ . The red line represents the FEM results, the blue line the prediction of Eq. (5.12) and the black line Eq. (5.9) for  $z_{\sigma}\sigma(\rho_s = 1\text{mM}) = -0.05 e/\text{nm}^2$  (Eq. (5.13)),  $R = 60 \text{ nm}$ ,  $b = 0$ ,  $\beta = -0.21$  (NaCl) and  $\rho_{\text{min}} = 1 \text{ mM}$  for short-circuited (a)-(c) and open-circuit (d)-(f) system.

Fig. 5.5 shows the dependence of the average fluid velocity  $\bar{u} = Q/(\pi R^2)$ , electric current  $I$  and salt flux  $J$  on  $\rho_{\text{max}}/\rho_{\text{min}} \in [1, 100]$ , with  $\rho_{\text{min}} = 1 \text{ mM}$ , for NaCl from the FEM calculations compared to the predictions of Eq. (5.12) (blue) and Eq. (5.9) (black), both for a short-circuit (a)-(c) and an open-circuit (d)-(f) system, for a charge regulation boundary condition with  $z_{\sigma}\sigma(\rho_s = 1\text{mM}) = -0.05 e/\text{nm}^2$  (Eq. (5.13) with  $\text{pH}-\text{pK} = 0.05$ ),  $b = 0 \text{ nm}$ ,  $R = 60 \text{ nm}$ ,  $\ell = 1.5 \mu\text{m}$ ,  $\rho_{\text{min}} = 1 \text{ mM}$ ,  $D_{\text{Na}} = 1.33 \times 10^{-9} \text{ m}^2/\text{s}$  and  $D_{\text{Cl}} = 2.03 \times 10^{-9} \text{ m}^2/\text{s}$  ( $\beta = -0.21$ ). Fig. 5.5 shows that Eq. (5.9) is very accurate in reproducing the FEM results. In all cases, Eq. (5.12) is less accurate than Eq. (5.9) but often surprisingly accurate given its simplifications, especially if  $\rho_{\text{max}}/\rho_{\text{min}} \lesssim 10$  in both short-circuit and open-circuit conditions. The agreement in the open-circuit case thus shows that, even if there are multiple driving forces (i.e. both  $\Delta V \neq 0$  and  $\Delta\mu \neq 0$ ) the formalism remains accurate. We have furthermore

compared the predictions and the FEM calculations for a non-zero slip length ( $b = 10$  nm), smaller radius ( $R = 40$  nm), higher surface charge ( $z_\sigma\sigma = -0.1$  e/nm<sup>2</sup>), smaller channel length ( $\ell = 375$  nm) and higher minimum salinity ( $\rho_{\min} = 20$  mM) and found good agreement for all parameter variations (see Appendix B.6 and article associated to this chapter). In addition, Fig. 5.5(d) shows that in an open-circuit system  $\Delta V_{\text{dif}}$  changes sign for large  $\Delta\mu$  since  $I_{\text{DO}}$  changes sign in the short-circuit case ( $I_{\text{DO}}$  changes sign due to the competition between  $L_{23}^{\text{surf}}$  and  $L_{23}^{\text{vol}}$ ). Moreover, Fig. 5.5(e) shows that the fluid flow first decreases, then increases and even changes sign with increasing  $\rho_{\max}/\rho_{\min}$ . This is the result of an intricate balance between diffusio-osmosis due to  $\Delta\mu$  and electro-osmosis due to  $\Delta V_{\text{dif}}$ . The balance between the diffusio-osmotic and electro-osmotic driving forces depends strongly on  $\beta$ , and is thus very different for KCl ( $\beta = 0$ ) than for NaCl ( $\beta = -0.21$ ), and additionally depends on the sign of  $z_\sigma$ . Both of these behaviours are in agreement with experimental observations and interpretations [114, 140].

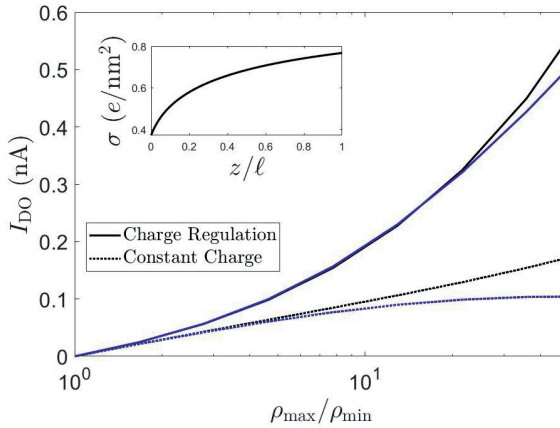


**Figure 5.6.:** The diffusio-osmotic current  $I_{\text{DO}}$  for KCl as a function of the salinity drop over the channel according to Eq. (5.12) (blue) and Eq. (5.9) (black) for both a constant charge (CC, dashed) and charge regulation (CR, full) boundary condition. For both CC and CR,  $z_\sigma\sigma(\rho_s = 1\text{mM}) = -0.25$  e/nm<sup>2</sup>,  $\rho_{\min} = 1$  mM,  $R = 40$  nm,  $b = 3$  nm and  $\ell = 1250$  nm. The inset shows the surface charge as a function of the lateral position  $z$ .

Recent experimental advances allow for direct comparison between theory and experiments for these kind of systems. For instance, measurements on osmotic power generation using a single boron nitride nanotubes (BNNT), carbon nanotubes (CNT) and MoS<sub>2</sub> nanopores, have been shown to surpass older Reverse Electrodialysis technologies based on much thicker membranes [141]. With the theory presented here, we can directly compare with recent experiments. Fig. 5.6 shows the (short-circuit) diffusio-

osmotic current  $I_{\text{DO}}$ , for both a constant charge and a charge regulating boundary condition Eq. (5.13), as a function of the salinity ratio  $\rho_{\text{max}}/\rho_{\text{min}}$  for a nanochannel with  $\rho_{\text{min}} = 1 \text{ mM}$ ,  $z_{\sigma}\sigma(\rho_s = 1\text{mM}) = -0.25 \text{ e/nm}^2$ ,  $R = 40 \text{ nm}$ ,  $b = 3 \text{ nm}$  and  $\ell = 1250 \text{ nm}$ , which can be directly compared to the diffusio-osmotic current measurements on BNNT by Siria et al. [127]. Here,  $\sigma(\rho_s = 1\text{mM})$  was chosen such that similar  $I_{\text{DO}}$  values were obtained. First of all, it is evident from Fig. 5.6 that, especially for large  $\rho_{\text{max}}/\rho_{\text{min}}$ , the charge regulation boundary condition has a significant effect on the predicted electric current. A charge regulation boundary condition (Eq. (5.13)) and the small slip length  $b = 3 \text{ nm}$  of BNNTs [142] are sufficient to obtain very similar values for  $I_{\text{DO}}$  (order 0.1 to 1 nA), but with a surface charge more than an order of magnitude smaller than estimated by Siria et al. [127]. Note that the contribution from the slip length, which, for large  $\sigma$ , scales with  $\sigma^2$  (see Eq. (5.21) and associated text), becomes increasingly dominant for increasing  $\sigma$  (but was taken  $b = 0$  in Ref. [127]). Even a relatively small slip length of  $b = 3 \text{ nm}$  can therefore significantly affect the predicted fluxes. Note furthermore that  $\sigma$  varies significantly as a function of the channel position  $z$ , see inset Fig. 5.6, which explains why the charge regulation boundary condition gives a larger  $I_{\text{DO}}$  compared to the constant charge boundary condition, and furthermore emphasises the importance of even a small but finite  $b$ .

The surface charge  $z_{\sigma}\sigma(\rho_s = 1 \text{ mM}) = -0.25 \text{ e/nm}^2$  is much smaller than the value obtained from conductivity measurements on BNNT by Ref. [127]. It has recently been shown, however, that the adsorbed  $\text{OH}^-$  contributes significantly to the conductivity and other properties of the channel [143]. Conduction via the Stern layer is not included in the current model, but an increased conduction will probably only lower the predicted surface charge even more. We have recently developed models for mobile surface charges [144, 145], and incorporating these in the current theory is subject of future research.

## 5.6. Reverse electro dialysis

Having established the accuracy of the theoretical framework of deriving  $\mathbf{G}$  from  $\mathbf{L}$ , we can use the derived equations to analyse the wide variety of different electrokinetic systems (Table 5.1) without the need for full FEM calculations (or other extensive numerical analyses) for each system separately. All electrokinetic systems are essentially described by  $\mathbf{G}$ , the only difference being the boundary conditions. As an example, we will use the conductivity matrix  $\mathbf{G}$  to analyse a single channel using Reverse Electrodialysis (RED), which are essentially intermediate between a short-circuit and open-circuit system.

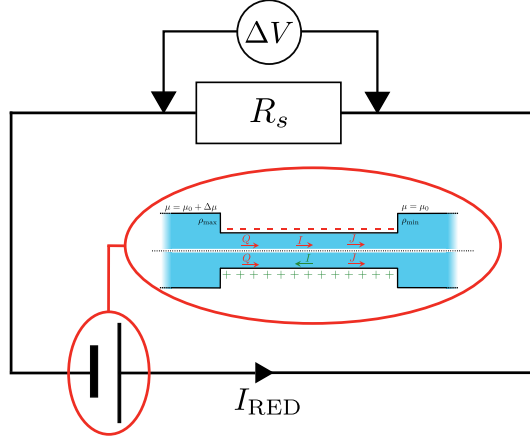


**Figure 5.7.:** Schematic representation of an RED circuit, where a diffusive-osmotic system is embedded in an electric circuit with a resistance  $R_s$ .

The electrokinetic RED system, schematically represented in Fig. 5.7, is embedded in an electric circuit and thus allows a non-zero current  $I = I_{\text{RED}}$  to flow through the system. However, the circuit also contains an (Ohmic) resistance  $R_s$  that harvests the electric energy, which requires a potential drop  $\Delta V$  in order for a non-zero current to flow. Assuming that  $R_s$  can be chosen freely, we will assume that  $R_s$  is chosen such that the generated electric power is optimised (as opposed to the energy conversion efficiency). It is straightforward to show that the generated power is maximised when  $R_s$  equals the resistance of the channel  $R_{ch} = \frac{\ell}{\pi R^2 G_{22}}$  [114, 121], which fixes the current to half the short-circuit current Eq. (5.2),

$$I_{\text{RED}} = \frac{1}{2} I_{\text{DO}} = \frac{1}{2} \frac{\pi R^2}{\ell} G_{23} \Delta \mu_{\text{ch}}, \quad (5.22)$$

with  $I_{\text{DO}}$  the short-circuit current, Eq. (5.2). Note that the resulting potential over the channel  $\Delta V = I R_s$  is half the open-circuit (diffusion) potential  $\Delta V_{\text{dif}}$ , Eq. (5.3), and that we must use  $\Delta \mu_{\text{ch}}$ , the chemical potential drop over the channel, instead of  $\Delta \mu$  to determine  $I_{\text{DO}}$ . This allows us to write the maximum generated areal power density  $\mathcal{P}_{\text{RED}}$  as

$$\mathcal{P}_{\text{RED}} = \frac{P_{\text{RED}}}{\pi R^2} = \frac{I_{\text{DO}}^2 R_{ch}}{4\pi R^2} = \frac{1}{4} \frac{(\Delta \mu_{\text{ch}})^2}{\ell} \frac{G_{23}^2}{G_{22}}, \quad (5.23)$$

where  $\mathcal{P}_{\text{RED}}$  is the generated electric power. Eq. (5.23) shows that the power density is inversely proportional to the length  $\ell$ , which (partially) explains the potential of

nanopores [128] compared to nanochannels, let alone microchannels. A smaller length decreases  $R_{ch}$  (and  $R_s$  is decreased accordingly) but increases the salinity gradient and thus  $I_{DO}$ . The energy conversion efficiency can be found by dividing the generated electrical power by the osmotic free energy dissipated by the mixing of the two solutions [52, 53],

$$\alpha_{\text{RED}} = \frac{\mathcal{P}_{\text{RED}}}{J_{\text{exc}}\Delta\mu} = \frac{\mathcal{P}_{\text{RED}}}{J\Delta\mu - 2\Delta\rho Q}, \quad (5.24)$$

see Appendix B.2 for a derivation why  $\alpha_{\text{RED}}$  is defined with  $J_{\text{exc}}$  and  $\Delta\mu$  instead of  $J$  and/or  $\Delta\mu_{ch}$ . Whether it is “better” to maximise the power or the efficiency depends on the goal and the available resources. In the case of diffusio-osmosis both fresh and salt water are available in abundance where rivers flow into the sea, so it makes sense to optimise for the generated power. A similar analysis can be performed for mechanical energy conversion, where a pressure drop  $\Delta p$  is used to generate an electric current (via  $G_{12}$ ), but osmotic energy converters have been shown to be able to produce more energy at a higher conversion efficiency [118, 119].

On the basis of Eq. (5.23) and Eq. (5.24), we are in the position to use the conductivity matrix  $\mathbf{G}$  to investigate the effect of system parameters on the RED performance without the need to run intensive FEM or other numerical calculations for each parameter set. As mentioned, two materials have shown great potential for osmotic energy conversion: CNTs and BNNTs. The reason for the success of the former is believed to be related to the small friction of water with the surface, i.e. a large slip length  $b$ , [49, 142, 146, 147], while for the latter the large surface charge is believed to be main cause [127], in addition to the large conductivities shown by both [127, 132, 143, 147]. For both materials, we assume a charge regulating boundary condition as in Eq. (5.13). There are many parameters to investigate, but here we will focus on 4 main aspects: the surface charge density  $\sigma$ , the slip length  $b$ , the minimum salt concentration  $\rho_{\min}$  and the mobility mismatch  $\beta$ .

As an example we will investigate a nanochannel with  $R = 40$  nm, although it should be kept in mind that for RED a smaller  $R$  generally results in a higher  $P_{\text{RED}}$  and  $\alpha_{\text{RED}}$ . However, the slip length of CNTs is known to vary with  $R$  [49], so a constant  $R$  allows us to assume a constant  $b$  for this analysis. We will use  $b_{\text{BNNT}} = 3$  nm as the slip length for BNNTs [142] and  $b_{\text{CNT}} = 30$  nm for the slip length of CNTs [49, 142].

Fig. 5.8 and Fig. 5.9 show the RED power and efficiency for  $\rho_{\min} = 1$  mM and  $\rho_{\min} = 20$  mM, respectively, for both KCl (a) & (c) ( $\beta = 0$ ) and NaCl (b) & (d) ( $\beta = -0.21$ ), for  $b = 0$  (black dotted),  $b = 3$  nm (red dot-dashed) and  $b = 30$  nm (blue full) as a function of  $z_\sigma\sigma$ . The horizontal axis represents the surface charge  $z_\sigma\sigma$  at  $\rho_s = 1$  mM. The surface charge of both BNNT and CNT surfaces originate from an  $\text{OH}^-$

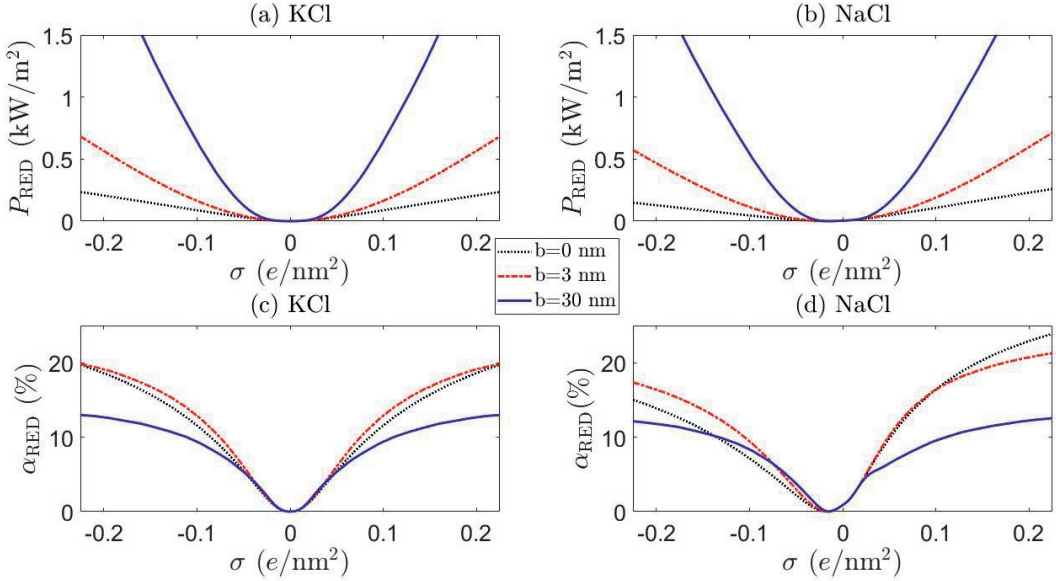


**Figure 5.8.:** The RED generated power  $P_{\text{RED}}$  (a) & (b) and efficiency  $\alpha$  (c) & (d) for KCl (a) & (c) ( $\beta = 0$ ) and NaCl (b) & (d) ( $\beta = -0.21$ ) as a function of the surface charge at  $\rho_s = 1$  mM, for channel lengths  $\ell = 1.5 \mu\text{m}$ ,  $\rho_{\text{max}} = 25$  mM,  $\rho_{\text{min}} = 1$  mM (so  $\Delta\mu = k_B T \log 25$ ) and radius  $R = 40$  nm ( $R \approx 4\lambda_{D,\text{min}}$ ). The dotted black line represent  $b = 0$ , the red dashed line represents  $b = 3$  nm (BNNT) and the full blue line represents  $b = 30$  nm (CNT).

adsorption reaction [127, 132, 143] and strictly only takes negative values. Positive values are included ( $\text{H}^+$  adsorption), however, for a more complete analysis. There are a few observation we can make from these figures.

First of all, a comparison of the black ( $b = 0$ ), red (BNNT,  $b = 3$  nm) and blue (CNT,  $b = 30$  nm) shows that not only a large but also a moderate slip length  $b$  has a significant effect on the electrokinetic properties of the system, as was also noted for mechanical energy conversion [148]. This confirms that the large slip length of CNTs makes these nanochannels so promising. In addition, Fig. 5.8 confirms the point emphasised above, that even a small  $b$  can have significant effects on the current through the channel, especially for large  $\sigma$ .

Secondly, we see that the predicted power can significantly differ between KCl and NaCl, especially for large  $\rho_{\text{min}}$ , shown in Fig. 5.9. Many experiments are performed with KCl, but it is not a priori clear whether these results can be extrapolated to NaCl (the main species of salt for large-scale applications of RED). The difference between these two salts originates from the mobility mismatch,  $\beta_{\text{KCl}} \approx 0$  and  $\beta_{\text{NaCl}} \approx -0.21$ , which not only affects the resulting fluxes but also breaks the charge inversion symmetry (see

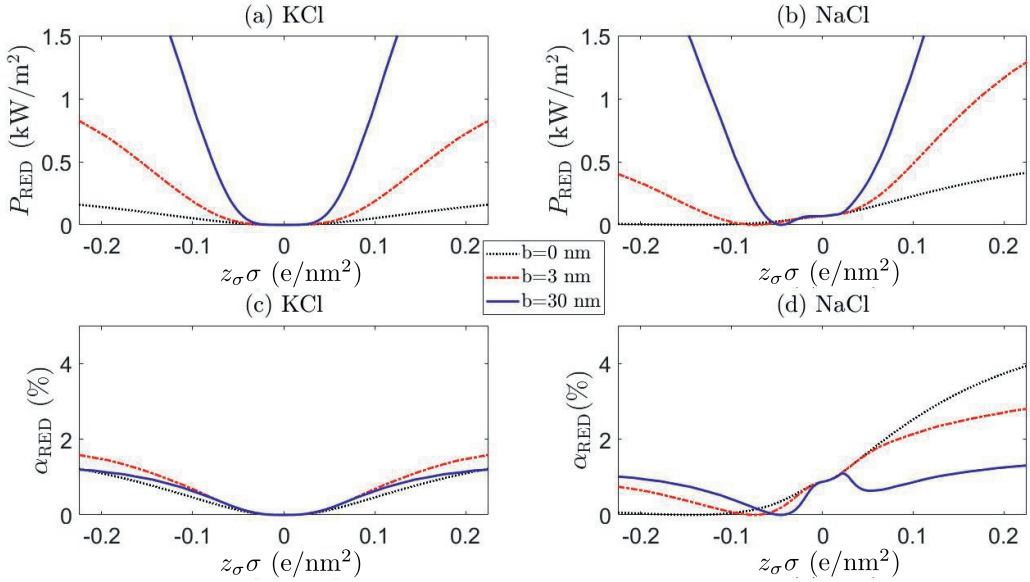


**Figure 5.9.:** As in caption Fig. 5.8, but with  $\rho_{\text{max}} = 500$  mM and  $\rho_{\text{min}} = 20$  mM.

Eq. (5.21), where the only terms that include  $\beta$  are proportional to  $z_{\sigma}$ ). If NaCl is the main constituent of the electrolyte, a positively charged surface is more effective than a negatively charged surface: a negatively charged surface will attract the cations to the surface, but  $\text{Na}^+$  has a lower mobility than  $\text{Cl}^-$ . The EDL thus has a lower overall mobility if  $z_{\sigma} < 0$  than if  $z_{\sigma} > 0$ . This provides a general rule that RED systems generate more power at a higher efficiency if  $z_{\sigma}\beta < 0$ , because then the ion with the highest mobility is the most abundant in the EDL.

A comparison of Fig. 5.8 and Fig. 5.9 furthermore emphasises the point that the generated power and efficiency do not purely depend on the concentration ratio (i.e.  $\Delta\mu$ ), but are both a function of the separate salinities  $\rho_{\text{min}}$  and  $\rho_{\text{max}}$  [121]. This is especially true for NaCl, for which the broken inversion symmetry is significantly more apparent for  $\rho_{\text{min}} = 20$  mM (Fig. 5.9) than for  $\rho_{\text{min}} = 1$  mM (Fig. 5.8). Especially if  $b = 0$ , the difference between the two cases is very pronounced (compare black dotted line Fig. 5.8(b) & (d) and Fig. 5.9(b) & (d)). The dependence on  $\rho_{\text{min}}$  can be understood by the fact that  $L_{23}^{\text{vol}}$ , and consequently  $G_{23}$  and  $I_{\text{DO}}$ , increase with  $\beta\rho_s$  (see Eq. (5.21)). All slip-length contributions are, however, independent of  $\rho_s$ , and all scale as  $b\sigma^2$  for large  $\sigma$  (see Eq. (5.21)).

We also find that the generated power for  $\rho_{\text{min}} = 20$  mM and  $\rho_{\text{max}} = 500$  mM is higher than for  $\rho_{\text{min}} = 1$  mM and  $\rho_{\text{max}} = 25$  mM if  $b = 0$ , especially for NaCl with  $z_{\sigma} > 0$ . However, the efficiency  $\alpha_{\text{RED}}$  is nearly an order of magnitude higher

for  $\rho_{\min} = 1$  mM than for  $\rho_{\min} = 20$  mM, even though the chemical potential drop  $\Delta\mu$  is the same in both cases. Both can be understood by the increased role played by the volume contributions  $\mathbf{L}^{\text{vol}}$  of Eq. (5.21). These contributions scale with  $\rho_s$ , so an increased  $\rho_{\min}$  naturally leads to a larger  $I_{\text{DO}}$  (if  $\beta \neq 0$  via  $L_{23}^{\text{vol}}$ ) and thus a larger  $P_{\text{RED}}$ . Similarly, the total salt flux  $J$  increases with  $\rho_{\min}$  ( $L_{33}^{\text{vol}} \propto \rho_s$ ) which, in turn, decreases  $\alpha_{\text{RED}}$  (see Eq. (5.24)).

Finally, note that  $P_{\text{RED}}$  and  $\alpha_{\text{RED}}$  develop a minimum, with a minimum value of zero, for NaCl with a small negative surface charge. This minimum shifts to larger values of  $\sigma$  if  $\rho_{\min}$  increases, since this minimum is given by the value of  $\sigma$  for which the volume and surface contributions to  $I$  cancel. If we take the surface charge of CNTs at  $\rho_s = 1$  mM to be  $z_\sigma\sigma = -(0.03 - 0.1) e/\text{nm}^2$  [49, 147], we even find that CNT are typically not far removed from the minimum observed in Fig. 5.9. We should note, however, that the location of this minimum depends on systems parameters such as  $R$  and  $b$ , so this does not mean that CNTs should not be used for RED. It does, on the other hand, stress the important point that  $\beta$ ,  $\sigma$ ,  $z_\sigma$  and  $\rho_{\min}$  are important parameters to keep in mind when optimising a given channel.

Note that our values for  $P_{\text{RED}}$  are of the same order of magnitude as measurements on BNNTs [127]. These values are also consistent with measurements on nanopores [128], where they found  $P_{\text{RED}}$  three orders of magnitude higher than for micron-thick membranes, with  $\ell$  three orders of magnitude lower. The predictions do certainly depend on the radius  $R$ , as RED typically generates more power per unit area and is more efficient for smaller  $R$  [121]. The present analysis, however, emphasis the point that different systems with differing  $R$ ,  $\rho_{\min}$ ,  $\sigma$ ,  $z_\sigma$ ,  $b$  and  $\beta$ , are optimised differently. There is of course an immense variety when it comes to nanochannels, but the framework presented in the chapter provides an accessible method with which these channels can be analysed. Moreover, the framework can be further improved, for example for smaller  $R$ , because the most restricting assumption of the Onsager matrix presented in this chapter, Eq. (5.21), is the assumption of non/weakly-overlapping EDLs, meaning that Eq. (5.21) is viable for  $R \gtrsim 12$  nm for  $\rho_{\min} > 10$  mM. There is no general analytic theory for the matrix elements of  $\mathbf{L}$  for arbitrary  $\lambda_D/R$ , but it is possible to take the thin-pore limit ( $\lambda_D \ll R$ ) of the Poisson-Boltzmann formalism to obtain analytical solutions [139]. In addition, the Poisson-Boltzmann formalism typically breaks down for  $\rho_s > 100$  mM, but there are theories to improve on Poisson-Boltzmann [149, 150]. Lastly, as already stated, it has been shown that surface conduction plays an important role for BNNTs and CNTs [143], which can further affect the (quantitative) predictions of the theory. This will be the subject of future research.

## 5.7. Summary & conclusion

In conclusion, we have presented a method to fully analyse the transport properties of electrokinetic channels driven by a pressure gradient, an electric field or a salinity gradient. We have calculated the full  $3 \times 3$  Onsager matrix  $\mathbf{L}$  which gives the volumetric flow rate, electric current and salt flux for a given (set of) driving force(s), which to the best of our knowledge was absent in the current literature. This includes an important contribution to the diffusio-osmotic electric current that has so far been overlooked. We then presented two methods to extend the local linear-response Onsager matrix  $\mathbf{L}$  to a global linear-response conductivity matrix  $\mathbf{G}$ , which can incorporate lateral heterogeneities. This furthermore allowed us to include more complex boundary conditions such as charge regulation boundary condition. We compared the predictions of the theory with numerically exact (Finite Element Method) solutions of the Poisson-Nernst-Planck-Stokes equations, which showed the remarkable accuracy of the theory under varying parameters and boundary conditions, in fact even to pore radii as small as three times the electric double layer thickness. Charge regulation was shown to have a significant effect on the predicted fluxes, and thus on the interpretation of recent experiment on nanochannels.

Having established the accuracy of the conductivity matrix  $\mathbf{G}$ , we used it to analyse Reverse Electrodialysis without the need to use extensive numerical calculations such as FEM. We compared typical values for Carbon Nanotubes and Boron Nitride Nanotubes, and showed, for example, that such systems behave differently when KCl is used compared to NaCl. Most notably, in the case of NaCl we showed that negatively charged surfaces such as CNTs and BNNTs are significantly less effective than positively charged surfaces, especially if salinities like those of fresh and sea water are used. We furthermore emphasised that the produced power does not solely depend on the chemical potential drop across the channel, but on the reservoir salinities separately. We thus found that systems with different surface charge, different type of salt and salinities are optimised differently. Electrokinetic systems present a very large parameter space, too large to fully explore here, but for this reason electrokinetic systems represent a great variability and applicability. The framework presented in this chapter provides an insightful and convenient method to analyse them.



## Chapter 6.

# Diffusio-osmotic entrance effects and interaction between channels

*In this chapter we further focus on diffusio-osmosis through an electrokinetic channel. As opposed to the previous chapter, however, we investigate the influence of the exterior of the channel on the transport properties. First, we identify the effects of the walls directly outside the channel, but then we consider the problem of upscaling. So far we have only discussed a single channel, but here we investigate a channel embedded in an array of channels, mimicking a membrane. We find that the behaviour of a membrane differs significantly from the behaviour of a single channel, since neighbouring channels can greatly diminish the transport through the channels. We then investigate the optimal membrane design, by varying the radius, length and channel-to-channel distance that maximises the electric current per unit membrane area.*

- *Section 6.2*  
*Discussion of diffusio-osmotic entrance effects and how the exterior surface charge influences the transport properties of a channel*
- *Section 6.3.2*  
*Explanation of the diffusio-osmotic interaction between two neighbouring channels*
- *Section 6.3.3*  
*Identification of an optimal distance between neighbouring channels that maximises the electric current per unit membrane area*
- *Section 6.3.3*  
*Presentation that membranes with needle-shaped channels produce higher fluxes than pore-shaped channels*

## 6.1. Introduction

In the previous chapter we have discussed how to incorporate lateral heterogeneities in a linear-response framework in order to determine the fluxes through a single nanochannel as a function of the applied driving forces. We focused mainly on diffusio-osmosis, where a salinity gradient is imposed on an electrokinetic channel. In Chapter 5 we analysed the transport behaviour of a single nanochannel, but in this chapter we shift the focus to the exterior of the channel and how this affects the fluxes through the channel. First, we will look in more depth at the diffusio-osmotic entrance effects already shortly mentioned in the previous chapter, where we found that the salinity profile persists outside the channel. Afterwards, we analyse the problem of upscaling, and investigate to what extent the results for a single channel can be extrapolated to an array of channels, i.e. to a membrane.

As in Chapter 5, we determine the salinity and fluid flow profiles by solving the Poisson-Nernst-Planck equations using the Finite Element Method (FEM) as employed by COMSOL Multiphysics. The fluid flow is determined by Stokes equation with an electric body force, the incompressibility condition and a no-slip boundary condition [41],

$$-\nabla p + \eta \nabla^2 \mathbf{u} + e(\rho_+ - \rho_-)\mathbf{E} = 0, \quad \nabla \cdot \mathbf{u} = 0, \quad u_z(r = R) = 0, \quad (6.1)$$

with the channel axis oriented in the  $z$  direction. Here  $p$  is the hydrostatic pressure (i.e. sum of the partial solvent pressure and osmotic pressure due to the ions),  $\mathbf{u}$  the fluid velocity vector,  $\eta$  the viscosity,  $R$  the radius of the channel,  $\mathbf{E}$  the electric field,  $e$  the proton charge,  $\rho_{\pm}$  the local cation/anion number density, and  $r \in [0, R]$  the coordinate normal to the surface. The ion fluxes  $\mathbf{j}_i$  are given by the Nernst-Planck equation [41],

$$\mathbf{j}_i = -D_i \nabla \rho_i + z_i \frac{D_i e}{k_B T} \rho_i \mathbf{E} + \rho_i \mathbf{u}, \quad (6.2)$$

with  $k_B$  the Boltzmann constant,  $T$  the temperature and  $\rho_i$ ,  $D_i$ ,  $z_i$  the density, the diffusion constant and the valency of ion species  $i = \pm$  respectively. For simplicity, we consider in this chapter KCl in water at room temperature, a 1:1 electrolyte with  $D_+ \approx D_- \approx 2 \times 10^{-9} \text{ m}^2/\text{s}$ . We can obtain the volumetric flow rate  $Q$ , electric current  $I$  and salt flux  $J$  as

$$\begin{aligned} Q &= 2\pi \int dr r u_z = \pi R^2 \bar{u}, & I &= 2\pi e \int dr r (j_{+,z} - j_{-,z}), \\ J &= 2\pi \int dr r (j_{+,z} + j_{-,z}), \end{aligned} \quad (6.3)$$

with  $\bar{u}$  the average fluid velocity. For a more detailed discussion of Eqs. (6.1) & (6.2), we refer the reader to Section 2.2.2 & 2.2.1.

## 6.2. Charge of the exterior

In the previous chapter we argued that entrance effects cannot be ignored in a consistent formalism for diffusio-osmosis. We argued, and confirmed with numerical calculations, that the salinities at the inlet and the outlet of the channel do not equal the reservoir salinities, but depend on the radius  $R$  and length  $\ell$  of the channel (see Fig. 5.4). This entrance effect originates from the change in geometry. In the channel, the salinity gradient is constant due to the quasi-1D nature of the cylindrical geometry, but far from the channel, in the reservoir, the salinity is constant. The concentration gradient must therefore transition from 0 (in the far field) to a constant value via a radial salinity profile at the in- and outlet. In this chapter, we will show that this salinity profile causes the exterior of the channel to play a very significant role in determining the transport properties of a diffusio-osmotic channel.

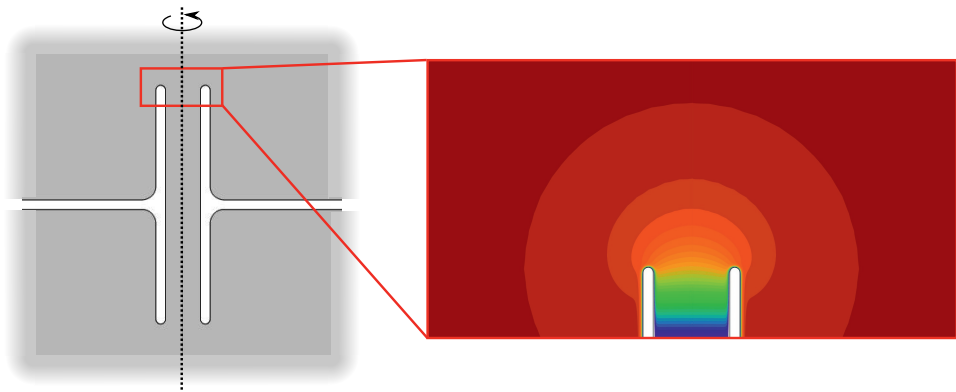


**Figure 6.1.:** A typical geometry of the channel as used for the FEM calculations, with  $R = 60$  nm and  $\ell = 750$  nm. The contour lines of the zoom show the lines of equal salinity, which clearly persist over the exterior of the channel.

Fig. 6.1 shows the salinity profile at the channel outlet, determined by Eq. (6.2). There is a clear transition from a linear to a radial salinity profile, which results in a salinity gradient over the walls outside the channel. This gradient will, of course, induce a diffusio-osmotic driving force itself, and for this reason the exterior of the channel cannot be ignored. It is important to note that this effect does not depend on the specific geometry of the exterior. Fig. 6.1 shows the most extreme case, of a single channel through a very thin membrane, as in that case the external geometry is curved

away maximally (i.e. makes a U-turn of  $180^\circ$ ). The same effect persists for a different exterior geometry, such as where the geometry makes a  $90^\circ$  turn instead of a  $180^\circ$  turn.

It is thus important to include the exterior of the channel in a complete analysis of diffusio-osmosis, although it is not yet clear how significant its role is. In order to investigate this, we compare two cases, one where the exterior of the channel carries the same surface charge as the internal geometry, and one where the exterior of the channel is charge neutral. Fig. 6.2 shows a colourmap of the axial component of the fluid flow  $u_z$  and the (white) fluid stream lines in the two cases, for both (a) & (b) a small salinity drop,  $\rho_{\max}/\rho_{\min} = 1.2$ , and (c) & (d) a large salinity drop,  $\rho_{\max}/\rho_{\min} = 25$ . Fig. 6.2 highlights a stark contrast between the cases with and without a charged exterior.

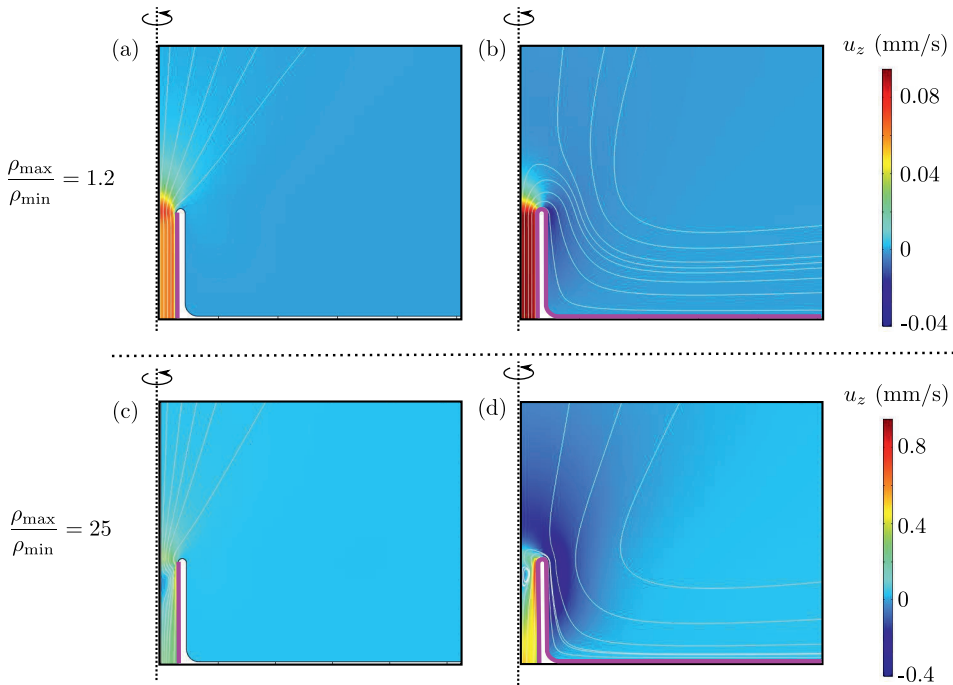


**Figure 6.2.:** Fluid flow streamlines for a diffusio-osmotic flow where the exterior of the channel is (a) & (c) charged and (b) & (d) uncharged, with  $\rho_{\min} = 1$  mM and (a) & (b)  $\rho_{\max} = 1.2$  mM and (c) & (d)  $\rho_{\max} = 25$  mM. The magenta lines denote the charged surfaces.

If the exterior of the channel is uncharged, the stream lines gradually diverge when they exit the channel. These ‘jet-like’ stream lines are what one would expect a priori, which makes it rather surprising that this is *not* observed in the case where the exterior of the channel is charged. In that case, the stream lines behave drastically different,

and follow the solid surface and remain roughly parallel to it. Moreover, the fluid flow slightly above the outlet of the channel is even directed *downwards*, towards the outlet, until they get close to the outlet and curve along the charged wall. Since there is a salinity gradient over the charged exterior surfaces, the diffusio-osmotic driving forces are present at the exterior walls. Since these driving forces are only located inside the EDL, they curve along with the solid surface, creating a ‘pull’ on the fluid parallel to the charged surface, which the streamlines follow. This effect is clearly present even for small salinity drop ( $\rho_{\max}/\rho_{\min} = 1.2$ ), and is therefore not a non-linear effect but intrinsic to diffusio-osmosis.

The above described effect is further enhanced for a larger salinity drop ( $\rho_{\max}/\rho_{\min} = 25$ ). However, Fig. 6.2 (c) & (d) also show non-linear diffusio-osmotic effects. For example, the flow profile inside the channel is no longer a plug flow for high salinity drops, as it is for  $\rho_{\max}/\rho_{\min} = 1.2$  (Fig. 6.2 (a) & (b)), but clearly changes with the axial coordinate  $z$ . Since the salinity changes drastically along the channel, so does the diffusio-osmotic driving force, and therefore it is not surprising that for increasing salinity drops  $u_z$  depends more significantly on  $z$ . A large enough salinity drop can even result in  $u_z$  (locally) changing sign, explaining the small vortex that develops at the outlet shown in Fig. 6.2(c) & (d), while concentrating the streamlines close to the surface such that the volumetric flow rate  $Q$  remains constant with respect to  $z$ .

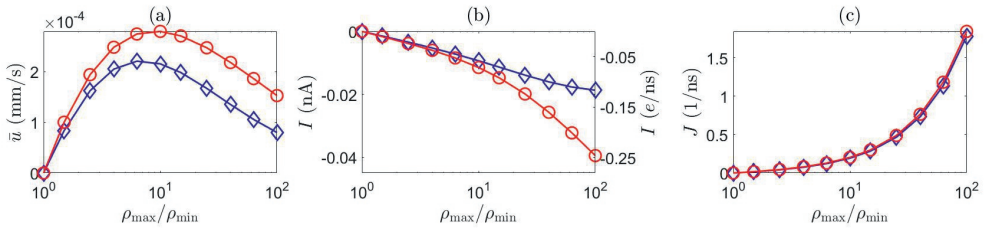


**Figure 6.3.:** (a) Average fluid velocity  $\bar{u}$  (b) electric current  $I$  and (c) salt flux  $J$  for the case where the exterior of the channel are charged (red circles) and uncharged (blue diamonds) for  $\rho_{\min} = 1$  mM,  $R = 60$ ,  $\ell = 1500$  nm and  $z_{\sigma}\sigma = -0.05 e/\text{nm}^2$ .

Not only is the fluid flow qualitatively affected by the exterior of the channel, the generated fluxes depend quantitatively on whether the exterior of the channel is charged or not. If the exterior of the channel is charged, the diffusio-osmotic forces provide an additional ‘pull’ on the fluxes, and thus increasing them. This is shown in Fig. 6.3, where we compare the average fluid velocity  $\bar{u} = Q/(\pi R^2)$ , electric current  $I$  and salt flux  $J$  for the case with (red) and without (blue) a charged exterior, for  $\rho_{\max}/\rho_{\min} \in [1, 100]$ . As can be clearly observed, when the exterior of the channel is charged both  $I$  and  $Q$  are significantly increased, especially for  $\rho_{\max} \gtrsim 10\rho_{\min}$ ,

due to the presence or absence of the ‘pull’ of the exterior, while  $J$  is approximately equal for both cases. The exterior of the channel has a negligible effect on  $J$  since the salinity profile is only weakly affected by the surface charge (and thus diffusio-osmosis). Here we should note that the case with an exterior surface charge is well described by the conductivity matrix  $\mathbf{G}$  discussed in Chapter 5, and thus behaves as expected. Moreover, Fig. 6.3 does not depend significantly on the shape of the exterior geometry. For example, the fluxes in the case where the charged surface makes a  $90^\circ$  turn instead of the  $180^\circ$ , as in Fig. 6.2, differ by no more than a few percent.

## 6.3. Interacting channels

### 6.3.1. Cell model

Now we turn to the problem of upscaling: we embed nanochannels in an array to simulate a membrane. This is a straightforward exercise if two neighbouring channels do not interact, but due to the above discussed entrance and outlet effects this is not necessarily the case. Suppose that there is another channel next to the one already considered, oriented parallel to it. If the channels are close enough, the external salinity profiles will overlap, giving rise to an interaction between neighbouring channels. Here we will analyse this interaction. It is, however, numerically too demanding to build a macroscopic array of nanochannels, but it is possible to mimic such an array by adopting a cell model [151–153].

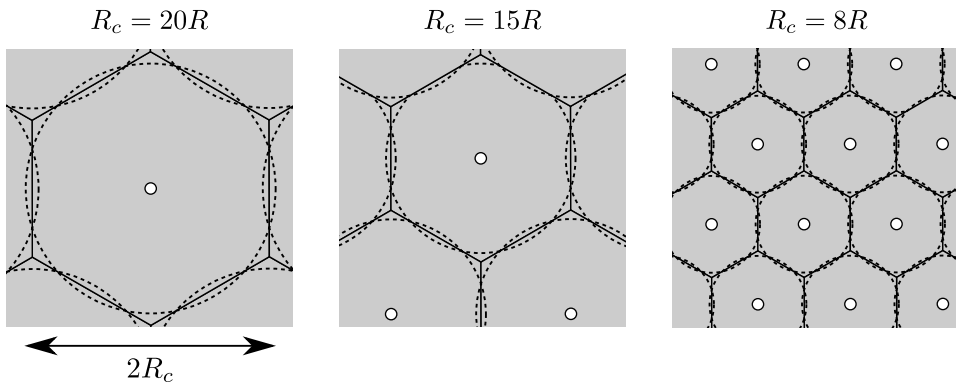


**Figure 6.4.:** Representation of a cell model used to mimic an array of channels, with  $R_c$  the radius of a cell and  $R$  the radius of a channel for (a)  $R_c = 20R$  ( $\Theta = 0.25\%$ ), (b)  $R_c = 15R$  ( $\Theta = 0.44\%$ ) and (c)  $R_c = 8R$  ( $\Theta = 1.56\%$ ). In the cell model, the radial flux at  $r = R_c$  (dashed line) vanishes.

A cell model effectively mimics a membrane with a regular distribution of channels. Consider  $N$  channels distributed regularly over an area  $A$ . Defining the Wigner-Seitz cells as cylindrical, the radius of the cell  $R_c$  is then defined such that the total area is equally distributed as over all  $N$  arrays, such that  $A/N = \pi R_c^2$ . In adopting a cell model, however, the information about the lattice the channels are oriented in is lost. Fig. 6.4 shows the cell model approximation for a triangular lattice. The full lines indicate the Voronoi cell of each channel, a hexagon in the case of a triangular lattice, but in a cell model this is approximated by a cylinder with radius  $R_c$  (dashed lines). The cell radius is approximately equal to the (average) channel-to-channel distance, and we will henceforth refer to  $R_c$  as such. Since the area of the membrane occupied by one channel is thus  $\pi R_c^2$ , we can introduce the areal fraction occupied by the channels  $\Theta = (R/R_c)^2$ , an important membrane parameter. The advantage of the cell model is that any radial flux at  $r = R_c$  (dashed lines in Fig. 6.4) vanishes due to the symmetry of the lattice. The cell model therefore reduces the complicated many-channel problem to an effective single-channel problem.

The most important and significant consequence of the cell model boundary condition is that the salinity profile changes drastically as a function of  $R_c$ . In the case of a single channel, i.e.  $R_c \rightarrow \infty$ , the salinity profile at the outlet of the channel was, as discussed above, determined by an open 3D diffusion equation, resulting in a radial profile as shown in Fig. 6.1. However, due to the vanishing radial fluxes at  $r = R_c$ , the geometry outside the channel is, just like inside the channel, essentially cylindrical (i.e. quasi-1D), although with a larger radius ( $R_c$ ) than the channel. For a single channel the salinity profile reduces asymptotically (proportional to the inverse of the distance to the channel exit) to the bulk value, but a salinity profile in a cylindrical geometry is linear in the axial coordinate. This crossover can be clearly seen in Fig. 6.5, which shows the steady state salinity profiles for  $R_c = 20R$  ( $\Theta = 0.25\%$ ),  $R_c = 15R$  ( $\Theta = 0.44\%$ ) and  $R_c = 8R$  ( $\Theta = 1.56\%$ ). Here we see the equal-density lines transition from radial to horizontal as  $R_c$  decreases.

This transition is important, since such a linear profile (in steady state) outside the channel now extends, contrary to the case of a single channel, over the entire reservoir. In practical applications, however, such steady states are rarely realised. It would take a very long time to reach such a steady state for macroscopic reservoirs, but in practical situations a constant bulk salinity can be enforced by stirring the reservoirs. This is, however, only effective up to a certain distance from the membrane, where frictional forces significantly slow down the fluid flow. This results in a bulk with a constant salinity, but with layer adjacent to the array of channels (i.e. membrane) where the local salinity differs from the reservoir salinity. This region is known as the unstirred layer (USL) or diffusion boundary layer (DBL) [154–157], because the salinity profile is largely unaffected by the external fluid flow due to its close proximity to the wall.

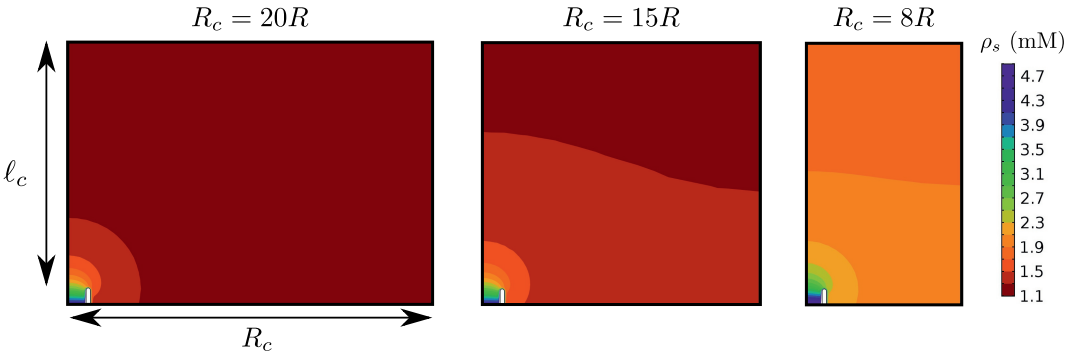


**Figure 6.5.:** Equal density contour lines for  $R_c = 5R$ ,  $R_c = 15R$  and  $R_c = 20R$  for  $\rho_{\min} = 1$  mM and  $\rho_{\max} = 25$  mM. The values of  $\rho_s$  used for the contour lines were cut off, and only a part the entire simulation domain is shown, for visualisation purposes. The contour lines crossover from a radial to linear as  $R_c$  decreases.

This layer is not to be confused with the hydration water layer of the surface, which is, depending on the solid, typically only a few water molecules thick [158, 159].

In this light we can, therefore, interpret the the numerical ‘reservoir’ length  $\ell_c$  as the USL thickness. At the boundary between the USL and the bulk fluid the salinity equals the externally imposed salinity at the edge, while inside the DBL the salinity profile is often approximated as linear [154, 156, 160]. The USL layer thus has the same properties as the region which acted as the ‘reservoir’ in the numerical simulation geometry, shown in Fig. 6.5, and we can safely equate  $\ell_c$  to the USL thickness. The USL thickness depends on, for example, the type of salt [156] and the amount and method of stirring [154], but typically takes values of the order of a few to hundreds of micrometers [156, 160, 161]. Here we will, however, not attempt to derive  $\ell_c$ , but consider the impact the size of the unstirred-layer thickness has on the transport properties of a single channel in the membrane, since it is known that decreasing the USL thickness improves the fluxes through (i.e. permeability of) the membrane [154, 157, 160, 162].

### 6.3.2. The channel-channel interaction

The USL thickness plays in important role in determining the salinity profile at the membrane. In the single channel case ( $R_c \rightarrow \infty$ ), where the salinity profile is radial, the characteristic length is given by the channel radius  $R$ , but for the linear profile the characteristic length is given by the USL thickness  $\ell_c$ . As  $R_c$  decreases, the length scale governing the diffusion profile changes from  $R$  to  $\ell_c$ . This transition can be observed

in Fig. 6.5. The steady state therefore depends strongly on the size of the bulk  $\ell_c$ , and consequently so do the fluxes through the channel.

Fig. 6.6 shows the average fluid velocity  $\bar{u}$ , electric current  $I$  and salt flux  $J$  as a function of  $R_c$ , the distance between two neighbouring channels, for  $\rho_{\min} = 1$  mM and  $\rho_{\max} = 25$  mM. All fluxes decrease significantly with  $R_c$ , and can result even in an order of magnitude reduction upon near contact. It is clear, thus, that we cannot simply extrapolate the transport properties of a single channel to an array of channels. This probably explains the large discrepancy, a difference of orders of magnitude, between flux densities observed for single nanochannels [25, 127] compared to membranes [141, 163], as has already been noted [164].

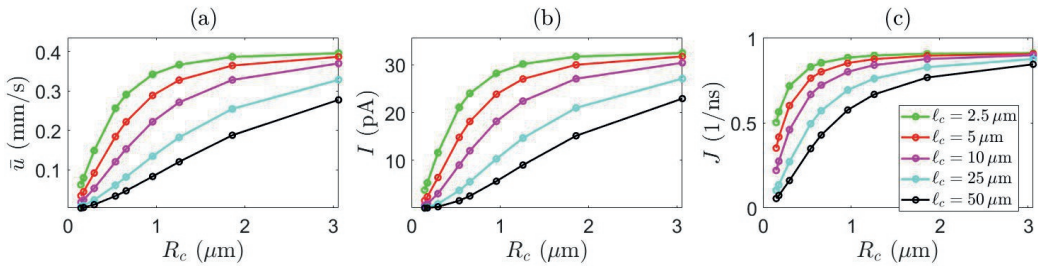


**Figure 6.6.:** (a) Average fluid velocity  $\bar{u}$ , (b) electric current  $I$  and (c) salt flux  $J$  as a function of  $R_c$  for  $\ell_c = \{2.5, 5, 10, 25, 50\}$   $\mu\text{m}$ ,  $R = 60$  nm,  $\ell = 750$  nm,  $z_\sigma\sigma = -0.05$  e/nm<sup>2</sup>,  $\rho_{\max} = 25$  mM and  $\rho_{\min} = 1$  mM.

The dependence of the transport properties on  $R_c$  and  $\ell_c$  is best understood by considering Fig. 6.7, which shows the salinity profile on the channel axis ( $r = 0$ ) as a function of the axial coordinate  $z \in [-\ell_c - \frac{1}{2}\ell, \ell_c + \frac{1}{2}\ell]$ . As discussed above, the salinity profile in the USL is essentially linear, and Fig. 6.7 shows that the concentration gradient does not only depend on  $\ell_c$  but also on  $R_c$ . The salinity gradient in the USL decreases with increasing  $R_c$ . The larger the salinity gradient in the USL, the lower (higher) the salinity at the channel inlet (outlet), therefore decreasing the salinity gradient through the channel itself.

The physics underlying Fig. 6.6 can be best understood by considering diffusion only, i.e. by ignoring, for now, the charged walls. In this case, the system reduces to a simple diffusion problem where two cylinders of length  $\ell_c$  and radius  $R_c$  (with salt concentrations  $\rho_{\max}$  as boundary conditions for one and  $\rho_{\min}$  for the other) are concentrically connected by a cylinder of length  $\ell$  and radius  $R$ . The equation for the radially averaged salinity follows a simple 1D diffusion equation, which can be solved by assuming that the total salt flux  $J$  is constant through the connected cylinders. This

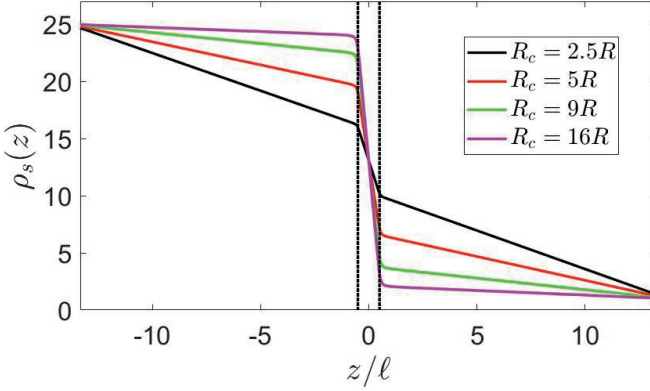


**Figure 6.7.:** The steady state salinity profiles at the channel axis ( $r = 0$ ) for  $R_c/R = \{2.5, 5, 9, 16\}$ , with  $\ell_c = 10 \mu\text{m}$ ,  $R = 60 \text{ nm}$ ,  $\ell = 750 \text{ nm}$ ,  $\rho_{\min} = 1 \text{ mM}$  and  $\rho_{\max} = 25 \text{ mM}$ .

allows us to solve for  $\rho_{\text{in}}$  and  $\rho_{\text{out}}$ , the salinity at the inlet and outlet respectively, as

$$\rho_{\text{in}} = \rho_{\min} + \frac{\Delta\rho}{2 + \frac{R_c^2 \ell}{R^2}}, \quad \rho_{\text{out}} = \rho_{\max} - \frac{\Delta\rho}{2 + \frac{R_c^2 \ell}{R^2}}, \quad (6.4)$$

with  $\Delta\rho = \rho_{\max} - \rho_{\min}$ . Interestingly, we find a dimensionless quantity  $\xi = \frac{R_c^2 \ell}{R^2}$ , composed of all geometric parameters,  $R_c$ ,  $R$ ,  $\ell_c$  and  $\ell$ , that fully fixes the salinity drop over the channel.

The importance of  $\xi$  is confirmed in Fig. 6.8, which shows the same fluxes as presented in Fig. 6.6 ( $\bar{u}$ ,  $I$  and  $J$ ) but now as a function of  $\xi$ . Fig. 6.8 shows a clear data collapse. This confirms that  $\xi$  is the dominant parameter that determines the interaction between the channels, and thus that the effect shown in Fig. 6.7 is the dominating cause of the interaction between the channels. For  $\xi \gg 1$ , the USL is so small that there is virtually no interaction between the channels since  $\rho_{\min} \approx \rho_{\text{out}}$  and  $\rho_{\max} \approx \rho_{\text{in}}$ . In the opposite limit of  $\xi \ll 1$  we have that  $\rho_{\text{in}} \approx \rho_{\text{out}}$  due to the large (relative) size of the USL.

### 6.3.3. Optimisation

We have now shown that all fluxes decrease significantly with increasing  $\ell_c$  and decreasing  $R_c$ . This would suggest that simply increasing  $R_c$  sufficiently negates the interaction between channels, but we must keep in mind that, ultimately, it is the flux per unit membrane area and not the flux per channel that must be optimised

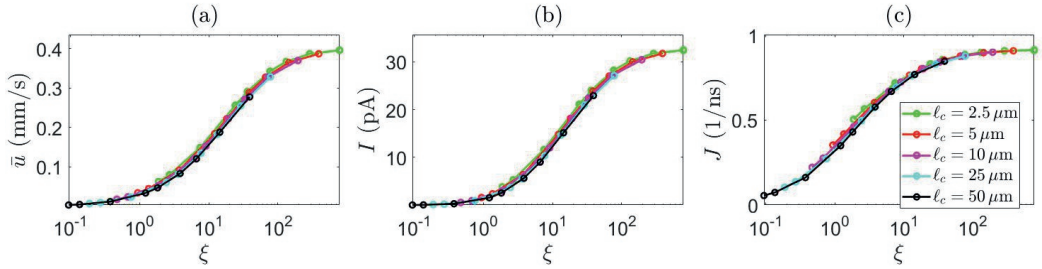


**Figure 6.8.:** (a) Average fluid velocity  $\bar{u}$ , (b) electric current  $I$  and (c) salt flux  $J$  as a function of  $\xi = \frac{R_c^2 \ell}{R^2 \ell_c}$  for  $\ell_c = \{2.5, 5, 10, 25, 50\} \mu\text{m}$ ,  $R = 60 \text{ nm}$ ,  $\ell = 750 \text{ nm}$ ,  $z_\sigma \sigma = -0.05 e/\text{nm}^2$ ,  $\rho_{\text{max}} = 25 \text{ mM}$  and  $\rho_{\text{min}} = 1 \text{ mM}$ .

in applications such as blue energy harvesting. In that sense, increasing  $R_c$  has an adverse effect on the flux density. The channel-to-channel distance  $R_c$  therefore has two competing effects on the flux density: a decreasing flux but an increasing channel density with decreasing  $R_c$ .

Fig. 6.9 shows the average fluid velocity  $\bar{u}$  ((a) & (d)), electric current  $I$  ((b) & (e)) and salt flux  $J$  ((c) & (f)) per unit area occupied by a channel  $\pi R_c^2$ , for both a pore-shaped channel ( $\ell/R = 2$ , (a)-(c)) and a needle-shaped channel ( $\ell/R = 25$ , (d)-(f)). The black dotted line represents the case if the fluxes would not depend on  $R_c$  or  $\ell_c$  (i.e.  $\bar{u}/I/J(R_c \rightarrow \infty)/(\pi R_c^2)$ ), and thus shows only the result of increasing the channel areal density. The USL thickness  $\ell_c$  indeed has a significant effect on the resulting flux densities, and reducing  $\ell_c$  can result in an order of magnitude improvement of the flux densities. In order to maximise  $\bar{u}$  and  $J$ , Fig. 6.9 shows that it is most advantageous to minimise  $R_c$  and pack the channels as close to each other as possible, even though the densities are significantly reduced due to the destructive interaction. Interestingly, however, we see that the electric current density develops an optimum, with respect to  $R_c$ , as  $\ell_c$  increases.

We can therefore immediately infer two conclusions from Fig. 6.9. Firstly, the best optimisation strategy for the electric current per unit of membrane area is, interestingly, not necessarily to minimise  $R_c$  (i.e. to pack channels as closely as possible). The exterior of the channel affects the fluxes through the channel: as  $R_c$  approaches  $R$  the destructive interaction between the channel is too strong. The best strategy is thus to leave enough space between the channels such that a large enough salinity gradient persist through the channel and over the surface charge of the exterior, but close enough that there is no excess of unused area. Secondly, we see that the pore-shaped channel, with a smaller aspect ratio, gives rise to a smaller  $Q$  and  $I$ , but larger  $J$  per unit membrane area. Based on standard linear-response theory this is surprising, since

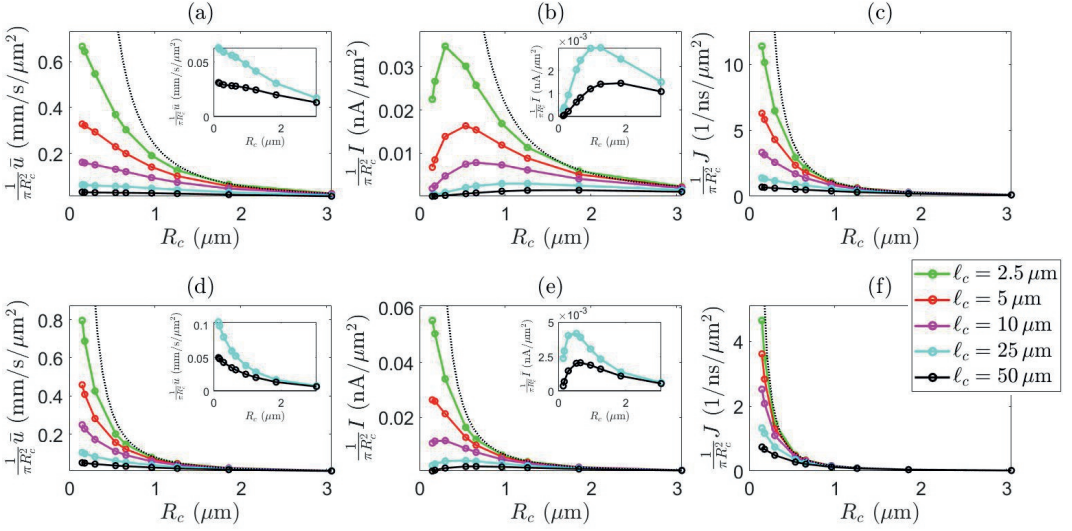


**Figure 6.9.:** (a) & (d) Average fluid velocity  $\bar{u}$  per unit area, (b) & (e) electric current  $I$  per unit area and (c) & (f) salt flux  $J$  per unit area for (a)-(c) a pore-shaped channel with  $R = 60$  nm,  $\ell = 120$  nm and (d)-(f) a needle-shaped channel with  $R = 60$  nm,  $\ell = 1500$  nm as a function of  $R_c$  for  $\ell_c = \{2.5, 5, 10, 25, 50\}$   $\mu\text{m}$ ,  $\text{nm}$ ,  $z_\sigma\sigma = -0.05 e/\text{nm}^2$ ,  $\rho_{\text{max}} = 25$  mM and  $\rho_{\text{min}} = 1$  mM. The dotted line represents the case if the fluxes would not depend on  $R_c$ , and the inset shows the case for  $\ell_c = 25, 50$   $\mu\text{m}$  for clarity.

the generated fluxes are inversely proportional to  $\ell$  (see Eq. (5.1)). The channel-channel interaction completely changes the dependence on  $\ell$ , since the entrance effects now essentially dominate the behaviour of the diffusion profile. As discussed in Section 5.3.3, the entrance effects become more significant the smaller the aspect ratio  $\ell/R$  of the channel is: needle-shaped channels ( $R \ll \ell$ ) show small entrance effects while pores ( $R \sim \ell$ ) are dominated by entrance effects. Needle-shaped channels therefore exhibit a weaker interaction between channels than pores do, and can therefore be packed closer together.

Fig. 6.9 furthermore shows that  $R_c^{\text{opt}}$ , the distance between neighbouring channels that optimises the electric current density, varies with all geometric parameters  $R$ ,  $\ell$  and  $\ell_c$ . This optimal  $R_c$  can be related to an optimal areal fraction occupied by the channels  $\Theta^{\text{opt}} = \left(\frac{R}{R_c^{\text{opt}}}\right)^2$ . The optimal areal fraction is shown in Fig. 6.10 for fixed  $R = 60$  nm and varying  $\ell$  (Fig. 6.10(a)), and for fixed  $\ell = 750$  nm and varying  $R$  (Fig. 6.10(b)). The optimal areal fraction depends strongly on the USL thickness  $\ell_c$ , which typically takes values of several tens of micrometers under experimental circumstances. For these circumstances, therefore, we find that  $\Theta^{\text{opt}}$  should be of the

order of one percent. Only for small  $\ell_c$ , of the order of a few micrometers, does  $\Theta^{\text{opt}}$  increase significantly. Fig. 6.10 furthermore shows that  $\Theta^{\text{opt}}$  increases with increasing  $\ell$  and decreasing  $R$ . The longer the channels, the larger  $\Theta^{\text{opt}}$ , so here too we find that needle-shaped channels perform better than pore-shaped channels, as the former can be packed closer together.

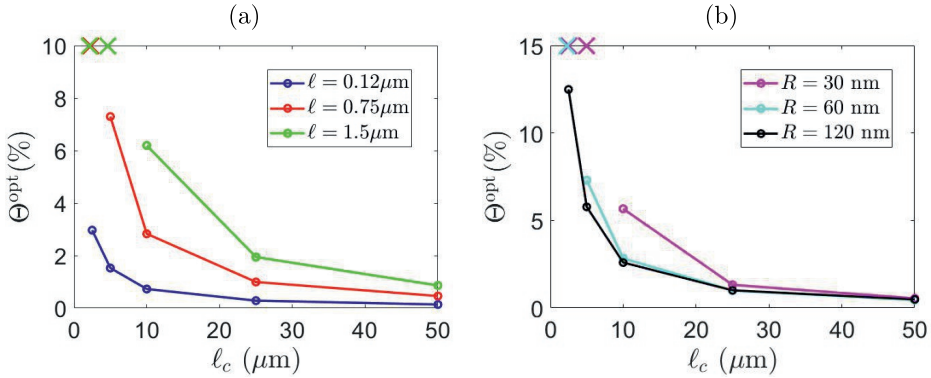


**Figure 6.10.:** Optimal areal fraction  $\Theta^{\text{opt}}$  occupied by the nanochannels for (a)  $R = 60$  nm and  $\ell = \{120, 750, 1500\}$  nm and (b)  $\ell = 750$  nm and  $R = \{30, 60, 120\}$  nm. Crosses indicate that  $R_c^{\text{opt}} \approx R$ .

Lastly, we consider how the interaction discussed in this chapter affects the electric power that can be harvested by the membrane using Reverse Electrodialysis (RED). For discussion of RED, see Section 5.6. Fig. 6.9 shows that the electric current per unit membrane area can decrease by an order of magnitude due to the interaction between the channels. In order to quantify the effect of the interaction, we compare the optimal RED power (Eq. (5.23)) generated by the membrane, i.e. using  $I(R_c^{\text{opt}})$ , to the hypothetical power generated by the same configuration of channels but without the interaction. The ratio between the membrane power density and the power density without an interaction can be expressed as

$$\frac{P_{\text{RED}}^{\text{mem}}}{P_{\text{RED}}^{\text{single}}} = \left( \frac{I(R_c^{\text{opt}})}{I(R_c \rightarrow \infty)} \right)^2 \frac{G_{\text{ch}}^{\text{single}}}{G_{\text{ch}}^{\text{mem}}}, \quad (6.5)$$

where  $P_{\text{RED}}^{\text{mem}}$  and  $G_{\text{ch}}^{\text{int}}$  are the RED power density and electric conductivity of a membrane composed of interacting channels, while  $P_{\text{RED}}^{\text{single}}$  and  $G_{\text{ch}}^{\text{single}}$  are the RED power density and electric conductivity of a membrane composed of free, non-interacting channels, respectively. The electric conductivities  $G_{\text{ch}}$  were determined using the conductivity matrix  $\mathbf{G}$  discussed in Chapter 5 and Eq. (6.4). Fig. 6.11 compares these two cases for varying  $R$  and  $\ell$ .

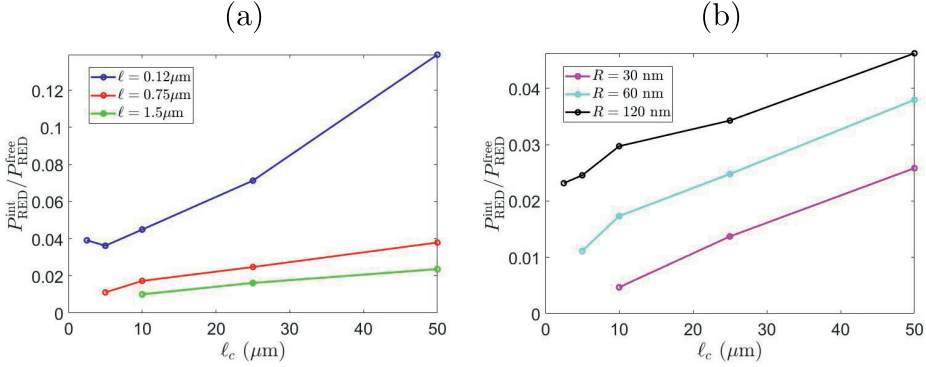


**Figure 6.11.:** Ratio between generated electric power of a membrane membrane with interacting channels  $P_{\text{RED}}^{\text{int}}$ , and free, non-interacting channels  $P_{\text{RED}}^{\text{free}}$  for (a)  $R = 60 \text{ nm}$  and  $\ell = \{120, 750, 1500\} \text{ nm}$  and (b)  $\ell = 750 \text{ nm}$  and  $R = \{30, 60, 120\} \text{ nm}$ . For the membrane with channel interactions, the electric current was evaluated at  $R_c = R_c^{\text{opt}}$ .

Since the electric current is proportional to  $I^2$ , and  $I$  decreases by an order of magnitude due to the channel interaction, we find that the generated electric power decreases by two orders of magnitude. The conductivities are also affected, but the effect on  $I$  dominates. The transition from a single to an array of channels thus greatly affects the generated electric power, and partly explains the great discrepancy between the electric power density reported by single nanochannels compared to membranes.

## 6.4. Summary & conclusion

In this chapter, we have considered how the exterior of a single nanochannel affects the diffusio-osmotic fluxes through it. Diffusio-osmosis is driven by a salinity gradient through a finite channel, and therefore exhibits entrance effects: salt diffusion transitions from a cylindrical, i.e. quasi-1D, to a open 3D geometry as salt leaves or enters the channel. The result is a salinity profile and thus a gradient over the exterior geometry. If the walls outside the channels also carry a net surface charge, like the inside of the channel, there is a non-zero diffusio-osmotic driving force outside the channel. As a result, we find that a channel with a charged exterior generates larger fluxes through the interior of the channel.

We then considered the problem of upscaling, and analysed how the transport properties of a single channel changes if it is embedded in a array of equal channels. In that case, if the channels are close enough, the external salinity profiles overlap, giving rise to an interaction between neighbouring channels. We showed that this channel-

channel interaction is always unfavourable, meaning that it significantly decreases the generated fluxes through the channels. We showed that this interaction is due to the salinity profile outside the channel. A single channel gives a radial salinity profile outside the channel, but in an array of channels, which we approximate with a cell model, the region outside the channel is no longer an open, 3D region but cylindrical, quasi-1D region. This leads to a linear, instead of a radial, salinity profile outside the channel. The salinity profile is confined to the unstirred layer, also known as the diffusion boundary layer, whose thickness significantly affects all fluxes through the array of channels.

We then analysed the flux density, the flux per unit membrane area, of such an array of channels. The flux density typically increases as the channels are more closely packed, since that results in less unused membrane area. We found that the salt flux and volumetric flow rate per unit area are optimised by minimising the channel-to-channel distance, while the electric current exhibits an optimum at intermediate distances. The existence and location of this optimum depends on geometrical parameters such as the channel radius  $R$  and length  $\ell$ , and under typical experimental conditions leads to an optimal areal fraction occupied by the channels of the order of one percent. We furthermore showed that the optimal areal fraction and the generated flux per unit membrane area is larger for needle-shaped channels ( $\ell \ll R$ ) as opposed to pore-shaped channels ( $\ell \sim R$ ), contrary to what one would expect based on the behaviour of a single channel (where the flux is inversely proportional to  $\ell$ ). Lastly, we showed that the channel-channel interaction reduces the generated electric power by between one and two orders of magnitude, and thus partly explains the large discrepancy between powers reported for these systems.

Upscaling of a single nanofluidic channel to an array of channels is thus no trivial exercise, and care must be taken how to distribute the channels over the membrane. Such an optimisation scheme, however, can help bridge the gap between the relatively high power densities of single nanochannels compared to the power densities exhibited by membranes.

## **Part III.**

# **Dynamic Interface & Dynamic Fluid**





# Chapter 7.

## Flow-induced surface charge heterogeneity: Numerical approach

*In this chapter, we study an electrokinetic system of a narrow long channel with charged walls connecting two reservoirs. Contrary to the previous part, in this chapter we go beyond the classical Helmholtz-Schmolukowski picture by considering the surprisingly strong combined effect of (i) Stern layer conductance and (ii) dynamic charge regulating rather than fixed surface charges.*

- *Section 7.2*  
*Introduction to a novel theory to describe a dynamic Stern layer charges coupled to dynamic charge regulation*
- *Section 7.3*  
*A novel steady state with a heterogeneous surface charge and zeta potential*
- *Section 7.4*  
*For a pulsed pressure drop our findings also provide a first-principles explanation for ill-understood experiments on the effect of flow on interfacial chemistry [D. Lis et al., Science 344, 1138 (2014)]*
- *Section 7.4*  
*Order of magnitude estimation of chemical rates by a comparison of experimental data with numerical predictions*

## 7.1. Introduction

In Chapter 5 we have extensively discussed the properties of electrokinetic systems and their transport properties. In this chapter, we will again consider a micro- or nanofluidic channel whose surface is charged due a chemi- or physisorption reaction. However, here we will relax the assumption that the ad- or desorption reaction has reached equilibrium, as we have done in all preceding chapters. In this chapter, we consider an electrokinetic system where the surface charge itself is a dynamic quantity. As a result, the systems develops a novel steady state, where the surface charge itself deviates from its equilibrium condition. Consequently, the transport properties of the channel are also affected, as these strongly depend on the surface charge. In this chapter, we discuss not only this novel steady state, but also the dynamic behaviour of this system. We then compare this to recent experiments, which showed that a fluid flow can reversibly alter the interfacial chemistry [165].

In this chapter, we consider an electrokinetic channel comprised of two parallel plates that bridge two large reservoirs and become charged when brought in contact with an electrolyte, and will thus generate an Electric Double Layer (see Section 1.2.2 for a discussion of the EDL). Here we consider the case of an applied pressure drop  $\Delta p$ , which generates a parabolic Poiseuille flow through the channel (see Section 2.2.2 for details). For simplicity, we assume a no-slip boundary condition. We further assume that the two reservoirs are not electrically connected, i.e. we consider an open-circuit condition discussed briefly in Chapter 5. Due to advection in the EDL, an applied pressure drop not only induces a fluid flow but also a net electric current. In closed-circuit conditions, discussed briefly in Chapter 5, this so-called “streaming current” can persist in a stationary state, but in open-circuit conditions the two reservoirs are not electrically connected and thus no net transport of charge can flow. This leads to the development of the so-called “streaming potential”  $\Delta V_S$  between the two reservoirs derived long ago by Helmholtz [30] and Smoluchowski [31]. The electric field associated to this potential drop, the streaming electric field  $E_z$ , induces an electric current equal in magnitude but opposite in direction to the streaming current, such that the total electric current vanishes. The value of  $\Delta V_S$  can be found by this zero-current condition, and can for example be found using the conductivity matrix  $\mathbf{G}$ , introduced in Section 1.3.2 and extensively discussed in Chapter 5,

$$\Delta V_S = -\frac{G_{12}}{G_{22}}\Delta p = \frac{-\zeta\epsilon}{\eta G_{\text{ch}}}\Delta p. \quad (7.1)$$

Here  $\zeta$  is the (zeta-)potential at the slipping plane,  $\epsilon$  and  $\eta$  the dielectric permittivity and the shear viscosity of the liquid, respectively,  $\Delta p$  the pressure drop that drives

the Poiseuille flow and  $G_{12}$  and  $G_{22}$  refer to elements of the conductivity matrix. The total electric conductivity of the channel,  $G_{\text{ch}} = G_b + 2G_s/H (= G_{22})$ , with  $H$  the plate separation, is well known to consist not only of a bulk contribution  $G_b$  but also of a surface contribution  $G_s/H$  that accounts for conduction processes close to the channel surfaces [15] (see Section 5.3).

The dimensionless Duhkin number  $\text{Du} = G_s/G_b H$  characterises the relative importance of the surface-to-bulk conduction [15]. It is important to realise that  $G_s = G_s^d + G_s^S$  not only contains a contribution  $G_s^d$  from the relatively high density of charge carriers in the diffuse part of the EDL, as first recognised by Bikerman in 1933 [166, 167], but *also* a contribution  $G_s^S$  from the quasi-2D Stern layer where the surface charges reside [14]. In fact, a substantial body of literature exists that not only confirms the finite charge mobility in the Stern layer for different types of (insulating) materials such as PMMA, silica or clay [1–3, 168–170], but even that the in-plane charge mobility is comparable to the mobility of simple ions in bulk electrolytes [168, 171, 172]. The lateral conductance in the Stern layer is the first key ingredient of this chapter.

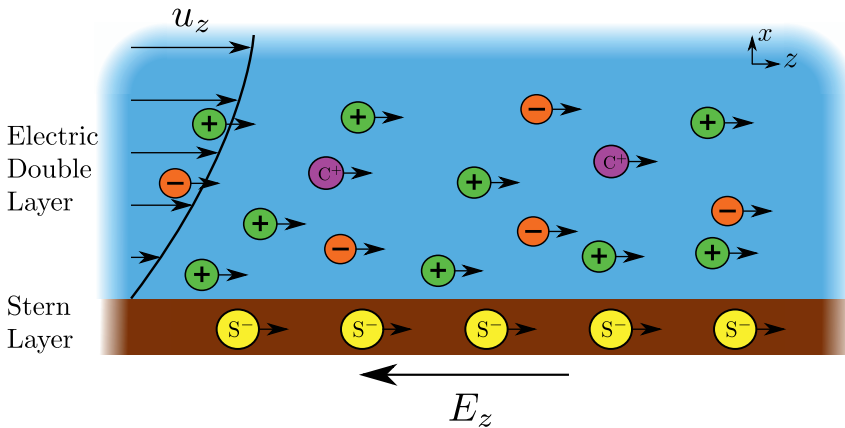


**Figure 7.1.:** Representation of the Stern layer, where the surface charges  $S^-$  (yellow) reside, and the Electric Double Layer where the inert salt (orange and green) and the counter ions  $C^+$  (purple) are located. The ions in the EDL move due to fluid flow  $u_z$ , the Stern layer ions move due to the streaming electric field  $E_z$ .

Eq. (7.1) stems from a linear-response analysis, in which the prefactor  $-\zeta\epsilon/\eta G_{\text{ch}}$  is assumed to be a constant for a given channel and transported fluid. Motivated by inherently heterogeneous biological surfaces and by microfluidic applications with patterned electrodes, extensions towards periodic [173] and step-like [174] variations of  $\zeta$  were considered. A heterogeneous  $\zeta$  not only leads to normal components of the ionic fluxes [173, 174], but also to the notion of the so-called healing length  $\ell =$

$G_s/G_b = HDu$  as the governing lateral length scale [174]. However, in this chapter we will show that defect-free and unpatterned surfaces, charged over a finite length, can exhibit flow-induced heterogeneities with the surface charge density and the zeta potential varying over the full length of the charged surface, even if  $Du \ll 1$ .

Here we consider a generic desorption reaction of a cation, where a fraction  $f$  of the neutral surface groups SC dissociates into a covalently bound negatively charged surface group  $S^-$  and a released cation  $C^+$ . The reaction  $SC \rightleftharpoons S^- + C^+$  is characterised by an equilibrium constant  $K$ , which together with the  $C^+$  concentration at the surface  $\rho_{C,s}$  determines the equilibrium Langmuir desorption isotherm  $f = (1 + \rho_{C,s}/K)^{-1}$  [129, 175, 176] (details in Section 2.1.3). Although the importance of charge regulation was indeed recognised in earlier works on the electrophoresis of colloidal particles, the underlying equilibrium Langmuir desorption isotherm has so far always been assumed [177, 178]. In this chapter, we will introduce *out-of-equilibrium* charge regulation as a second key ingredient, in which the rates of adsorption ( $k^{\text{ads}}$ ) and desorption ( $k^{\text{des}}$ ) play a key role individually rather than only their ratio  $K = k^{\text{des}}/k^{\text{ads}}$ . In fact, by tuning the chemical rates to the reaction-limited regime, we will see that our theory provides a natural first-principles explanation for puzzling recent experiments that show a profound influence of a fluid flow on the interfacial chemistry [165], provided Stern-layer conduction and out-of-equilibrium charge regulation are taken into account simultaneously. We expect that this intricate interplay between dynamic charge regulation and Stern-layer conduction will play an equally important role in many nanoflow problems of recent interest [18–20, 25].

## 7.2. Theory

The system we consider in this chapter, sketched in Fig. 7.2, consists of two bulk aqueous reservoirs connected by a wide rectangular channel of length  $\ell$  and height  $H$ , with lateral and normal Cartesian coordinates,  $z \in [-\ell/2, \ell/2]$  and  $x \in [0, H]$ , with translational invariance in the lateral  $y$  direction. The reservoirs contain three monovalent ionic species labelled by  $i = +, -, C$  with valency  $z_+ = z_C = -z_- = 1$  and with bulk concentrations  $\rho_{i,b}$ , satisfying neutrality  $\sum_i z_i \rho_{i,b} = 0$ . The Debye screening length is given by  $\lambda_D = \sqrt{\epsilon k_B T / e^2 \sum_i z_i^2 \rho_{i,b}}$ , with  $k_B$  the Boltzmann constant,  $T$  the temperature, and  $e$  the proton charge.

We denote the time- and position-dependent ionic density profiles and currents (flux densities) by  $\rho_i(\mathbf{r}, t)$  and  $\mathbf{j}_i(\mathbf{r}, t)$ , respectively, the electric potential by  $\psi(\mathbf{r}, t)$ , the (identical) surface charge density in the planes  $x = 0$  and  $x = H$  by  $-\epsilon\sigma(x, t)$  (with  $\sigma$  a positive quantity), and the fluid velocity profile by  $\mathbf{u}(\mathbf{r}, t)$ . The ion current  $\mathbf{j}_i$  is composed of diffusive, conductive, and advective contributions, and is related to  $\partial_t \rho_i$

by the continuity equation. The Poisson equation accounts for Coulomb interactions, and the incompressible Navier-Stokes equation, including an electric body force and a pressure gradient  $\nabla p$ , describes the fluid flow. Collecting all this we obtain the well-known Poisson-Nernst-Planck-Navier-Stokes (PNPNS) equations, introduced in Section 2.2.1 and 2.2.2, with Gauss's law and no-slip boundary conditions,

$$\begin{aligned}
 \frac{\partial \rho_i}{\partial t} &= -\nabla \cdot \mathbf{j}_i; \quad \mathbf{j}_i = -D \left( \nabla \rho_i + \frac{e z_i \rho_i}{k_B T} \nabla \psi \right) + \rho_i \mathbf{u}; \\
 \rho_m \frac{\partial \mathbf{u}}{\partial t} &= -\rho_m (\mathbf{u} \cdot \nabla) \mathbf{u} - \nabla p + \eta \nabla^2 \mathbf{u} - \sum_i z_i e \rho_i \nabla \psi; \\
 \nabla \cdot \mathbf{u} &= 0; \quad \nabla^2 \psi = -\frac{e}{\epsilon} \sum_i z_i \rho_i; \\
 \mathbf{u}_s &= 0; \quad \mathbf{n}_s \cdot \nabla \psi_s = \frac{e \sigma}{\epsilon}.
 \end{aligned} \tag{7.2}$$

Here  $D$  is the diffusion constant, assumed to be equal for all ion species, and  $\rho_m$  is the mass density of water. Throughout this chapter the subscript "s" denotes a surface quantity, e.g.  $\mathbf{u}_s$  is the fluid velocity at the surface and  $\mathbf{n}_s$  is the unit surface normal pointing into the water.

The standard PNPNS equations (7.2) are to be contrasted with the novel boundary conditions that we impose in this chapter, where we describe regulation of the density of surface charges  $\sigma$  combined with Stern layer conductance. The bottom and the top surfaces each contain an identical, chemically homogeneous patch for  $z \in [-\ell/2, \ell/2]$  that can become negatively charged due to the desorption reaction  $\text{SC} \rightleftharpoons \text{S}^- + \text{C}^+$ . Therefore, a non-vanishing cationic counterion current  $-\mathbf{n}_s \cdot \mathbf{j}_{\text{C},s}(z)$  entering the surface is possible, whereas the other two ionic species  $\pm$  are chemically inert and satisfy the no-flux boundary conditions  $\mathbf{n}_s \cdot \mathbf{j}_{\pm,s} = 0$ . Within the Stern layer we introduce the lateral (surface) electric current  $-e j_\sigma(z)$ , satisfying the continuity equation for the surface charge density as

$$\frac{\partial \sigma}{\partial t} = -\frac{\partial j_\sigma}{\partial x} + \mathbf{n}_s \cdot \mathbf{j}_{\text{C},s}, \tag{7.3}$$

which explicitly couples the 3D flux of cations as a source term for the 2D surface density. We describe the net flux of  $\text{C}^+$  towards the surface in terms of simple reaction kinetics with an adsorption flux  $k^{\text{ads}} \sigma \rho_{\text{C},s}$  and a desorption flux  $k^{\text{des}} (\Gamma - \sigma)$ , with  $\Gamma$  the total number of chargeable sites per unit area. Additionally, we assume a Nernst-Planck like equation for  $j_\sigma$ , with a diffusive and a conduction contribution, where the former

is modified to account for forbidden multiple ad- and desorption on a single site [179]:

$$j_\sigma(z) = -D_s \left( \frac{1}{1 - \sigma/\Gamma} \frac{\partial \sigma}{\partial z} - \frac{e\sigma}{k_B T} \frac{\partial \psi_s}{\partial z} \right); \quad (7.4)$$

$$-\mathbf{n}_s \cdot \mathbf{j}_{C,s} = -k^{\text{des}}(\Gamma - \sigma) + k^{\text{ads}}\sigma\rho_{C,s}, \quad (7.5)$$

where  $D_s$  the surface diffusion constant, which we have seen to be comparable to the bulk diffusion coefficient  $D$ . The diffusion contribution ( $\propto \partial_z \sigma$ ) must in general be adjusted by a factor  $(1 - \sigma/\Gamma)^{-1}$  as the surface groups cannot be multiply occupied [179]. Furthermore, we assume that  $D_s$  does not depend on  $\sigma$ . Even though for high concentrations the diffusion constant depends non-trivially on the concentration [180],  $\sigma$  is sufficiently small to safely assume  $D_s$  to be constant since at most a few percent of the total number of sites is charged. Similarly, we have assumed that the bulk diffusion constant  $D$  in Eq. (7.2) is homogeneous throughout the system, while in general this depends on for example the distance to the surface [181]. For simplicity, we leave out these higher order effects.

Eq. (7.4) can be derived by applying the Dynamic Density Functional Theory, see Section 2.2.1, to the Density Functional set up for the surface charges derived in Section 2.1.3 (see Appendix C.1 for derivation). If we impose equilibrium conditions, in particular  $\mathbf{j}_C = 0$ , Eqs. (7.3) - (7.5) reduce to the standard Langmuir desorption isotherm where  $\sigma/\Gamma$  equals the fraction  $f$  of charged sites introduced above (see Section 2.1.3). In the case of a pressure-induced flow, however, the streaming potential generates an in-plane electric field component  $-\partial_z \psi_s$ , which according to Eq.(7.4) not only drives a finite  $j_\sigma$  if  $D_s \neq 0$ , but, for a charge-regulating surface, *also* a finite  $\mathbf{n}_s \cdot \mathbf{j}_{C,s}$  and a surface heterogeneity  $\partial_x \sigma$  according to Eqs. (7.3) and (7.5). Consequently, the zeta potential  $\zeta(z) = \psi(z, x = 0) - \psi(z, x = H/2)$  becomes heterogeneous too, and hence a non-trivial self-consistency problem emerges in which the streaming potential not only determines  $\zeta(z)$  but also depends on it (due to Eq. (7.1)). Interestingly, this flow-induced surface heterogeneity does *not* require relatively narrow channels or high Du.

### 7.3. Steady state

We solve the set of non-linear equations (7.2)-(7.5) numerically using the Finite Elements software COMSOL Multiphysics. For computational reasons we take at each side of the chargeable surface an uncharged patch of length  $\ell/2$  to allow entrance and exit effects on the fluid flow driven by a pressure drop  $\Delta p$  to essentially die out (see C.2 for details). Due to the crucial role played by the chemical reaction we must fully resolve the EDL in

order to accurately determine  $\rho_{C,s}$ . The thin-EDL approximation [41] is therefore not possible here. In this chapter we choose parameters that represent silica at pH = 6.5, such that  $-\log_{10} \rho_{C,b}(\text{M}) = 6.5$ ,  $\Gamma = 4.6 \text{ nm}^{-2}$ , and  $\text{p}K = 6.75$  (an average over the widely varying reported values [4, 182, 183]), with millimolar added salt concentrations,  $\rho_{\pm,b} \simeq 1 \text{ mM}$ , such that  $\lambda_D = 10 \text{ nm}$ . The single reaction mechanism assumed here is actually too simple to capture the behaviour of silica quantitatively, but it serves our purposes here as a generic case. Under these conditions, the equilibrium surface charge and potential are  $-e\sigma_{\text{eq}} = -0.069 \text{ e/nm}^2$  and  $\zeta_{\text{eq}} = -93 \text{ mV}$ . Throughout we set  $D = 10^{-9} \text{ m}^2/\text{s}$  such that  $G_b = 7.5 \text{ mS/m}$  and  $G_s^d \approx 1.2 \text{ nS}$  [184]. In agreement with Stern-layer mobilities discussed above, we either set  $D_s = D$  or  $D_s = 0$  to study presence or absence of Stern-layer conductance, respectively. We furthermore focus on a channel height  $H = 1 \mu\text{m}$ , i.e.  $H \gg \lambda_D$  and  $\text{Du} \simeq 0.16$ . Apart from the channel length  $\ell$  the only remaining system parameter is the time scale of the adsorption-desorption process, which will be fitted to experiments below. For computational efficiency we set  $k^{\text{des}} = 2 \times 10^{-4} \text{ s}^{-1}$  for now, which is comparable to certain photocatalytic rates [185] and comfortably in the reaction-limited regime as we will see.

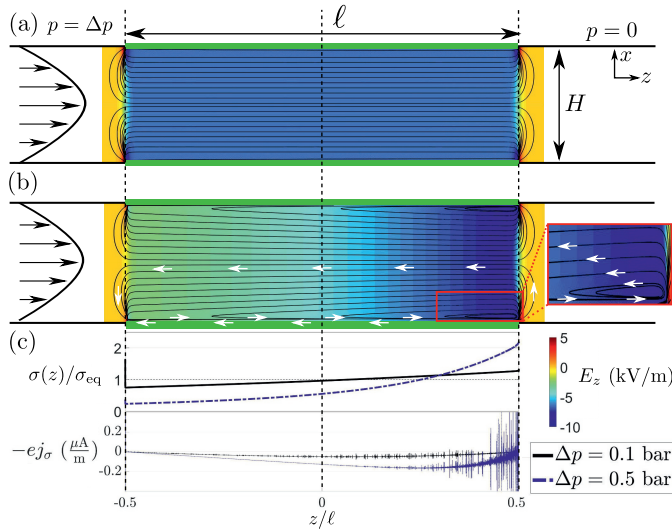


**Figure 7.2.:** Streamlines of the net charge flux and colour map of the tangential electric field  $E_x$  near the charged surfaces (green stripes) of a rectangular channel with a pressure drop  $\Delta p = 0.5 \text{ bar}$  between in- and outlet at  $z = \pm\ell/2$ , (a) with vanishing Stern-layer conduction ( $D_s = 0$ ) resulting in a fixed surface charge of  $-e\sigma_{\text{eq}} = -0.069 \text{ e/nm}^2$  that mimics silica at pH=6.5, and in (b) with non-zero Stern-layer conductance and our dynamic charge regulation model. (c) Flow-induced heterogeneous surface charge density  $\sigma(z)$  and surface electric current  $-ej_\sigma$  for  $\Delta p = 0.1, 0.5 \text{ bar}$  for the parameters of case of (b).

In Fig. 7.2 we show the steady-state field lines of the ionic charge flux  $\mathbf{j}_e = \sum_i z_i \mathbf{j}_i$  and a colourmap of the  $z$ -component of the electric streaming field  $E_z$  for a channel of height  $H = 1 \mu\text{m}$  and total length  $\ell = 60 \mu\text{m}$ , and a pressure drop  $\Delta p = 0.5 \text{ bar}$ , in (a) without Stern layer conduction ( $D_s = 0$ ), and in (b) in the presence of both Stern layer conduction ( $D_s = D$ ) and dynamic charge regulation. The resulting maximum fluid velocity is approximately  $0.1 \text{ m/s}$ , three orders of magnitude higher than the electro-osmotic slip velocity induced by the electric field, i.e. the body forces (last term of the Navier-Stokes equation (7.2)) are negligible (see Appendix C.3 for a more detailed discussion). A striking difference between (a) and (b) are the non-parallel field lines in (b), even far outside the EDL, and a much weaker electric field especially for  $z \in [-\ell/2, 0]$  in (b). We can trace these two features back to a non-zero surface current  $j_\sigma(z)$  and a strong heterogeneity of the surface charge profile  $\sigma(z)$ ; both extend over the full width  $\ell$  as shown in Fig. 7.2(c). This shows that, in addition to the inherent heterogeneities of silica in equilibrium conditions [186], surfaces can exhibit dynamical heterogeneities. We note that the diffusive and conductive contributions to  $j_\sigma$ , shown in Eq. (7.4), are counteracting and individually three orders of magnitude larger than  $j_\sigma$ , i.e. both are essential to obtain this steady state. The near-cancellation is the cause of the numerical noise observed for  $j_\sigma$ , and furthermore leads to the surprising conclusion that the effects persist even for  $\text{Du} \ll 1$ . Fig. 7.2(b) also shows that  $\mathbf{j}_e$  and  $E_z$  depend not only on  $x$  but also on  $z$ , even far outside the EDL. Note that a lateral heterogeneous charge current has also been reported in the case of a (highly conducting) metallic surface [187].

For  $\Delta p = 0.1 \text{ bar}$ , the heterogeneous profile  $\sigma(z)$  shown in Fig. 7.2(c) is essentially linear in  $z$ , locally lower/higher by about  $\pm 25\%$  of  $\sigma_{eq}$  at the inlet/outlet side of the chargeable area. For  $\Delta p = 0.5 \text{ bar}$ , however,  $\sigma(z)$  is strongly nonlinear with deviations ranging from  $-75\%$  to as high as  $+100\%$  from  $\sigma_{eq}$  at the edges. In equilibrium, such a change in the surface charge would correspond to a pH varying between 4.9 and 7.4, i.e. concentrations of  $\text{C}^+$  that are a factor of 10 higher and lower. Moreover, the laterally averaged charge in this case decreases to a value as low as  $\langle \sigma \rangle = 0.7 \sigma_{eq}$ . Additionally,  $\langle \zeta \rangle$  also decreases compared to its equilibrium value, which causes a breakdown of Eq. (7.1) (see Appendix C.4 for a more detailed discussion). Therefore the local as well as the average surface charge are not at all (quasi-)static quantities, but fully dynamic properties of the solid-fluid interface that can be tuned by the fluid flow in the channel. The sharp peaks of  $\sigma$  at  $z \simeq \pm \ell/2$  in Fig. 7.2(c) are expected in a range of  $\lambda_D$  next to an uncharged area [188].

The properties of this novel steady state can be understood as a balance of different time scales, which we will derive and discuss in detail in Chapter 8. We can identify three different time scales that govern the dynamics of the Stern layer, (i) the diffusion time  $\tau_{\text{dif}} \propto \ell^2/D_s$ , the time for a charge in the Stern layer to diffuse a lateral distance

$\ell$ , which is of the order of seconds here, (ii) the conduction time  $\tau_{\text{cond}} \propto \sigma_{\text{eq}}/j_{\sigma}$ , the time for a charge in the Stern layer to traverse a lateral distance  $\ell$  due to the in-plane electric field  $-\partial_z \psi_s$ , which is also of the order of seconds here, and (iii) the chemical reaction time  $\tau_{\text{reac}} = (k^{\text{des}} + k^{\text{ads}} \rho_{C,s})^{-1}$  of the order of an hour here. We found that significant heterogeneities only occur if  $\tau_{\text{reac}}$  exceeds the others, i.e. if the system is in the reaction-limited rather than in the diffusion- or conduction-limited regime. This can be qualitatively understood, e.g., if  $\tau_{\text{reac}} \ll \tau_{\text{cond}}$  chemical equilibration would take place before any conductive flux can develop. Note also that  $\tau_{\text{cond}} \propto D_s^{-1}$  confirms the crucial role played by a finite surface conduction, since  $D_s = 0$  would cause the system to be conduction- rather than reaction-limited. As long as this ordering of time-scales is obeyed and  $D_s/D = \mathcal{O}(1)$ , as noted already on the basis of Refs. [168, 171, 172] the exact value of  $D_s$  has no significant effect on the presented results. These time scales will be discussed more extensively in Chapter 8, where we will derive these from the governing equations, Eqs. (7.2)-(7.5).

## 7.4. Dynamics

So far we have seen that the stationary state of a charge-regulating and conducting surface exposed to a fluid flow becomes heterogeneously charged in a stationary state. In an exciting experiment in 2014, however, the full relaxation dynamics of the surface charge of silica upon an applied water pressure *pulse* was measured in an experiment that combines microfluidics and Sum Frequency Generation (SFG) [165], albeit only at the central position (here  $z = 0$ ) in the channel. By ruling out alternative interpretations the authors of [165] attribute their time-dependent SFG-signal to a time-dependent surface charge  $\sigma(z = 0, t)$ . Here we confirm this interpretation by showing that our theory provides a microscopic explanation for the time dependence of the surface charge, which in the experiments (see inset Fig. 7.3 or Fig. 2D of [165]) consists of a quasi-instantaneous initial reduction by 40% (on the time scale of seconds) upon switching on the flow followed by a further reduction of an additional 10% on the time scale of minutes, and upon switching off the flow a very slow relaxation (on the time scale of tens of minutes) back to equilibrium.

In Fig. 7.3 we show a time-dependent pressure pulse (blue) similar to the experimental one as well as the surface charge density  $\sigma(z = 0, t)$  (red) that follows from our theory. Here we use the same silica parameters and bulk concentrations as before in Fig. 7.2(b), again at pH = 6.5 but now with the desorption rate  $k^{\text{des}} = 6 \times 10^{-6} \text{ s}^{-1}$  as the only “fit”-parameter. This corresponds to  $\tau_{\text{reac}} = 1.7 \times 10^3 \text{ s}$ , which sets the transient behaviour of  $\sigma(0, t)$ . This is also consistent with the experimental observation that  $\sigma$  remains constant during such a pressure pulse for large enough  $\rho_{C,b}$  [165], since

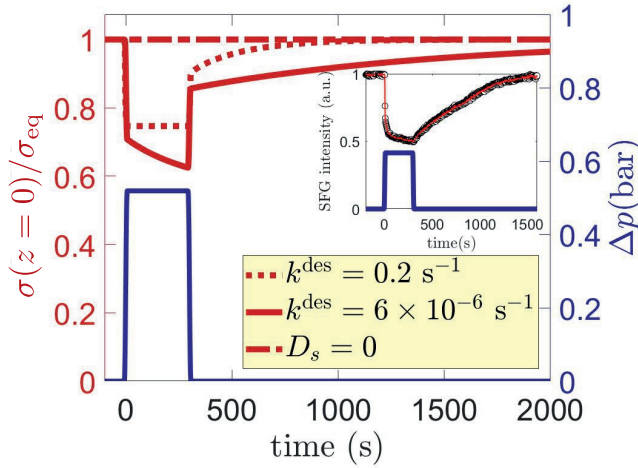


**Figure 7.3.:** Time-dependent pressure drop  $\Delta p(t)$  (blue) in a channel of dimensions  $H = 1 \mu\text{m}$  and  $\ell = 40 \mu\text{m}$ , together with the resulting surface charge  $\sigma(z = 0, t)$  in the middle of the channel, for a silica surface at  $\text{pH} = 6.5$  (see text) with desorption rate  $k^{\text{des}} = 6 \times 10^{-6} \text{ s}^{-1}$  ( $\tau_{\text{reac}} = 1.7 \times 10^3 \text{ s}$ ) (red), to be compared with the experimental data of [165] shown in the inset. The red dot-dashed line shows the case of a non-conducting Stern layer with  $D_s = 0$ , and the dotted line the case with desorption rate  $k^{\text{des}} = 0.2 \text{ s}^{-1}$  (such that  $\tau_{\text{reac}} = 0.05 \text{ s}$ ).

$\tau_{\text{reac}} \propto \rho_{C,b}^{-1}$ , such that the system is no longer reaction-limited for increased counter ion concentration. The channel dimensions for the results shown in Fig. 7.3,  $H = 1 \mu\text{m}$  and  $\ell = 40 \mu\text{m}$ , are for computational reasons smaller than in the experiment by a factor of 500, although the aspect ratio is the same. We checked that this time dependence is hardly dependent on  $\ell$  and  $H$  for fixed pressure drop amplitude  $\Delta p = 0.5 \text{ bar}$  and aspect ratio  $\ell/H = 40$  (see Appendix C.4). The similarity between the time-dependent experimental SFG-signal and  $\sigma(z = 0, t)/\sigma_{eq}$  is striking, except perhaps for the strong short-time relaxation immediately after switching off the flow, which is present in our calculations (see Fig. 7.3) but absent in the experiment (inset). This is probably due to the greatly differing system size. The relaxation of the surface charge profile after switching off the flow is a diffusion process, and is therefore governed by  $\tau_{\text{dif}}$ , which is proportional to  $\ell^2$ .

For comparison, Fig. 7.3 also shows the surface charge for the case of a non-conducting Stern layer with  $D_s = 0$  (dotted red), which is virtually indistinguishable from  $\sigma_{eq}$ . By increasing the desorption rate, such that the system becomes less reaction-limited, the transient behaviour speeds up and the steady-state approaches the equilibrium state, as can be observed from the dashed line in Fig. (7.3). This confirms the time scale analysis discussed above, and will be discussed in more detail in Chapter 8.

## 7.5. Summary & conclusion

In conclusion, we apply the classical PNPNS equations (7.2) to pressure-driven flow through a channel with newly formulated boundary conditions for out-of-equilibrium charge regulation and a conducting Stern-layer. For realistic system parameters, in particular for silica surfaces, this theory predicts a strong flow-induced heterogeneity of the surface charge and the zeta potential, even for a chemically homogeneous silica surface with  $Du \ll 1$ . The traditional Helmholtz-Smoluchowski relation (7.1) for the streaming potential, which assumes a laterally constant zeta potential, breaks down for these regulating and conducting surfaces, provided the system is reaction-limited, i.e. the chemical reaction is the slowest process. In this reaction-limited regime, a non-zero conductive flux in the Stern layer must be largely compensated by an opposite diffusive surface flux (i.e. by a heterogeneous surface charge) in order to prevent steady-state charge accumulation at the edges due to slow reaction kinetics. The resulting surface charge profile has a reduced lateral average surface charge compared to equilibrium. Our theory also provides a microscopic picture for measurements on the full time-dependence of the the relaxation dynamics of the surface charge after switching on and off a tangential flow [165]. We have therefore shown that the combination of a non-zero surface conduction and (s)low chemical ad- and desorption rates can have dramatic impact on the interpretation of electrokinetics in micro- and nanofluidic experiments, for which the surface charge and zeta potential are a vital component. We expect that these or similar mechanisms also play a role in electro-osmotic and diffusio-osmotic phenomena, which are interesting topics for future research in the context of e.g. blue energy harvesting [24, 25] and catalysis [189].

## Acknowledgements

We thank Jeffrey Everts and Sela Samin for their important contributions to the work presented in this chapter.



# Chapter 8.

## Flow-induced surface charge heterogeneity: Analytical approach

*In the previous chapter we have numerically shown that the emergence of a new steady state when both the fluid and the surface charge are out-of-equilibrium. In this chapter, we will study this novel steady state analytically instead of numerically, and derive three time scales that fully characterise the qualitative behaviour of the system. We will therefore not repeat an extensive introduction here, for this we refer the reader to Section 7.1.*

- *Section 8.2  
Approximate solutions to the equations solved numerically in Chapter 7*
- *Section 8.3  
Identification of three governing time scales  $\tau_{\text{reac}}$ ,  $\tau_{\text{dif}}$  and  $\tau_{\text{cond}}$ , and associating each time scale to a physical process:  $\tau_{\text{reac}}$  to the adsorption/desorption reactions,  $\tau_{\text{dif}}$  to diffusion of the surface charges and  $\tau_{\text{cond}}$  to conduction of the surface charges*
- *Sections 8.3.1, 8.3.2 and 8.3.3  
Identification of three regimes, defined by which of the three time scales is dominant (slowest), and the different quantitative and qualitative behaviour of each regime*

## 8.1. The (linearised) Poisson-Nernst-Planck equations

As in Chapter 7, we consider an electrokinetic system consisting of two water reservoirs connected by a rectangular channel with height  $H$  and length  $\ell$ . We denote the normal and lateral Cartesian coordinate of the channel by  $x \in [0, H]$  and  $z \in [-\ell/2, \ell/2]$ , respectively, and assume translational invariance in the  $y$  direction. The top ( $x = H$ ) and bottom ( $x = 0$ ) surface of the channel carry chargeable surface groups, and of course an associated Electric Double Layer (EDL) (see Section 1.2.2 for a discussion of the EDL). For simplicity we assume both surfaces to be equal, such that the plane at  $x = \frac{1}{2}H$  is a plane of symmetry of the system. Without loss of generality, we take the fluid flow in the positive  $z$  direction. The reservoirs contain three different ionic species labelled by  $i = +, -, C$ , with valency  $z_+ = -z_- = 1$  and  $z_C$ . Charge neutrality in the bulk demands  $\sum_i z_i \rho_{b,i} = 0$ , with  $\rho_{b,i}$  the bulk concentration of ion  $i$  in the two reservoirs, i.e. we do not consider diffusio-osmotic processes here. This fixes the Debye screening length, as  $\lambda_D = \sqrt{\epsilon k_B T / (e^2 \sum_i z_i^2 \rho_{b,i})}$ , the typical thickness of the EDL, with  $k_B$  the Boltzmann constant,  $T$  the temperature, and  $e$  the elementary charge.

We denote the position and time dependent concentration and flux of ion species  $i$  by  $\rho_i(\mathbf{r}, t)$  and  $\mathbf{j}_i(\mathbf{r}, t)$ , respectively, the electric potential by  $\psi(\mathbf{r}, t)$  and the fluid velocity and pressure by  $\mathbf{u}(\mathbf{r}, t)$  and  $p(\mathbf{r}, t)$ , respectively. These quantities are governed by the Poisson-Nernst-Planck-Navier-Stokes (PNP-NS) equations [41], see Section 2.2.1 and 2.2.2 for details,

$$\begin{aligned} \frac{\partial \rho_i}{\partial t} &= -\nabla \cdot \mathbf{j}_i; \quad \mathbf{j}_i = -D \left( \nabla \rho_i + \frac{e z_i \rho_i}{k_B T} \nabla \psi \right) + \rho_i \mathbf{u}; \\ \rho_m \frac{\partial \mathbf{u}}{\partial t} &= -\rho_m (\mathbf{u} \cdot \nabla) \mathbf{u} - \nabla p + \eta \nabla^2 \mathbf{u} - \sum_i z_i e \rho_i \nabla \psi; \\ \nabla \cdot \mathbf{u} &= 0; \quad \nabla^2 \psi = -\frac{e}{\epsilon} \sum_i z_i \rho_i, \end{aligned} \quad (8.1)$$

where  $D$  is the diffusion constant (assumed for simplicity to be equal for all ionic species), and  $\rho_m$  the mass density of the fluid.

These equations are then to be coupled to a dynamic Stern layer. In our theoretical framework, we treat the density of surface charges  $\sigma(z, t)$ , a 2D analogue of  $\rho_i(\mathbf{r}, t)$ , as a dynamic variable. The surface charges are produced by a chemical reaction  $SC \rightleftharpoons S^- + C^+$ , where the counter ion  $C^+$  desorbs from the surface leaving behind a covalently bound surface group  $S^-$ . Therefore,  $\sigma(z, t)$  is not necessarily a locally conserved quantity, which must be taken into account in the continuity equation. Denoting the flux of surface charges in the  $z$ -direction by  $j_\sigma(z, t)$ , the 2D analogue of  $\mathbf{j}_i(\mathbf{r}, t)$ , we can

write the continuity equation for  $\sigma(z, t)$  as

$$\frac{\partial \sigma}{\partial t} = -\frac{\partial j_\sigma}{\partial z} + \hat{\mathbf{n}}_s \cdot \mathbf{j}_{C,s}, \quad (8.2)$$

where  $\hat{\mathbf{n}}_s = \pm \hat{\mathbf{x}}$  is the unit vector normal to the charged surface and  $\hat{\mathbf{x}}$  the unit vector in the  $x$  direction. The production rate of surface charges is governed by the chemical rate equations, where the surface charge production (annihilation) rate is proportional to the density of uncharged (charged) sites. The resulting equations that govern the dynamics of the Stern layer, and therefore can be seen as the boundary conditions to the PNP-NS equations (8.1), are given by

$$\frac{\partial \psi_s}{\partial z} = -\frac{z_\sigma e \sigma}{\epsilon}; \quad \mathbf{u}_s = 0; \quad (8.3)$$

$$j_\sigma = -D_s \left( \frac{1}{1 - \sigma/\Gamma} \frac{\partial \sigma}{\partial z} + z_\sigma \frac{e \sigma}{k_B T} \frac{\partial \psi_s}{\partial z} \right); \quad (8.4)$$

$$\hat{\mathbf{n}}_s \cdot \mathbf{j}_{C,s} = R = k^{\text{des}}(\Gamma - \sigma) - k^{\text{ads}} \sigma \rho_{C,s}, \quad (8.5)$$

with  $D_s$  is the diffusion constant of the surface charges,  $z_\sigma = -z_C$  the valency of the surface charges,  $\Gamma$  the density of surface sites, and  $k^{\text{ads}}$  and  $k^{\text{des}}$  the adsorption and desorption rate constants, respectively. Here, and throughout this work, we use the subscript "s" to denote surface quantities, such that  $\mathbf{u}_s = 0$  enforces a no-slip boundary condition and  $\rho_{C,s}(z) \equiv \rho_C(x = 0, z)$  the counter ion concentration at the surface.

## 8.2. Solving the equations

The governing equations (8.1)-(8.5) cannot be solved analytically in general. In this chapter, however, we will show how to obtain approximate solutions to these equations. As is common in pressure-driven electrokinetic systems, we neglect not only the inertial terms in the Navier-Stokes equation (low Reynolds number, see Section 2.2.2), but also the electric body forces on the fluid [41], such that we can ignore the final term on the right hand side of the Navier-Stokes equation (8.1). The latter approximation can be justified for set-ups with  $H \gg \lambda_D$ , and by realising that the body force is localised in the EDL while the pressure gradient extends over the entire channel height. This approximation is confirmed by our numerical calculations (see Appendix C.3), which show that including the electric body force has no significant effect (smaller than one per cent) on the steady state surface charge profile. The Navier-Stokes equation then reduces to the Stokes equation, and is now decoupled from other quantities. This allows us to solve for  $\mathbf{u}$  and  $p$  (see Section 2.2.2), resulting for an applied pressure drop

$\Delta p$  to the standard Poiseuille flow,

$$\mathbf{u}(x) = -\frac{\partial p}{\partial z} \frac{x(H-x)}{2\eta} \hat{\mathbf{z}}, \quad (8.6)$$

with  $\hat{\mathbf{z}}$  the unit vector in the  $z$  direction and  $\frac{\partial p}{\partial z} = -\frac{\Delta p}{\ell}$ .

In the following analysis we will focus solely on the net charge density  $\rho_e(\mathbf{r}, t) = \sum_i z_i \rho_i(\mathbf{r}, t)$  and electric current  $\mathbf{j}_e(\mathbf{r}, t) = \sum_i z_i \mathbf{j}_i(\mathbf{r}, t)$ ,

$$\mathbf{j}_e = -D \left( \nabla \rho_e + \frac{e\rho}{k_B T} \nabla \psi \right) + \rho_e \mathbf{u}, \quad (8.7)$$

with  $\rho(\mathbf{r}, t) = \sum_i z_i^2 \rho_i(\mathbf{r}, t)$  the total local ionic strength. As is common in a linearised theory of electrokinetic systems, we assume here that  $\rho$  is constant throughout the system and equal to its bulk value,  $\rho = \sum_i z_i^2 \rho_{i,b}$ . In steady state,  $\nabla \cdot \mathbf{j}_e = 0$ , and combining this with the Poisson equation eliminates the electric potential in favour of the charge density. We then obtain the governing equation for  $\rho_e(x, z)$ ,

$$\left( -D \frac{\partial^2}{\partial x^2} - D \frac{\partial^2}{\partial z^2} + \frac{D}{\lambda_D^2} + u_z(x) \frac{\partial}{\partial z} \right) \rho_e(x, z) = 0. \quad (8.8)$$

We can simplify Eq. (8.8) using scaling arguments. From Chapter 7, we know that the fluid flow will induce heterogeneities in the  $z$  direction over the full channel length  $\ell$ , and therefore we estimate that  $\partial/\partial z \sim 1/\ell$ . We also know that  $\rho_e$  reduces quickly to 0 within a few  $\lambda_D$  in the  $x$  direction, and hence  $\partial/\partial x \sim 1/\lambda_D$ . This allows us to define a few characteristic time scales for the EDL,

$$\tau_\ell = \frac{\ell^2}{D}; \quad \tau_{\text{EDL}} = \frac{\lambda_D^2}{D}; \quad \tau_{\text{adv}} = \frac{\ell}{u_z(\lambda_D)}. \quad (8.9)$$

Here,  $\tau_\ell$  is the characteristic time for an ion in bulk to diffuse the lateral length  $\ell$ , and is of the same order of magnitude as the first term of Eq. (8.8). Additionally,  $\tau_{\text{EDL}}$  is the characteristic equilibration time of an EDL, and is of the same order of magnitude as the second and third term of Eq. (8.8). Lastly,  $\tau_{\text{adv}}$  is the characteristic time it takes for an ion in the EDL to be advectively transported from one end of the channel to the other. Since  $\rho_e$  is only non-zero in the EDL, we evaluate  $u_z$  at  $x = \lambda_D$ . For our geometry,  $\ell \gg \lambda_D$ , and thus we can conclude that  $\tau_{\text{EDL}} \ll \tau_\ell$ , meaning that the diffusion in the lateral direction (first term Eq. (8.8)) is negligible compared to diffusion in the normal direction (second term Eq. (8.8)). Moreover, for pressure drops  $\Delta p$  no larger than 1 bar,  $\eta \sim 1$  mPa s, the viscosity of water, and channel dimensions  $H \sim 1 \mu\text{m}$  and  $\ell \sim 10 \mu\text{m}$ , we find a typical fluid velocity  $u_z(\lambda_D) < 10^{-2}$  m/s for physically relevant

salt concentrations in water. Since  $D/\lambda_D \sim 0.1\text{m/s} > u_z(\lambda_D)$  for our parameter choice of interest, we have  $\tau_{\text{EDL}} \ll \tau_{\text{adv}}$  implying that convection in the lateral direction (last term Eq. (8.8)) is negligible with respect to diffusion in the normal direction. After inserting typical orders of magnitude, one indeed finds that  $\tau_{\text{EDL}}$  is of the order of (tens of) nanoseconds, while  $\tau_{\text{adv}}$  is of the order of milliseconds or larger. Eq. (8.8) now reduces to a simple differential equation,

$$\frac{\partial^2 \rho_e}{\partial x^2} = \frac{1}{\lambda_D^2} \rho_e \quad \Rightarrow \quad \rho_e(x, z) = -\zeta(z) \rho e^{-x/\lambda_D}, \quad (8.10)$$

where  $\zeta(z)$  is an integration constant that remains to be found. As we will show below, we can identify  $\zeta(z) = \beta e(\psi(0, z) - \psi(\frac{1}{2}H, z))$  as the (heterogeneous) dimensionless zeta potential at steady state. The second integration constant has been set to zero since  $\rho_e(x \rightarrow \frac{1}{2}H, z) = 0$  for  $H \gg \lambda_D$ . Eq. (8.10) is analogous to the equilibrium linear Poisson-Boltzmann equation for the charge density, and is a direct consequence of  $\tau_{\text{EDL}} \ll \tau_{\text{adv}}, \tau_\ell$ : the EDL is equilibrated in the  $x$  direction as convection is typically not strong enough to deform the EDL significantly.

To determine the integration constant  $\zeta(z)$ , we apply the boundary conditions Eqs. (8.2)-(8.5). To facilitate the calculations, we make use of the fact that for the majority of surfaces only a small fraction of the sites are charged,  $\sigma \ll \Gamma$ . For instance, only a few percent of the surface groups of silica are charged under typical conditions ( $3 < \text{pH} < 11$ ,  $1 \text{ mM} < \rho_s < 100 \text{ mM}$ ) [4]. With this assumption, the equation for  $\sigma(z)$  simplifies to

$$D_s \left( \frac{\partial^2 \sigma}{\partial z^2} + \frac{z\sigma e}{k_B T} \frac{\partial}{\partial z} \left( \sigma \frac{\partial \psi_s}{\partial z} \right) \right) + k^{\text{des}} \Gamma - (k^{\text{des}} + k^{\text{ads}} \rho_{C,s}) \sigma = 0. \quad (8.11)$$

Eq. (8.11) constitutes a diffusion-conduction-reaction problem coupled to the 3D-channel via the in-plane electric field  $-\partial\psi_s/\partial z$  and the counter ion density  $\rho_{C,s}$ . As a consequence, three regimes will arise depending on which process is dominant. This is reminiscent of a convection-diffusion problem [190] with a linear/exponential density profile for diffusion/convection dominated systems. In our case, the role of convection in the Stern layer is played by conduction, but we will analogously find a linear/exponential in the diffusion/conduction limited regime.

Since the fluid flow is in the positive  $z$  direction, the  $z$  component of the streaming electric field must have the same sign as the surface charge such that no net charge is transported between the two reservoirs. It is convenient to separate the sign and magnitude of the streaming electric field. Thus, we define  $E \equiv -\frac{z\sigma e}{k_B T} \frac{\partial \psi_s}{\partial z}$ , where  $E$  is a positive quantity with dimensions of inverse length that characterises the strength of

the streaming electric field. To solve for  $\sigma(z)$ , we further assume that both  $\rho_{C,s}$  and  $E$  are spatially constant. While this is a valid assumption in simple electrokinetic systems, the numerical calculations of the Chapter 7 have shown that such approximations are no longer valid when both Stern-layer conduction and finite chemical rates are taken into account. Nevertheless, approximating  $E$  and  $\rho_{C,s}$  to be spatially constant allows us to solve for  $\sigma(z)$  and determine  $\rho_e$ ,  $\mathbf{j}_e$  and  $E$ . In principle one could then reinsert the solutions in Eq. (8.11) and obtain an improved  $\sigma(z)$ ,  $\rho_{C,s}$  and  $E$ . However, we will refrain from applying an iterative scheme and aim for an analytical and qualitative understanding of the electrokinetic phenomena.

For a spatially constant  $E$  and  $\rho_{C,s}$ , Eq. (8.11) is straightforward to solve. Since  $z_\sigma^2 = 1$ , we find

$$\sigma(z) = \sigma_{\text{eq}} \left( 1 + a_+ e^{k_+ z} + a_- e^{k_- z} \right), \quad (8.12)$$

with  $a_\pm$  integration constants and  $\sigma_{\text{eq}} \equiv \Gamma(1 + \rho_{C,s}/K)^{-1}$  the equilibrium surface charge density (Langmuir equation, see Section 2.1.3). The wavenumbers  $k_\pm = \frac{1}{2}E \pm \frac{1}{2}\sqrt{E^2 + 4\lambda_{\text{reac}}^{-2}}$  set the relevant lateral length scales, with  $\lambda_{\text{reac}} \equiv \sqrt{D_s \tau_{\text{reac}}}$  (discussed in more detail in Section 8.3), and  $\tau_{\text{reac}} = \left( k^{\text{des}} + k^{\text{ads}} \rho_{C,s} \right)^{-1}$ , the characteristic time scale of the chemical reaction. The amplitudes  $a_\pm$  can be determined by imposing that the surface current vanishes at the endpoints of the charged surface,  $j_\sigma(\pm \frac{1}{2}\ell) = (-D_s \partial_x \sigma + D_s E \sigma)|_{x=\pm \frac{1}{2}\ell} = 0$ . The integration constants  $a_\pm$  are then found to be

$$a_\pm = \frac{E}{k_\mp} \frac{\sinh \frac{1}{2} k_\mp \ell}{\sinh \frac{1}{2} (k_\pm - k_\mp) \ell}. \quad (8.13)$$

Note that  $\sigma(z)$  does not depend on the valency  $z_\sigma$ , that  $E \rightarrow 0$  and  $\sigma(z) \rightarrow \sigma_{\text{eq}}$  in equilibrium. For a non-zero  $E$ , we find a double exponential profile. This reduces to either a linear profile for  $k_\pm \ell \ll 1$ , or a single exponential profile if  $k_\pm \ell \gg 1$ .

The final unknown, the integration constant  $\zeta(z)$ , can be determined using Eq. (8.5), which couples  $\sigma(z)$  to  $\rho_e(0, z)$  (see Appendix C.5), where we used that  $\hat{\mathbf{x}} \cdot \mathbf{j}_C(0, z) = z_C \hat{\mathbf{x}} \cdot \mathbf{j}_e(0, z)$ , since  $\hat{\mathbf{x}} \cdot \mathbf{j}_+(x, 0) = \hat{\mathbf{x}} \cdot \mathbf{j}_-(x, 0) = 0$ . Using the expression for  $\rho_e$ , Eq. (8.10), and  $\sigma$ , Eq. (8.12), we find

$$\zeta(z) = \zeta_{\text{eq}} \left( 1 + a_+ e^{k_+ z} + a_- e^{k_- z} \right). \quad (8.14)$$

Here, we identified the dimensionless equilibrium zeta potential  $\zeta_{\text{eq}} = z_\sigma 4\pi \lambda_B \lambda_D \sigma_{\text{eq}}$  from linear Poisson-Boltzmann theory. Comparing Eq (8.12) with Eq. (8.14), we see

that  $\zeta(z)$  is proportional to the steady state surface charge, and can therefore indeed be interpreted as the steady state zeta potential.

To determine  $E$  in the stationary state, we impose that at any position  $z$  no net current passes through any cross section area. This condition is a direct consequence of the vanishing divergence of  $\mathbf{j}_e$  and the open circuit geometry, hence

$$z_\sigma j_\sigma(z) + \int_0^{\frac{1}{2}H} dx j_{e,z}(x, z) = 0, \quad (8.15)$$

where  $z_\sigma j_\sigma(z)$  is the net charge current through the Stern layer, determined using Eqs. (8.4) and (8.12), and due to symmetry we only need to integrate over half the channel height. Eq. (8.15) is a local condition, and we will in general find  $E$  to depend on  $z$  (see below). This, however, contradicts our previous assumption that  $E$  is spatially constant, and it is at this point that our analytic approach is inconsistent. Nevertheless, the results of this analytic approach allow us to obtain approximate solution which agree qualitatively with the full numerical solutions, and provides us physical insight in the system by identifying three separate regimes.

### 8.3. Three electrokinetic regimes

We identify two physically important length scales, that appear in the definition of the wavenumbers  $k_\pm$ ,

$$\lambda_{\text{reac}} = \sqrt{D_s \tau_{\text{reac}}}; \quad \lambda_{\text{cond}} = \frac{1}{E}. \quad (8.16)$$

We can interpret the first length scale  $\lambda_{\text{reac}}$  as the typical distance a surface charge traverses diffusively during a time  $\tau_{\text{reac}}$ , that is, the typical distance travelled between ad- and desorption. The conductive length scale  $\lambda_{\text{cond}}$  can be interpreted as the distance a monovalent ion needs to travel laterally in order to gain an energy equal to  $k_B T$  due to the streaming electric field. The dynamics of the system is fully determined by the ratios between  $\lambda_{\text{reac}}$ ,  $\lambda_{\text{cond}}$ , and the channel length  $\ell$ .

Alternatively, we can identify an equivalent time scale for each length scale using the surface diffusion constant  $D_s$ . Eq. (8.16) shows that  $\tau_{\text{reac}}$  is the equivalent time scale of  $\lambda_{\text{reac}}$ . By introducing a conductive velocity  $v_{\text{cond}} = D_s E$  and a diffusive velocity  $v_{\text{dif}} = D_s / \ell$ , we can transform  $\ell$  and  $\lambda_{\text{cond}}$  into equivalent time scales,

$$\tau_{\text{dif}} = \frac{\ell}{v_{\text{dif}}} = \frac{\ell^2}{D_s} \quad \tau_{\text{cond}} = \frac{\lambda_{\text{cond}}}{v_{\text{cond}}} = \frac{1}{D_s E^2}. \quad (8.17)$$

We can interpret  $\tau_{\text{dif}}$  as the characteristic time for a Stern-layer charge to diffuse across the channel length, and  $\tau_{\text{cond}}$  as the characteristic time after which a Stern-layer charge has gained one thermal energy unit due to the streaming electric field. Together with  $\tau_{\text{reac}}$ , the three time scales can be used equivalently to the three length scales to characterise the electrokinetic system, as we can express the ratio between every pair of length scales as the ratio between the two equivalent time scales:

$$\frac{\lambda_{\text{reac}}}{\ell} = \sqrt{\frac{\tau_{\text{reac}}}{\tau_{\text{dif}}}}; \quad \frac{\ell}{\lambda_{\text{cond}}} = \sqrt{\frac{\tau_{\text{dif}}}{\tau_{\text{cond}}}}; \quad \frac{\lambda_{\text{cond}}}{\lambda_{\text{reac}}} = \sqrt{\frac{\tau_{\text{cond}}}{\tau_{\text{reac}}}}. \quad (8.18)$$

The three distinct characteristic times allow us to identify three electrokinetic regimes, defined by the smallest time (or associated length). While the three length scales appear naturally in the analytical description, we found it more intuitive to consider the three time scales when considering the different dynamical regimes. In the reaction-dominated regime, characterised by the near-equilibrium of the adsorption/desorption process,  $\tau_{\text{reac}} \ll \tau_{\text{cond}}, \tau_{\text{dif}}$  (and hence  $\lambda_{\text{reac}} \ll \ell, \lambda_{\text{cond}}$ ), to be discussed in Section 8.3.1, we obtain the standard Helmholtz-Smoluchowski picture with a constant surface charge and electric field, except for a region of size  $\lambda_{\text{reac}}$  around the edges at  $z = \pm \frac{1}{2}\ell$ . In the diffusion-dominated regime,  $\tau_{\text{dif}} \ll \tau_{\text{cond}}, \tau_{\text{reac}}$  ( $\ell \ll \lambda_{\text{cond}}, \lambda_{\text{reac}}$ ), discussed in Section 8.3.2, the surface charge is heterogeneous over the entire surface and linear in the lateral position  $z$ . Consequently, the streaming electric field  $E$  is also heterogeneous, but we find that the streaming potential approximately conforms to the Helmholtz-Smoluchowski equation Eq. (7.1). However, in the conduction-dominated regime  $\tau_{\text{cond}} \ll \tau_{\text{reac}}, \tau_{\text{dif}}$  (and hence  $\lambda_{\text{cond}} \ll \lambda_{\text{reac}}, \ell$ ), to be discussed in Section 8.3.3, the Helmholtz-Smoluchowski equation no longer holds, and both  $\sigma$  and  $E$  are heterogeneous and nonlinear functions of  $z$ .

### 8.3.1. Reaction-dominated regime

In the first regime, we consider systems where the chemical reaction rates are the fastest process in the system. In this regime, therefore, we expect to find an equilibrated and thus constant surface charge, and consequently the standard Helmholtz-Smoluchowski equation (7.1). In terms of time scales we have  $\tau_{\text{reac}} \ll \tau_{\text{dif}}, \tau_{\text{cond}}$ , and thus  $\lambda_{\text{reac}} \ll \ell, \lambda_{\text{cond}}$ . It should be noted that, since  $\tau_{\text{cond}}, \tau_{\text{dif}} \propto D_s^{-1}$ , a system without Stern-layer conduction ( $D_s = 0$ ) cannot be diffusion- or conduction-dominated and is in fact always in the reaction-dominated regime. The resulting equations in the reaction-dominated regime do not depend on the ratio  $\lambda_{\text{cond}}/\ell$ , which we can therefore leave unspecified, but they do depend on  $\lambda_{\text{reac}}/\ell$ . In this limit, the wavenumbers can be approximated by  $k_+ = -k_- = \lambda_{\text{reac}}^{-1}$  which simplifies the solution for  $\sigma(z)$ , Eq. (8.12),

the Stern-layer flux  $j_\sigma(z)$  (see Appendix C.5) for the general expression), and the surface charge production rate  $R(z)$ , Eq. (8.5), as

$$\sigma(z) = \sigma_{\text{eq}} \left( 1 + E\lambda_{\text{reac}} \frac{\sinh z/\lambda_{\text{reac}}}{\cosh \frac{1}{2}\ell/\lambda_{\text{reac}}} \right); \quad (8.19)$$

$$j_\sigma(z) = D_s \sigma_{\text{eq}} E \left( 1 - \frac{\cosh z/\lambda_{\text{reac}} - E\lambda_{\text{reac}} \sinh z/\lambda_{\text{reac}}}{\cosh \frac{1}{2}\ell/\lambda_{\text{reac}}} \right) \quad (8.20)$$

$$\approx D_s \sigma_{\text{eq}} E \left( 1 - \frac{\cosh z/\lambda_{\text{reac}}}{\cosh \frac{1}{2}\ell/\lambda_{\text{reac}}} \right); \quad (8.21)$$

$$R(z) = \frac{\sigma_{\text{eq}} E \lambda_{\text{reac}}}{\tau_{\text{reac}}} \frac{\sinh z/\lambda_{\text{reac}}}{\cosh \frac{1}{2}\ell/\lambda_{\text{reac}}}. \quad (8.22)$$

In Figs. 8.1(a) and 8.1(b) we plot  $\sigma(z)$  and  $j_\sigma(z)$ , respectively, for several values of  $\ell/\lambda_{\text{reac}}$  smaller and larger than unity. From  $\lambda_{\text{reac}} \ll \ell$ , we can deduce from Eqs. (8.19)-(8.22) that  $\sigma(z) \approx \sigma_{\text{eq}}$ ,  $j_\sigma(z) \approx D_s \sigma_{\text{eq}} E$  and  $R \approx 0$  for all  $z$  except within a few  $\lambda_{\text{reac}}$  away from  $z = \pm \frac{1}{2}\ell$ . Fig. 8.1 shows this deviation near  $z = \pm \frac{1}{2}\ell$  for both  $\sigma(z)$  and  $j_\sigma(z)$ , which is clearly visible for several values of  $\ell/\lambda_{\text{reac}}$ . This edge effect is a direct result of the boundary condition  $j_\sigma(\pm \frac{1}{2}\ell) = 0$ , that stems from the fact that our surface has finite length. In order for a non-zero  $j_\sigma$  to develop, counter ions must adsorb at the inlet and desorb at the outlet, which is only possible if  $\sigma$  deviates from  $\sigma_{\text{eq}}$ . This explains the heterogeneities of  $\sigma$  shown in Fig. 8.1 that persist even for large  $\ell/\lambda_{\text{reac}}$ . Even in the classical Helmholtz-Smoluchowski setting, a finite Stern-layer conduction implies that at the edges of the surface  $\sigma$  deviates from its equilibrium value. The range of this inhomogeneity is given by  $\lambda_{\text{reac}}$ , as can be seen in Fig. 8.1. Consequently, the Stern-layer current and surface charge profile are constant up to a few  $\lambda_{\text{reac}}$  from the edges of the surface. The amplitude of the relative deviation is, interestingly, given by  $\lambda_{\text{reac}}/\lambda_{\text{cond}}$ . This edge effect exists purely due to the surface charge discontinuity at  $z = \pm \frac{1}{2}\ell$ , but  $\lambda_{\text{reac}}$  is nevertheless not to be confused with the healing length  $\ell_H = HDu$  introduced by Khair and Squires [174], with  $Du$  the Duhkin number (see Section 7.1), which also arises in the absence of Stern-layer conduction.

Imposing a vanishing net current at every position  $z$ , according to Eq. (8.15), we find the streaming electric field  $E$ ,

$$z_\sigma E = \frac{|\partial_z p| \zeta_{\text{eq}} \epsilon}{\eta G_b} \left[ 1 + \frac{1}{H} \frac{D_s \sigma_{\text{eq}}}{D\rho} \right]^{-1}, \quad (8.23)$$

with  $\partial_z p$  a short-hand notation for  $\frac{\partial p}{\partial z}$ . In the reaction-dominated limit, we recover the standard Helmholtz-Smoluchowski equation (7.1) with a spatially constant electric

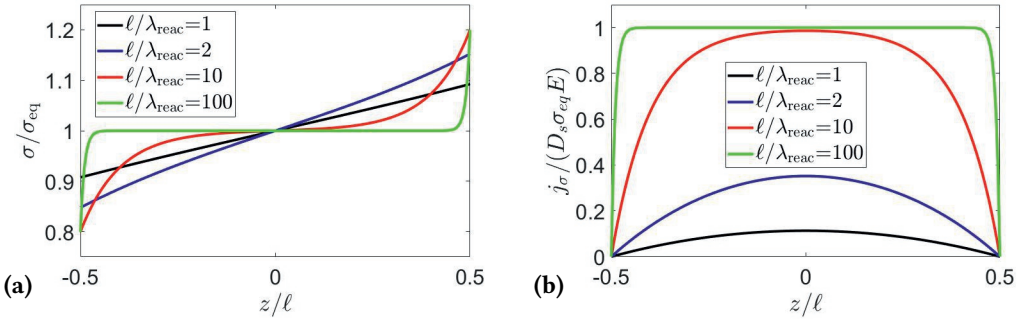


**Figure 8.1.:** Surface charge density  $\sigma(z)$  (a) and Stern-layer current  $j_\sigma(z)$  (b) between channel inlet ( $z = -\frac{1}{2}\ell$ ) and outlet ( $z = \frac{1}{2}\ell$ ), in the limit  $\lambda_{\text{reac}} \ll \lambda_{\text{cond}}$  according to Eqs. (8.19) and (8.21) for varying values of  $\ell/\lambda_{\text{reac}}$ . For (a) we used  $\lambda_{\text{reac}}/\lambda_{\text{cond}} = 0.2$  ( $j_\sigma$  does not depend on this quantity). As  $\ell/\lambda_{\text{reac}}$  decreases, the system leaves the reaction-dominated regime and enters the diffusion-dominated regime (for which  $\lambda_{\text{reac}} \ll \lambda_{\text{cond}}$  holds) and  $\sigma$  and  $j_\sigma$  become increasingly heterogeneous.

field, consistent with our initial assumption. However, just like  $j_\sigma$  and  $\sigma$ ,  $E$  is actually not constant close to the edges and Eq. (8.23) only holds several  $\lambda_{\text{reac}}$  from  $z = \pm\frac{1}{2}\ell$ . The contributions of the edge effect to the streaming potential  $\Delta V_S = \frac{k_B T}{e} \int_{-\frac{1}{2}\ell}^{\frac{1}{2}\ell} dx E$  are negligible (note the antisymmetric nature of the edge effect). Furthermore, we can identify, using Eq. (8.23), the Stern-layer contribution to the surface conduction  $G_s = D_s \sigma_{\text{eq}} e^2 / (k_B T) = G_s^S$ . The latter is proportional to the charge carrier density  $\sigma$  in the Stern layer and a 2D-analogue of the volume conductivity  $G_b = D \rho e^2 / (k_B T)$ . Note that in our calculations, the EDL surface conductivity  $G_s^{\text{EDL}}$ , which originates from the increased ion density in the EDL, does not appear since we assumed that  $\rho$  is spatially constant.

### 8.3.2. Diffusion-dominated regime

In the second dynamic regime, the diffusion time  $\tau_{\text{dif}}$  is the smallest time scale, and the channel length  $\ell$  is the smallest length scale,  $\ell \ll \lambda_{\text{cond}}, \lambda_{\text{reac}}$ . Consequently, this implies that the dimensionless streaming potential  $\frac{e}{k_B T} \Delta V_S \sim E \ell = \ell / \lambda_{\text{cond}}$  is small. Analogous to the Helmholtz-Smoluchowski regime, the ratio between the other two lengths,  $\lambda_{\text{cond}} / \lambda_{\text{reac}}$ , will have no significant impact on the results. We can use Eq. (8.19), which was derived assuming only  $\lambda_{\text{reac}} \ll \lambda_{\text{cond}}$ , by imposing  $\ell \ll \lambda_{\text{reac}}$  to find the

surface charge, flux and chemical production rate as

$$\begin{aligned}\sigma(z) &\approx \sigma_{\text{eq}}(1 + Ez); \\ j_\sigma &\approx \frac{1}{2}D_s\sigma_{\text{eq}}E\frac{\tau_{\text{dif}}}{\tau_{\text{reac}}}\left(1 - \frac{z^2}{\left(\frac{1}{2}\ell\right)^2}\right); \\ R(z) &\approx \frac{\sigma_{\text{eq}}E}{\tau_{\text{reac}}}z.\end{aligned}\tag{8.24}$$

In this parameter regime, we thus recover a linear profile for the surface charge density  $\sigma(z)$  also found numerically in Chapter 7 (Fig. 7.2), and shown here in Fig. 8.1(a). We can intuitively understand this linear profile by realising that the system is diffusion dominated. For a surface with translation invariance in one direction, the steady state would then be given by a linear profile. The linear profile is maintained because the chemical reaction is not fast enough to force  $\sigma$  to the equilibrium value ( $\tau_{\text{reac}} > \tau_{\text{dif}}$ ). Additionally, since  $j_\sigma \propto \tau_{\text{dif}}/\tau_{\text{reac}}$ , the surface flux is very small, as can be observed in Fig. 8.1(b). At steady state, the surface charge profile is therefore determined by a balance between the conduction caused by  $E$  and diffusion in the opposite direction, which explains why the slope of  $\sigma(z)$  is given by the electric field  $E$ . This result is analogous to a diffusion-dominated convection-diffusion problem. Within the diffusion-dominated regime, we obtain from Eq. (8.15) a new expression for the streaming electric field,

$$z_\sigma E(z) = \frac{|\partial_z p| \zeta_{\text{eq}} \epsilon}{\eta G_b} \left[ 1 + |\zeta_{\text{eq}}| \left( \frac{2\lambda_D}{H} - \frac{|\partial_z p| \epsilon}{\eta G_b} z \right) \right]^{-1} = \frac{z_\sigma E^{HS}}{1 - E^{HS} z}.\tag{8.25}$$

Here we introduced  $E^{HS} = \frac{|\partial_z p| |\zeta_{\text{eq}}| \epsilon}{\eta G_b}$ , an inverse length scale proportional to the (magnitude of the) streaming electric field as predicted by the Helmholtz-Smoluchowski equation (7.1) without Stern-layer conduction, with  $\zeta_{\text{eq}}$  the dimensionless equilibrium zeta potential. Note that the solution does not depend on  $D_s$  (except for the restriction that  $\tau_{\text{reac}} \gg \tau_{\text{dif}} \propto D_s^{-1}$ ) due to the vanishing  $j_\sigma$ . The streaming electric field is, similar to  $\sigma(z)$ , heterogeneous. The impact of Stern-layer conduction is thus indirect in this case, and not direct via a charge current ‘leaking’ through the Stern layer as in the reaction-dominated regime. The Stern-layer conduction now allows for a heterogeneous surface charge to develop, which causes the heterogeneity of the channel and all other results discussed here.

The result in Eq. (8.24) agrees qualitatively with the full numerical solutions, where the electric field and surface charge density are smaller at the inlet and larger at the outlet with respect to  $E^{HS}$ , see Fig. 7.2. Both the analytical and numerical solutions

are equal to the Helmholtz-Smoluchowski result in the center ( $z = 0$ ) of the channel. The analytical solution does, however, overestimate the heterogeneity (slope) of  $\sigma(z)$  and  $E(z)$ . The reason for this is that we assumed that the counter ion concentration at the surface,  $\rho_{C,s}$ , does not depend on the surface charge. In reality it does, since an increased surface charge attracts more counter ions. The lack of this regulation mechanism explains the overestimation of the surface charge and electric field.

Eq. (8.25) additionally allows us to derive an expression for the streaming potential,

$$\frac{e}{k_{\text{B}}T} \Delta V_S = - \int_{-\frac{1}{2}\ell}^{\frac{1}{2}\ell} dz \frac{z_\sigma E^{HS}}{1 - E^{HS}z} = z_\sigma \log \left( \frac{1 - \frac{1}{2}E^{HS}\ell}{1 + \frac{1}{2}E^{HS}\ell} \right) \approx \frac{e}{k_{\text{B}}T} \Delta V_S^{HS}, \quad (8.26)$$

where  $\frac{e}{k_{\text{B}}T} \Delta V_S^{HS} \equiv -z_\sigma \ell E^{HS}$  is the streaming potential predicted by the Helmholtz-Smoluchowski. For small  $\Delta V_S$ , which, as we have discussed above, is always the case in the diffusion-dominated regime, we find that the streaming potential can be accurately estimated using the standard Helmholtz-Smoluchowski expression,  $\Delta V_S \approx \Delta V_S^{HS}$ . The lateral heterogeneity therefore has no significant effect on  $\Delta V_S$ . This can be explained by the quasi-antisymmetric profile of  $\sigma(z)$ , and the fact that the streaming potential is a laterally integrated quantity. This, combined with the tendency to measure at the center of the channel, might explain why such lateral heterogeneities have not been observed yet. Note that Eq. (8.26) breaks down for  $|\Delta V_S| \rightarrow 1$ . However, we are in the regime where  $\ell \ll \lambda_{\text{cond}}$ , which implies that  $\frac{e}{k_{\text{B}}T} \Delta V_S \approx E\ell \ll 1$ . The streaming potential will therefore not diverge, but the system will change to a new regime as  $\Delta V_S$  increases. Lastly, we can derive a surprisingly simple expression for the surface charge difference between inlet and outlet in the diffusion-dominated regime,

$$\Delta\sigma \equiv \sigma\left(\frac{1}{2}\ell\right) - \sigma\left(-\frac{1}{2}\ell\right) = \int_{-\frac{1}{2}\ell}^{\frac{1}{2}\ell} dz \partial_z \sigma(z) \approx \frac{e\sigma_{\text{eq}}}{k_{\text{B}}T} \Delta V_S \approx \frac{e\sigma_{\text{eq}}}{k_{\text{B}}T} \Delta V_S^{HS}. \quad (8.27)$$

The streaming potential thus gives the fractional difference in surface charge between the inlet and outlet, providing a good measure of the heterogeneity of the system. Given that in this regime the streaming potential is approximately equal to the Helmholtz-Smoluchowski result, Eq. (8.27) gives an a priori measure of the heterogeneity, although one should keep in mind that in general our results overestimate the actual heterogeneity.

### 8.3.3. The conduction-dominated regime

The third regime, the conduction-dominated regime, is reached when  $\tau_{\text{cond}} (\lambda_{\text{cond}})$  is the smallest time (length) scale,  $\tau_{\text{cond}} \ll \tau_{\text{dif}}, \tau_{\text{reac}}$  (and hence  $\lambda_{\text{cond}} \ll \ell, \lambda_{\text{reac}}$ ), such

that the wavenumbers can be approximated as  $k_+ \approx E_s$  and  $k_- \approx 0$ . Here too, the ratio of the remaining lengths does not impact the results. This allows us to simplify Eq. (8.12) significantly. The surface charge profile is no longer linear or anti-symmetric compared to the equilibrium value  $\sigma_{\text{eq}}$ , but rather exponential, while  $j_\sigma$  vanishes

$$\sigma(z) = \sigma_{\text{eq}} \frac{\frac{1}{2}E\ell}{\sinh \frac{1}{2}E\ell} e^{Ez}, \quad j_\sigma = -D_s \partial_z \sigma + E\sigma = 0. \quad (8.28)$$

It should be noticed that  $j_\sigma$  only vanishes because we assumed a constant  $E$ . However, we have already seen that this is no longer generally the case, and  $j_\sigma$  will in fact not exactly vanish in a fully self-consistent analysis, but this analysis does show that  $j_\sigma$  is small. Our numerical calculations confirm that in this regime, as well as in the diffusion-dominated regime,  $j_\sigma$  is negligible compared to the bulk fluxes (see Fig. 7.2) as the chemical reaction rates are too small for a significant surface flux to develop. Note that the exponential profile Eq. (8.28) is analogous to a convection-dominated convection-diffusion problem. If we take  $\ell \ll \lambda_{\text{cond}}$  ( $E\ell \ll 1$ ), we recover the same linear profile as in the diffusion-dominated regime Eq. (8.24).

To determine  $E$  in the conduction-limited regime we again impose a vanishing net charge current for every  $z$ , Eq. (8.15), from which we obtain the condition

$$\zeta_{\text{eq}} \frac{\frac{1}{2}E\ell}{\sinh E\ell} e^{Ez} \left( 2\lambda_D E - \frac{|\partial_z p| H \epsilon}{\eta G_b} \right) + z_\sigma E H = 0. \quad (8.29)$$

Eq. (8.29) can be solved numerically for  $E(z)$ , and we obtain qualitatively similar behaviour as in the full numerical calculations as shown in Chapter 7 (see Fig. 7.2). In Fig. 8.2 we plot the resulting surface charge profile according to Eqs. (8.28) and (8.29) for several values of the pressure drop across the channel. For small pressure drops, the surface charge profile is roughly linear, corresponding to the diffusion-dominated regime. For larger pressure drops, the profile becomes highly nonlinear, increasing exponentially as  $z$  approaches the outlet position at  $z = \frac{1}{2}\ell$ . The point where the profile crosses the equilibrium surface charge is, contrary to the diffusion-dominated regime, no longer at  $z = 0$ . Our semi-analytical results agree qualitatively but not quantitatively with the numerical calculations presented in Chapter 7. In particular, the surface charge close to  $z = \frac{1}{2}\ell$  is much larger in the semi-analytical results. The reason for this must again reside in the assumption that  $\rho_{C,s}$  is constant, similar to the diffusion-dominated regime.

There is, in fact, one qualitative discrepancy between the numerical calculations and the current analysis. In the numerical calculations the average surface charge decreases with an increasing pressure drop, while Fig. 8.2 shows that the average

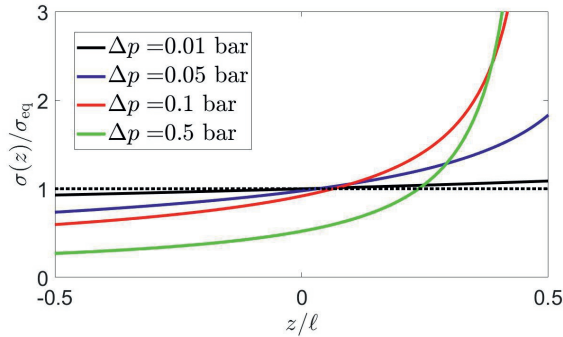


**Figure 8.2.:** Surface charge profile  $\sigma(z)$  induced by the electric field  $E(z)$ , obtained numerically as a solution to Eq. (8.29), for several values of the pressure drop  $\Delta p$ . The profiles cross the equilibrium value at  $z > 0$ , and agree qualitatively with the full numerical solutions of Chapter 7.

surface increases with an increasing pressure drop. The reason for this probably lies again in the missing charge regulation mechanism discussed above, such that the exponential increase of  $\sigma(z)$  greatly overestimates the average surface charge. Consequently, the predicted streaming potential is also overestimated, and cannot be accurately determined in the current analytical approach. The breakdown of the theory is not unexpected in this respect, as our linearised theory and lack of regulation work best for small driving forces. Lastly, we note that multiplying Eq. (8.29) with  $\ell$ , we see that the solution is given in terms of  $E\ell$  rather than  $E$ , if  $\Delta p$  is fixed. Hence, in this regime,  $\sigma$  is invariant under changes in  $\ell$  if  $\Delta p = -\ell\partial_x p$  is fixed, as was in fact also suggested by the numerical solutions.

## 8.4. Summary & conclusion

In this chapter we revealed some consequences of a chemically and physically dynamic Stern layer on electrokinetic phenomena. By allowing the surface charges to diffuse across the Stern layer and by assigning a finite rate to the adsorption and desorption reactions, we showed that a simple electrokinetic system develops novel properties. We identified three dynamical regimes, schematically represented in Fig. 8.3. These regimes can be identified using three time scales (or equivalent lengths): the chemical reaction time scale  $\tau_{\text{reac}} = (k^{\text{des}} + k^{\text{ads}}\rho_{C,s})^{-1}$ , the diffusive time scale  $\tau_{\text{dif}} = \ell^2/D_s$  and the conductive time scale  $\tau_{\text{cond}} = 1/(D_s E^2)$ . Here,  $E = -\frac{e}{k_B T}\partial_z\psi_s$  is proportional to the streaming electric field and with the dimension of inverse length. The particular regime is determined by which of the three time scales is the smaller one. There are

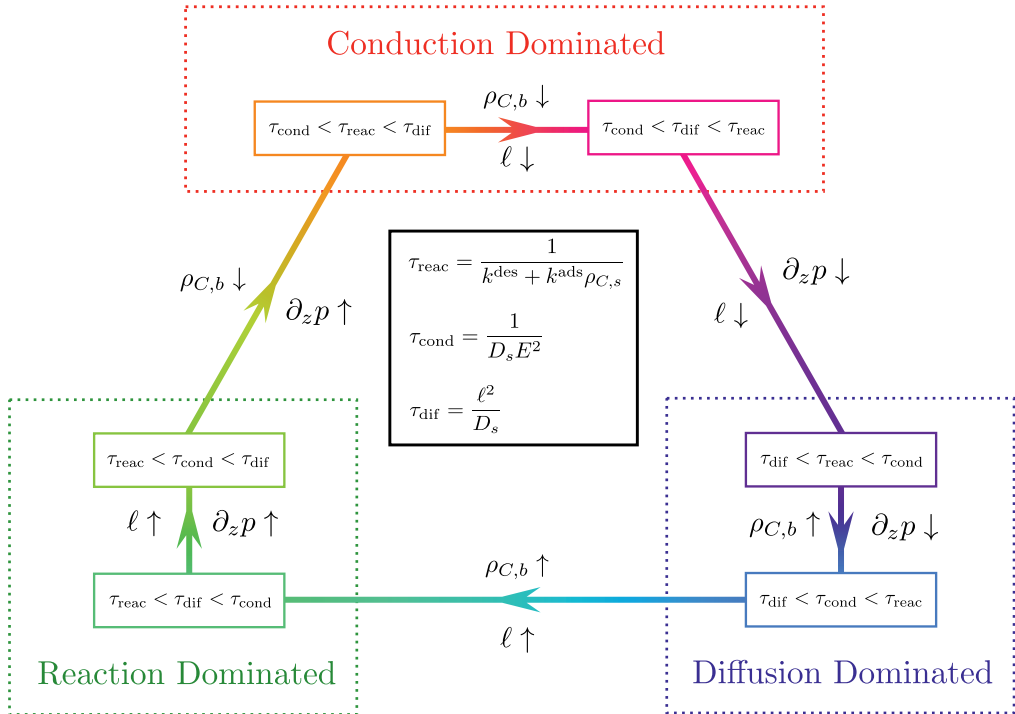


**Figure 8.3.:** Schematic representation of the three regimes and how to transition between them. Each regime is given for each of the 6 possible orderings of the three governing time scales  $\tau_{\text{cond}}$ ,  $\tau_{\text{dif}}$  and  $\tau_{\text{reac}}$ .

three basic parameters to change the regime of the electrokinetic system: the pressure gradient  $\partial_z p$  changes the conduction time  $\tau_{\text{cond}}$  and length  $\lambda_{\text{cond}}$ , the bulk counter ion density (for example, the pH of the solution) alters  $\tau_{\text{reac}}$  and  $\lambda_{\text{reac}}$ , while  $\tau_{\text{dif}}$  varies with  $\ell$ . Note that the bulk ionic strength  $\rho$  is also an experimentally tunable parameter, which has a similar effect as the pressure gradient; increasing  $\rho$  decreases  $E$  and thus increases  $\tau_{\text{cond}}$  and  $\lambda_{\text{cond}}$ . In order to transition between the three regimes, the ordering of the time scales must be changed, which is schematically represented in Fig. 8.3.

The first regime, the reaction-dominated regime, emerges when the chemical reaction rates are the fastest process,  $\tau_{\text{reac}} \ll \tau_{\text{dif}}, \tau_{\text{cond}}$ . Due to the high chemical rates we find a mostly constant surface charge profile, except for a region of size  $\lambda_{\text{reac}}$  away from the ends of the surface. Moreover, we recover the standard Helmholtz-Smoluchowski equation (7.1) for the streaming electric field, from which we can read off an explicit expression for the Stern-layer conductivity. The system falls under the second regime, the diffusion-dominated regime, if  $\ell$  is the smallest length scale,

or equivalently if  $\tau_{\text{dif}}$  is the smallest time scale. In this regime, the system develops a linear surface charge profile equal to the equilibrium value at the middle of the surface. Although the surface charge and thus the streaming electric field are laterally heterogeneous, the resulting streaming potential is within a good approximation equal to the Helmholtz-Smoluchowski expression, the streaming potential in the case of vanishing Stern-layer conductance. For large streaming potential and slow reaction rates,  $\tau_{\text{cond}} \ll \tau_{\text{dif}}, \tau_{\text{reac}}$ , the system reaches the final regime, the conduction-dominated regime. The surface charge profile is then exponential, and is no longer equal to the equilibrium value in the center of the channel. Consequently, the streaming electric field is also exponential, and can be found numerically. In the conduction-dominated regime, the electric field and thus the streaming potential differ significantly from the Helmholtz-Smoluchowski expression.

We believe that this theoretical framework provides both a deeper physical understanding of the processes at work for a dynamic Stern layer, and is able to predict what properties to expect from an experimental setup. A difficulty is the chemical rates, which seem to be unknown for many surface-electrolyte combinations. Perhaps, by exploring the behaviour of the surface charge by altering the pressure drop or system size, our framework might actually provide insight in the numerical values of the chemical rates.

# Appendix A.

## Part I

### A.1. Surface complexation model

In order to describe the experimental data, we use a basic Langmuir-type adsorption model as explained in Section 2.1.3, where we have explained how to set up a Langmuir adsorption isotherm for an arbitrary number of different reactions and reactions steps by posing the problem in terms of adsorption coefficient  $\alpha_i$ . The most general case we consider is the competition between a monovalent ( $\text{Cs}^+$ ) and divalent ( $\text{Ca}^{2+}$ ) for the same adsorption sites, while an anion can coadsorb on either of the adsorbed cations.

As argued in the main text, we must adopt the model such that the total cation coverage is limited to approximately 66%, the maximum occupancy found experimentally. We can incorporate this using the model proposed by Pashley [58], which assigns an area of occupation to an adsorbed cation larger than the area of an adsorption site. This provides the constraint

$$\Gamma (1 - \sigma_{\text{SCs}}A_{\text{Cs}} - \sigma_{\text{SCsCl}}A_{\text{CsCl}} - \sigma_{\text{SCa}}A_{\text{Ca}} - \sigma_{\text{SCaCl}}A_{\text{CaCl}}) = \sigma_{\text{S}}. \quad (\text{A.1})$$

Here,  $\sigma_i$  and  $A_i$  are the areal density of surface group  $i$ , respectively, and  $\Gamma$  is the total areal density of cavities. For simplicity, we will assume that the area occupied by an ion pair is equal to the area occupied by a bare adsorbed ion, i.e.  $A_{\text{Cs}} = A_{\text{CsCl}} = A$ . Defining for simplicity  $a_i \equiv \Gamma A_i$ , we set  $a_{\text{Cs}} = a_{\text{Ca}} \equiv a = \frac{3}{2}$ , which effectively limits the  $\text{Cs}^+$  and  $\text{Ca}^{2+}$  occupancy to  $\frac{2}{3}$ . This reflects the observed limit in  $\text{Cs}^+$  occupancy

measured with surface X-ray diffraction and imposes the same restriction on  $\text{Ca}^{2+}$  due to the mechanism proposed in the main text. The governing equations then become

$$\begin{aligned}
 \frac{\sigma_{\text{SCs}}}{\Gamma} &= \frac{\alpha_{\text{Cs}}}{1 + a \alpha_{\text{Cs}} (1 + \alpha_{\text{CsA}}) + a \alpha_{\text{Ca}} (1 + \alpha_{\text{CaA}})}; & \alpha_{\text{Cs}} &= \frac{\rho_{\text{Cs},s}}{K'_{\text{Cs}}}, \\
 \frac{\sigma_{\text{SCa}}}{\Gamma} &= \frac{\alpha_{\text{Ca}}}{1 + a \alpha_{\text{Cs}} (1 + \alpha_{\text{CsA}}) + a \alpha_{\text{Ca}} (1 + \alpha_{\text{CaA}})}; & \alpha_{\text{Ca}} &= \frac{\rho_{\text{Ca},s}}{K'_{\text{Ca}}}, \\
 \frac{\sigma_{\text{SCsA}}}{\Gamma} &= \frac{\alpha_{\text{Cs}} \alpha_{\text{CsA}}}{1 + a \alpha_{\text{Cs}} (1 + \alpha_{\text{CsA}}) + a \alpha_{\text{Ca}} (1 + \alpha_{\text{CaA}})}; & \alpha_{\text{CsA}} &= \frac{\rho_{\text{A},s}}{K'_{\text{CsA}}}, \\
 \frac{\sigma_{\text{SCaA}}}{\Gamma} &= \frac{\alpha_{\text{Ca}} \alpha_{\text{CaA}}}{1 + a \alpha_{\text{Cs}} (1 + \alpha_{\text{CsA}}) + a \alpha_{\text{Ca}} (1 + \alpha_{\text{CaA}})}; & \alpha_{\text{CaA}} &= \frac{\rho_{\text{A},s}}{K'_{\text{CaA}}}.
 \end{aligned} \tag{A.2}$$

Instead of using the bulk concentrations of the individual ions, we will use the total salinity  $\rho \equiv \rho_{\text{Cs},b} + \rho_{\text{Ca},b} = [\text{Cs}^+] + [\text{Ca}^{2+}]$  and fraction of divalent ions  $f \equiv \rho_{\text{Ca},b}/\rho$ . If  $\text{A}^-$  is the anion of the added salt, the concentration of the anion in the bulk is given by  $\rho_{\text{A},b} = \rho_{\text{Cs},b} + 2\rho_{\text{Ca},b} = (1 + f)\rho$ , but if  $\text{A}^-$  is  $\text{OH}^-$  this concentration is given by  $\rho_{\text{A},b} = 10^{(-14+\text{pH})}\text{M} = 10^{-8.2}\text{M}$  ( $\text{pH} = 5.8$  for all data considered here).

In order to find the equilibrium configuration, we must relate the (dimensionless) surface potential  $\phi_0$  to the surface charge. The surface potential is fixed by the net surface charge, and their relation can be determined within the Poisson-Boltzmann formalism. In Section 2.1.2 we considered the case of a monovalent salt, which must be adjusted since we now have  $\text{Ca}^{2+}$ . Starting from the Poisson-Boltzmann equation (1.3) we find for a  $\text{CaCl}_2/\text{CsCl}$  mixture

$$\frac{\partial^2 \phi}{\partial x^2} = 8\pi\lambda_B \rho \left( (1 - f) \sinh \phi + f (e^\phi - e^{-2\phi}) \right), \tag{A.3}$$

where  $x$  is the direction normal to the surface. Multiplying this equation with  $\frac{\partial \phi}{\partial x}$ , we can integrate this equation once to obtain

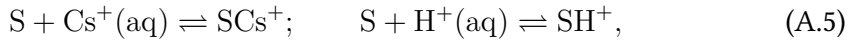
$$\frac{1}{2} \left( \frac{\partial \phi}{\partial x} \right)^2 = 8\pi\lambda_B \left( (1 - f) \cosh \phi + f \left( e^\phi + \frac{1}{2} e^{-2\phi} \right) + C \right), \tag{A.4}$$

where the integration constant  $C = -1 - \frac{1}{2}f$  is chosen such that in the bulk ( $x \rightarrow \infty$ ) both the potential and the electric field vanish. Evaluating Eq. (A.4) at the surface, we can invoke Gauss' law  $e \frac{\partial \phi}{\partial x}(x = 0) = -4\pi\lambda_B \sigma_e$  with  $e\sigma_e = (e\sigma_{\text{Cs}} + 2e\sigma_{\text{Ca}} + e\sigma_{\text{SCaCl}} -$

$e\sigma_{\text{int}}$ ) the net muscovite surface charge, and  $-e\sigma_{\text{int}}$  the intrinsic muscovite surface charge. For given experimental parameters  $f$ ,  $\rho$  and model parameters  $K'_{\text{Cs}}$ ,  $K'_{\text{Ca}}$ ,  $K'_{\text{CsCl}}$  and  $K'_{\text{CaCl}}$ , Eqs. (A.2) and (A.4) form a complete set of equations that can be solved numerically for the surface densities  $\sigma_{\text{Cs}}$ ,  $\sigma_{\text{Ca}}$ ,  $\sigma_{\text{CsCl}}$  and  $\sigma_{\text{CaCl}}$  and the surface potential  $\phi_0$ . We found no evidence that this set of nonlinear equations shows multiple solutions.

## A.2. $\text{Cs}^+/\text{H}^+$ competition model

The main text uses a surface complexation model where the role of  $\text{H}^+$  competition is found not to be needed for a good fit of the data in the parameter range used. Nevertheless, it is the most commonly used surface complexation model, so we discuss here the  $\text{Cs}^+/\text{H}^+$  competition model. In this model, we assume the following two surface complexation reactions



and the resulting equilibrium conditions with  $K'_\text{H}$  the equilibrium constant of the protonation reaction. Here we assume that the intrinsic surface charge of muscovite is equal to half the total adsorption site density,  $-e\sigma_{\text{int}} = -\frac{1}{2}e\Gamma$ , as one would expect. The net surface charge is then obtained as  $e\sigma_e = e\sigma_{\text{SCs}} + e\sigma_{\text{SH}} - \frac{1}{2}e\Gamma$ . To limit the  $\text{Cs}^+$  occupancy to  $\frac{2}{3}$  we take  $a_{\text{Cs}} = \frac{2}{3} = a_{\text{H}}$ . The result presented below is unaltered for  $a_{\text{Cs}} \leq a_{\text{H}} \leq 1$  ( $\text{H}^+$  is smaller than  $\text{Cs}^+$ ). Fig. A.1 shows the best fit of the  $\text{Cs}^+/\text{H}^+$  proton competition model, using  $\text{p}K_{\text{Cs}} = {}^{10}\log K'_{\text{Cs}}(M) = 1.0$  and  $\text{p}K_{\text{H}} = 3.9$ . These fits are, however, statistically and visually not an acceptable reproduction of the data, and therefore, based on the currently presented data, we are forced to reject the  $\text{Cs}^+/\text{H}^+$  competition model. If we exclude the  $\text{Cs}^+$  occupancy data for salinities exceeding 100 mM, the fit parameters do not change significantly.

Since the basic  $\text{Cs}^+/\text{H}^+$  competition model fails to reproduce the experimental data, we also explored an extended model that includes a Stern layer capacitance. This capacitance takes into account that the protons adsorb at a different height compared to the  $\text{Cs}^+$  ions. The region between the protons and the  $\text{Cs}^+$  ions is assumed to be charge neutral. This can effectively be taken into account by shifting

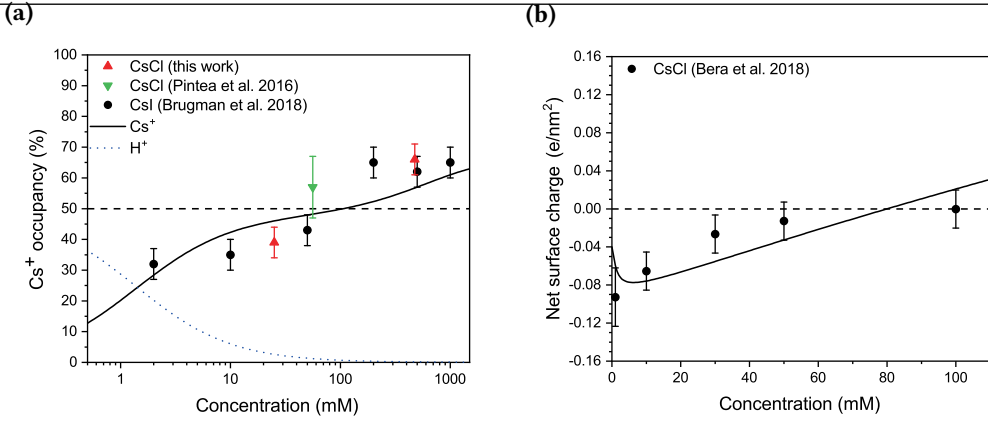


**Figure A.1.:** Best fit results of the Cs<sup>+</sup>/H<sup>+</sup> competition model for (a) the Cs<sup>+</sup> coverage  $\theta_{SCs}$  (black solid line)[72, 73] and proton coverage  $\theta_H$  (blue dotted line) and (b) the net surface charge of the muscovite-electrolyte interface  $e\sigma_e$ , measured by Bera et al. [65]. The horizontal dashed line indicates the occupancy of Cs<sup>+</sup> required to compensate the muscovite negative surface charge. The parameters used are  $pK_{Cs} = 1.0$  and  $pK_H = 3.9$ .

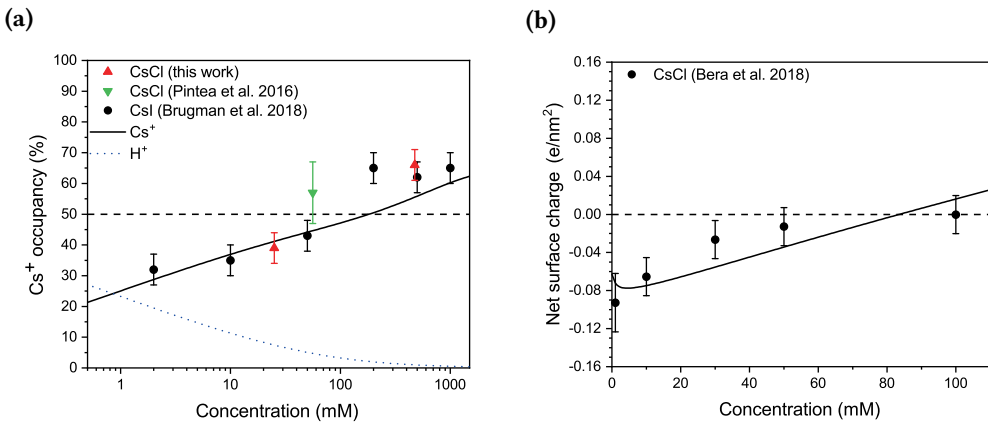


**Figure A.2.:** Best fit results of the Cs<sup>+</sup>/H<sup>+</sup> competition model with a Stern layer capacitance for (a) the Cs<sup>+</sup> coverage  $\theta_{SCs}$  (black solid line)[72, 73] and proton coverage  $\theta_H$  (blue dotted line) and (b) the net surface charge of the muscovite-electrolyte interface  $-e\sigma_e$ , measured by Bera et al. [65]. The horizontal dashed line indicates the occupancy of Cs<sup>+</sup> required to compensate the muscovite negative surface charge. The parameters used are  $pK_{Cs} = 1.4$ ,  $pK_H = 3.0$  and  $C_s = 2.4 \text{ F/m}^2$ .

the Boltzmann distribution (see Eq. (1.2)) for the protons at the surface by  $e\sigma_0/C_s$ , where  $e\sigma_0 = e\sigma_{SH} - \frac{1}{2}e\Gamma$  the surface charge of the muscovite surface (excluding the

contribution from the  $\text{Cs}^+$  ions) and  $C_s$  the Stern layer capacitance,

$$\rho_{\text{H,s}} = \rho_{\text{H,b}} e^{-e/(k_{\text{B}}T)(\psi_0 + \sigma_0/C_s)}, \quad (\text{A.6})$$

with  $\rho_{\text{H,s}}$  and  $\rho_{\text{H,b}}$  the proton concentration at the surface and in the bulk water respectively. The result of the best fit, using  $\text{p}K_{\text{Cs}} = 1.4$ ,  $\text{p}K_{\text{H}} = 3.0$  and  $C_s = 2.4 \text{ F/m}^2$ , is shown in Fig. A.2. Including the Stern capacitance does improve the quality of the fit, but this model does not resolve the issues already apparent without the Stern layer capacitance.

### A.3. Hydroxide coadsorption

We argue in the main text that anion coadsorption is required to fit the experimental data, and use  $\text{Cl}^-$  or  $\text{I}^-$  as the most likely anions. A priori, however, we can not ignore a similar role of  $\text{OH}^-$ . This scenario is discussed here. In the hydroxide coadsorption model we use two adsorption reactions



Note that for this model the reaction  $\text{SCs}^+ + \text{H}_2\text{O} \rightleftharpoons \text{SCsOH} + \text{H}^+$  is equivalent to a  $\text{OH}^-$  adsorption reaction as both reactions result in the same set of equations. We denote the equilibrium constants as  $\text{p}K_{\text{Cs}}$  and  $\text{p}K_{\text{CsOH}}$ , respectively. We can, in principle, also replace  $\text{OH}^-$  with  $\text{HCO}_3^-$  coadsorption. Since both the  $\text{OH}^-$  and  $\text{HCO}_3^-$  concentrations are independent of the salinity, the prediction of either model will be equal, except for the value of the coadsorption reaction constant (due to the different bulk densities of the two anions).

Statistically, the quality of the  $\text{OH}^-$  coadsorption model is slightly better than the  $\text{Cl}^-$  coadsorption model, as can also be visually be observed by comparing Fig. A.3 and Figs. 4.3a and 4.4a from the main text. Physically, however, the  $\text{Cl}^-$  coadsorption model is more likely. The  $\text{OH}^-$  coadsorption constant is very high, a direct consequence of the relatively low  $\text{OH}^-$  concentration at  $\text{pH} = 5.8$ . Such a large  $\text{p}K$  value would imply a strong  $\text{pH}$  dependence, especially at high  $\text{pH}$ , assuming that  $\text{OH}^-$  coadsorption is

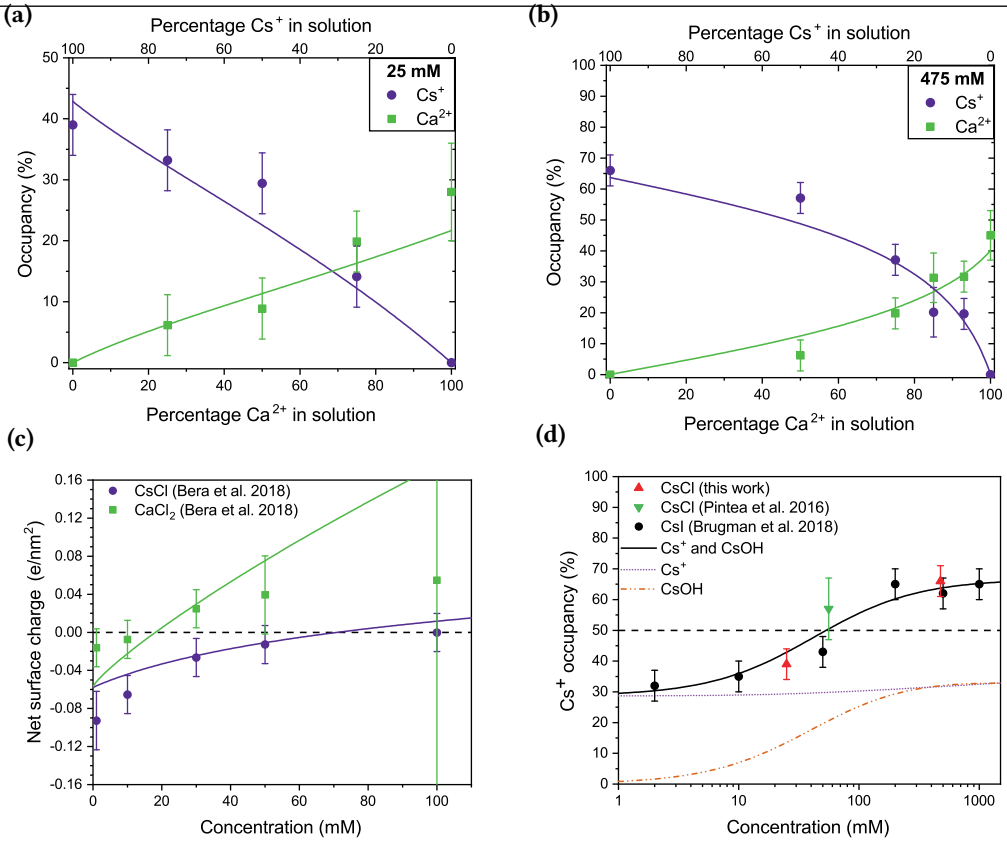


**Figure A.3.:** Cesium (purple) and calcium (green) coverages for (a) 25 mM and (b) 475 mM, (c) the associated net surface charge [65] and (d) the Cs<sup>+</sup> coverage as a function of salinity [72, 73]. The error bars indicate the experimental uncertainty and the purple and green solid lines shows the best fit of the Cs<sup>+</sup>/Ca<sup>2+</sup>/OH<sup>-</sup> model for cesium and calcium respectively. The horizontal dashed line indicates the occupancy of Cs<sup>+</sup> required to compensate the muscovite negative surface charge. The parameters used are  $-\sigma_{\text{int}} = -0.3\Gamma$ ,  $\text{p}K_{\text{Cs}} = 1.3$ ,  $\text{p}K_{\text{CsOH}} = 8.0$ ,  $\text{p}K_{\text{Ca}} = 0.7$  and  $\text{p}K_{\text{CaOH}} = 8.5$ .

reversible. This is in direct contradiction with zeta potential measurements [64, 77, 78, 86]. We should not, however, exclude the possibility that both ions play a role, and that both adsorption reactions could be important.

## A.4. Lateral interaction between adsorbed ions

A possible and common extension of the Langmuir adsorption model is to include a lateral interaction between the adsorbed ions, as has already been discussed in Section 2.1.3. The adsorption energy gained by an adsorbing ion depends in that case on the amount and species of the ions that are already adsorbed, and gives an adjusted Boltzmann equation for the counter ion

$$\alpha_{\text{Cs}} = \frac{\rho_{\text{Cs},s}}{K'_{\text{Cs}}} \exp(-\chi_{\text{Cs}}\theta_{\text{SCs}} - \chi_{\text{CsCa}}\theta_{\text{SCa}}) \quad (\text{A.8})$$

where  $\chi_{\text{Cs}}$  and  $\chi_{\text{CsCa}}$  quantify the interaction strengths between two adsorbed  $\text{Cs}^+$  ions and an adsorbed  $\text{Cs}^+$  and  $\text{Ca}^{2+}$  ion, respectively. Positive values of the interaction parameters correspond to a lateral attraction, negative values correspond to a lateral repulsion. We obtain  $\alpha_{\text{Ca}}$  by exchanging all ‘Cs’ in the subscripts in Eq. (A.8) by ‘Ca’ and vice versa (note that  $\chi_{\text{CsCa}} = \chi_{\text{CaCs}}$ ). The interaction parameters  $\chi_{\text{Cs}}$ ,  $\chi_{\text{Ca}}$  and  $\chi_{\text{CsCa}}$  can then be treated as additional fit parameters. Non-zero interaction parameters have in general a noticeable but no great impact on the best fit, which prevents us from obtaining definite values for the interaction parameters. We can, however, identify some general trends from these fits. For example, a positive value (i.e. a lateral attraction) of  $\chi_{\text{Cs}}$  tends to decrease the quality of the fit, while a negative value (repulsion) tends to increase the quality of the fit. Conversely, a positive value of  $\chi_{\text{Ca}}$  tends to slightly increase the quality of the fit. The best fit is obtained, however, is a lateral repulsion between adsorbed  $\text{Cs}^+$  and  $\text{Ca}^{2+}$  ions. Fig. A.4 shows the result for the best fit with  $\chi_{\text{Cs}} = 0 = \chi_{\text{Ca}}$  and  $\chi_{\text{CaCs}} = -6$ . This short analysis suggests that the adsorbed cations do not mix well, although we cannot make a definitive statement based on the current data alone.

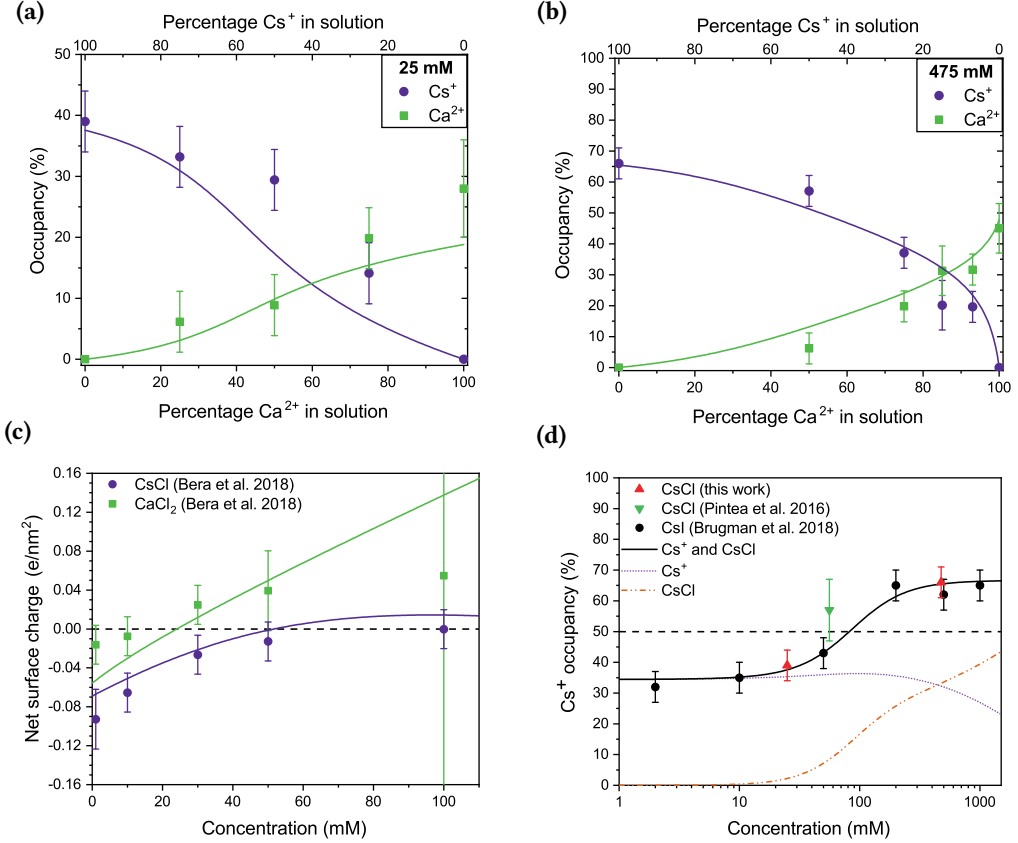


**Figure A.4.:** Cesium (purple) and calcium (green) coverages for (a) 25 mM and (b) 475 mM, and (c) the associated net surface charge [65] and (d) the Cs<sup>+</sup> coverage as a function of salinity. [72, 73] The error bars indicate the experimental uncertainty and the purple and green solid lines shows the best fit of model including lateral interactions for cesium and calcium respectively. The horizontal dashed line indicates the occupancy of Cs<sup>+</sup> required to compensate the muscovite negative surface charge. The parameters used are  $-\sigma_{\text{int}} = -0.36\Gamma$ ,  $\text{p}K_{\text{Cs}} = 1.3$ ,  $\text{p}K_{\text{CsCl}} = 0.7$ ,  $\text{p}K_{\text{Ca}} = 1.0$  and  $\text{p}K_{\text{CaCl}} = 0.5$ ,  $\chi_{\text{Cs}} = \chi_{\text{Ca}} = 0$  and  $\chi_{\text{CaCs}} = -6$ .

# Appendix B.

## Part II

### B.1. Poisson-Boltzmann identities

For the calculation of  $\mathbf{L}$  we assume that channel radius  $R$ , is significantly larger than the Debye length. This allows us to significantly simplify the equations in cylindrical coordinates for quantities evaluated close to the surface. In this case, we make a coordinate transformation  $s = R - r$  such that

$$\nabla^2 f = \frac{1}{r} \frac{\partial}{\partial r} \left( r \frac{\partial f}{\partial r} \right) \approx \frac{\partial^2 f}{\partial s^2}, \quad \int_0^R dr 2\pi r f(r) \approx 2\pi R \int_0^R ds f(s), \quad (\text{B.1})$$

for any function  $f(r)$  that only takes non-zero values inside the EDL. Therefore, if we are only considering quantities inside the EDL all calculations are basically the same if we consider a cylinder or parallel plate geometry, except for a prefactor. The parallel plate expressions can be found by simply substituting  $\pi R \rightarrow H$ , with  $H$  the plate separation. The error for the cylindrical geometry is of the order of  $\lambda_D/R$ , but for the parallel plate geometry the only error occurs as soon as the EDL overlap.

The equilibrium Poisson-Boltzmann expressions for a 1:1 salt that we assume to hold for the electric double layer can be found in Section 2.1.2. Next, we define a set of integrals as a function of the EDL potential which we encounter in the calculation of the Onsager coefficients. Each of these integrals are defined such they are positive, where  $\kappa = \lambda_D^{-1}$  is the inverse Debye length,  $\sigma$  the density of surface charges,  $z_s$  the sign

of the surface charge,  $\phi_0$  the dimensionless surface potential and  $\sigma^* = (2\pi\lambda_B\lambda_D)^{-1}$ ,

$$\begin{aligned}
 P_1 &= \frac{z_s}{\lambda_D} \int_0^\infty ds \phi(s) = 2(\text{Li}_2(|\gamma|) - \text{Li}_2(-|\gamma|)) \\
 P_2 &= \frac{1}{\lambda_D} \int_0^\infty ds (\cosh \phi(s) - 1) = 2(\cosh \frac{1}{2}\phi_0 - 1) = \frac{\sqrt{\sigma^{*2} + \sigma^2} - \sigma^*}{2\rho_s\lambda_D} \\
 P_3 &= \frac{1}{\lambda_D^2} \int_0^\infty ds s (\cosh \phi(s) - 1) = 4 \log \cosh \frac{1}{4}\phi_0, \\
 P_4 &= \frac{1}{\lambda_D^3} \int_0^\infty ds s^2 (\cosh \phi(s) - 1) = 2\text{Li}_2(\gamma^2) \\
 P_5 &= -\frac{z_s}{\lambda_D} \int_0^\infty ds (\phi - \phi_0)(\cosh \phi - 1) = 2z_s \left( 2 \sinh \frac{1}{2}\phi_0 - \phi_0 \right) = 4 \frac{|\sigma|}{\sigma^*} - 2|\phi_0|, \\
 P_6 &= -\frac{1}{\lambda_D} \int_0^R ds (\cosh \phi - 1) \log(1 - \gamma^2 e^{-\kappa s}) = 2P_3 \cosh^2 \frac{1}{4}\phi_0 - P_2 \\
 P_3 P_2 - 2P_6 &= 2P_2 - 4P_3
 \end{aligned} \tag{B.2}$$

The first integral  $P_1$  can be solved by rewriting  $\phi(s)$  in terms of the polylogarithmic function  $\text{Li}_1$ , and for the integrals  $P_2$ - $P_6$  we can use the Poisson-Boltzmann identities

$$\begin{aligned}
 \phi(s) &= 2 \log \frac{1 + \gamma e^{-\kappa s}}{1 - \gamma e^{-\kappa s}} = -\text{Li}_1(\gamma e^{-\kappa s}) + \text{Li}_1(-\gamma e^{-\kappa s}), \\
 2(\cosh \phi - 1) &= \frac{\rho_+ + \rho_- - 2\rho_s}{\rho_s} = \frac{4\gamma e^{-\kappa s}}{(1 - \gamma e^{-\kappa s})^2} - \frac{4\gamma e^{-\kappa s}}{(1 + \gamma e^{-\kappa s})^2}.
 \end{aligned} \tag{B.3}$$

## B.2. Symmetry Onsager matrix

Regardless of the origins of  $\mathbf{L}$ , the definition of  $\mathbf{L}$  with the excess salt flux  $J_{\text{exc}} = J - 2\rho_s Q$  instead of the total salt flux  $J$  ensures that  $\mathbf{L}$  is symmetric. The Onsager matrix is namely symmetric only if the flux and the associated driving force are congruent, such that the product of the flux and the driving force gives the dissipation

rate due to that flux [50–52]. We can write the dissipation rate  $T\dot{S}$  as [52]

$$T\dot{S} = - \sum_{i=0}^2 j_i \Delta\nu_i, \quad (\text{B.4})$$

where  $\Delta\nu_i$  is the total electrochemical potential difference of the  $i$ th species between the two reservoirs and  $i = 0$  for the solvent,  $i = 1$  for the cation and  $i = 2$  for the anion. We can write down the electrochemical potential of the ions as

$$\Delta\nu_i = v_i \Delta p + \Delta\mu_i + z_i e \Delta V, \quad (\text{B.5})$$

with  $v_i$ ,  $\rho_i$  and  $z_i$  the volume of a particle, the density and the valency of species  $i$ ,  $\Delta p$  the pressure drop,  $\Delta V$  the voltage drop and  $\Delta\mu_i = k_B T \Delta(\log \rho_i)$  the chemical potential drop across the channel. Note that  $\Delta\mu_1 = \Delta\mu_2$  due to the charge neutrality of the reservoirs. We assume the solvent to be incompressible, and therefore we can write the partial solvent pressure  $\Delta p_0$  as

$$\Delta\nu_0 = v_0 \Delta p_0. \quad (\text{B.6})$$

Now we can use van 't Hoff's law to write the total pressure  $p$  as

$$p = p_0 + \Pi = p_0 + 2\rho_s k_B T, \quad (\text{B.7})$$

with  $\Pi$  the partial solute pressure. Note that in equilibrium,  $p$  is constant even if  $\Pi$  is not. Now we can write the dissipation rate as

$$\begin{aligned} T\dot{S} &= -j_0 v_0 \Delta p_0 - (j_1 v_1 + j_2 v_2) \Delta p - J \Delta\mu - I \Delta V, \\ &= -Q \Delta p + j_0 v_0 \Delta\pi - J \Delta\mu - I \Delta V, \end{aligned} \quad (\text{B.8})$$

where we have defined the volume flux  $Q = j_0 v_0 + j_1 v_1 + j_2 v_2$ , solute or salt flux  $J = j_1 + j_2$ , charge flux  $I = e(j_1 - j_2)$  and chemical potential drop  $\Delta\mu = k_B T \Delta(\log \rho_s)$  (equal for both ions due to charge neutrality in the bulk). For dilute solutions we have

that  $Q \approx j_0 v_0$ , and we can rewrite

$$\begin{aligned} T\dot{S} &= -Q\Delta p + 2k_B T Q \Delta\rho_s - J\Delta\mu - I\Delta V \\ &= -Q\Delta p - J_{\text{exc}}\Delta\mu - I\Delta V, \end{aligned} \quad (\text{B.9})$$

where we have identified the excess salt flux  $J_{\text{exc}}$

$$J_{\text{exc}} = J - 2k_B T Q \frac{\Delta\rho_s}{\Delta\mu}. \quad (\text{B.10})$$

In order for  $\mathbf{L}$  to be symmetric,  $J_{\text{exc}}$  is congruent to  $\Delta\mu$ . Additionally, (B.10) shows how to obtain the total salt flux  $J$  from the excess salt flux  $J_{\text{exc}}$  even if  $\Delta\mu \neq 0$ . Note that

$$\lim_{\Delta\rho_s \rightarrow 0} k_B T \frac{\Delta\rho_s}{\Delta\mu} = \lim_{\Delta\rho_s \rightarrow 0} k_B T \frac{\Delta\rho_s}{\log\left(1 + \frac{\Delta\rho_s}{\rho_1}\right)} = \rho_s, \quad (\text{B.11})$$

with  $\Delta\rho_s = \rho_2 - \rho_1$  the salinity drop over the channel.

### B.3. Derivation $\mathbf{G}^{\text{vol}}$

The volume contributions of the Onsager matrix are given by

$$\mathbf{L}^{\text{vol}} = \begin{pmatrix} L_{11} & 0 & 0 \\ 0 & me^2\rho_s & me\beta\rho_s \\ 2\rho_s L_{11} & 2(me\beta + L_{12})\rho_s & 2(m + L_{13})\rho_s \end{pmatrix}, \quad (\text{B.12})$$

with  $m = \frac{D_+ + D_-}{2k_B T}$  the salt mobility, with the inverse

$$\left(\mathbf{L}^{\text{vol}}\right)^{-1} = \begin{pmatrix} \frac{1}{L_{11}} & 0 & 0 \\ -\frac{L_{11}}{\beta} & -\frac{m + L_{13}}{2meB} \frac{1}{\rho_s(z)} & \frac{\beta}{2B} \frac{1}{\rho(z)} \\ \frac{e}{B} & \frac{\beta(me + L_{12})}{2meB} \frac{1}{\rho_s(z)} & -\frac{e}{2B} \frac{1}{\rho_s(z)} \end{pmatrix}. \quad (\text{B.13})$$

with  $B = \beta^2(me + L_{12}) - e(m + L_{13})$  a constant. Given a linear  $\rho_s(z) = \rho_1 + \frac{z}{\ell}\Delta\rho$ , with  $\Delta\rho = \rho_2 - \rho_1$ , we have that

$$\int_0^\ell dz \frac{1}{\rho_s(z)} = \ell \frac{\log \frac{\rho_2}{\rho_1}}{\Delta\rho}, \quad (\text{B.14})$$

and we find  $(\Delta\mu = k_B T \log \frac{\rho_2}{\rho_1})$

$$\mathbf{G}^{\text{vol}} = \begin{pmatrix} L_{11} & 0 & 0 \\ 0 & 2De^2 \frac{\Delta\rho}{\Delta\mu} & 2De \frac{\Delta\rho}{\Delta\mu} \beta \\ \frac{k_B T \Delta\rho}{\Delta\mu} L_{11} & 2(De + k_B T L_{12}) \frac{\Delta\rho}{\Delta\mu} \beta & 2(D + k_B T L_{13}) \frac{\Delta\rho}{\Delta\mu} \beta \end{pmatrix} \quad (\text{B.15})$$

## B.4. Entrance effects

As mentioned in the main text, the salinity at both ends of the channel are not equal to the salinities imposed on the bulk,  $\rho_{\text{max}}$  and  $\rho_{\text{min}}$ . The effect is not necessarily strong, but a small change in especially the low salinity can have a significant effect on the (local) conductivity. It is therefore important to take these entrance effects into account, and the predictions are indeed much more accurate if we do. We cannot solve for the concentration profile exactly (due to the complicated fluid flow and electrostatic potential profile), but we can get a good estimate by assuming that the concentration profile outside the channel drops off over a typical distance  $R$ . Since the diffusion equation has no intrinsic length scale, the geometric length  $R$  should characterise the concentration gradients outside the channel. Therefore we approximate

$$\rho_{\text{out}} \approx \rho_{\text{min}} + R \partial_z \rho_s, \quad \rho_{\text{in}} \approx \rho_{\text{max}} - R \partial_z \rho_s, \quad (\text{B.16})$$

where  $\rho_{\text{out}}$  is the salinity at the outlet (low salinity side) and  $\rho_{\text{in}}$  the salinity at the entrance (high salinity side). Note that the salinity gradient must be expressed in terms of  $\rho_{\text{out}}$  and  $\rho_{\text{in}}$ ,  $\partial_z \rho_s = \frac{\rho_{\text{out}} - \rho_{\text{in}}}{\ell}$  which we can plug into Eq. (B.16) and solve for  $\rho_{\text{out}}$

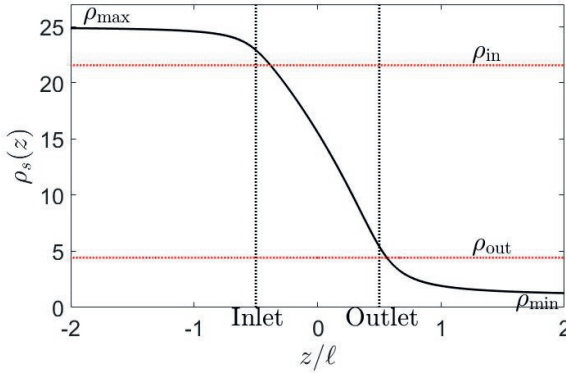


**Figure B.1:** Density profile at the axis of the channel calculated with FEM (black full line) for  $R = 60$  nm and  $\ell = 300$  nm. The dashed red lines indicate the inlet and outlet salinity  $\rho_{\text{in}}$  and  $\rho_{\text{out}}$ , and the black dashed lines indicate the location of the inlet ( $z = -\frac{1}{2}\ell$ ) and outlet ( $z = \frac{1}{2}\ell$ ).

and  $\rho_{\text{in}}$  to find

$$\rho_{\text{out}} \approx \rho_{\text{min}} + \frac{R}{\ell + 2R} \Delta\rho, \quad \rho_{\text{in}} \approx \rho_{\text{max}} - \frac{R}{\ell + 2R} \Delta\rho, \quad (\text{B.17})$$

where  $\Delta\rho = \rho_{\text{max}} - \rho_{\text{min}}$  is the imposed salinity drop across the channel. As has been shown in the main text, the entrance effects are relevant even for needle-shaped channels. As the aspect ratio increases, however, the entrance effects become even stronger. For example, Fig. B.1 shows the entrance effects for a channel with  $R = 60$  nm and  $\ell = 300$  nm. Here we see that  $\rho_{\text{in}}$  is almost a factor 5 larger than  $\rho_{\text{min}}$ , significantly affecting the total conductivity.

## B.5. Simulation domain

For each simulation domain use the boundary conditions.

- 1 (Red) Axis of rotational symmetry. All normal derivatives and velocities are zero,  $\mathbf{n} \cdot \nabla \rho_i = 0 = \mathbf{n} \cdot \nabla \psi = \mathbf{n} \cdot \mathbf{u}$
- 2 (Dark blue) Inlet reservoir, where we fix the pressure  $p = \Delta p$ , salinities  $\rho_{\pm} = \rho_{\text{max}}$  and potential  $\psi = \Delta V$

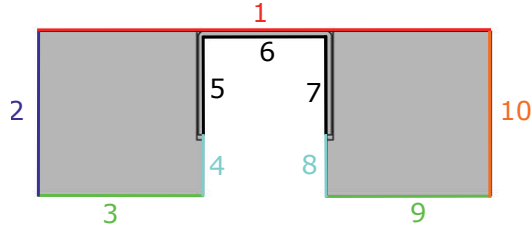


**Figure B.2.:** Domain on which the governing equations are solved numerically with the boundaries marked (boundary conditions explained in the text).

- 3,9 (Green) To simulate an infinite bulk, we impose no-slip boundary conditions  $u_z = 0$  on the side of the bulk if  $\Delta p \neq 0$ , and otherwise an open boundary (force free boundary), and impose a fixed salinity ( $\rho_{\pm} = \rho_{\max}$  for 3 and  $\rho_{\pm} = \rho_{\min}$  for 9).
- 4,8 (Cyan) Hard walls with slip boundary condition  $\mathbf{n}_s \cdot \nabla \mathbf{u}_t = b\mathbf{u}_t$  (with  $\mathbf{u}_t$  the tangential component of the velocity), zero-charge  $\mathbf{n} \cdot \nabla \psi = 0$  and no-flux boundary conditions,  $\mathbf{n} \cdot \mathbf{J}_i = 0$
- 5,6,7 (Black) The charged wall. The same boundary conditions as 4/8 except for a charged boundary condition  $\mathbf{n} \cdot \nabla \psi = -\frac{\sigma}{\epsilon}$ , with  $\epsilon$  the permittivity and the surface charge  $\sigma$  determined by the wished boundary condition (constant charge, charge regulation etc.).
- 10 (Orange) Outlet reservoir,  $\rho_{\pm} = \rho_{\min}$ ,  $\psi = 0$  and an open-boundary condition for the fluid.

## B.6. Validation theory: parameter variation

Below we will show the validation of the presented theories under a constant charge boundary condition, for the diffusio-osmotic current  $I_{\text{DO}}$ , average fluid velocity  $\bar{u} = \frac{Q_{\text{DO}}}{\pi R^2}$  and salt flux  $J_{\text{DO}}$ , for both an open- and closed-circuit condition. The red line represents the FEM results, the blue line the analytic approach (Eq. 5.12), the black line exact approach (Eq. 5.9). The uncertainty of  $I_{\text{DO}}$  increases with  $\rho_{\max}/\rho_{\min}$ , and is typically of the order of a few pico Ampères for  $\rho_{\max}/\rho_{\min} = 25$ . We furthermore compare the numerical solutions and the predictions by **G** for  $\rho_{\min} = 20$  mM and  $b = 10$  nm.

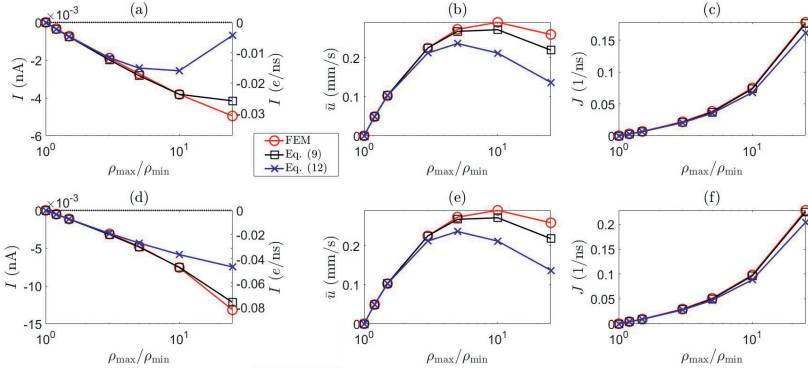


**Figure B.3.:** NaCl (a)-(c) KCl (d)-(f),  $z_{\sigma}\sigma = -0.05 e/\text{nm}^2$ ,  $R = 30 \text{ nm}$ ,  $\ell = 1.5 \mu\text{m}$ ,  $b=0 \text{ nm}$ , and  $\rho_{\min} = 1 \text{ mM}$ .

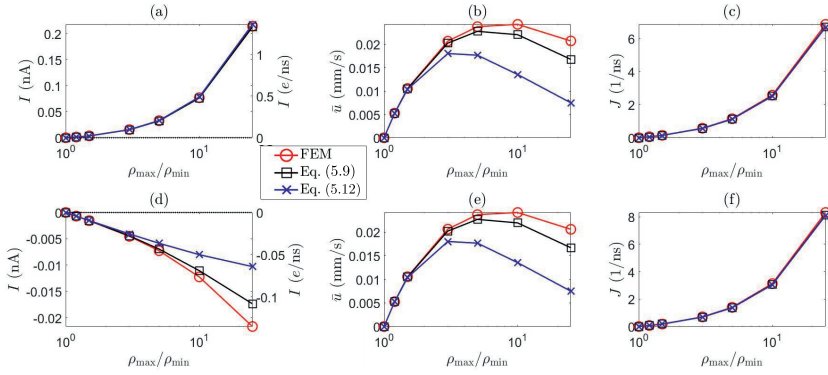


**Figure B.4.:** NaCl (a)-(c) KCl (d)-(f),  $z_{\sigma}\sigma = -0.05 e/\text{nm}^2$ ,  $R = 60 \text{ nm}$ ,  $\ell = 1.5 \mu\text{m}$ ,  $b=0 \text{ nm}$ , and  $\rho_{\min} = 20 \text{ mM}$ .

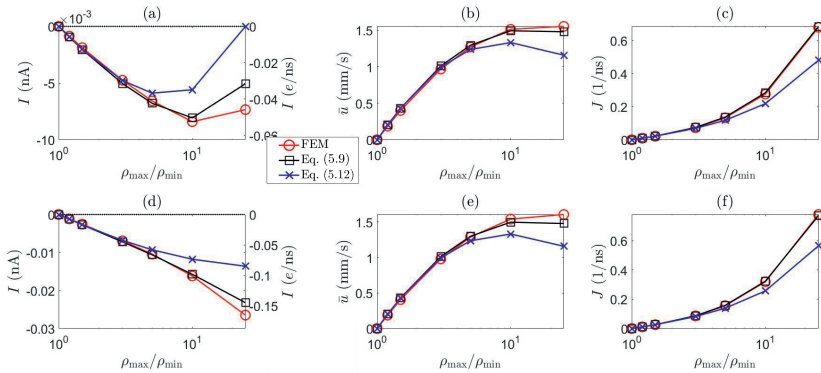


**Figure B.5.:** NaCl (a)-(c) KCl (d)-(f),  $z_{\sigma}\sigma = -0.05 e/\text{nm}^2$ ,  $R = 60 \text{ nm}$ ,  $\ell = 1.5 \mu\text{m}$ ,  $b=10 \text{ nm}$ , and  $\rho_{\min} = 1 \text{ mM}$ .

# Appendix C.

## Part III

### C.1. Current of surface charges

We consider a system consisting of bulk (region  $\mathcal{R}$ ) and a surface (given by a region  $\mathcal{S}$ , with bulk ions (densities  $\rho_i(\mathbf{r})$ , with  $\mathbf{r} \in \mathcal{R}$ ) and surface ions (surface densities  $\sigma(\mathbf{r}_s)$ , with  $\mathbf{r}_s \in \mathcal{S}$ ) that are bound to  $\mathcal{S}$  via a chemical reaction. Here  $i$  labels the bulk ion species. The total free energy functional is a combination of a bulk and surface contribution  $\mathcal{F}[\{\rho_i\}, \sigma] = \mathcal{F}_b[\{\rho_i\}] + \mathcal{F}_s[\sigma]$ , see Eq. (2.4) and Eq. (2.22) ( $\chi = 0$ ).

$$\begin{aligned}\mathcal{F}_b &= k_B T \sum_i \int_{\mathcal{R}} d^3 \mathbf{r} \rho_i(\mathbf{r}) [\log(\rho_i(\mathbf{r}) \Lambda_i^3) - 1] + \frac{1}{2} \int_{\mathcal{R}} d^3 \mathbf{r} \rho_e(\mathbf{r}) \phi(\mathbf{r}), \\ \mathcal{F}_s &= k_B T \int_{\mathcal{S}} d^2 \mathbf{r}_s \left[ \sigma(\mathbf{r}_s) \log\left(\frac{\sigma(\mathbf{r}_s)}{\Gamma}\right) + (\Gamma - \sigma(\mathbf{r}_s)) \log\left(1 - \frac{\sigma(\mathbf{r}_s)}{\Gamma}\right) \right] \\ &\quad + \frac{1}{2} z_\sigma \int_{\mathcal{S}} d^2 \mathbf{r}_s \sigma(\mathbf{r}_s) \phi(\mathbf{r}_s).\end{aligned}\tag{C.1}$$

with  $\phi(\mathbf{r}, t) = e\psi(\mathbf{r}, t)/(k_B T)$  the dimensionless electrostatic potential,  $\rho_e = \sum_i z_i \rho_i$  the volumetric local charge density,  $\Gamma$  the surface density of chargeable sites and  $z_\sigma$  the valency of the surface charges. There is no free energy of binding included ( $g = 0$  in Eq. (2.22)), which is accounted for by the ad- and desorption rates  $k^{\text{ads}}$  and  $k^{\text{des}}$  in the continuity equation (7.3). We can use the formalism of Dynamic Density Functional Theory of the dissolved ions, as discussed Section 2.2.1, for the surface charges. We

can thus find the current of surface charges  $j_\sigma$  as the 2D analogue of Eq. 2.27,

$$\begin{aligned} \mathbf{j}_\sigma(\mathbf{r}_s, t) &= -D_s \sigma(\mathbf{r}_s, t) \nabla_S \left( \frac{\delta \beta \mathcal{F}_s[\sigma]}{\delta \sigma(\mathbf{r}_s)} \Big|_{\sigma(\mathbf{r}_s, t)} \right) \\ &= -D_s \left( \frac{\Gamma \nabla_S \sigma(\mathbf{r}_s, t)}{\Gamma - \sigma(\mathbf{r}_s, t)} + z_\sigma \sigma(\mathbf{r}_s, t) \nabla_S \phi(\mathbf{r}_s, t) \right), \end{aligned} \quad (\text{C.2})$$

where we introduced the diffusion coefficient  $D_s$  for the charges in the Stern layer.

## C.2. Simulation domain

We solved the governing (7.2) in a geometry shown in Fig. C.1. This domain is two dimensional because we have translation symmetry in the  $y$  direction. Since the system is symmetric in the plane at  $x = \frac{1}{2}H$ , only half of the system has to be included in the calculations. The boundary condition on this plane is thus that all normal derivatives vanish.

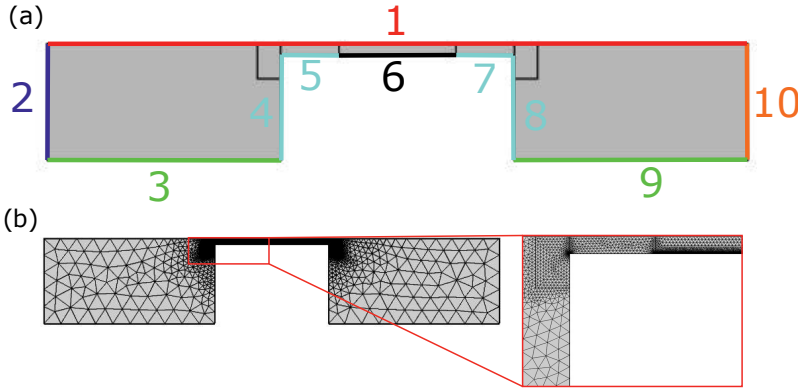


**Figure C.1.:** Domain on which the governing equations are solved numerically: (a) domain with the boundaries marked (boundary conditions explained in the text and (b) a representation of the typically used mesh. The system size used is  $H = 1 \mu\text{m}$  and  $\ell = 5 \mu\text{m}$ .

For each simulation domain we can write down the boundary conditions.

- 1 (Red) All normal derivatives and velocities are zero,  $\mathbf{n} \cdot \nabla \rho_i = 0 = \mathbf{n} \cdot \nabla \psi = \mathbf{n} \cdot \mathbf{u} = 0$

- 2 (Dark blue) Inlet reservoir, where we fix the pressure  $p = \Delta p$ , salinities  $\rho_{\pm} = \rho_s$ ,  $\rho_C = \rho_{C,b}$  and potential  $\psi = 0$
- 3,9 (Green) To simulate an infinite bulk, we impose slip boundary conditions  $u_x = 0$  on the side of the bulk (in order to prevent fluid escaping via these surfaces), and impose a zero-flux boundary condition  $\hat{\mathbf{x}} \cdot \mathbf{j}_i = 0$  for the ion fluxes.
- 4,5,7,8 (Cyan) Hard walls with no-slip and no-flux boundary conditions,  $\mathbf{u} = 0$  and  $\mathbf{n} \cdot \mathbf{j}_i = 0$
- 6 (Black) The charged wall. The same boundary conditions for  $\rho_{\pm}$ , and  $\mathbf{u}$  as 4/5/7/8, but for the counter ion we impose the chemical rate equation  $\mathbf{n}_s \cdot \mathbf{j}_C = -R$  with  $R$  given by Eq. (7.5), and for  $\psi$  we impose Gauss' law as in Eq. (7.2).
- 10 (Orange) Outlet reservoir. To simulate an infinite bulk we impose that all diffusive fluxes and the electric field are zero,  $\mathbf{n} \cdot \nabla \rho_i = 0 = \mathbf{n} \cdot \nabla \psi$ , while we fix  $p = 0$ .

In order to solve for the surface charge density  $\sigma$ , we couple this two dimensional domain to a one dimensional domain where we solve the governing equations for  $\sigma$ , Eqs. (C.2)-(7.5). This coupling can be achieved by the general (or linear) extrusion operator of COMSOL, which projects the value of  $\rho_{C,s}$  from the 2D geometry on the 1D geometry, and the value of  $\sigma$  from the 1D geometry on the 2D geometry. The additional boxes created at the entrance and exit of the channel help to refine the mesh in these regions, where a finer mesh is needed than in the in- and outlet reservoirs (see Fig. C.1). At the former, mesh elements should be no larger than  $0.1H$ , and at the corner we chose a slightly refined mesh to reduce numerical inaccuracies. Furthermore, at boundary 6 a very fine mesh is required as the full Electric Double Layer must be resolved (since  $\rho_{C,s}$  must be determined with accuracy at the surface). In the double layer, a grid of no fewer than 8 points per Debye length was required for consistently reliable results, although the specific grid might vary with system size. This mesh smoothly transitions to the coarser mesh away from the charged surface towards the center of the channel. For typical values of  $H = 1\mu\text{m}$  and  $\ell = 30\mu\text{m}$ , this results in a number of grid points of the order of  $10^5$  and a calculations time of the order of an hour for the full dynamical calculations and a typical desktop computer. This includes equilibration, transition to steady state upon application of pressure pulse and

re-equilibration after the pressure drop has subsided to zero (calculation time depends strongly on value of  $\ell$  and  $H$ ).

### C.3. Electric body force

In Chapters 7 and 8 we assumed that the electric body force in the Navier-Stokes equation is negligible in pressure-driven electrokinetic systems. The electric body force is proportional to the local net charge density, and therefore is only non-zero in the Electric Double Layer. Although comparable in magnitude, the pressure gradient extends through the whole channel, and since we have that  $H \gg \lambda_D$  we can therefore a priori expect that the electric body force will have a negligible effect compared to the applied pressure gradient. To test this assumption, we numerically calculated the surface charge profile in the conduction-dominated regime, shown in Fig. C.2. In the

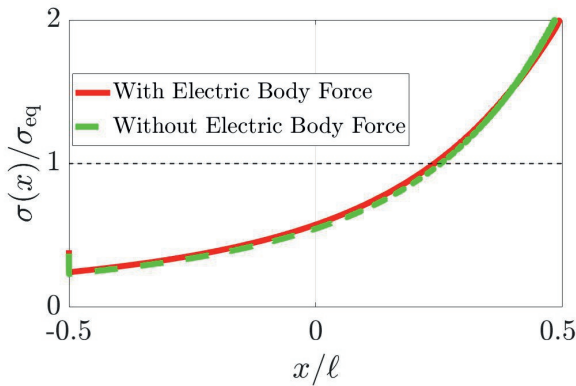


**Figure C.2.:** The surface charge profile at steady state in the conduction-dominated regime with (red full line) and without (green dashed line) the electric body force included in the Navier-Stokes equation. The channel length  $\ell = 30 \mu\text{m}$ , channel height  $H = 1 \mu\text{m}$  and a pressure drop  $\Delta p = 0.5 \text{ bar}$  was used.

conduction-dominated regime, the electric field is large and thus the electric body force is relatively large. Regardless, Fig. C.2 shows that including the electric body force has no significant impact on the surface charge profile at steady state. We can thus safely neglect the electric body force and still obtain the same quantitative behaviour.

## C.4. The system size

Experimental system sizes of streaming potential or streaming current set-ups can vary largely, but commonly occur on larger scales than the sub-millimetre sized system we consider. For example, in the experiment of Lis et al. [165],  $H = 0.5 \text{ mm}$  and  $\ell = 20 \text{ mm}$ . These sizes are numerically out of reach, however, since the smallest length scale of our system is the Debye length  $\lambda_D \simeq 10 \text{ nm}$ . Therefore we varied  $H$  and  $\ell$  over values that are numerically more feasible:  $H = \{0.5, 1, 2\} \mu\text{m}$  and  $\ell = \{10, 20, 30, 40\} \mu\text{m}$  with a fixed  $\Delta p$ , see Fig. C.3a, where we plot the laterally averaged zeta potential  $\langle \zeta \rangle$ . Here we see that  $\ell$  does not significantly affect the resulting  $\langle \zeta \rangle$  of the system. In fact, the effect of  $H$  is mainly due to the surface conduction  $G_s$ .

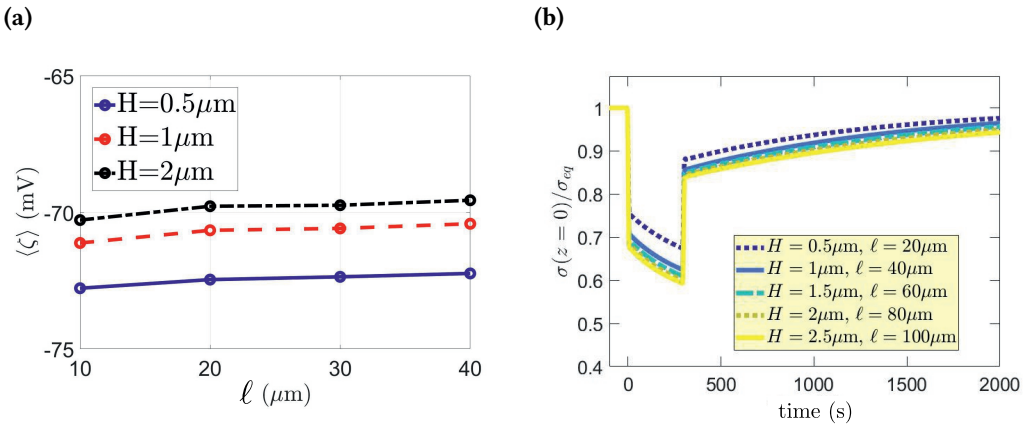


**Figure C.3.:** (a) The average  $\zeta$ -potential  $\langle \zeta \rangle$  of the charged channel surface in the steady state as a function of the channel length  $\ell$  and channel height  $H$ . Parameters were chosen here in order to represent silica at  $\text{pH}=6.5$ . (b) The surface charge in the middle of the surface,  $\sigma(z = 0, t)$ , as a function of time for  $\ell = 20, 40, 60, 80, 100 \mu\text{m}$  while maintaining  $\ell/H = 40$ . Parameters were chosen here too in order to represent silica at  $\text{pH}=6.5$ . The pressure drop  $\Delta p = 0.5 \text{ bar}$  was equal for all curves.

Similarly, we can inspect the effect of system size on the transient behaviour. Fig. C.3b shows the transient behaviour for several values of  $\ell$  and  $H$ . The ratio  $\ell/H = 40$  is held fixed, as it is the same ratio as in the experiment of Lis et al. Fig. C.3b shows the effect of scaling up the system. While there is some effect for smaller system sizes, the transient behaviour seems to approach an asymptote as  $\ell$  increases (the difference between  $\ell = 80 \mu\text{m}$  and  $\ell = 100 \mu\text{m}$  is hardly discernible). This suggests that, when

$\Delta p$  is held fixed, scaling up the system should not significantly impact the properties of both the transient and steady state behaviour, and that the results presented here are also valid for larger systems.

## C.5. Derivation of zeta potential and net charge current

The integration constant  $\zeta(z)$  of the solution to the charge density  $\rho_e(x, z)$ , Eq. (8.10), can be determined using the rate equation, Eq. (8.5). We rewrite the counter ion flux as  $\hat{\mathbf{x}} \cdot \mathbf{j}_C(0, z) = z_C \hat{\mathbf{x}} \cdot \mathbf{j}_e(0, z)$  and use the expression for the net charge flux  $\mathbf{j}_e$ , Eq. (8.7), and solution to  $\rho_e$ , Eq. (8.10), to find

$$z_C \hat{\mathbf{x}} \cdot \mathbf{j}_e(0, z) = z_\sigma D \left( \lambda_D^{-1} \rho \zeta(z) + 4\pi \lambda_B \rho \sigma(z) \right) = k^{\text{des}} \Gamma - \left( k^{\text{des}} + k^{\text{ads}} \rho_{C,s} \right) \sigma(z), \quad (\text{C.3})$$

where we have used the electrostatic boundary condition  $\hat{\mathbf{x}}_s \cdot \nabla \psi_s = -z_\sigma e \sigma / \epsilon$  to eliminate the electrostatic potential  $\psi$ . Now we can use the solution to  $\sigma$ , Eq. (8.12), to derive an expression for  $\zeta(z)$ ,

$$\begin{aligned} z_\sigma \frac{D}{\lambda_D} \rho \zeta(z) &= k^{\text{des}} \Gamma - \left( k^{\text{des}} + k^{\text{ads}} \rho_{C,s} - D \lambda_D^{-2} \right) \sigma(z), \\ &= z_\sigma \frac{D}{\lambda_D} \rho \zeta_{\text{eq}} + \sigma_{\text{eq}} (\tau_{\text{EDL}}^{-1} - \tau_{\text{reac}}^{-1}) (a_+ e^{k_+ z} + a_- e^{k_- z}) \end{aligned} \quad (\text{C.4})$$

Here, we used that  $k^{\text{des}} \Gamma - \left( k^{\text{des}} + k^{\text{ads}} \rho_{C,s} \right) \sigma_{\text{eq}} = 0$  by definition and identified the expression for the dimensionless equilibrium zeta potential  $\zeta_{\text{eq}} = z_\sigma 4\pi \lambda_B \lambda_D \sigma_{\text{eq}}$  from linear Poisson-Boltzmann theory. As argued in the text, we know that  $\tau_{\text{EDL}} = \lambda_D^2 / D \gg \tau_{\text{reac}}$ . Using the identity  $\rho \lambda_D = (4\pi \lambda_B \lambda_D)^{-1}$  we can rewrite the expression for  $\zeta(z)$  as

$$\zeta(z) = \zeta_{\text{eq}} + \frac{\sigma_{\text{eq}}}{z_\sigma \rho \lambda_D} \left( a_+ e^{k_+ z} + a_- e^{k_- z} \right) = \zeta_{\text{eq}} \left( 1 + a_+ e^{k_+ z} + a_- e^{k_- z} \right). \quad (\text{C.5})$$

To determine  $E$ , we impose that at any position  $z$  no net current passes through any channel slice with normal  $\hat{z}$ . This condition is a direct consequence of the vanishing divergence of  $\mathbf{j}_e$  and the open circuit geometry. Using the symmetry of the system we thus demand that

$$z_\sigma j_\sigma(z) + \int_0^{\frac{1}{2}H} dx j_{e,z}(x, z) = 0, \quad (\text{C.6})$$

where  $z_\sigma j_\sigma(z)$  is the net charge current through the Stern layer. Using Eq. (8.7), and the solution to  $\rho_e$ , Eq. (8.10), we find the net charge current through the liquid

$$\begin{aligned} \int_0^{\frac{1}{2}H} dx j_{e,z}(x, z) &= -D\partial_z \int_0^{\frac{1}{2}H} dx \rho_e + z_\sigma D\rho \int_0^{\frac{1}{2}H} dx E + \frac{\partial_z p}{2\eta} \int_0^{\frac{1}{2}H} dx x(H-x)\rho_e, \\ &\approx 2D\rho \left( \lambda_D \partial_z \zeta(z) + \frac{1}{2} z_\sigma E H - \frac{\partial_z p H \lambda_D^2}{2D\eta} \zeta(z) \right) \end{aligned} \quad (\text{C.7})$$

where we have used that  $H \gg \lambda_D$  and included a factor  $z_\sigma$  in the second term on the right hand side since  $E$  was defined as a positive quantity. Lastly, we use Eq. (8.12) and (8.4) to derive an expression for the Stern-layer current

$$j_\sigma(z) = -D_s(\partial_z \sigma - E\sigma) = D_s E \sigma_{\text{eq}} + D_s k_- a_+ e^{k_+ z} + D_s k_+ a_- e^{k_- z}, \quad (\text{C.8})$$

where we used that  $E - k_\pm = k_\mp$ . Eqs. (C.5), (C.7) and (C.8) can then be inserted in Eq. (C.6) which can then in principle be solved for the streaming electric field  $E$ .



# Bibliography

- [1] J. Sonnefeld, M. Löbbus, and W. Vogelsberger, *Colloids and Surfaces A: Physico-chemical and Engineering Aspects* **195**, 215 (2001), ISSN 0927-7757.
- [2] P. Leroy and A. Revil, *Journal of Colloid and Interface Science* **270**, 371 (2004), ISSN 0021-9797.
- [3] R. Saini, A. Garg, and D. P. J. Barz, *Langmuir* **30**, 10950 (2014), pMID: 25148210.
- [4] T. Hiemstra, J. D. Wit, and W. V. Riemsdijk, *Journal of Colloid and Interface Science* **133**, 105 (1989), ISSN 0021-9797.
- [5] U. Sivan, *Curr. Opin. Colloid Interface Sci.* **22**, 1 (2016), ISSN 1359-0294.
- [6] I. C. Bourg, S. S. Lee, P. Fenter, and C. Tournassat, *J. Phys. Chem. C* **121**, 9402 (2017).
- [7] Y. Marcus, *Chemical Reviews* **109**, 1346 (2009), ISSN 0009-2665.
- [8] K. D. Collins, G. W. Neilson, and J. E. Enderby, *Biophysical Chemistry* **128**, 95 (2007), ISSN 0301-4622.
- [9] J. Mähler and I. Persson, *Inorganic Chemistry* **51**, 425 (2012), ISSN 0020-1669.
- [10] H. Helmholtz, *Annalen der Physik* **165**, 353 (1853).
- [11] M. Gouy, *J. Phys. Theor. Appl.* **9**, 457 (1910).
- [12] R. B. Schoch, J. Han, and P. Renaud, *Rev. Mod. Phys.* **80**, 839 (2008).
- [13] R. van Roij, *Soft Condensed Matter*, lecture notes, (Utrecht University, 2018).
- [14] J. Overbeek, in *Colloid Science I, Irreversible Systems*, edited by H. Kruyt (Elsevier, 1952), chap. 5, pp. 194–244.
- [15] J. Lyklema, *Fundamentals of Interface and Colloid Science*, vol. II (Academic Press, 1995).
- [16] M. Tagliazucchi and I. Szleifer, *Materials Today* **18**, 131 (2015), ISSN 1369-7021.

- [17] B. Abécassis, C. Cottin-Bizonne, C. Ybert, A. Ajdari, and L. Bocquet, *New Journal of Physics* **11**, 075022 (2009).
- [18] S. J. Kim, Y.-C. Wang, J. H. Lee, H. Jang, and J. Han, *Phys. Rev. Lett.* **99**, 044501 (2007).
- [19] N. Laohakunakorn and U. F. Keyser, *Nanotechnology* **26**, 275202 (2015).
- [20] C. B. Picallo, S. Gravelle, L. Joly, E. Charlaix, and L. Bocquet, *Phys. Rev. Lett.* **111**, 244501 (2013).
- [21] W. Sparreboom, A. van den Berg, and J. C. T. Eijkel, *Nature Nanotechnology* **4**, 713 EP (2009), review Article.
- [22] R. T. Wilkin and D. C. DiGiulio, *Environmental Science & Technology* **44**, 4821 (2010), pMID: 20469895.
- [23] W. F. Paxton, P. T. Baker, T. R. Kline, Y. Wang, T. E. Mallouk, and A. Sen, *Journal of the American Chemical Society* **128**, 14881 (2006), pMID: 17105298.
- [24] J. Feng, M. Graf, K. Liu, D. Ovchinnikov, D. Dumcenco, M. Heiranian, V. Nandigana, N. R. Aluru, A. Kis, and A. Radenovic, *Nature* **536**, 197 (2016).
- [25] A. Siria, P. Poncharal, A.-L. Bianco, R. Fulcrand, X. Blase, S. T. Purcell, and L. Bocquet, *Nature* **494**, 455 (2013).
- [26] B. Hille, *Biophysical Journal* **22**, 283 (1978), ISSN 0006-3495.
- [27] A. Alcaraz, E. M. Nestorovich, M. L. López, E. García-Giménez, S. M. Bezrukov, and V. M. Aguilella, *Biophysical Journal* **96**, 56 (2009), ISSN 0006-3495.
- [28] M. Queralt-Martín, E. García-Giménez, V. M. Aguilella, P. Ramirez, S. Mafe, and A. Alcaraz, *Applied Physics Letters* **103**, 043707 (2013).
- [29] L. Landau and E. Lifshitz, *Fluid Mechanics* (Elsevier Ltd., 2011).
- [30] H. Helmholtz, *Annalen der Physik* **243**, 337 (1879), ISSN 1521-3889.
- [31] M. Smoluchowski, *Phys. Z.* **6**, 529 (1905).
- [32] R. Hunter, *Zeta potential in colloid science: principles and applications* (Academic Press, London, U.K., 1981).
- [33] P. Hohenberg and W. Kohn, *Phys. Rev.* **136**, B864 (1964).
- [34] C. Ebner, W. F. Saam, and D. Stroud, *Phys. Rev. A* **14**, 2264 (1976).

- [35] R. Evans, *Advances in Physics* **28**, 143 (1979).
- [36] J. Hansen and I. McDonald, *Theory of simple liquids*, vol. IV (Academic Press, 2013).
- [37] N. Boon, Ph.D. thesis, Utrecht University (2012).
- [38] D. L. Chapman, *The London, Edinburgh, and Dublin Philosophical Magazine and Journal of Science* **25**, 475 (1913).
- [39] B. W. Ninham and V. Parsegian, *Journal of Theoretical Biology* **31**, 405 (1971), ISSN 0022-5193.
- [40] E. J. W. Verwey and J. T. G. Overbeek, *The theory of the stability of lyophobic colloids* (Dover publications, Mineola, New York, 1999 (Original work published in 1948)).
- [41] R. Hunter, *Foundations of Colloid Science* (Clarendon Press: Oxford, U.K., 1992).
- [42] M. Ricci, P. Spijker, and K. Voitchovsky, *Nat. Commun.* **5** (2014).
- [43] V. L. Kolev, K. D. Danov, P. A. Kralchevsky, G. Broze, and A. Mehreteab, *Langmuir* **18**, 9106 (2002).
- [44] A. Archer, *J. Chem. Phys.* **130**, 014509 (2009).
- [45] U. M. B. Marconi and P. Tarazona, *The Journal of Chemical Physics* **110**, 8032 (1999).
- [46] U. M. B. Marconi and P. Tarazona, *Journal of Physics: Condensed Matter* **12**, A413 (2000).
- [47] D. C. Tretheway and C. D. Meinhardt, *Physics of Fluids* **14**, L9 (2002).
- [48] A. Ajdari and L. Bocquet, *Phys. Rev. Lett.* **96**, 186102 (2006).
- [49] E. Secchi, S. Marbach, A. Niguès, D. Stein, A. Siria, and L. Bocquet, *Nature* **537**, 210 EP (2016).
- [50] L. Onsager, *Phys. Rev.* **37**, 405 (1931).
- [51] L. Onsager, *Phys. Rev.* **38**, 2265 (1931).
- [52] J. C. Fair and J. F. Osterle, *The Journal of Chemical Physics* **54**, 3307 (1971).

- [53] P. B. Peters, R. van Roij, M. Z. Bazant, and P. M. Biesheuvel, *Phys. Rev. E* **93**, 053108 (2016).
- [54] R. P. Rastogi, R. C. Srivastava, and S. N. Singh, *Chemical Reviews* **93**, 1945 (1993), ISSN 0009-2665.
- [55] S. J. Brugman, B. L. Werkhoven, E. R. Townsend, P. Accordini, R. van Roij, and E. Vlieg, *Journal of Colloid and Interface Science* **559**, 291 (2020), ISSN 0021-9797.
- [56] T. Austad, A. RezaeiDoust, and T. Puntervold, in *SPE improved oil recovery symposium* (Society of Petroleum Engineers, 2010).
- [57] A. Lager, K. J. Webb, C. J. J. Black, M. Singleton, and K. S. Sorbie, *Petrophysics* **49** (2008).
- [58] R. M. Pashley, *J. Colloid Interface Sci.* **83**, 531 (1981).
- [59] R. M. Pashley and J. N. Israelachvili, *J. Colloid Interface Sci.* **97**, 446 (1984).
- [60] S. R. van Lin, K. K. Grotz, I. Siretanu, N. Schwierz, and F. Mugele, *Langmuir* (2019).
- [61] P. Fenter, C. Park, K. L. Nagy, and N. C. Sturchio, *Thin Solid Films* **515**, 5654 (2007).
- [62] S. S. Lee, P. Fenter, K. L. Nagy, and N. C. Sturchio, *Nat. Commun.* **8** (2017).
- [63] C. Qiu, P. J. Eng, C. Hennig, and M. Schmidt, *Langmuir* **34**, 12270 (2018).
- [64] P. G. Hartley, I. Larson, and P. J. Scales, *Langmuir* **13**, 2207 (1997).
- [65] B. Bera, N. Kumar, M. H. G. Duits, M. A. Cohen Stuart, and F. Mugele, *Langmuir* **34**, 13574 (2018).
- [66] W. de Poel, S. Pintea, J. Drnec, F. Carla, R. Felici, P. Mulder, J. A. A. W. Elemans, W. J. P. van Enckevort, A. E. Rowan, and E. Vlieg, *Surf. Sci.* **619**, 19 (2014), ISSN 0039-6028.
- [67] W. L. Bragg, *Atomic structure of minerals* (Cornell University Press, 1937).
- [68] G. Gaines Jr., *J. Phys. Chem.* **61**, 1408 (1957).
- [69] W. de Poel, S. L. Vaessen, J. Drnec, A. H. J. Engwerda, E. R. Townsend, S. Pintea, A. E. F. de Jong, M. Jankowski, F. Carlà, R. Felici, et al., *Surf. Sci.* **665**, 56 (2017).
- [70] S. S. Lee, P. Fenter, K. L. Nagy, and N. C. Sturchio, *Langmuir* **28**, 8637 (2012).

- [71] S. S. Lee, P. Fenter, K. L. Nagy, and N. C. Sturchio, *Geochim. Cosmochim. Acta* **123**, 416 (2013).
- [72] S. Pinteá, W. de Poel, A. E. F. de Jong, V. Vonk, P. van der Asdonk, J. Drnec, O. Balmes, H. Isern, T. Dufrane, R. Felici, et al., *Langmuir* **32**, 12955 (2016).
- [73] S. J. T. Brugman, E. R. Townsend, M. M. H. Smets, P. Accordini, and E. Vlieg, *Langmuir* **34**, 3821 (2018).
- [74] H. Sakuma and K. Kawamura, *Geochim. Cosmochim. Acta* **75**, 63 (2011).
- [75] M. L. Schlegel, K. L. Nagy, P. Fenter, L. Cheng, N. C. Sturchio, and S. D. Jacobsen, *Geochim. Cosmochim. Acta* **70**, 3549 (2006).
- [76] K. Kobayashi, Y. Liang, S. Murata, T. Matsuoka, S. Takahashi, N. Nishi, and T. Sakka, *Langmuir* **33**, 3892 (2017).
- [77] S. Nishimura, H. Tateyama, K. Tsunematsu, and K. Jinnai, *J. Colloid Interface Sci.* **152**, 359 (1992), ISSN 0021-9797.
- [78] P. J. Scales, F. Grieser, and T. W. Healy, *Langmuir* **6**, 582 (1990).
- [79] N. Debacher and R. Ottewill, *Colloids and Surfaces* **65**, 51 (1992), ISSN 0166-6622, in honour of Professor Anita Bailey.
- [80] R. M. Pashley, *Adv. Colloid Interface Sci.* **16**, 57 (1982).
- [81] C. Park, P. A. Fenter, N. C. Sturchio, and K. L. Nagy, *Langmuir* **24**, 13993 (2008).
- [82] P. Kékicheff, S. Marcĕlja, T. J. Senden, and V. E. Shubin, *J. Chem. Phys.* **99**, 6098 (1993).
- [83] P. Claesson, P. Herder, P. Stenius, J. Eriksson, and R. Pashley, *J. Colloid Interface Sci.* **109**, 31 (1986), ISSN 0021-9797.
- [84] V. E. Shubin and P. Kékicheff, *J. Colloid Interface Sci.* **155**, 108 (1993), ISSN 0021-9797.
- [85] P. J. Scales, F. Grieser, T. W. Healy, L. R. White, and D. Y. C. Chan, *Langmuir* **8**, 965 (1992).
- [86] S. Nishimura, P. J. Scales, H. Tateyama, K. Tsunematsu, and T. W. Healy, *Langmuir* **11**, 291 (1995).
- [87] C. Krishnamoorthy and R. Overstreet, *Soil Sci.* **69**, 87 (1950).

- [88] S. Adapa and A. Malani, *Sci. Rep.* **8**, 12198 (2018).
- [89] D. Martin-Jimenez, E. Chacon, P. Tarazona, and R. Garcia, *Nat. Commun.* **7** (2016).
- [90] H. Sakuma, H. Nakao, Y. Yamasaki, and K. Kawamura, *J. Appl. Sol. Chem. Model.* **1**, 1 (2012).
- [91] N. Radenović, D. Kaminski, W. van Enckevort, S. Graswinckel, I. Shah, M. in't Veld, R. Algra, and E. Vlieg, *J. Chem. Phys.* **124**, 164706 (2006).
- [92] S. S. Lee, P. Fenter, C. Park, N. C. Sturchio, and K. L. Nagy, *Langmuir* **26**, 16647 (2010).
- [93] A. Meleshyn, *J. Phys. Chem. C* **113**, 17604 (2009).
- [94] S. Pintea, W. de Poel, A. E. F. de Jong, R. Felici, and E. Vlieg, *Langmuir* **34**, 4241 (2018).
- [95] L. Xu and M. Salmeron, *Langmuir* **14**, 5841 (1998).
- [96] E. Ferrage, C. Tournassat, E. Rinnert, L. Charlet, and B. Lanson, *Clays and Clay Minerals* **53**, 348 (2005), ISSN 0009-8604.
- [97] I. Siretanu, D. Ebeling, M. P. Andersson, S. L. S. Stipp, A. Philipse, M. C. Stuart, D. Van Den Ende, and F. Mugele, *Sci. Rep.* **4**, 4956 (2014).
- [98] R. D. Shannon, *Acta Crystallogr. A* **32**, 751 (1976).
- [99] Y. Marcus, *Chem. Rev.* **88**, 1475 (1988).
- [100] C. Park, P. A. Fenter, K. L. Nagy, and N. C. Sturchio, *Phys. Rev. Lett.* **97**, 016101 (2006).
- [101] Y. Levin, A. P. dos Santos, and A. Diehl, *Phys. Rev. Lett.* **103**, 257802 (2009).
- [102] W. Haynes, ed., *CRC Handbook of Chemistry and Physics* (Taylor & Francis, 2012).
- [103] O. Y. Samoilov, *Discuss. Faraday Soc.* **24**, 141 (1957).
- [104] Y. Marcus, *Biophys. Chem.* **51**, 111 (1994), ISSN 0301-4622.
- [105] G. Engel and H. G. Hertz, *Ber. Bunsenges. Phys. Chem.* **72**, 808 (1968).
- [106] H. D. B. Jenkins and Y. Marcus, *Chemical Reviews* **95**, 2695 (1995).

- [107] K. Yoshida, K. Ibuki, and M. Ueno, *J. Solution Chem.* **25**, 435 (1996), ISSN 1572-8927.
- [108] Z. Chen, Y. Zhao, X. Xu, C. Liu, and L. Yang, *Comput. Mater. Sci.* **171**, 109256 (2020), ISSN 0927-0256.
- [109] D. J. Bonthuis, S. Gekle, and R. R. Netz, *Langmuir* **28**, 7679 (2012), PMID: 22414296.
- [110] D. Ben-Yaakov, D. Andelman, R. Podgornik, and D. Harries, *Curr. Opin. Colloid Interface Sci.* **16**, 542 (2011), ISSN 1359-0294.
- [111] R. P. Rastogi, R. C. Srivastava, and S. N. Singh, *Chemical Reviews* **93**, 1945 (1993).
- [112] M. Elimelech and W. A. Phillip, *Science* **333**, 712 (2011), ISSN 0036-8075.
- [113] D. Branton, D. W. Deamer, A. Marziali, H. Bayley, S. A. Benner, T. Butler, M. D. Ventura, S. Garaj, A. Hibbs, X. Huang, et al., *Nature Biotech.* **26**, 1146 (2008).
- [114] Y. He, M. Tsutsui, R. H. Scheicher, X. S. Miao, and M. Taniguchi, *ACS Sensors* **1**, 807 (2016).
- [115] M. M. Hatlo, D. Panja, and R. van Roij, *Phys. Rev. Lett.* **107**, 068101 (2011).
- [116] S. Pennathur, J. Eijkel, and A. van den Berg, *Lab Chip* **7**, 1234 (2007).
- [117] B. B. Sales, M. Saakes, J. W. Post, C. J. N. Buisman, P. M. Biesheuvel, and H. V. M. Hamelers, *Environmental Science & Technology* **44**, 5661 (2010), PMID: 20568741.
- [118] F. H. J. van der Heyden, D. J. Bonthuis, D. Stein, C. Meyer, and C. Dekker, *Nano Letters* **6**, 2232 (2006), PMID: 17034089.
- [119] M.-C. Lu, S. Satyanarayana, R. Karnik, A. Majumdar, and C.-C. Wang, *Journal of Micromechanics and Microengineering* **16**, 667 (2006).
- [120] J. W. Post, H. V. M. Hamelers, and C. J. N. Buisman, *Environmental Science & Technology* **42**, 5785 (2008), PMID: 18754509.
- [121] D.-K. Kim, C. Duan, Y.-F. Chen, and A. Majumdar, *Microfluidics and Nanofluidics* **9**, 1215 (2010).
- [122] A. Achilli, T. Y. Cath, and A. E. Childress, *Journal of Membrane Science* **343**, 42 (2009), ISSN 0376-7388.
- [123] Q. She, X. Jin, and C. Y. Tang, *Journal of Membrane Science* **401-402**, 262 (2012), ISSN 0376-7388.

- [124] A. P. Straub, A. Deshmukh, and M. Elimelech, *Energy Environ. Sci.* **9**, 31 (2016).
- [125] D. Brogioli, *Phys. Rev. Lett.* **103**, 058501 (2009).
- [126] H. G. Park and Y. Jung, *Chem. Soc. Rev.* **43**, 565 (2014).
- [127] A. Siria, P. Poncharal, A.-L. Biance, R. Fulcrand, X. Blase, S. T. Purcell, and L. Bocquet, *Nature* **494**, 455 EP (2013).
- [128] J. Feng, M. Graf, K. Liu, D. Ovchinnikov, D. Dumcenco, M. Heiranian, V. Nandigana, N. R. Aluru, A. Kis, and A. Radenovic, *Nature* **536**, 197 EP (2016).
- [129] B. W. Ninham and V. Parsegian, *Journal of Theoretical Biology* **31**, 405 (1971), ISSN 0022-5193.
- [130] D. Y. Chan and D. Mitchell, *Journal of Colloid and Interface Science* **95**, 193 (1983), ISSN 0021-9797.
- [131] P. M. Biesheuvel and M. Z. Bazant, *Phys. Rev. E* **94**, 050601 (2016).
- [132] E. Secchi, A. Niguès, L. Jubin, A. Siria, and L. Bocquet, *Phys. Rev. Lett.* **116**, 154501 (2016).
- [133] C. Lee, C. Cottin-Bizonne, A.-L. Biance, P. Joseph, L. Bocquet, and C. Ybert, *Phys. Rev. Lett.* **112**, 244501 (2014).
- [134] L. Cao, F. Xiao, Y. Feng, W. Zhu, W. Geng, J. Yang, X. Zhang, N. Li, W. Guo, and L. Jiang, *Advanced Functional Materials* **27**, 1604302 (2017).
- [135] M. Z. Bazant, K. Thornton, and A. Ajdari, *Phys. Rev. E* **70**, 021506 (2004).
- [136] T. Mouterde and L. Bocquet, *The European Physical Journal E* **41**, 148 (2018).
- [137] B. L. Werkhoven and R. van Roij, arXiv:1911.13156 (2019).
- [138] D. C. Prieve, J. L. Anderson, J. P. Ebel, and M. E. Lowell, *Journal of Fluid Mechanics* **148**, 247 (1984).
- [139] L. Bocquet and E. Charlaix, *Chem. Soc. Rev.* **39**, 1073 (2010).
- [140] M. Yang, X. Yang, Q. Wang, K. Wang, X. Fan, W. Liu, X. Liu, J. Liu, and J. Huang, *RSC Adv.* **4**, 26729 (2014).
- [141] J. Veerman, M. Saakes, S. Metz, and G. Harmsen, *Journal of Membrane Science* **327**, 136 (2009), ISSN 0376-7388.

- [142] G. Tocci, L. Joly, and A. Michaelides, *Nano Letters* **14**, 6872 (2014), ISSN 1530-6984.
- [143] B. Grosjean, M.-L. Bocquet, and R. Vuilleumier, *Nature Communications* **10**, 1656 (2019).
- [144] B. L. Werkhoven, J. C. Everts, S. Samin, and R. van Roij, *Phys. Rev. Lett.* **120**, 264502 (2018).
- [145] B. L. Werkhoven, S. Samin, and R. van Roij, *The European Physical Journal Special Topics* **227**, 2539 (2019), ISSN 1951-6401.
- [146] M. Majumder, N. Chopra, R. Andrews, and B. J. Hinds, *Nature* **438**, 44 (2005).
- [147] P. Pang, J. He, J. H. Park, P. S. Krstić, and S. Lindsay, *ACS Nano* **5**, 7277 (2011), ISSN 1936-0851.
- [148] Y. Ren and D. Stein, *Nanotechnology* **19**, 195707 (2008).
- [149] I. Borukhov, D. Andelman, and H. Orland, *Phys. Rev. Lett.* **79**, 435 (1997).
- [150] J. Pedro de Souza and M. Z. Bazant, *ArXiv e-prints* (2019).
- [151] S. Alexander, P. M. Chaikin, P. Grant, G. J. Morales, P. Pincus, and D. Hone, *The Journal of Chemical Physics* **80**, 5776 (1984).
- [152] E. Trizac, L. Bocquet, M. Aubouy, and H. H. von Grünberg, *Langmuir* **19**, 4027 (2003).
- [153] B. Zoetekouw and R. van Roij, *Phys. Rev. Lett.* **97**, 258302 (2006).
- [154] T. J. Pedley, *Quarterly Reviews of Biophysics* **16**, 115–150 (1983).
- [155] J. C. Mathai, A. Missner, P. Kügler, S. M. Saparov, M. L. Zeidel, J. K. Lee, and P. Pohl, *Proceedings of the National Academy of Sciences* **106**, 16633 (2009), ISSN 0027-8424.
- [156] P. Pohl, S. M. Saparov, and Y. N. Antonenko, *Biophysical Journal* **75**, 1403 (1998), ISSN 0006-3495.
- [157] C. Hanneschlaeger, A. Horner, and P. Pohl, *Chemical Reviews* **119**, 5922 (2019), ISSN 0009-2665.
- [158] N. Schwierz, D. Horinek, and R. R. Netz, *Langmuir* **26**, 7370 (2010), ISSN 0743-7463.

- [159] D. Laage, T. Elsaesser, and J. T. Hynes, *Chemical Reviews* **117**, 10694 (2017), ISSN 0009-2665.
- [160] S. Pawlowski, V. Geraldes, J. G. Crespo, and S. Velizarov, *Journal of Membrane Science* **502**, 179 (2016), ISSN 0376-7388.
- [161] R. I. Sha'afi, G. T. Rich, V. W. Sidel, W. Bossert, and A. K. Solomon, *The Journal of General Physiology* **50**, 1377 (1967), ISSN 0022-1295.
- [162] N. E. Barlow, G. Bolognesi, S. Haylock, A. J. Flemming, N. J. Brooks, L. M. C. Barter, and O. Ces, *Scientific Reports* **7**, 17551 (2017), ISSN 2045-2322.
- [163] S. Balme, T. Ma, E. Balanzat, and J.-M. Janot, *Journal of Membrane Science* **544**, 18 (2017), ISSN 0376-7388.
- [164] J. Gao, X. Liu, Y. Jiang, L. Ding, L. Jiang, and W. Guo, *Small* **15**, 1804279 (2019).
- [165] D. Lis, E. H. G. Backus, J. Hunger, S. H. Parekh, and M. Bonn, *Science* **344**, 1138 (2014), ISSN 0036-8075.
- [166] J. J. Bikerman, *Zeitschrift für Physikalische Chemie* **163**, 378 (1933).
- [167] J. J. Bikerman, *Kolloid-Zeitschrift* **72**, 100 (1935), ISSN 1435-1536.
- [168] J. Lyklema and M. Minor, *Colloids and Surfaces A: Physicochemical and Engineering Aspects* **140**, 33 (1998), ISSN 0927-7757.
- [169] M. Löbbus, J. Sonnfeld, H. P. van Leeuwen, W. Vogelsberger, and J. Lyklema, *Journal of Colloid and Interface Science* **229**, 174 (2000), ISSN 0021-9797.
- [170] R. O'Brien and W. Rowlands, *Journal of Colloid and Interface Science* **159**, 471 (1993), ISSN 0021-9797.
- [171] M. Minor, A. J. van der Linde, and J. Lyklema, *Journal of Colloid and Interface Science* **203**, 177 (1998), ISSN 0021-9797.
- [172] M. Löbbus, H. P. van Leeuwen, and J. Lyklema, *Colloids and Surfaces A: Physicochemical and Engineering Aspects* **161**, 103 (2000), ISSN 0927-7757.
- [173] A. Ajdari, *Phys. Rev. Lett.* **75**, 755 (1995).
- [174] A. S. Khair and T. M. Squires, *Journal of Fluid Mechanics* **615**, 323 (2008).
- [175] D. Y. Chan and D. Mitchell, *Journal of Colloid and Interface Science* **95**, 193 (1983), ISSN 0021-9797.

- [176] I. Popa, P. Sinha, M. Finessi, P. Maroni, G. Papastavrou, and M. Borkovec, *Phys. Rev. Lett.* **104**, 228301 (2010).
- [177] C. Zukoski and D. Saville, *Journal of Colloid and Interface Science* **114**, 32 (1986), ISSN 0021-9797.
- [178] C. S. Mangelsdorf and L. R. White, *Journal of the Chemical Society, Faraday Transactions* **86**, 2859 (1990).
- [179] R. Kutner, *Physics Letters A* **81**, 239 (1981), ISSN 0375-9601.
- [180] Y. Levin, J. J. Arenzon, and M. Sellitto, *EPL (Europhysics Letters)* **55**, 767 (2001).
- [181] M. D. Carbajal-Tinoco, R. Lopez-Fernandez, and J. L. Arauz-Lara, *Phys. Rev. Lett.* **99**, 138303 (2007).
- [182] C. Macias-Romero, I. Nahalka, H. I. Okur, and S. Roke, *Science* **357**, 784 (2017), ISSN 0036-8075.
- [183] J. Sonnefeld, M. Löbbus, and W. Vogelsberger, *Colloids and Surfaces A: Physicochemical and Engineering Aspects* **195**, 215 (2001), ISSN 0927-7757.
- [184] A. Delgado, F. González-Caballero, R. Hunter, L. Koopal, and J. Lyklema, *Journal of Colloid and Interface Science* **309**, 194 (2007), ISSN 0021-9797, elkin 06, International Electrokinetics Conference, June 25-29, Nancy, France.
- [185] K. Vinodgopal and P. V. Kamat, *Environmental Science & Technology* **29**, 841 (1995).
- [186] C. Macias-Romero, I. Nahalka, H. I. Okur, and S. Roke, *Science* **357**, 784 (2017), ISSN 0036-8075.
- [187] J. F. Duval, G. K. Huijs, W. F. Threels, J. Lyklema, and H. P. van Leeuwen, *Journal of Colloid and Interface Science* **260**, 95 (2003), ISSN 0021-9797.
- [188] N. Boon and R. van Roij, *The Journal of Chemical Physics* **134**, 054706 (2011).
- [189] S. M. Davidson, R. G. H. Lammertink, and A. Mani, *Phys. Rev. Fluids* **3**, 053701 (2018).
- [190] C. Lee, C. Cottin-Bizonne, A.-L. Biance, P. Joseph, L. Bocquet, and C. Ybert, *Phys. Rev. Lett.* **112**, 244501 (2014).



# Discussion and outlook

As a starting PhD candidate you have no idea where your research will end up. There is a starting point, of course, but you never know what you will find in four years of research, what interesting new paths your research will lead you to. This thesis has been divided into three separate parts for this reason. All three parts are connected, but arose from separate ideas and coincidences that led us to investigate what we found worthwhile. Here, we shortly summarise each part, and consider the important lessons we have learned from them which can benefit future research.

In part I we investigated ion adsorption on a mineral surface. We focussed specifically on  $\text{Cs}^+$  and  $\text{Ca}^{2+}$  adsorption on mica, but that does not mean that all conclusions of that part are only relevant to this specific case. We presented three approaches to investigate the system, Surface X-Ray Diffraction, Atomic Force Microscopy and surface complexation models. If we would have used only one of these three, the results of the research would have been very different from what is presented in this part. Only by combining all three methods in one single analysis, we found properties that we would not have found otherwise, and for this reason more closely reflect the actual properties of the system. This is the most important lesson we should take away from part I. Even model systems, such as the atomically flat mica surface investigated in this part, are complex systems, but applying multiple approaches to investigate them help greatly to answer the important questions. If we then want to investigate even more complex systems, such as naturally occurring materials, we must be even more cautious and methodical.

In part II we investigated nanofluidic systems, and mostly focused on diffusio-osmosis, a nanofluidic system with an imposed salinity gradient. In this part we investigated the general and unique transport properties of diffusio-osmotic systems. The most promising application of diffusio-osmosis is the harvesting of electric energy from mixing fresh and salt water. An important aspect of implementation is optimisation, and this is the aim of part II, to develop a theory to describe diffusio-osmotic systems such that nanofluidic systems can be properly optimised. As opposed to for example electro-osmosis, diffusio-osmosis is a difficult type of nanofluidic system to analyse because of the intrinsic heterogeneity of a diffusio-osmotic channel. This does, however, give diffusio-osmotic systems unique transport properties that can be utilised. In part II we explained the intrinsic heterogeneity and entrance effects that are

inevitably found in diffusio-osmotic channels, and then showed how these affect the transport properties of a single channel. Moreover, we show how an array of channels, i.e. a membrane, is dominated by entrance effects, and that each separate channel has qualitatively different transport properties compared to a single channel. For future research it is important to keep in mind that these unique properties must be taken into account when analysing a given diffusio-osmotic system. The framework developed in this part provides a method to handle these challenges, and to best optimise diffusio-osmotic nanofluidic channels.

In part III we studied micro- and nanofluidic devices on a more fundamental level. It is often assumed that the surface charges on the walls of the device are static, but here we relax this assumption and investigated the implications of mobile surface charges. This led to the discovery novel dynamic and steady state which can have significant impact on the transport properties nanofluidic device, including the ones discussed in part II. On the one hand, this is important for the interpretation of experiments on electrokinetic systems, but on the other hand these can be utilised for new designs. These properties are very surface specific, since they depend not only on the type of ad- and desorption reactions taking place at the solid-water interface, but also on the rates of these reactions. Interestingly, this poses a new way of investigating the surface chemistry, which is usually difficult, by observing the electrokinetic behaviour of the surface.

For all three parts, there is much more to investigate. This seems to be a general truth of science: the more you investigate something, the more questions you encounter and the more there is to investigate. This may be the larger, overarching lesson to learn not just from this thesis, but from all works of science. Whatever you investigate, the closer you look at something, the more complex you will find it to be. There is no end to science, no final question to ask and answer.

# Samenvatting voor iedereen

Mijn doel hier is om zo goed mogelijk het resultaat van 4 jaar onderzoek samen te vatten. Dit wil ik op zo'n manier proberen uit te leggen dat ook mensen zonder een natuurkundige achtergrond het kunnen begrijpen. Dit is een interessante uitdaging, en niet alleen omdat ik veel jargon naar het Nederlands moet vertalen. Als je even door dit proefschrift bladert, zul je gelijk zien dat wiskundige formules essentieel zijn voor de theoretische natuurkunde. Hoewel dit het moeilijk maakt om gespecialiseerd theoretisch natuurkundig materiaal uit te leggen, zal ik toch mijn uiterste best doen om uit te leggen wat deze vergelijkingen ons vertellen. Zoals één van de grootste namen van de moderne thermodynamica, J.W. Gibbs, ooit zei: "*One of the principal objects of theoretical research in my department of knowledge is to find the point of view from which the subject appears in its greatest simplicity*" (Eén van de hoofdtaken van theoretisch onderzoek is, naar mijn weten, de invalshoek te vinden van waar het onderwerp op de simpelste manier te begrijpen is). Zelf leer ik in ieder geval veel van het schrijven van dit hoofdstuk. Om nog een andere grote natuurkundige te quoten, Albert Einstein; *If you can't explain it simply, you don't understand it well enough* (als je iets niet op een simpele manier kan uitleggen, snap je het niet goed genoeg).

## Statistische fysica

We beginnen bij de basis. Materie bestaat uit kleine deeltjes, atomen. Atomen zijn zo klein dat het moeilijk is om het je voor te stellen: atomen zijn typisch niet meer dan een paar Ångstrom, waarbij 1 Ångstrom gelijk is aan  $10^{-10}$  m = 0,000000001 meter, oftewel één tienmiljardste van een meter. Het idee dat materie bestaat uit atomen is al heel oud. Het idee werd ongeveer 2500 jaar geleden als eerst geopperd door de Griekse filosofen Democritus en Leucippus. Ze beredeneerden, puur theoretisch en zonder experimenten, dat de wereld om ons heen moet bestaan uit kleine, ondeelbare deeltjes die voor altijd in beweging zijn. Zij hebben ons het woord 'atoom' gegeven, afgeleid van het Grieks voor ondeelbaar, ἄτομον (atomon). We weten echter nu dat atomen nog verder opgedeeld kunnen worden, maar onder normale, veel voorkomende, niet extreme omstandigheden (zoals een glas water) zijn ze te beschouwen alsof ze de ondeelbare deeltjes zijn waar materie uit bestaat.

Ondanks dat atomen zo klein zijn, weten we tegenwoordig heel goed hoe atomen zich gedragen. We weten dat alles om ons heen een collectie van atomen is. Als we weten hoe een enkel atoom zich gedraagt, zou je dus denken dat het rechttoe rechtaan zou zijn om de wereld om ons heen te beschrijven. In principe is dat zo, maar het probleem is dat zelfs voorwerpen die voor ons klein zijn een onvoorstelbaar groot aantal atomen bevatten. Een glas water bevat ongeveer  $10^{25}$  (1 met 25 nullen) watermoleculen, elk een collectie van 3 atomen. Het is voor ons moeilijk zo'n groot getal voor te stellen. Om hier een beeld van te geven: stel je een schijf van 3 terabyte (3 biljoen bytes) voor, je komt (ongeveer) uit op  $10^{25}$  als elke afzonderlijke byte van deze schijf zelf een schijf is van 3 terabyte! Oftewel, het aantal water moleculen in één glas water is groter dan het aantal glazen dat ik nodig heb om al het water op aarde op te vangen. Als ik de eigenschappen van dit glas water wil beschrijven is het uitermate onhandig om uit te rekenen wat elk los watermolecuul zal doen.

Statistische fysica kan ons hierbij helpen. Het doel van statistische fysica is om het gedrag van een collectie van atomen te beschrijven, zonder elk atoom los te beschrijven. Zo gaat de statistische fysica over eigenschappen als druk, volume en temperatuur van gassen en vloeistoffen. Dit zijn allemaal alleen eigenschappen van collecties atomen en niet van een atomen zelf. Dit is wat statistiek doet, en vandaar de naam 'statistische fysica'.

Statistische fysica is op twee punten heel anders dan de statistiek die we doorgaans tegenkomen. Ten eerste, veel statistiek die we tegenkomen gaat over mensen. Mensen verschillen onderling heel veel, wat statistiek heel moeilijk maakt, maar atomen verschillen eigenlijk maar heel weinig van elkaar. Ten tweede zijn er veel meer atomen dan dat er mensen zijn. Een algemene regel in statistiek is hoe meer data, en hoe meer elk geval op elkaar lijkt, hoe nauwkeuriger de statistiek wordt. Het enorme aantal atomen, en het feit dat ze zoveel op elkaar lijken, is dus eigenlijk een groot voordeel voor statistische fysica; dit maakt de statistiek, en dus de voorspellingen van de statistische fysica, heel precies en generaliseerbaar.

## Vaste stof-Water Grensvlakken

In dit proefschrift kijken we naar verschillende eigenschappen van een grensvlak tussen een vaste stof en water, met wat zout opgelost in het water. Wat is hier zo interessant aan? Stel ik heb een glas water, dan zijn er veel meer moleculen ver weg van het glas dan dat er moleculen naast het grensvlak zijn. Je zou in eerste instantie dus niet verwachten dat het glas-water grensvlak belangrijk is om het systeem als geheel te begrijpen. Het interessante van grensvlakken is echter, dat dit de plek is waar twee verschillende stoffen wisselwerken. Of dat nou twee vaste stoffen zijn, een vaste

stof en een vloeistof (zoals in het glas water), een vaste stof en een gas of een vloeistof en een gas, grensvlakken zijn de locaties waar twee verschillende stoffen met elkaar wisselwerken.

In dit proefschrift kijken we naar het grensvlak tussen een vaste stof en water. Dit soort grensvlakken komen overal voor. Niet alleen in een glas water, maar ook biologische systemen en onze aarde zelf (denk aan grondwater) zitten er vol mee simpelweg omdat bijna overal op het aardoppervlak water te vinden is. Het is dus niet meer dan logisch dat we vaste stof-water grensvlakken beter willen begrijpen. Daarnaast zit in water altijd wel een klein beetje zout, en dit kan grote gevolgen hebben voor het grensvlak. Daarom is het belangrijk eerst te bespreken wat zout eigenlijk is.

## Zout in water

Een zoutmolecuul bestaat uit twee of meerdere ionen. Een molecuul is een collectie atomen die één geheel vormen (denk aan een watermolecuul,  $\text{H}_2\text{O}$ , dat bestaat uit 2 waterstof atomen en 1 zuurstof atoom). Een ion is een atoom (of molecuul) met een netto elektrische lading, al is een zout molecuul altijd netto ladingsneutraal. Een positief geladen ion noemen we een kation, een negatief geladen ion heet een anion. Keukenzout, natrium chloride ( $\text{NaCl}$ ), is bijvoorbeeld een combinatie van een natriumion  $\text{Na}^+$  als kation en een chloride-ion  $\text{Cl}^-$  als anion. Water heeft de belangrijke eigenschap dat het een uitstekend oplosmiddel is. Doordat water een sterke wisselwerking heeft met geladen deeltjes, is het zeer effectief in het scheiden van twee ionen zodra een zout molecuul in water terecht komt. Om het op een natuurkundige manier te zeggen: het systeem verlaagt de totale energie door de ionen van elkaar te scheiden. In ruil daarvoor krijgt elk ion dan een schil van water om zich heen, de zogeheten hydratie-schil, en door deze schil verlaagt het systeem de totale energie. Dit is schematisch weergegeven in figuur C.4. De oranje bollen zijn de negatief geladen anionen, de groene bollen de positief geladen kationen en de rode 'Mickey Mouse' met grijze oren stelt een water molecuul voor (water,  $\text{H}_2\text{O}$ , bestaat uit 1 zuurstof atoom (O), het rode gezicht, en 2 waterstof atomen ( $\text{H}_2$ ), de grijze oren).

Opgelost zout heeft een belangrijke invloed op de eigenschappen van het water. Water zonder zout, gedeïoniseerd of gedemineraliseerd water, geleidt bijvoorbeeld zeer slecht stroom, terwijl water met een klein beetje zout heel goed geleidt. Dit komt omdat de ionen een elektrische lading dragen, waardoor de elektrische stroom via de ionen van de ene naar de andere kant kan komen.

## Adsorptie en desorptie

Maar waarom zijn de ionen zo belangrijk voor het vaste-stof water grensvlak? Omdat de ionen geladen zijn, zullen ze een sterke wisselwerking hebben met een grensvlak als dat zelf ook een netto elektrische lading draagt; de ionen met dezelfde lading worden afgestoten en de ionen met tegengestelde lading zullen worden aangetrokken tot het oppervlak. Dit klinkt misschien als een bijzondere situatie, maar dat is het niet. Bijna elk oppervlak zal spontaan elektrisch geladen worden als je het in contact brengt met water. Dit geldt voor oppervlaktes van steen tot plastic, en is dus verre van een uitzonderlijke situatie. Maar waar komt deze lading vandaan? Het antwoord ligt bij de ionen zelf. De lading ontstaat uit adsorptie of desorptie reacties van het oppervlak met de ionen. Bij een desorptie reactie laat het oppervlak ionen los, de vaste stof lost deels op. Omdat het oppervlak neutraal begint en een geladen deeltje los laat, zal het ion een netto geladen oppervlak achter laten. Adsorptie is het omgekeerde proces, bij adsorptie blijft een ion uit het water vast zitten op het oppervlak en geeft het zo een netto lading.

Er zijn verschillende mechanismes waardoor ionen ad- en/of desorberen, bijvoorbeeld door het breken (of vormen) van een chemische binding tussen het ion en het oppervlak. Het meest voorkomende mechanisme heeft echter te maken met de hydratatie schil, de schil van water om elk ion heen (zoals afgebeeld in Figuur C.4). Sommige ionen kunnen namelijk energie winnen door aan het oppervlak te zitten, zoals afgebeeld in

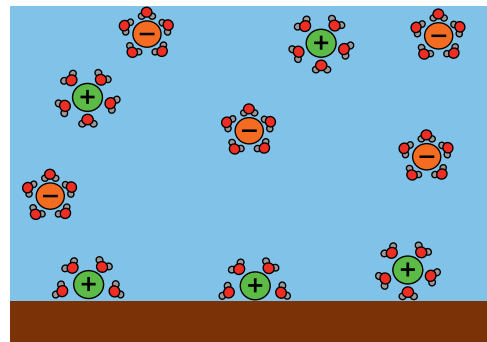


**Figure C.4.:** Ionen opgelost in water met een hydratatie schil of geadsorbeerd op het vaste oppervlak.

zout en oppervlak. De evenwichtssituatie ziet er over het algemeen dus anders uit voor verschillende soorten keuzenzout, zoals natrium chloride NaCl, natrium jodide NaI en kalium jodide KI. Alle vaste stof-water grensvlakken zijn dus anders; dit maakt ze niet alleen interessant, maar maakt het ook mogelijk de eigenschappen (zoals totale lading en hoeveelheid geadsorbeerde ionen) te bepalen door het juiste oppervlak en soort zout te kiezen. Los van de details van de adsorptie- en desorptie-mechanismen blijft het resultaat hetzelfde: het grensvlak tussen het water en de vaste stof zal spontaan een netto lading ontwikkelen.

## Elektrische Dubbellaag

Een direct en belangrijk gevolg van een geladen oppervlak is de zogeheten elektrische dubbellaag, de hoofdrolspeler van dit proefschrift. Het geladen oppervlak zal ionen met tegengestelde lading aantrekken en ionen met dezelfde lading afstoten. Stel het oppervlak is negatief geladen, dan trekt het positief geladen ionen aan en zullen we dus vlakbij het oppervlak meer positief geladen kationen vinden dan negatief geladen anionen. Vandaar de naam 'dubbellaag', omdat twee lagen van tegengesteld geladen deeltjes zich vlak naast elkaar bevinden. Er is echter wel een verschil tussen de lagen. De laag op het oppervlak zit vast op het oppervlak, maar de andere laag bestaat uit ionen die nog vrij kunnen bewegen in het water. Dit komt door zogeheten thermische fluctuaties, die ontstaan uit de chaotische bewegingen van alle atomen en moleculen die voortdurend met grote snelheid tegen elkaar botsen, als een enorme verzameling biljart ballen die vrij kunnen blijven bewegen omdat er op de atomische schaal geen wrijving is. Dit is hetzelfde mechanisme dat zorgt voor diffusie, zoals het spontaan verspreiden van een kleurstof in water (al is roeren over het algemeen een stuk sneller).

Normaliter zijn er op elke plek in het water ongeveer evenveel kationen als anionen te vinden (water zelf is netto ongeladen), maar de Elektrische Dubbellaag is hierop dus een belangrijke uitzondering. Het is een gebied in het water waar zich een netto elektrische lading bevindt, doordat er gemiddeld meer kationen dan anionen (of andersom) zijn. De Elektrische Dubbellaag is niet groot, zelden groter dan enkele tientallen nanometers (1 nanometer is één miljardste van een meter). Op grote schaal zal de Elektrische Dubbellaag dus geen grote invloed hebben op het water en de vaste stof zelf, je zal deze bijvoorbeeld niet merken in je glas water, maar het beïnvloedt wel hoe de twee stoffen met elkaar wisselwerken.

Daarentegen wordt de elektrische dubbellaag steeds belangrijker hoe kleiner de schaal is, omdat de verhouding tussen het oppervlak en volume dan toeneemt. De oppervlakte/volume verhouding is zeer belangrijk voor processen die aan het oppervlak plaatsvinden. Neem als voorbeeld water verdamping, een proces dat via het water-lucht grensvlak gaat. Als je een bepaalde hoeveelheid water wil laten verdampen gaat dit sneller als je het water uitspreidt als een plas dan dat je het in een beker bewaard. Dit

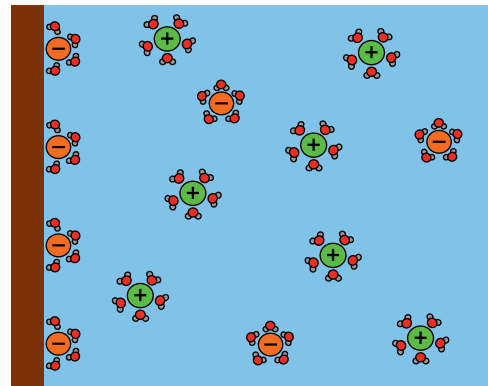


**Figure C.5.:** De Elektrische Dubbellaag als gevolg van oppervlak met negatieve lading.

komt omdat een plas water een groter water-lucht grensvlak heeft dan datzelfde volume water in de vorm van een beker. Om dezelfde reden zal bij hele kleine systemen de Elektrische Dubbellaag dan ook de dominante factor zijn die het gedrag van het systeem bepaalt. Dit soort systemen zijn op veel plekken te vinden. Zo zit elk levend wezen er vol mee, en zijn ze bijvoorbeeld ook voor geologie een belangrijk fenomeen om rekening mee te houden. In dit proefschrift bestuderen we microfluidische en nanofluidische apparaten, een algemene term voor zulke kleine systemen, en bestuderen we de invloed van de elektrische dubbellaag op zulke systemen.

## Microscopische kanalen

Micro- en nanofluidische apparaten zijn in essentie waterleidingen: een kanaal of set van kanalen waar water doorheen kan stromen, maar dan microscopisch klein. Zoals de naam suggereert, is een typische afmeting ergens tussen een nanometer (1 miljardste meter) en een micrometer (1 miljoenste meter). Deze micro- en nanofluidische apparaten hebben echter hele andere eigenschappen dan de waterleidingen die bijvoorbeeld in huizen gebruikt worden. Eén van de voornaamste redenen hiervoor is de elektrische dubbellaag; hoe kleiner het kanaal is, hoe groter de relatieve invloed hiervan. Een belangrijke vraag voor micro- en nanofluidische apparaten is hoe waterstroom wordt beïnvloed (of zelfs opgewekt) door de elektrische dubbellaag.

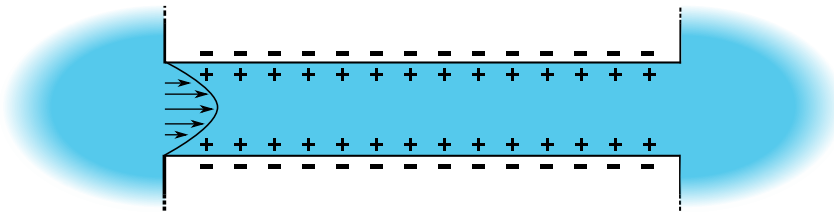


**Figure C.6.:** Een typisch microscopisch, elektrokinetisch kanaal met een geladen wand die twee water reservoirs met elkaar verbindt.

De wisselwerking tussen vloeistofstroom en de Elektrische Dubbellaag geeft nanofluidische apparaten unieke eigenschappen, en dus interessante toepassingen. Zo worden nanofluidische apparaten gebruikt om individuele DNA moleculen te scheiden (zodat die gelezen kunnen worden), maar ze kunnen bijvoorbeeld ook gebruikt worden om energie op te wekken. Dit laatste wordt momenteel al toegepast op de Afsluitdijk, waar men Reverse Electrodialysis (Omgekeerde Elektrodialyse) gebruikt om energie te winnen uit het mengen van zoet- en zoutwater.

## Deel I

Dit proefschrift is in 3 delen gesplitst. In het eerste deel bespreken we ons onderzoek naar een vaste stof-water grensvlak in evenwicht. We proberen uit te zoeken hoe het grensvlak er precies uit ziet en we onderzoeken hoe verschillende soorten ionen zich gedragen bij dit grensvlak. Als vaste stof hebben we gekozen voor muscoviet mica, een soort klei, dat de bijzondere eigenschap heeft dat het oppervlak plat is op atomisch niveau. Dit is belangrijk, omdat dit het mogelijk maakt een zeer precieze experimentele techniek te gebruiken, Surface X-Ray Diffraction (oppervlakte röntgendiffractie). Hierbij wordt röntgenstraling op het oppervlakte geschoten, en aan de hand hoeveel waarheen weerkaatst is te achterhalen wat voor en hoeveel atomen er aan het oppervlak zit. Zo is te achterhalen hoeveel van een bepaald kation aan het oppervlak zit, cesium ( $\text{Cs}^+$ ) en calcium ( $\text{Ca}^{2+}$ ) in ons geval, in verhouding tot het zoutgehalte en compositie van het water.

Data van oppervlakte röntgendiffractie hebben we gecombineerd met Atomic Force Microscopy (atomische kracht microscoop). Dit is een heel andere meettechniek, waarbij men een naald van enkele tot tientallen nanometers naar het oppervlak laat zakken en de kracht van het oppervlak op deze naald meet. Aan de hand van deze kracht is te achterhalen hoeveel lading er netto op het oppervlak zit, en dus hoeveel meer (of minder) kationen dan anionen op het oppervlak zit.

In deel I hebben we een model ontwikkeld waarmee we beide data sets kunnen verklaren. Het is relatief makkelijk om een model te schrijven voor elke losse dataset, maar diezelfde modellen zijn niet in staat de andere dataset te verklaren. We moesten dus huidige modellen herzien totdat we een model hadden dat beide datasets kon verklaren. Als een model beide datasets tegelijk kan reproduceren, weten we met meer zekerheid dat dat model accurater de werkelijke situatie weerspiegelt. Zo hebben we bijvoorbeeld gevonden dat, hoewel mica negatief geladen is, er ook een verbazingwekkend grote hoeveelheid anionen aan het oppervlak zit. Daarnaast hebben we ook de competitie tussen twee verschillende kationen, cesium en calcium, onderzocht, die beide op dezelfde plek proberen te adsorberen. Zo hebben we gevonden dat cesium liever adsorbeert dan calcium, wat we konden relateren aan de energie van de hydratatieschil.

## Deel II

Terwijl in deel I alles in evenwicht was en stil stond, onderzoeken we in deel II wat er gebeurt als het water niet stil staat maar kan stromen. We onderzoeken een microscopisch kanaal met geladen wanden, en analyseren de transport eigenschappen van

zo'n kanaal. Deze transport eigenschappen worden namelijk sterk beïnvloed door de elektrische dubbellaag.

We ontwikkelen een theoretische methode waarmee de transport eigenschappen van microscopische kanalen geanalyseerd kunnen worden. Als voorbeeld richten we ons op het geval dat het kanaal twee reservoirs verbindt met verschillende zoutconcentraties, bijvoorbeeld een reservoir met zout en een reservoir met zoet water. De zoutconcentratie heeft een directe invloed op de elektrische dubbellaag, en daarmee dus indirect ook op de transport eigenschappen van het kanaal. Bij een groot verschil in zout concentratie, bijvoorbeeld bij rivier- en zeewater, zijn eerdere methodes niet meer accuraat. Daarom hebben wij in deel II een methode ontwikkeld waarmee we dit soort situaties wel accuraat kunnen beschrijven.

Als voorbeeld analyseren we een omgekeerd elektrolyse systeem, een systeem dat een elektrische stroom kan opwekken uit het mengen van zoet en zout water via zo'n kanaal. Met onze theoretische methode kunnen we voorspellen wat er gebeurt als de eigenschappen van het kanaal veranderen, zoals de grootte of de materiaal soort van het kanaal. Zo'n analyse kan bijdragen aan het optimaliseren van Omgekeerd Elektrolyse apparaten.

Bij deze theoretische methode lag de focus op een enkel kanaal. Omgekeerd Elektrolyse, echter, werkt niet met maar één kanaal met veel van dit soort kanalen verdeeld over een oppervlak, een membraan (een vast oppervlak met kleine gaten/kanalen). Het is dus belangrijk om te onderzoeken of de eigenschappen van een enkel kanaal ook gelden voor een membraan. In het laatste hoofdstuk van dit deel onderzoeken we dit, en vinden dat het gedrag van een collectie kanalen niet altijd hetzelfde is als de som van de individuele kanalen. We vinden een wisselwerking tussen twee naburige kanalen die de stroom door de kanalen dempt. In principe zou je verwachten dat de stroom door een membraan het grootst is als de kanalen zo dicht mogelijk op elkaar zitten, maar door deze wisselwerking vinden we dat het optimale ontwerp de kanalen niet te dicht op elkaar zet, maar ook niet te ver uit elkaar.

## Deel III

In het laatste deel gaan we nog een stap verder dan in deel II, en laten we niet alleen het water vrij stromen, maar behandelen we ook het grensvlak van het microscopische kanaal zelf als een dynamisch onderdeel. We onderzoeken wat er gebeurt als de lading op het oppervlak, zoals de geadsorbeerde ionen in figuur C.4, zelf ook vrij kunnen bewegen (het is namelijk eerder al experimenteel aangetoond dat dit het geval is). De elektrische dubbellaag is een direct gevolg van de ladingen op het oppervlak,

en dus kunnen de oppervlakte ladingen indirect, via de elektrische dubbellaag, de eigenschappen van het microscopische kanaal beïnvloeden.

In dit laatste deel onderzoeken we deze invloed eerst met numerieke berekeningen, wat inhoudt dat we bewegingsvergelijkingen van de ionen en het water met een computer programma oplossen, en daarna met analytische berekeningen, wat inhoudt dat we de vergelijkingen met pen en papier oplossen. Het voordeel van de eerste aanpak is dat het meer nauwkeurige oplossingen geeft van de relevante vergelijkingen, en het voordeel van de tweede aanpak is dat we beter fysisch inzicht in het systeem krijgen.

We kijken weer naar een microscopisch kanaal waar water door stroomt, en we ontdekken dat de oppervlakte ladingen met de vloeistof mee gaan bewegen. Aangezien de oppervlakte ladingen niet in het water zitten, is dit in eerste instantie niet logisch, maar wij vinden een fysisch mechanisme dat verklaart hoe het water indirect toch de oppervlakte ladingen kan beïnvloeden. Dit mechanisme zorgt ervoor dat de oppervlakte lading bij de ingang van het kanaal lager is dan bij de uitgang van het kanaal. Zo'n inhomogene oppervlakte ladingsverdeling heeft een grote invloed op de transport eigenschappen van het microscopische kanaal, omdat deze oppervlaktelading de elektrische dubbellaag maakt.

In dit deel bespreken we hoe deze inhomogene ladingsverdeling gevormd wordt, en welke processen de eigenschappen van deze ladingsverdeling bepalen. We identificeren de drie processen die de ladingsverdeling bepalen: de adsorptie en desorptie van de ionen, diffusie (spontane beweging door thermische fluctuaties) en de elektrische geleiding van de geadsorbeerde ladingen. Hoe de ladingsverdeling eruit ziet, wordt uiteindelijk bepaald door welk proces het snelst is.

## Slotwoord

In deze samenvatting heb ik de statische en dynamische eigenschappen van een grensvlak tussen een vaste stof en water besproken, alsook de resultaten van mijn onderzoek van de afgelopen 4 jaar. Ten slotte is het de moeite waard de inhoud van dit proefschrift in een brede context te plaatsen.

In het eerste deel hebben we de adsorptie en competitie van cesium en calcium ionen besproken. Deze competitie is relevant omdat calcium ionen,  $\text{Ca}^{2+}$ , twee keer zoveel lading dragen vergeleken met cesium ionen,  $\text{Cs}^+$ . Als een oppervlak gevuld is met calcium ionen is er dus nog ruimte voor een extra anion vergeleken met een oppervlak gevuld met alleen cesium ionen. Nu blijkt dit een belangrijk fenomeen voor olie winning. Olie bevat namelijk componenten met een negatieve lading, die dus kunnen blijven 'plakken' op calcium maar niet op cesium. Door geadsorbeerd calcium

in olierijk gesteente te vervangen met cesium, laat het gesteente meer olie los. Dit is mogelijke verklaring voor de observatie dat er meer olie vrij komt als er zoet water i.p.v. zee water wordt gebruikt bij oliewinning. Een groter begrip van dit proces is dus uitermate belangrijk voor de olie industrie.

In de laatste twee delen heb ik microscopische (nanofluidische) kanalen besproken, waar de interessante en unieke eigenschappen van een grensvlak tussen een vaste stof en water naar voren komen. De huidige techniek is ver genoeg ontwikkeld om volop gebruik te kunnen maken van nanofluidische kanalen. Als voorbeeld heb ik al omgekeerd elektrolyse genoemd, wat op de Afsluitdijk gebruikt wordt om energie op te wekken. Deze techniek valt onder de grotere koepel van blauwe energie. Het doel van blauwe energie is om stroom op te wekken uit het mengen van zoet en zout water, en nanofluidische kanalen zijn veelbelovend voor blauwe energie. Een beter begrip van dit soort kanalen helpt om blauwe energie beter te maken.

Daarnaast worden nanofluidische kanalen gebruikt om opgeloste deeltjes met nauwkeurigheid te beheren. Voor goede nauwkeurigheid is goed begrip nodig, dus hoe beter ons begrip hoe beter we materialen op de microscopische schaal kunnen beheersen. Hoe groter ons begrip, hoe beter onze technologie wordt, en hierom wordt hier veel onderzoek naar gedaan. Een mooi voorbeeld hiervan is dat nanofluidische kanalen gebruikt worden om apparaten te bouwen die DNA moleculen kunnen lezen. Verder weten we dat cellen nanofluidische kanalen gebruiken. Zenuwcellen werken door zout in en uit de cel te transporteren, wat een interessante samenwerking tussen biologie en natuurkunde presenteert. De grote complexiteit van biologische systemen zorgt dat er nog vele open vragen zijn in deze discipline, maar dit betekent dat wij hier nog veel van kunnen leren. Ik hoop dat mijn werk de wetenschap helpt het begrip te vergroten, zodat we het optimale uit deze interessante en veelbelovende systemen kunnen halen.

Na vier jaar onderzoek wordt één ding snel duidelijk: hoe dieper je in een onderwerp duikt, hoe complexer het blijkt te zijn, en hoe meer onbeantwoorde vragen je zal ontdekken. Dit is een belangrijke les die voor iedereen geldt, en volgt niet alleen uit mijn proefschrift maar uit elke proefschrift. Wetenschap kent geen einde, het is een eindeloos proces waarin we telkens meer nieuwe vragen stellen. Er zal nooit een laatste vraag zijn om te stellen, te onderzoeken en te beantwoorden, maar het was me een genoegen een steentje hieraan bij te dragen.

# Acknowledgements

In dit proefschrift heb ik het resultaat van vier jaar onderzoek gepresenteerd. Onderzoek doe je natuurlijk niet in een vacuüm, en hier wil ik de mensen bedanken die hebben bijgedragen aan het tot stand komen van dit proefschrift.

Ten eerste wil ik diegene bedanken die de grootste en belangrijkste bijdrage aan dit proefschrift heeft geleverd, mijn begeleider René van Roij. Al vanaf mijn master had ik door dat jij een geweldige begeleider bent, en wist al vanaf het begin dat ik een goede keuze had gemaakt om bij jou onderzoek te doen. Ik kon altijd bij jou terecht met een vraag of probleem, je nam mijn ideeën serieus en luisterde enthousiast naar wat ik te zeggen had. Tegelijkertijd accepteerde je mijn ideeën niet zomaar, en liet je me altijd werken om eerst mezelf, en daarna jou te overtuigen. Bij elk overleg kwam je met suggesties en ideeën waar ik zelf niet aan gedacht had. Je forceerde me niet alleen altijd kritisch te kijken naar mijn eigen werk, maar ook goed na te denken waar we met het onderzoek heen wilde.

Ten tweede wil ik mijn collega's van het Rock-on-Chip consortium bedanken. De samenstelling van deze groep is vaak veranderd gedurende vier jaar, maar ik heb ervan genoten onderdeel te zijn van de constante kern met Simone, Martin en Sander: we hebben samen altijd wat leuks weten te maken van de internationale en groepsbijeenkomsten. Hoewel we allemaal een heel andere achtergrond hadden, was het altijd leuk om regelmatig samen te komen en zo gaandeweg ons onderzoek vorm te geven. In het bijzonder wil ik Sander en Aram bedanken voor een zeer prettige samenwerking. De slimme opmerkingen van onze leiders Frieder en Igor zorgden ervoor dat ik niet alleen maar op een theoretisch natuurkundige manier naar mijn onderzoek keek, en spoorde me aan mijn onderzoek in een grotere context te plaatsen.

I would also like to thank my colleagues of the theoretical soft condensed matter group, Jeffrey, Mathijs, Bram, Guiseppe, Sela, Tara, Jeroen, Cheng, Peter and Willem, due to you I have enjoyed my four years in this group. Mathijs, ik heb genoten van onze samenwerking en heb veel van je geleerd. Jeffrey, ik vond het leuk om met jou een kantoor te delen en je vele ideeën aan te horen, waarvan één heeft geleid tot mijn eerste artikel. Jeroen, bedankt voor de vele lunchpauzes, ik heb altijd genoten van deze welkome onderbreking waar we alle aspecten van het leven bespraken. Willem, ik vind het erg leuk dat jij deel van mijn werk heb opgepakt, en mooi om te zien hoe jij daar je eigen draai aan geeft: ik heb er vertrouwen in dat je er iets moois van gaat maken. Of

course I would also like to thank all other colleagues at the ITP, who have made my four years at the institute very enjoyable. Ook wil ik alle vrienden buiten natuurkunde bedanken voor de nodige afleiding en de vele gezellige middagen en avonden.

Als laatst wil ik ook mijn familie bedanken. Als eerste mijn ouders, Mieke en John, jullie zijn mijn hele leven al een constante steun, waar ik jullie niet genoeg voor kan bedanken. Ten tweede mijn broers en zussen bedanken, Loes, Paul, Tom en Floor, ondanks lastige periodes hebben we altijd een leuk gezin weten te vormen, en ik vind het geweldig dat die nu alleen maar leuker wordt met de nieuwe aanwinsten Tessa, Marit en Oscar. Als laatst wil ik mijn vriendin Sophie bedanken. Je bent niet alleen een constante steun, maar je blijft me ook altijd uitdagen. Ik zeg het waarschijnlijk niet vaak genoeg, maar jouw steun en toewijding waren gedurende mijn promotie erg belangrijk voor mij, en dat zal het in de toekomst ook zeker blijven.

# About the author

Ben Lucas Werkhoven was born on June 14 1991 in Utrecht, the Netherlands. Growing up in Vleuten, he attended the Christelijk Gymnasium in Utrecht and graduated in 2009. In 2012 he obtained his bachelors degree in Physics and Astronomy cum laude, with a thesis on confined electron in a single doped quantum dot. In the same year he enrolled in the master Theoretical Physics at Utrecht University, from which he graduated cum laude in 2015, with a master thesis on harvesting vibrational energy with a droplet engine under the supervision of prof. dr. René van Roij. Afterwards, he continued with a PhD study under prof. dr. René van Roij on the static and dynamic behaviour of solid-water interfaces. This thesis is an account of the main results of this research.

